

CHEMICAL SYNTHESIS AND CHARACTERIZATION OF BIOCOMPOSITE WITH IMPROVED MECHANICAL PROPERTIES AND STUDY OF ITS BIOCMPATIBILITY

Thesis Submitted for the Award of the Degree of

DOCTOR OF PHILOSOPHY

in

Biotechnology

By

Bableen Flora

Registration Number: 11617875

Supervised By

Dr. Anjuvan Singh (15950)

Department of Biotechnology (Professor)

Lovely Professional University



LOVELY PROFESSIONAL UNIVERSITY, PUNJAB

2024

DECLARATION

I, hereby declared that the presented work in the thesis entitled “Chemical Synthesis and Characterization of Biocomposite with improved Mechanical properties and study of its biocompatibility” (in fulfilment of degree of **Doctor of Philosophy (Ph. D.)**) is outcome of research work carried out by me under the supervision of Dr. Anjuvan Singh, working as Professor in the Department of Biotechnology, School of Biosciences & Bioengineering of Lovely Professional University, Punjab, India. In keeping with general practice of reporting scientific observations, due acknowledgements have been made whenever work described here has been based on findings of another investigator. This work has not been submitted in part or full to any other University or Institute for the award of any degree.


(Signature of Scholar)

Name of the scholar: Bableen Flora

Registration No.: 11617875

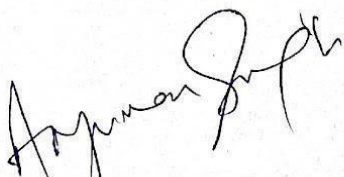
Department/school: Biotechnology/ School of Biosciences & Bioengineering

Lovely Professional University,

Punjab, India

CERTIFICATE

This is to certify that the work reported in the Ph. D. thesis entitled “Chemical Synthesis and Characterization of Biocomposite with improved Mechanical properties and study of its biocompatibility” submitted in fulfillment of the requirement for the reward of degree of **Doctor of Philosophy (Ph.D.)** in the Department of Biotechnology, School of Biosciences & Bioengineering, is a research work carried out by Bableen Flora, registration number of 11617875, is bonafide record of his/her original work carried out under my supervision and that no part of thesis has been submitted for any other degree, diploma or equivalent course.



(Signature of Supervisor)

Name of supervisor: Dr. Anjuvan Singh

Designation: Professor

Department/school: Department of Biotechnology, School of Biosciences & Bioengineering

University: Lovely Professional University, Phagwara, Punjab (INDIA)

ABSTRACT

Instead of focusing on separate biomaterials like ceramic, metallic, and polymeric materials, researchers are more interested in synthesizing bio composites. In order to achieve the desirable properties, the composites have been synthesized using different materials. Bioactive ceramics have garnered considerable interest due to their biocompatibility, including of Hydroxyapatite (HA) that has been found to be the most suitable substitute for bone auxiliary, since it is the mineral component of bone matrix that most closely mimics the bone. The intrinsic low strength of HA hinders its usage as a long bone replacement and load-bearing structure. As a result, it is vital to produce composite constituents with enhanced biomechanical properties as, hardness and young's modulus. The objective of this research is to synthesize hydroxyapatite-based composites with enhanced mechanical properties, good biocompatibility and acceptable biodegradability. In this endeavor, the synthesis of binary composite is reported. At first, the hydroxyapatite has been synthesized using chemical precipitation method and later the pretreatment to the synthesized hydroxyapatite and graphene oxide has been done. The calcination of hydroxyapatite was done whereas reduction of graphene oxide has also been employed. The characterization of synthesized hydroxyapatite powders has been done so as to evaluate the structural changes occurred after obtaining the materials. Afterwards, the calcined hydroxyapatite and reduced graphene oxide has been blended through in different ratios so as to obtain the binary composite through ball milling. The binary composites of (Hydroxyapatite: Reduced graphene oxide) HA:rGO has been made in ratios of 90:10 namely HrG1, 80:20 namely HrG2, 70:30 namely HrG3, 60:40 namely HrG4 and 50:50 namely HrG5. Further, these composites have been investigated through FTIR, XRD along with mechanical characteristics such as compressive strength and Young's modulus of elasticity. In order to boost up the mechanical properties heat treatment of 2 hours at 200°C has been employed to the pellets containing the composite of hydroxyapatite and reduced graphene oxide (HA/rGo) and then were examined for mechanical characteristics. Additionally, the biodegradable polymer carboxymethyl cellulose (CMC) has been used to reinforce the binary composite. Further, the variant of binary composite has been further reinforced with the biodegradable polymer named carboxymethyl cellulose (CMC). The polymer addition into the binary blend HrG4 that has attained the highest Compressive strength leads to the formation of ternary blend. Different percentage compositions of carboxymethyl

cellulose have been incorporated in blends for hydroxyapatite, reduced graphene oxide and carboxymethyl cellulose found to be 60:30:10 in B1, 60:20:20 in B2 and 60:10:30 in B3. Thereafter, these ternary composites have been subjected to heat treatment under constant pressure of 7.8 psi at two different temperatures of 100°C and 150°C and for three-time intervals. After being heat treatment of the ternary composites, the structural and morphological characterization has been done. The novel ternary composite has been scrutinized for the Compressive strength using universal testing machine (UTM) and for the hydrophilicity through water contact angle measurement (WCA). Further, the obtained data for the ternary blends has been optimized using grey-Taguchi approach. The grey-Taguchi method has been implemented for the working conditions of processing temperature, processing time and the compositions of the carboxymethyl cellulose. Whereas the wettability and the mechanical strength has been taken as the outcomes for the experiments.

Nevertheless, the biodegradability and biomineralization assays also have been performed for the optimized blends. Moreover, the biological compatibility of the prepared ternary composite has been evaluated using MTT assay.

On calcination of the hydroxyapatite, an elevation in the crystallinity has been observed from $42.49 \pm 1.2\%$ in hydroxyapatite (HA) to $73.09 \pm 1.5\%$ in calcined hydroxyapatite (cHA). The successful thermal reduction has been achieved and validated through FTIR and XRD in which a clear peak shift from 26.35° to 11.6° has been obtained. Further the binary composites of the calcined hydroxyapatite and reduced graphene oxide has been characterized and the morphology has also been studied using FESEM. The surface roughness has been obtained to be decreasing on increasing the concentration of reduced graphene oxide. Further, the mechanical studies for the blends of calcined hydroxyapatite and reduced graphene oxide have been performed. The maximum compressive strength for HrG4 to be 185.16 ± 4.87 MPa. Further, the carboxymethyl cellulose has been incorporated to the composite of calcined hydroxyapatite and reduced graphene oxide so as to obtain ternary composite. The ternary composite of calcined hydroxyapatite, reduced graphene oxide and carboxymethyl cellulose has been fabricated through heating under pressure. The Compressive strength and the wettability have been determined for the different variants of the ternary composites which further have been optimized using grey-Taguchi approach. As per grey relational grade analysis (GRG), composition has the highest effect on the outcomes followed by the processing time and

temperature. Nevertheless, the desirability test also has been employed which validates the obtained experimental data. The obtained R^2 for GRG analysis found to be 0.994 whereas the predicted determined as 0.964 showing the least difference, hence the success of the experimental data obtained. Furthermore, the morphology of the ternary composites revealed the agglomeration and on analyzing the water contact angle, it has been found that the ternary composite of HA/rGO/CMC is hydrophilic in nature. Finally, after being evaluated using the MTT assay, it was found that the ternary composite was non-toxic and showed biodegradability because of the presence of carboxymethyl cellulose.

Keywords: Hydroxyapatite, Reduced graphene oxide, Carboxymethyl cellulose, ImageJ, Surface roughness, Wettability, Grey-Taguchi, Biodegradability

ACKNOWLEDGEMENTS

In this moment of accomplishment, I would like to express my gratitude and pay homage to the person who played a crucial role in guiding and supporting me throughout this research journey, Dr. Anjuvan Singh. Without his unwavering encouragement and guidance, this work would not have been possible.

First and foremost, I would like to extend my deepest appreciation to my guide, Dr. Anjuvan Singh. From the very early stages of this research, he stood by my side and provided invaluable support. I am truly grateful for her unwavering dedication and the countless hours he devoted to reviewing my thesis progress, offering valuable suggestions, and making necessary corrections. His courage and conviction have always been a great source of inspiration for me, and I hope to continue working with his noble thoughts. I can only express my thanks to him through my future work. My indebtedness to him goes beyond what he can comprehend.

I would like to express my heartfelt gratitude to the members of the Doctoral Research Committee (DSC), Their constructive comments and feedback have significantly contributed to the improvement of the quality of this thesis. Amidst their busy schedules, I am grateful that they accepted the responsibility of being committee members.

I am especially grateful to Dr Swastik Pradhan, Assistant Professor, Department of Mechanical Engineering, Lovely Professional University and Dr Piyush Kumar Gupta Department of Life Sciences, Sharda School of Basic Sciences and Research, Sharda University, Greater Noida for enriching my experience during my time at Lovely Professional University. Their presence has made a significant difference. I would also like to extend my gratitude to Dr Gil Goncalves, TEMA / Department of Mechanical Engineering, Campus Universitário de Santiago | 3810-193 Aveiro for their valuable support and assistance in my research work. Further, I would also like to express my special gratitude to Dr Mahesh Kumar Sah, Assistant Professor, Department of Biotechnology from Dr B R Ambedkar National Institute of Technology, Jalandhar whose assistance has been invaluable.

Words fail me when expressing my appreciation for my father Mr. Manjit Singh Flora, my mother Mrs. Harjit Kaur, my sister Mrs. Sonia Flora Panesar, my husband Mr. Ajay Talwar and my son Arjun Ajay Talwar whose motivation, love, and unwavering confidence in me have lightened my burden. Their support has been immeasurable.

Finally, I would like to express my deepest gratitude to Dr. Harpinder Singh, Head of Laboratory, School of Mechanical Engineering, Dr Jai Inder Singh and Mr. Sunminder Singh School of Mechanical Engineering and all those individuals who have played a crucial role in the successful completion of this thesis. To those I could not mention personally, I apologize. It is through the support and encouragement of numerous individuals, including well-wishers, friends, colleagues, and various institutions, that this thesis has reached its completion. This has truly been an unforgettable experience for me.

Thank you to each and every person who has contributed in their own way to the realization and success of this study. Your support will always be cherished.

- Bableen Flora

TABLE OF CONTENT

CONTENT		PAGE NO.
Declaration		i
Certificate		ii
Abstract		iii-v
Acknowledgment		vi
List of Tables		x
List of Figures		xi-xiii
List of Abbreviations		xiv-xv
CHAPTER 1: INTRODUCTION		1-6
1.1	Need and Scope of Present Research	4
1.2	Outline of thesis	5
1.2	Graphical Abstract	6
CHAPTER 2: LITERATURE SURVEY		7
2.1	Background of biomaterials	8
2.2	Biomaterials and Types of Biomaterials	9
2.2.1	Metallic Biomaterials	10
2.2.2	Ceramic biomaterials	10-12
2.2.3	Polymeric Biomaterials	12-14
2.2.4	Composite Biomaterials	14-16
2.2.5	Nanomaterials	18
2.2.6	Smart Biomaterials	18-19
2.3	Biomaterial types on basis of generation	19-20
2.4	Fabrication of Biomaterials	21-25
2.4.1	Solvent casting and Particulate Leaching	22
2.4.2	Melt Molding	22
2.4.3	Gas foaming	22
2.4.4	Electrodeposition	23
2.4.5	Stereolithography	23
2.4.6	Fused Deposition Modeling	23
2.4.7	3D Bioprinting	23
2.5	Hydroxyapatite	26-28
2.6	Reduced graphene oxide	29-32
2.7	Carboxymethyl Cellulose	32-35
2.8	Research gap and Scope of Research	35-36
2.9	Objectives of the Research	37
CHAPTER 3: MATERIALS AND METHODS		38
3.1	Pre-treatment of ceramic and carbon-based components	39
3.1.1	Synthesis of Hydroxyapatite and Calcination of prepared Hydroxyapatite	40
3.1.1.1	Chemical Synthesis of Hydroxyapatite	40

3.1.1.2	Calcination of Hydroxyapatite	41
3.1.2	Reduction of Graphene oxide	41-42
3.2	Preparation of reduced graphene oxide and hydroxyapatite composites	42-43
3.3	Characterization of Binary composites	44-46
3.4	Thermal pressing	46
3.5	Preparation of Ternary composites	46-48
3.6	Characterization of ternary composites	48
3.7	Physiochemical characterization	48-49
3.7.1	X-ray Diffraction	48-49
3.7.2	Fourier Transform Infrared Spectroscopy	49
3.7.3	Thermo gravimetric analysis	49
3.8	Grey-Taguchi Optimization	50-53
3.8.1	Grey Relational Analysis (GRA)	51
3.8.2	ANOVA analysis	52
3.8.3	Desirability test	53
3.9	Mechanical Behaviour	54-58
3.10	Surface roughness and Wettability of composites	58-60
3.11	Biomineralization in SBF Solution	60-61
3.12	In-Vitro Biodegradation	61-62
3.13	Cell Culture and Cytotoxicity	62-63
3.14	Statistical Analysis	63-64
CHAPTER 4: RESULTS & DISCUSSION		65
<i>Part I: Processing and characterization of additives for Biomaterial preparation</i>		66
4.1	Synthesis of hydroxyapatite and calcination of prepared hydroxyapatite	
4.1	FTIR analysis	66-67
4.2	XRD analysis	67-68
4.3	Thermal reduction of Graphene oxide	68
4.4	Synthesis of Binary composite of calcined hydroxyapatite and reduced graphene oxide	71
4.4.1	Characterization of composites using FTIR analysis	71
4.4.2	Characterization of composites using XRD analysis	72-74
4.4.3	Morphology of binary composites	74-76
4.4.4	Surface roughness of composites	76-79
Part II: Study of Mechanical Properties of Biomaterial fillers		79-80
4.5	<i>Mechanical Behaviour of composites</i>	80-82
Part III: Biomaterial fabrication steps with addition of appropriate polymer to additives and characterization		83

4.6	Selection of ideal Processing temperature	83-84
4.6.1	Physiochemical characterization	85-86
4.6.1.1	FTIR analysis	85-87
4.6.1.2	XRD analysis	88-90
4.6.2	Compressive strength of composites	91-93
4.6.3	Orthogonal array of experimental result	93-95
4.7	Study of compressive strength through ANOVA analysis	95-98
4.8	An examination of Wettability using ANOVA	99-101
4.9	GRG examination using ANOVA	102-105
4.10	Desirability Function Analysis (DFA) based optimization	105-108
4.11	Analysis of Regression	109-111
4.12	Morphological analysis	111-114
4.13	Surface roughness of composites	114-117
4.14	Wettability	117-118
4.15	Thermal behavior of Composites	118-120
PART IV: Biological compatibility testing Parameters		121
4.16	In-vitro biomineralization of composites	121
4.17	Cytotoxicity Assay	122-125
4.18	In-vitro Biodegradation	126-127
CHAPTER 5: SUMMARY AND CONCLUSION		128-132
BIBLIOGRAPHY		133-158
PUBLICATIONS		159-160

LIST OF TABLES

<u>Table no.</u>	<u>Description</u>	<u>Page No.</u>
Table 2.1	Different forms of Polymeric Biomaterial	14
Table 2.2	Various composites and their application in Tissue engineering	16
Table 2.3	Different fabrication methods with perks, challenges and Parameters	24-25
Table 2.4	Hydroxyapatite composites for different applications with major Outcomes	27-28
Table 2.5	Use of reduced graphene oxide composites for different Applications	32
Table 3.1	Percentage of cHA and rGO used for different Blends	42
Table 3.2	Ceramic based polymeric blends of HA,rGO, CMC thermally pressed at different temperature and various time intervals	48
Table 3.3	Concentration of Ions in grams for Simulated body Fluid (SBF)	61
Table 4.1	Atomic Spacing in blends of HA &rGO	74
Table 4.2	Roughness parameters of blends of Hap and rGO	79
Table 4.3	Composition of Hydroxyapatite, reduced graphene oxide	84
Table 4.4	Experimental details for composite synthesis	93-94
Table 4.5	Calculation of Grey relational Grade	94
Table 4.6	ANOVA analysis for compressive strength	97
Table 4.7	ANOVA analysis of the wettability	100
Table 4.8	ANOVA analysis of GRG	103
Table 4.9	Description of Predicted and Adjusted values of the outputs	110
Table 4.10	Roughness means & RMS of ceramic based polymeric composites	116

LIST OF FIGURES

<u>Figure</u>	<u>Description</u>	<u>Page no.</u>
Figure 2.1	Classification of Biomaterials	9
Figure 2.2	Classification of Nanomaterial	18
Figure 2.3	Generation of Biomaterial	20
Figure 2.4	Categorization of Biofabrication methods	21
Figure 2.5	Different methods for reduction of graphene oxide	30
Figure 2.6	Applications of reduced graphene oxide	31
Figure 2.7	Properties of Carboxymethyl cellulose	33
Figure 3.1	Schematic diagram for preparation of binary composite	41
Figure 3.2	Flowchart to demonstrate overall experimental procedure	43
Figure 3.3	Schematic representation of X-ray diffraction	44
Figure 3.4	The schematic representation of FTIR spectroscopy	45
Figure 3.5	The flowchart to demonstrate the overall experimental Procedure	47
Figure 3.6	Flowchart representation of Grey-Taguchi approach for Optimization	50
Figure 3.7	The setup of Universal testing machine (UTM)	55
Figure 3.8	The experimental setup for the mechanical behavior of the composites	56
Figure 3.9	Microhardness test	57
Figure 3.10	Flowchart describe calculation of surface roughness using FESEM images through ImageJ	59
Figure 3.11	Wettability of surface using contact angle measurement	60
Figure 3.12	The experimental procedure for the biodegradation assay	62
Figure 4.1	FTIR analysis of HA and cHA	67
Figure 4.2	XRD peaks of cHA and HA	68

Figure 4.3	FTIR analysis of GO & rGO	69
Figure 4.4	XRD peaksfor GO & rGO	70
Figure 4.5	Pellets of cHAP &rGO composites in different ratios	71
Figure 4.6	FTIR spectra of composites of Hap & rGO	72
Figure 4.7	XRD analysis of blends of hydroxyapatite and reduced graphene oxide	73
Figure 4.8 (a)	Morphology of starting material hydroxyapatite, graphene oxide and reduced graphene oxide	74
Figure 4.8 (b)	Morphology of composites of calcined hydroxyapatite and reduced graphene oxide (a)cHA(b)HrG1(c)HrG2 (d)HrG3 (e)HrG4(f) HrG5	75
Figure 4.9	Particle size analysis of composites of Hap &rGO	76
Figure 4.10	Surface roughness (a-a2) HrG1, (b-b2) HrG2, (c-c2) HrG3,(d-d2) HrG4, (e-e2) HrG5	77-78
Figure 4.11	Statistical analysis of compressive strength	80
Figure 4.12	Stress-Strain graph for different composite variations of HA & rGO	81
Figure 4.13	FTIR analysis of blends pressurized heating at 200°C and 350°C	83
Figure 4.14	FTIR peaks for blend B1, B2, B3 thermal pressing at 100°C and 150°C and blend of calcined hydroxyapatite and reduced graphene oxide	86
Figure 4.15	FTIR analysis of carboxymethyl cellulose (CMC)	87
Figure 4.16(a)	XRD peaks of thermal pressing polymeric blends at 100°C &150°C and HrGO blend	89
Figure 4.16(b)	Crystallinity of blends B1,B2,B3 thermal pressing at 100°C & 150°C	90
Figure 4.17	Compressive strength of hydroxyapatite and reduced graphene oxide blend and ceramic-based polymeric blend thermal pressing at 100°C and 150°C	91
Figure 4.18	Vicker's hardness and modulus of calcined hydroxyapatite and reduced graphene oxide and ceramic-based polymeric blends thermal pressing at 100°C and 150°C	92
Figure 4.19	Normality plot of compressive strength of composite	96
Figure 4.20	Effect of processing parameters on compressive strength of polymeric blends with 3D surface (a1, b1, c1) and contour plot (a2, b2, c2) for polymeric blend	98

Figure 4.21	Normality plot for wettability of composite	99
Figure 4.22	Effect of processing parameters on the wettability of polymeric blend with 3D surface (a1, b1, c1) and contour plot (a2, b2, c2) for the composite	101
Figure 4.23	Normality plot of grey relational grade (GRG)	102
Figure 4.24	Analysis of processing conditions with grey relational grade (GRG) through 3D surface (a1, b1, c1) and contour plot (a2, b2, c2) for the blend	104
Figure 4.25	Plot for desirability	105
Figure 4.26	Effect of output response with respect to composition and temperature after using desirability approach	106
Figure 4.27	Effect of output responses with respect to time and temperature after using desirability approach	107
Figure 4.28	Effect of output response with respect to time and composition after using desirability approach	108
Figure 4.29	Average percentage error of (a) Compressive strength (b) Wettability (c) GRG	111
Figure 4.30	SEM micrographs of hydroxyapatite and reduced graphene oxide (HrG4), Polymeric blends B1, B2 and B3 thermal pressing at 100°C and 150°C	112
Figure 4.31	The PDI for various blends using Dynamic Light Scattering (DLS)	114
Figure 4.32(a)	SEM images, 3D plots and Surface plot for HArGO (a1-a3), B1-100(b1-b3), B2-100 (c1-c3), B3-100(d1-d3)	115
Figure 4.32(b)	SEM images, 3D plot and Surface plot for B1-150(e1-e3), B2-150 (f1-f3), B3-150 (g1-g3)	116
Figure 4.33	Wettability of thermal pressing blend of hydroxyapatite, reduced graphene oxide and carboxymethyl cellulose with comparison to blend of hydroxyapatite and reduced graphene oxide	119
Figure 4.34	TGA analysis of CMC, rGO and thermally pressed blend for 5min, 10min and 20min.	121
Figure 4.35	Apatite layer formation 1 st week, 3 rd week and 4 th week for blend of hydroxyapatite, reduced graphene oxide and carboxymethyl cellulose	123
Figure 4.36	Cell Viability study using MTT assay of blends HArGO, B1, B2 and B3 cultured for 24 hrs and 72 hrs (n=4, *p<0.001)	124
Figure 4.37	Cell Viability of blends B1, B2 and B3 at different concentration of 25mg/ml and 50mg/ml	125
Figure 4.38	FITC and DAPI stained blend of hydroxyapatite and reduced graphene oxide and blends inclusive carboxymethyl cellulose along HA & rGO namely B1, B2 and B3	126

Figure 4.39	Biodegradation % weight loss with respect to time	127
-------------	---	-----

LIST OF ABBREVIATIONS

316L SS	316L Stainless steel
Au	Gold
C6H9O6	Butylperoxycarbonyl carbonate
CaP	Calcium phosphorous
CCD-986SK	Fibroblast cell line
CH2O	Formaldehyde
cHA	Calcined hydroxyapatite
CH-PLA	Chitosan-poly lactide
Cl-	Chloride
CNT	Carbon nanotube
Colo-205	Epithelial cells
CS	Chitosan
DAPI	4,6-diamidino-2-phenylindole
DMEM	Dulbecco's Modified eagle's medium
DMSO	Dimethyl Sulfoxide
DS	Dispersion strength
EM	Electromagnetic
F-	Flouride
FESEM	Field Emission scanning electron microscope
FITC	Fluorescein isothiocyanate
FTIR	Fourier transform infrared spectroscopy
Gd	Gadolinium
Gel	Gelatin
GO	Graphene oxide
GPa	Giga Pascal
GRA	Grey relational Analysis
GRG	Grey relational grade
Hap/HA	Hydroxyapatite
HA-SP	Photochromic dye spirogyra conjugated to ligand hyaluronic acid
HT-29	Colon Cancer Cells
HUVEC	Human umbilical vein endothelial cells
LDH	Layered double hydroxide
MBG	Mesoporous Bioactive glass
MCF-10	Non-tumorigenic epithelial cell line
MDCK	Madin-Darby canine kidney cells
MG-63	Fibroblast cell lines
MKN-45	Cellosaurus cell line
MPa	Mega Pascal
mSF/SF	Silk fibroin microfibers
MTT	3-(4,5-dimethylthiazol-2-yl)-2,5-diphenyl tetrazolium bromide
NaBH4	Sodium tetrahydridoborate
NaCMC	Sodium carboxymethyl cellulose

NaOH	Sodium hydroxide
NGF	Nerve Growth factor
NIH3T3	Fibroblast cell lines
NiO	Nickel Oxide
OH	Hydroxyl
PCL	Polycaprolactone
PEEK	Polyether ether ketone
PEG	Polyethyl glycol
PGS	Poly (glycerol sebacate)
PHB	Polyhydroxybutyrate
PLA	Poly lactic acid
PLGA	Poly (lactic-co-glycolic acid)
PMMA	Polymethyl Methacrylate
PU	Polyurethane
PVA	Polyvinyl alcohol
rGO/RGO	Reduced graphene oxide
SBF	Simulated Body fluid
SSe	Total squared error
SST	Total squared deviation
T-47D	Breast cancer cells
UTM	Universal testing machine
WCA	Water contact angle
WPI	Whey Protein Isolate
XRD	X-ray Diffraction
Zn	Zinc
ZrB2	Zirconium diboride
β-TCP/TCP	Tri Calcium Phosphate

Chapter 1

INTRODUCTION

INTRODUCTION

Millions of individuals worldwide suffer from conditions affecting the bones and joints, including rheumatoid arthritis, osteoarthritis, and fractures. The injury most often treated in orthopedic procedures is a bone fracture, which requires a fixation device in order to regenerate the bone properly (1). According to allied market research, the worldwide orthopedic implant market was valued at \$49.4 billion in 2023 and is expected to rise at a compound annual growth rate (CAGR) of 4.4% from 2024 to 2033, reaching \$76.4 billion by that time. The growing prevalence of musculoskeletal disorders and orthopedic conditions, technological developments in implant materials and designs, the growing demand for minimally invasive surgical procedures, and the expansion of healthcare services availability in developing nations are the main factors propelling the growth of the orthopedic implants market as shown in the following Figure 1.

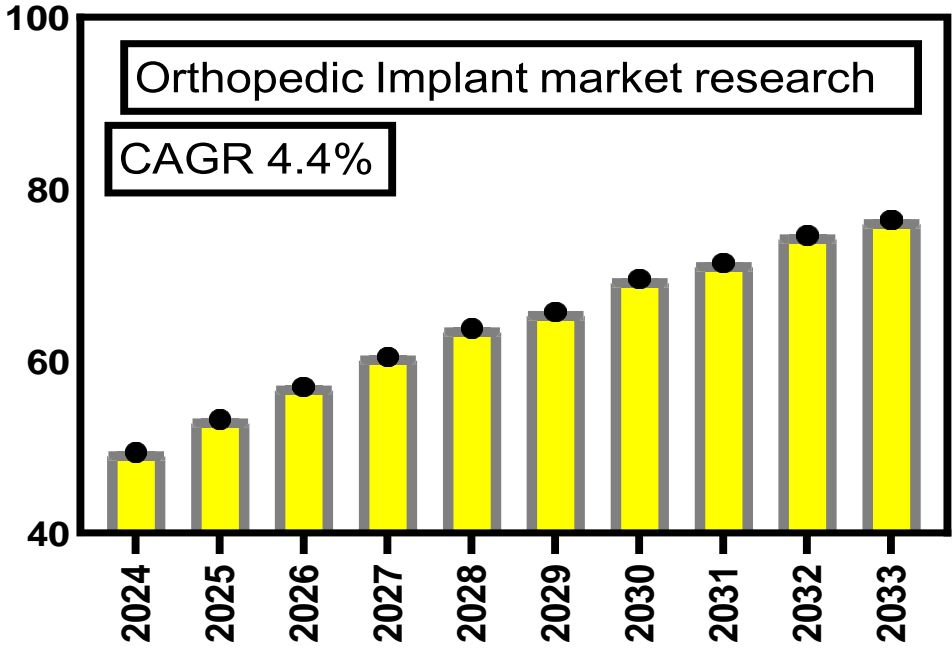


Figure 1.1 Orthopedic Implant Market report

As a result, a lot of researchers have concentrated on creating novel biomaterials for orthopedic purposes. Nowadays, many orthopedic applications use metallic implanted devices. According to Chandra Mohan and co-workers, metallic implants are linked to an array of difficulties, including corrosion, metal incompatibility, magnetism effect, osteoporosis, and delayed fracture healing at the implantation site (2). Additionally, the bulky metallic particles have an impact on the production of new cells in the bone. Stress shielding is also triggered by the metallic implant and the modulus of the metallic implants do not match to that of the bone. Furthermore, metallic implants necessitate additional procedures for the purpose of removing the implanted devices (3). For orthopedic applications, researchers are currently emphasizing on creating biodegradable, non-toxic, and temporary implants. Ceramic materials have become another candidate to substitute the metal implants because of their superior mechanical, biological, and biocompatible qualities. Ceramics do, however, have several drawbacks, including their tendency to be brittle and their low tensile and fracture toughness (4). Thus, the issues with metals and ceramic implantable devices have been resolved through the use of biodegradable materials. Second surgery is not required as the material degrades itself over time and supports the formation of new bone cells as well (5).

Hydroxyapatite (HA) is an apatite-family ceramic. The term "apatite" is derived from the Greek word apatite, that means "deception." Because of the variation in form and color, Hydroxyapatite (HA) was given this name (6–8). Apatite refers to a class of materials with crystal densities ranging from 3.16×10^{-3} to 3.14×10^{-3} g/mm³ and the formula $L_{10}(MO_4)_6(N)_2$. The formula $L_{10}(MO_4)_6(N)_2$ implies a divalent metal cation (Ca^{2+}) as L, a pentavalent phosphorus cation (P^{5+}) denoted by M, and an anionic radical N, including one of Cl^- , F^- , or OH^- (9,10). Calcium phosphate-based ceramics are of tremendous interest as synthetic biomaterials and thus frequently used in a variety of medical applications. HA is a calcium phosphate ceramic material that has excellent biocompatibility and innocuous nature aids in the bone healing process (11–13).

multidisciplinary domains as in life sciences and medicine. Calcium phosphate-based ceramics are of tremendous interest as synthetic alternatives. Numerous sources for the extraction of hydroxyapatite have been reported for instance eggshells, coral, fish bone, chicken bone and many more (14).

1.1 NEED AND SCOPE OF PRESENT RESEARCH

Thus, the issues with metals and ceramic implantable devices have been resolved through the use of composite materials. Addition of robust and biodegradable material not only prevents the second surgery but also supports the formation of new bone cells as well (5). In order to obtain the advantages of each constituent material without altering the physical, chemical, and mechanical properties of each material, composite materials become another promising approach for tissue regeneration. Combining the two or distinct components results in the formation of composites. The composites are composed of two basic materials known to be filler and the matrix. The matrix is the base of the composite material which has been reinforced with other components known as fillers so as to ameliorate its properties. It also has been reported that the compressive strength for cortical bone found to be 200 ± 36 MPa, with elastic modulus of 18.6 ± 28.8 GPa whereas for cancellous bone, compressive strength ranges from 1.5-3.8 MPa with elastic modulus ranging from 100-157 MPa (15). In addition, the microhardness of cortical bone reported to be 0.62-0.74 GPa whereas for cancellous bone it is found to be 0.63 ± 0.11 GPa (16).

Hydroxyapatite (HA) being the basic material already present in the bones found to be one of the vital aces in the field of bone regeneration. The need to improvise the mechanical properties of the hydroxyapatite as well as the biodegradability and biocompatibility is another important area to explore. The carbon base materials inclusive of graphene and its oxide possess High electrical, mechanical, and electrochemical characteristics. It has been reported that the reduced graphene oxide was found to boost up the mechanical properties including mechanical strength, hardness of reinforcing the material to carboxymethyl cellulose (17). Furthermore, Jabbari and colleagues found that Silk fibroin/chitosan/reduced graphene oxide scaffolds with a weight ratio of 84:7:9 had improved mechanical strength and biocompatibility(18). Another class of biomaterial that can be employed to create a viable scaffold is polymers. Polymer addition has been done to increase the mechanical strength even more without sacrificing the biodegradability and biocompatibility of the composite. It has been described that the polymers distribute evenly across the material and

withstand the higher loads (19,20). Carboxymethyl cellulose (CMC), sometimes called cellulose gum, is an anionic substance that is made of cellulose and carboxymethyl groups. Kukrety and colleagues have provided a thorough description of how carboxymethyl cellulose is extracted from cellulase-based natural resources such as sugarcane bagasse, cotton stalks, banana stems, paper sludge, and sago waste (21). Its uses in many industries are expanded by its many attributes, including biodegradability, innocuous nature, low production costs, and an abundance of natural resources. CMC and its blend have a wide range of applications in the fields of drug delivery (22,23), skin tissue engineering (24), bone tissue engineering (25,26) and wound healing (27,28). Furthermore, CMC demonstrates a wide range of applications in quality of water (29), the textile sector (30,31), and packaging for food (32). Recent research by Basu et al. shown the CMC-based film effectiveness in wound healing in both normal and diabetic models of animals (33). Through solvent mixing and freeze drying, chitosan, carboxymethyl cellulose, and a zinc and iron-loaded hydroxyapatite scaffold were created. These materials demonstrated antimicrobial properties, decreased degradation behavior, and increased bone cell proliferation (34).

In the present work, in order to achieve the compressive strength and microhardness near to the human bone as aforementioned, the hydroxyapatite has been calcined and reinforced by reduced graphene oxide and later with carboxymethyl cellulose to make a ternary novel composite. Further, the hydroxyapatite has been synthesized by chemical precipitation method and calcined to improve the crystallinity. Further reduced graphene oxide (rGO) has been formed via thermal treatment and reinforced to calcined hydroxyapatite to form the binary composite. Further, the binary composite has been characterized using XRD, FTIR, FESEM and studied thoroughly for the mechanical as well as for the biocompatibility. The best variant of this binary composite has been further used to fabricate the ternary composite by including another filler namely carboxymethyl cellulose which not only ameliorated its mechanical properties but also gear up its biological compatibility. Further the ternary blend of hydroxyapatite, reduced graphene oxide and carboxymethyl cellulose has been further analyzed through FTIR, XRD. Nevertheless, the ternary composite has been optimized by using grey-Taguchi approach and the optimized ternary blends has been further investigated for the mechanical and biological studies.

1.2 Outline of the thesis

The entire thesis work has been divided into five chapters, which are as follows: Chapter 1

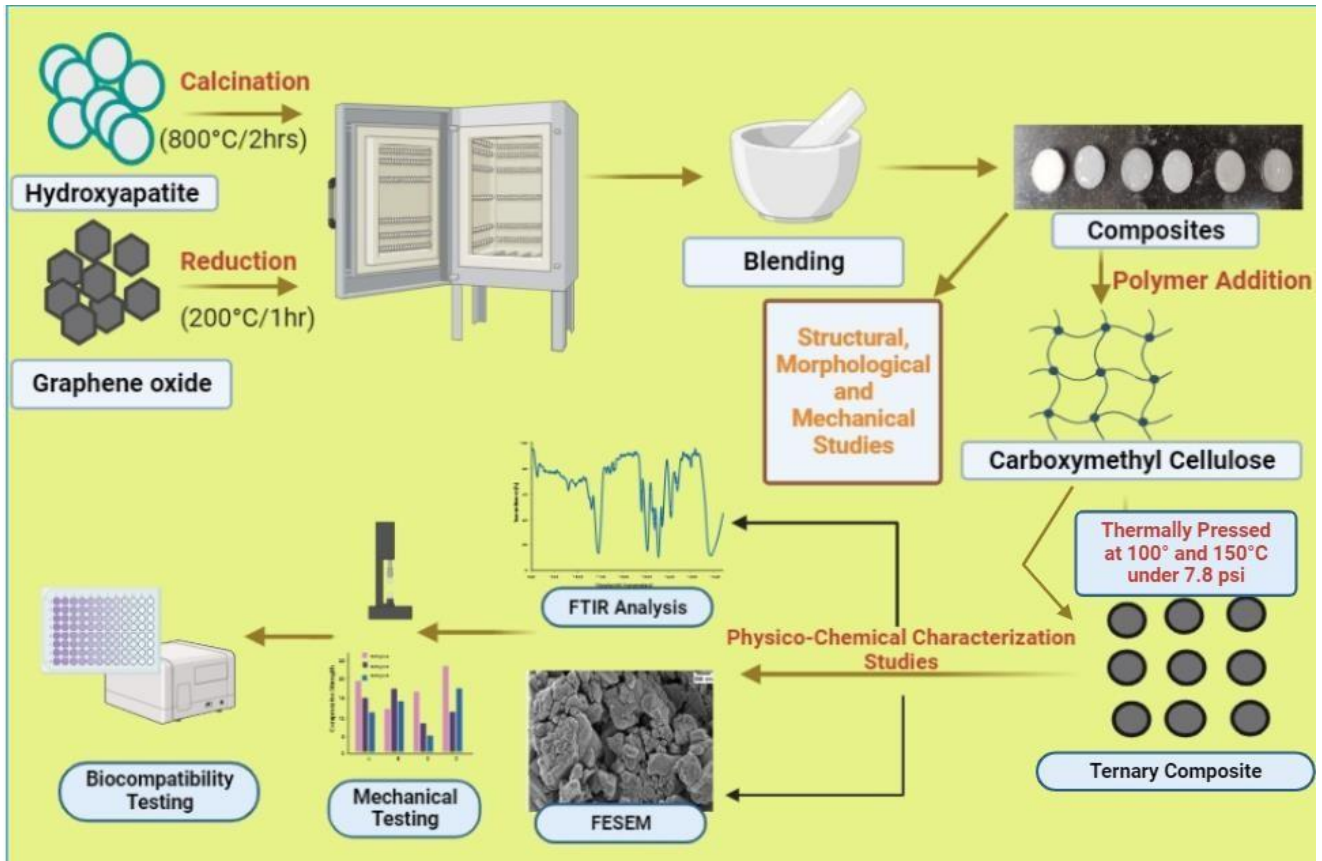
gives an introduction to the research and its significance. Chapter 2 includes a review of the literature, including principles and fundamental understanding of basis of different materials, as well as potential improvements in the efficacy of hydroxyapatite-based composites for regeneration of tissue. It was also highlighted for potential methods for boosting the attributes of hydroxyapatite to make it more effective for tissue regeneration applications. Various properties of reduced graphene oxide and carboxymethyl cellulose has also been detailed in this chapter and can be used for reinforcement and can be a good candidate for the application into biomedical applications. Chapter 3 describes the materials and procedures used to manufacture hydroxyapatite-based composite, as well as their physical, chemical, and biological properties.

Chapter 4 discusses the results and discussion of experimental work, which is divided into the following sections with each objective in each part:

Part I describes the processing and characterization of biomaterial preparation additives. Part II describes the objective that investigate the mechanical properties of biomaterial fillers.

Part III focuses on biomaterial production procedures such as polymer addition to the additive and characterization. Furthermore, the optimization of the mechanical properties of the polymeric biomaterial using the grey-Taguchi approach has been explained. Part IV displays the biological compatibility criteria of the ternary blend. Chapter 5 contains a brief review and conclusion of the thesis work, as well as future research recommendations.

GRAPHICAL ABSTRACT



Chapter 2

LITERATURE SURVEY

LITERATURE SURVEY

Today, biomaterials play an important role in medicine, restoring function and promoting healing after injury or sickness. Natural or synthetic biomaterials are utilized in medical applications to maintain, augment, or repair damaged tissue or a biological function. The usage of biomaterials stretches back to antiquity, when ancient Egyptians utilized sutures composed of animal sinew. Biomaterials is a modern field that includes medicine, physics, chemistry and life sciences as well as the latest impacts from tissue engineering and materials science. Because of advancements in tissue engineering, regenerative medicine, and other fields, the discipline has grown dramatically in the last decade.

2.1 Background of Biomaterials

Biomaterials are natural or man-made materials that are utilized to maintain or totally replace the function of malfunctioning tissues in the human body. The entire or partial replacement of flawed or unhealthy tissues has enhanced quality of life and extended average longevity which has spurred interest in the subject of biomaterials. Despite the fact that biomaterials an emerging interdisciplinary field but its practical uses stretch back thousands of years. Glass eyes, metal noses, and ivory teeth recovered on Egyptian corpses are excellent examples (35). The renown iron-based hooks and wooden legs of the pirates are also famous instances. The skull of the Tlailotlacan woman from ancient Teotihuacan (Mexico) was reported who died around 1600 years ago with dental implants in the form of embedded mineral stones as replacement teeth. In a similar vein bronze and copper replacements for bones from thousands of years ago that were designed to be inserted in the human body should be regarded as biomaterials. Due to a lack of superior materials, copper implants were particularly popular until the mid-nineteenth century. Stainless steel soon eliminated copper. Gold has been used in dentistry for over 2000 years. In his writings, Hippocrates recalls sutures made of gold are being utilized to join tissues. Biomaterials include devices made from cadaver bones and ivory in the 1880s for use in orthopedics(36). Further, the sterilization has been introduced by Lister that has been implemented in surgical procedures. Nevertheless, Metal nails, total hip replacement, cornea substitutes have been invented in the early in early 1940s. Later, the Artificial heart and its valve also valve has also come been come to light in the 1980sin 1980s (35). Also, the hip arthroplasty was introduced arthroplasty introduced that

was used to replace hip joint (37).

2.2 Biomaterials and types of Biomaterials

Biomaterials are substances embedded within or utilized in association with the body that have been developed to possess properties that closely mimic those of the biological system, remain sufficiently stable for the intended use, to have acceptable levels of bioactivity, and either partially or entirely replace the functions of flawed, or failing tissues.

Biomaterials can be classified on to basis of origin as well as on the basis of generations. On the basis of origin, the biomaterials have been divided into four groups namely, metals, Polymers, Ceramics and composites as shown in Figure 2.1 On the other hand, the biomaterials can be classified on the basis of development with the time and described as first generation, second generation, third generation and fourth generation demonstrated in Figure 2.3 below.

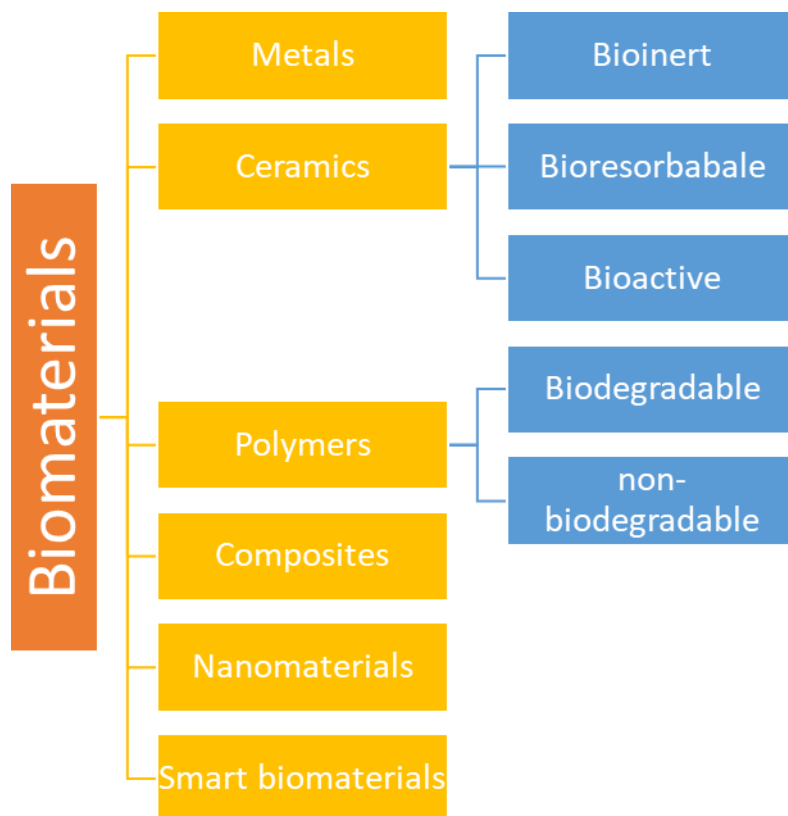


Figure 2.1: Classification of Biomaterials

2.2.1 Metallic Biomaterials:

Metallic biomaterials inclusive of stainless steel, titanium alloys, and cobalt chromium molybdenum alloys, which are used to make implants for surgery and prosthetic devices that substitute disabled body parts caused by trauma, disease, or ingrained conditions. Cobalt chromium molybdenum alloys and stainless steel are the most commonly used cobalt base alloys for bone grafts due to their superior features such as higher strength, hardness, creep resistance and biocompatibility (38). Metals possess limitation as stiffness, get corroded and have high specific weight and density due to which metals are hard to process (39). Basara and co-workers developed a novel composite using titanium carbide (Ti_3C_2Tx) MXene with polyethylene glycol through 3D printing and reported biocompatibility on analyzing cardiomyocytes (40).

Owing to higher mechanical properties, permitted biological compatibility, corrosion resistance, and low cost (41), 316L SS is frequently employed in bone restoration and substitution for acetabular cup of hip joint, plates and screws (42). Some of the metallic implants available under the trade name of Ti6Al4V for titanium alloy, Vitallium for Cobalt chromium alloy and Orthinox for stainless steel (43). Furthermore, the magnesium-based alloys have also been used successfully showing higher mechanical strength and reasonable biocompatibility (44,45). In addition, some of the biodegradable metallic biomaterials have also been reported. Toghyani and co-workers successfully obtained MgF₂ coated porous Mg from the sucrose and it degrades over time (46). Further, porous Zinc scaffolds have been fabricated through additive manufacturing for the application into bone tissue engineering (47). The different iron-based biomaterials and bulk metallic glasses have been elaborated (48).

2.2.2 Ceramic Biomaterials:

Bio-ceramics, both natural and synthetic, are intended to form a strong link with bone and have emerged as a contender to metallic implants. Bio-ceramic materials used for hard and soft tissue repair and regeneration can be categorized based on the composition, framework, and characteristics. Bio-ceramics are a class of inorganic and non-metallic ceramics utilized for the recuperation and regrowth of diseased or damaged musculoskeletal system and periodontal abnormalities. Ceramic materials for orthopedic load-bearing coverings (hip acetabular cups),

bone grafts and bone cements, and implants for teeth have been designed (49). Bio-ceramics are distinguished by their high biological compatibility, osteo-conductivity, corrosion resistance, and hard brittle surface. Bio-ceramics have low fracture toughness, brittleness, poor elasticity, and extreme stiffness. The development of bio-ceramic materials is at the forefront of health-related issues in many countries (50). Arguably, research into ceramic biomaterials has reached a level of involvement and sophistication comparable only to electronic ceramics. Despite the fact that calcium phosphate-based coatings on hip, knee and dental implants have a long history of clinical success, quest of improving the longevity of implants and to impart them with better physiological properties is high up on the agenda of numerous research groups around the world. Coating the stem of modern cementless endoprostheses with a layer of plasma-sprayed hydroxyapatite improves the ingrowth of bone cells and thus assists in anchoring the implant to the cortical bone matter. However, since the high temperature process of plasma spraying leads to incongruent melting and thus thermal decomposition of the hydroxyapatite, knowledge of the complex transformation sequence is essential to design coatings with optimum stability and hence biological performance. This contribution reviews recent research into the thermal history of thermally sprayed calcium phosphate coatings as well as their in vitro behaviour in contact with simulated body fluid that limits the use of bio-ceramics for tissue engineering (TE). Bio-ceramics are broadly categorized as follows:

- 2.2.2.1 Bioinert: These bio-ceramics showed zero interaction with the tissue into which the bio-ceramic has been integrated and it provides support to the structural framework. On the pros side, these ceramics reduced wear showed excellent tribological properties whereas on the cons side, such material showed poor fracture toughness, dislocation, slow crack growth and disastrous failure (51–54). Tantalum oxide, Alumina and Zirconia are some of the examples.
- 2.2.2.2 Bioresorbable: The calcium-phosphates and Hydroxyapatite are some of the important biodegradable ceramics. These ceramics possess high stiffness, biocompatible, better osseointegration traits but are limited to thermal instability. Biodegradable materials entirely breakdown into body tissue fluid due to the chemical structure of the materials (55,56). Calcium phosphate (CaP) bio-ceramics are widely used in the field of bone regeneration, both in orthopedics and in dentistry, due to their good biocompatibility, osseointegration and osteoconduction. A wide variety of CaPs are presented, from the individual phases to nano-CaP, biphasic and triphasic CaP formulations, composite CaP coatings and cements,

functionally graded materials (FGMs), and antibacterial CaPs. We conclude by foreseeing the future of CaPs (57). A variety of biodegradable implants made of polymers, ceramics, and metals were developed and tested in humans. Controlled degradation of bioresorbable bio ceramics may be more advantageous to patients. Calcium phosphates are widely employed in both dentistry and orthopedics for bone tissue engineering. The bone structure comprises of calcium phosphate therefore, the salts calcium and phosphates have been employed to substitute and strengthen bone tissue for many years. Calcium phosphate bio-ceramics exhibit biological absorption and bioactivity. Calcium phosphate can be encountered in a variety of forms, the most common of which being hydroxyapatite (HA) and -tricalcium phosphate (-TCP) in therapeutic uses. The bioactivity is determined by their chemical structure and crystallinity. Nonstoichiometric apatite structures with CO^{-2}_3 and HPO^2 ions are extremely dispersible and resorbable. Similarly, tricalcium phosphate is easier to absorb than stoichiometric apatites like HAp. The calcium to phosphate ratios and forms of calcium phosphate ceramics are discussed in detail by Hasirci and co-worker (35).

2.2.2.3 Bioactive: Bioactive ceramics possess higher stability, superior cell proliferation and stability but being brittle these materials possess lower strength, toughness and ductility (51). According to the researchers, bioactive glasses are biocompatible ceramics that, when exposed to biological fluids, develop a Hydroxyapatite layer that fosters strong chemical interactions with tissues (58). Ceramic-based implants displayed high bioactivity and biocompatibility in an in-vivo conditions, as well as corrosion resistance. Ceramic implants outperformed polymer and metal-based implants in terms of osseointegration and osseointegration activity inside the human body, promoting rapid healing of shattered and diseased bones. The only drawbacks of ceramic biomaterials are their brittleness and tendency to rupture under tensile conditions, which limits their full use in load carrying bones (59).

2.2.3 Polymeric biomaterials

Polymeric biomaterials, consisting of repeated monomer subunits bound by a covalent link, have found extensive application in the biomedical area owing to their extremely versatile and adaptable physio-chemical, and biological characteristics. Naturally occurring polymers are often biodegradable, plentiful, and easy to handle (60) whereas Synthetic polymers can have their properties easily adjusted and come in a wide range of compositions. The mechanical and

biological properties of polymers can be concurrently enhanced using techniques inclusive of copolymerization, and blending. Its minimal immunogenicity and effective control and replication of molecular structure are the greatest benefits. The aforementioned advantages can certainly satisfy the requirements of regenerative medicine (61). Nowadays, implants, tissue replacements, drug delivery methods, bio adhesives, biological sensors, suture components, and ophthalmic devices are evident in the applications for polymeric biomaterials. Natural polymers exhibit low immunogenicity and high biocompatibility in lieu of which natural polymers can be used for long term implants. A naturally occurring protein found in the skin as well as in connective tissue cells is collagen and have been extensively used for the synthesis of scaffolds and implants for tissue engineering and regeneration (62–64). In the field of tissue engineering, natural polymers such as collagen, keratin, fibronectin, and laminin are also being investigated for their potential (65–67). The most researched natural polysaccharides for biomaterial applications are alginate, chitin, chitosan, and other gums (68,69). Rapid degradation, poor mechanical strength and high susceptibility to contamination setback the use of natural polymers. Natural polymers further have been grouped into two categories polysaccharide based and protein based. Polysaccharides have excellent degradability, bioactivity, simplicity of chemical manipulation, inexpensive manufacturing costs and mimics the extracellular matrix (70). Chitosan, Heparin, Alginate, Carrageenan, Cellulose, Starch are some of the polysaccharides based natural polymers. whereas Collagen, Gelatin, Fibrin, Silk fibroin extensively used protein based natural fibres.

For patients who experience allergic reactions to natural polymers, synthetic polymers are the most suitable alternatives. Synthetic polymers do not induce persistent immunogenic inflammation and are less immune-stimulating. Synthetic polymers exhibit superior mechanical properties in comparison to natural polymers (71). The synthetic polymers can also have their biodegradability altered, which enables them for use in tissue engineering applications. The Synthetic polymers have been divided into degradable polymers inclusive of Polyethylene glycol, Polyhydroxybutyrate (PHB), polycaprolactone (PCL), Polyvinyl Alcohol (PVA), Polyethylenimine and non-degradable including Polyurethane, Poly methyl methacrylate (PMMA), Polyethylene terephthalate, Polyethersulfone (72). Because of their effectiveness in biomedical applications, a number of synthetic polymers, including polylactic acid (PLA), polyvinyl alcohol (PVA), polycaprolactone (PCL), and poly lactic-co-glycolic acid (PLGA), are the most researched (73–75). Different kinds of polymers, both natural and synthetic, can be generated in numerous designs such as films, hydrogels, 3D printed implants, microneedles, nanogels and scaffolds (76–78).

Table 2.1: Different forms of the Polymeric biomaterials

S.No.	Formulations	Polymer Used	Applications	References
1	Microneedles	Poly(lactic acid (PLA)	Drug delivery System	(79)
2	Microrobots	Poly (lactic-co-glycolic acid)	Anti-inflammatory response	(80)
3	Micelles	Poly((N-vinylpyrrolidone)-block-poly (vinyl acetate)) (PVP-b-PVAc)	Drug delivery	(81)
4	Aerogel	Nanocellulose	Skin tissue engineering	(82)
5	Hydrogel	Collagen I, Agarose, Alginate, Fibrin, and Collagen Chitosan	Skeletal muscle tissue engineering	(83)
6	Membrane	Poly (lactic-co-glycolic acid)	Periodontal tissue regeneration	(84)
7	Microparticle	PLA and PLGA	Anti-inflammatory activities	(85)
8	Film	Chitosan	Skin tissue engineering	(86)
9	Sponges	Chitosan	Bone tissue engineering	(87)
10	Bioinks	Gelatin	Cartilage regeneration	(88)

2.2.4 Composites biomaterials

Composites are materials made up of multiple components, each of which has unique structural and physio-chemical properties and works synergistically to provide the ideal mixture. The earliest engineered composites were created for the automotive and aerospace sectors to provide durable, robust, and stable materials whose performance surpassed specifications. Research on engineered composites began in the 1960s. The incorporation of two materials in which one acts as a reinforcement in the form of fibres, sheets, or particles encased within the other material, the matrix, is commonly referred to as a composite.

Table 2.2: Various Composites and applications in tissue engineering

S.No	Composite	Fabrication Method	Major Findings	Application	Reference
1	PLA/Hap	3D printing	Biocompatible on human MG-63 osteoblast cell lines Compressive stress 53 ± 0.2 MPa.	Bone tissue engineering	(89)
2	Collagen/Hap/Deoxy	Freeze casting method	Biocompatible on Bone marrow-derived mesenchymal stem cells (BMSCs) Antibacterial activity for <i>S. aureus</i> and <i>P. aeruginosa</i>		(90)
3	Strontium Chitosan/MMT	Freeze drying method	Biocompatible on Human primary osteoblast (hOBs)		(91)
4	HA/Zein	Calcium oleate-based solvothermal method	Maximum tensile strength of 114 ± 8 MPa Cytotoxicity observed in Mouse mesenchymal stem cells		(92)
5	Collagen/ β -TCP	3-axis printing system	Bio-ink of collagen/cells/ β -TCP has been made. Osteogenic in MC3T3-E1 and hASCs cells		(93)
6	Ti-Forsterite/PHB	Sol-gel and dip coating Technique	Biom mineralization in SBF and Biocompatibility on		(94)

			MG63 cells observed		
7	WPI/gelatin/CaP	Ultrasonication	Biocompatible in human osteoblast-like MG-63 cells		(95)
8	MBG/Silk fibroin and MBG/PCL	3D printing	Compressive strength of 20MPa, Osteogenic gen markers in mice has been detected qRT-PCR technique		(96)
9	Collagen/CMC	Lyophilization	Biocompatible on Keratinocyte Elastic modilus of Bilayer of collagen and chitosan found to be 523.92 ± 156.26 kPa	Skin tissue engineering	(97)
10	Collagen/Elastin	Lyophilization, Electrospinning	Biocompatible on human fibroblast and human keratinocytes		(98)
11	Polypyrrole/Chiosan/ Collagen	Electrospinning	Scaffold showing electrical conductivity to be 164.274×10^{-3} s/m Biocompatible on SHSY5Y human neuroblastoma cells.		(99)
12	<i>mSF/PGS and CS/PGS</i>	Particulate leaching and freeze-drying	Biocompatible on fibroblast of mice. Pore size of 50-250 μ m obtained		(100)
13	PU/CS/CNT	Electrospinning and Electro spraying	Highest Tensile strength of about 13 MPa for 1%LDH obtained.	Cardiac tissue engineering	(101)

			Scaffold found to be biocompatible on SH-SY5Y cells		
14	PVA/Silk Fibroin	Electrospinning	Highest Tensile strength found to be 4.67 ± 1.11 MPa		(102)

S.NO.	Composite	Fabrication Method	Major Findings	Application	Reference
15	PLA/Chitosan	Electrospinning	The maximum Young's modulus found to be 83.67 ± 14.51 MPa. PLA /Chitosan showed viability on Cardiomyocytes assessed through LDH assay kit		(103)
16	PCL/CNT	3D printing	Average maximum Peak load found to be 1.27 ± 0.07 mN Slight proliferation in the H9c2 myoblast cells observed		(104)
17	PLA/Polyaniline	Electrospinning	Water contact angle found to be decreased from $138.6^\circ \pm 0.7$ to $127.2^\circ \pm 1.2$. An APPJ (atmospheric pressure plasma jet) treatment has been done.	Nerve tissue engineering	(105)
18	PPy/SF	3D printing Electrospinning	Biocompatibility on Schwann cells		(106)

Different composites inclusive of polymers, natural fibers, carbon nanotubes, ceramics, metals have been described in the table above along with the fabrication methods and the applications into tissue engineering.

2.2.5 Nanomaterials

One of the most cutting-edge technologies of the modern era, nanotechnology focuses on the creation of materials and structures with dimensions ranging from one to one hundred nanometers (107). The physical-chemical and biological characteristics of materials at nano size scale differ greatly from those of materials in bulk at greater sizes. Nanomaterials possess unique mechanical, biological, and physico-chemical characteristics that can be used in a wide range of applications due to their extremely small size, enormous surface area, and big surface to volume ratio. Thus, nanotechnology has transformed practically every aspect of our daily lives as well as scientific subjects (108). A plethora of opportunities in healthcare have been made possible by the use of nanotechnology in medicine, or "nanomedicine," including those related to disease diagnosis (109), and drug delivery (110), bioimaging (111,112), tissue engineering, and regenerative therapies (113,114). Numerous medications including those for diabetes (115), infections (116) and inflammation (117), have made use of nanomaterials. As a carrier system for the m-RNA-based Covid-19 vaccine, nanoparticles have been used in medicine for the first time recently (118). Furthermore, different types of nanomaterials utilized in Alzheimer's disease and their therapeutic applications were detailed by Faiyaz and colleagues (119).

Nanomaterials can be further classified on the basis of origin and dimensions. Nanomaterials based on the source can be further divided into carbon-based materials inclusive of Fullerene, graphene and its derivatives, carbon tubes and carbon fibres, Inorganic based nanomaterials including Metal- based, Metal-oxide, Lipid-based and ceramic based are some of the major nanomaterials. In addition, Organic-based materials include Ferritin, Micelles, Liposome whereas composite-based materials include the mixture of two or more types of nanomaterials (V. Singh et al., 2020).

On the other hand, the nanomaterial size can be used as another aspect to classify the nanomaterials. On the basis of dimensions, there are four groups of nanomaterials. All the dimensions of the zero-dimensional nanomaterials lie in nanometre scale of less than 100nm. Quantum dots, fullerenes, magnetic and polymeric nanoparticles are some of the instances of these nanomaterials (121).

Furthermore, one dimension reveals the dimension of nanomaterial is under nanoscale in one direction only. Metals, metal-oxides and carbon-based materials are some of the examples of 1D

nanomaterials (122).

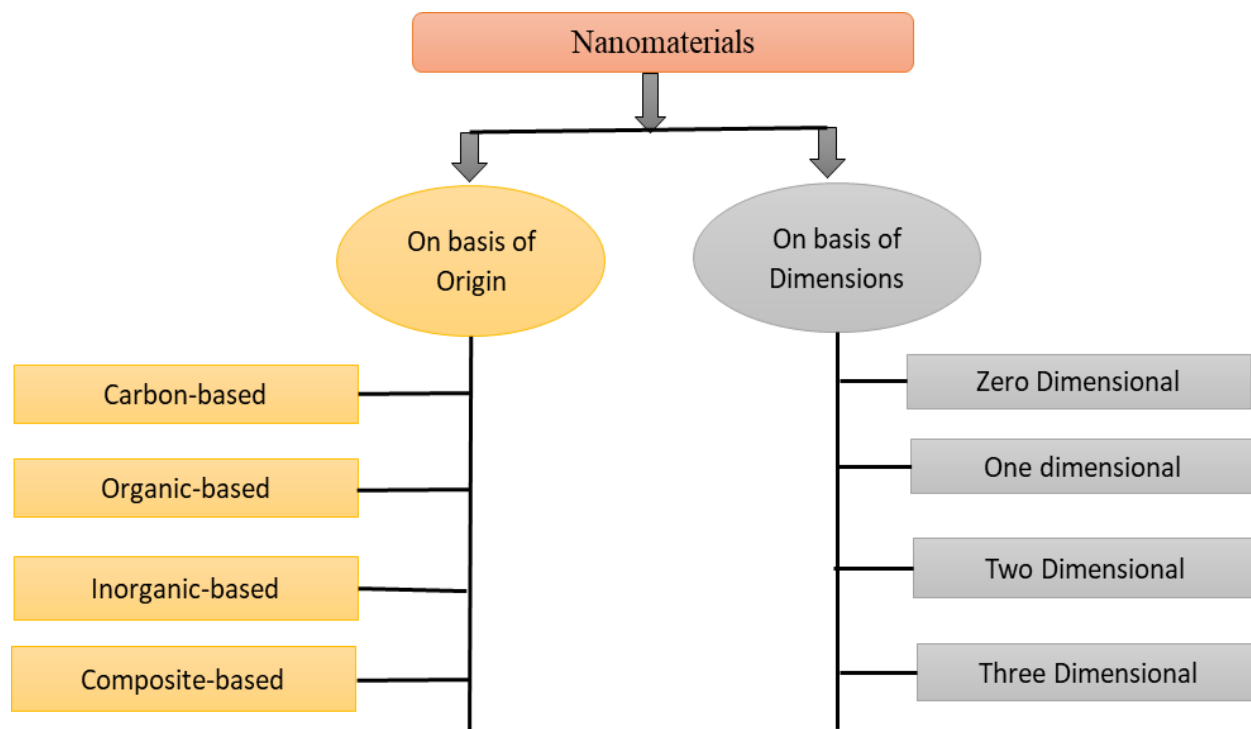


Figure 2.2: Classification of Nanomaterials

Similarly, the 2D nanomaterials exhibit the nanoscale dimensions in two directions only. Graphene, Graphene oxide, reduced graphene oxide, silicates, hydroxides, dual layers, black phosphorus are important instances of 2D nanomaterials (123). Lastly, if the material possesses nanometre dimensions in three directions, then they are recognized as three dimensional nanomaterials. Three dimensional nanomaterials take the interest of the researchers to develop complex 3D nanostructures to be used in solar cells, biomedical devices and robotics (124).

2.2.6 Smart biomaterials

Developments in the fields of medicine, biology, physio-chemical, and biomaterials have contributed to the generation of smart and functional biomaterials, which are now being used in medical applications and aids in healing the wounds and repair various biological functions (125,126). However, owing to their intricate interactions with biological components and unforeseen responses, these biomaterials still require additional improvement (127).

As a result, the future clinical applications of functional and intelligent biomaterials for enhancing patient health and quality of life will be ensured by their excellent design and development. However, smart hydrogels, stimuli-responsive and 3D bioprinting have been employed in order to fabricate the smart biomaterials (128). Furthermore, the immune-modulated biomaterials have also taken the interest of the researchers that ameliorate the biomaterial and tissue interaction (129).

2.3 Biomaterials types on the basis of the generations

Biomaterials can be classified on the basis of the time span and the properties of the biomaterials used. With the advancement in the technology, the improvement in the synthesis of biomaterials has been noticed. Presently, the significant emphasis that scientists are focusing on creating fourth-generation biomaterials.

2.3.1 FIRST GENERATION BIOMATERIALS: First generation biomaterials are those that have been around for a long time and are often bioinert in nature. During that time, these materials were often referred to as prostheses. The primary goals of the first generation of research were to decrease host rejection and produce skeletal characteristics that resembled injured tissue. According to reports, first-generation biomaterials include metals, alloys and wood (130).

2.3.2 SECOND GENERATION BIOMATERIALS: Conversely, the second generation of biomaterials consists of an enhanced designed form of biomaterials. There have been reports of bioactive and bioresorbable biomaterials in this generation. During this time, bioceramics and polymers were used more frequently. Second-generation materials include ceramics and polymers, both natural and manmade. Bone cements are instances of second-generation biomaterials (131).

2.3.3 THIRD GENERATION BIOMATERIALS: The latest developments in matrix and fillers are the focal point of the third generation of biomaterials. Moreover, this generation has fostered connections between cells and genes. The third generation reduces the likelihood of host rejection, increases biocompatibility, and enhances physio-chemical properties. In this generation, the ideas of biodegradability, bio-inertness, and bioactivity come together to build nanomaterial that persist in complicated bodily functions. In this generation, additional elements like increased porosity and mechanical strength have been added. In this period of biomaterials, metal, polymers, ceramics, and composites have all been employed extensively (132).

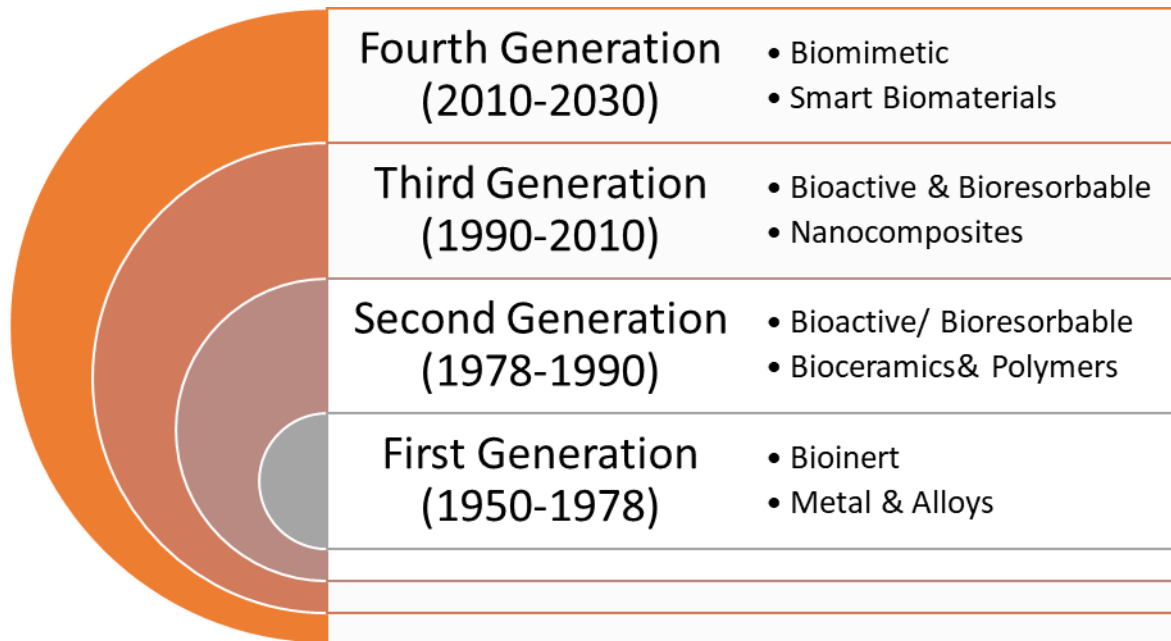


Figure 2.3: Generations of biomaterials

4. FOURTH GENERATION BIOMATERIALS:

The biomimetic behaviour of the biomaterials is the focus of fourth generation biomaterials. Emphasis has been given to carefully developed smart biomaterials, that consist of composite biomaterials, cells, and biological moieties. The biomimetic behaviour of the biomaterials is the focus of fourth generation biomaterials. Emphasis has been given to carefully crafted smart biomaterials, that include composite biomaterials, cells, and biological moieties. Future developments in this generation of biomaterials will include a thorough understanding of enhanced production techniques, control over drug release kinetics, and resemblance to natural tissue (133,134).

The Figure 2.3 above demonstrates the way by which biomaterials have evolved. In this technophile world, cells, growth factors and biomaterials together are integrated so as to obtain the engineered composite for the tissue engineering purposes whereas earlier only one property has been used for the same as shown in generation 1st and 2nd.

2.4 Fabrication of Biomaterials

In order to develop materials for medical purposes that interact with biological tissues, various methods have been employed to contrive the biomaterials. The fabrication methods can be divided into groups according to the nature of the biomaterial (such as metals, polymers, or ceramics) and its intended application. Several typical techniques for creating biomaterials have been illustrated below. The fabrication methods have been classified on the basis of material used and on the basis of technological advancements. The conventional and advanced methods have been used nowadays. In this tech-savvy world, the smart biomaterials have been developed using advanced methods of 3D Printing. Further, different materials have been treated differently in order to ameliorate properties of biomaterials. Nevertheless, the composite biomaterials have developed the leapfrog opportunities in the field of tissue engineering. In order to develop a promising material an appropriate fabrication method should be implemented.

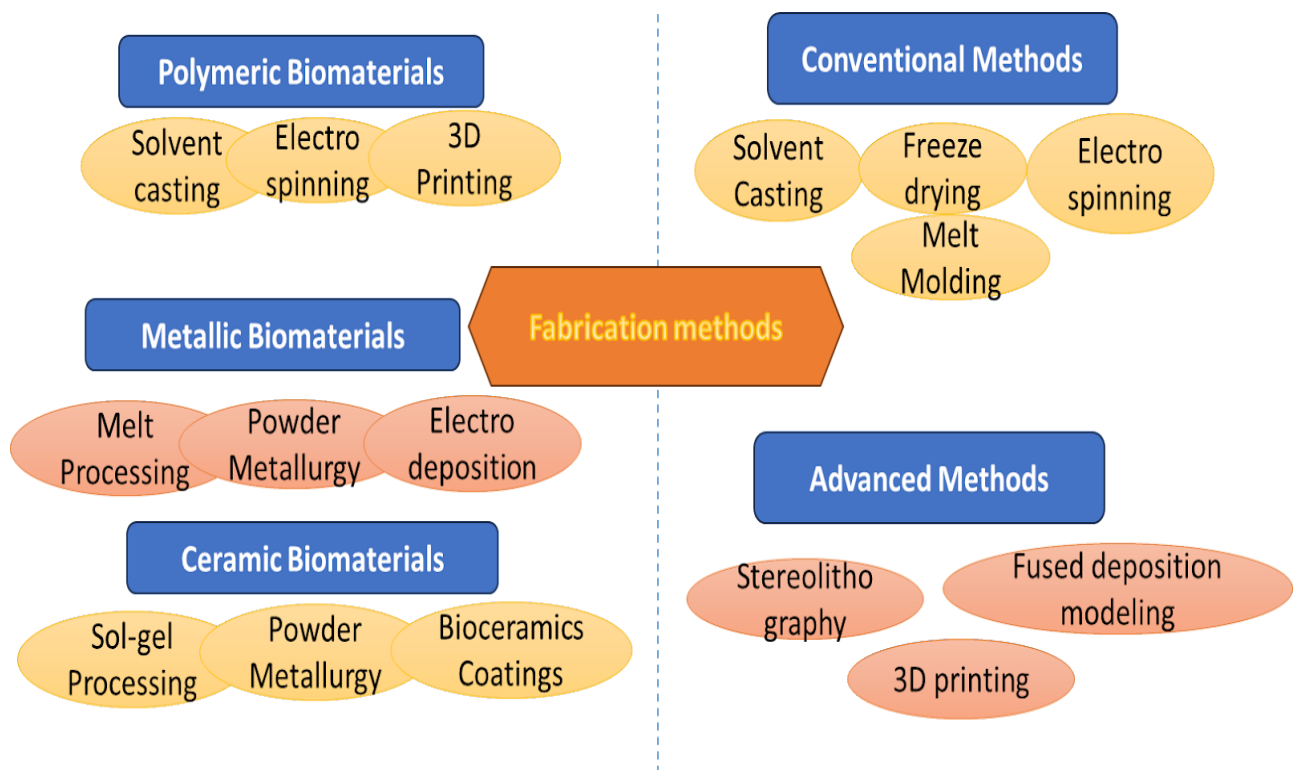


Figure 2.4: Categorization of Bio fabrication methods
Some of the biomaterial fabrication methods have been discussed below

2.4.1 Solvent Casting and Particulate leaching

This method involves dissolving the polymer in a volatile solvent that has a homogenous distribution of porogens. Subsequently, the solvent evaporates, leading to the synthesis of a polymer network that traps the porogen. Lastly, the scaffolds are

submerged in an appropriate porogen solvent to leach the porogen, creating pores in the matrix (135). Three-dimensional biodegradable porous scaffolds play an important role in tissue engineering. A new polymer based on maleated poly (lactic-co-glycolic acid) (MPLGA) was synthesized using direct melt copolymerization from maleic anhydride (MAH), D, L-lactide, and glycolide monomers. MPLGA porous biodegradable scaffolds were prepared by a solution-casting/salt-leaching method. The effects of content and size of the NaHCO_3 porogen on the compressive strength of the MPLGA scaffolds were investigated, and the effect of content of the porogen on the porosity of the MPLGA scaffolds was also studied. The results indicated that MAH was grafted onto PLGA successfully and MPLGA scaffolds with interconnective and open pore structure were obtained. Increasing content of NaHCO_3 porogen resulted in an increase of porosity and decrease of the compressive strength of the MPLGA scaffolds with the compressive strength of the scaffolds also decreasing with increasing porogen(136). Porogens are typically either water-soluble inorganic salts like NaCl or organic substances like collagen and gelatin (137).

2.4.2 Melt molding

Melt molding is a simple, traditional method that makes use of thermoplastic polymers. The polymer is first heated and then cast in a mold with an appropriate three-dimensional structure based on the tissue defect. The technique is straightforward and doesn't necessitate the use of organic solvents. Also, it gives control over morphological properties including pore size and interconnectivity(138).

2.4.3 Gas foaming

In this method, an inert gas has been passed at higher temperature and then undergone freeze drying leading to formation of microstructure with closed pores and low interconnectivity, hence exhibiting low mechanical strength (139,140).

2.4.4 Electrospinning

One popular method for creating nanofiber (NF) polymers and composites is electrospinning. Once the surface tension is balanced by the electrostatic force generated by the high-voltage source, an electrically charged jet of polymer solution would explode into a cone. The jet hardens into NFs when the solvent finally evaporates (141,142).

2.4.5 Stereolithography (SLA)

One of the additive manufacturing techniques is stereolithography. In this method, the laser curing of photosensitive resin has been employed but this method is limited to epoxy/HA and polymer/ceramic composites (143,144).

2.4.6 Fused deposition modelling (FDM)

This type of additive manufacturing technique can be used for Hydrogels, thermoplastics and ceramics. Low resolution and high shear force are some of its drawbacks. This manufacturing process can be implemented to bioprinting the scaffolds for cell culturing and for synthesizing the rigid, soft models for surgery (145).

2.4.7 3D Bioprinting

3D bioprinting is one of the advanced methods used for the synthesis of biomaterials. Additionally, the process of 3D bioprinting has been implemented step by step. Data Acquisition (146,147), Biomaterial Screening (148), computational designing (149) and printing parameters. Further three different types of bioprinters inclusive of Inkjet, Extrusion 3D and Laser-assisted have been reported (150).

Table 2.3 Different Fabrication methods with their Perk, Challenges and Parameters

S.No.	Fabrication Method	Perks	Challenges	Processing Parameters	References
1	Solvent Casting	Cost-effective	Selection of appropriate solvent for the synthesis of bio-composite	Solvent mixing followed by drying of the sample (1-10°C/min)	(151)

2	Electrospinning	Ease to obtain nanoscale	Solvent used may be cytotoxic	Voltage (10-30kV), Flow rate (0.01-1ml/h)	(152)
3	Melt molding	Expensive	Only thermoplastic materials can be processed	High temperature (180° to 250C°)	(153)
4	Gas Foaming	Porous, light weight structure can be obtained	Controlled temperature and pressure required	High temperature (180° to 220° C), CO ₂ or N ₂ gas required	(154)
5	Sol-Gel	Wide variety of materials can be processed, Lower processing temperature	Long processing time	pH range (2-10) Gelation time from min to hours	(152)
6	Fused Deposition Modelling (FDM)	Thermoplastics can be processed	Poor surface quality, low strength	Temperature from 180° to 250° C required	(155)
7	Stereolithography	High resolution with smooth structure obtained	Expensive, Post curing required	UV light required	(155)
8	Selective Laser Sintering	Post processing not required	High operating temperature hinders	Laser power, Scan speed, Laser spot size, post-processing	(156)

			porosity	conditions need to monitor	
9	Inkjet Printing	Minimal material wastage	Reduces the mechanical strength	Ink viscosity, Drop Volume, print speed need to be checked	(155)
10	Thermal-induced phase separation	Low processing temperature	Only Organic solvents required	Polymer concentration, Solvent selection, Temperature, Quenching rate need to monitor	(157)

Table 2.3 above collectively showed the processing parameters the pros and cons of the different fabrication methods. Biomaterial fabrication has become feasible due to additive manufacturing (AM). In order to create biomimetic tissue or organs and functional organs, researchers accelerate the bioprinting process by employing additional techniques. For decades, advanced technologies have been employed to fabricate three-dimensional organs that mimics to the natural tissue. The world has revolutionized as a result of robotics, deep learning, machine learning, organ-on-a-chip, and big data. 4D bioprinting incorporates cells and stimulus responsiveness within the structure. Additionally investigated are robotics, biosensors, and bio actuators(158).

2.5 Hydroxyapatite

Calcium phosphates (CaPs) have piqued the interest of scientists since the early 1900s as raw materials for the synthesis of bone substitutes for use in biomedical applications. In 1920, the first study was conducted on rabbits, using CaPs as a reinforcement material to heal critical size bone lesions. Being osteogenic in-vitro and in-vivo, as well as their physio-mechanical traits that mimics the human bone, a wide range of medical specialties, including spinal surgery, orthopaedics, cranial restoration, bone implants, fracture repair, and dental surgery, utilize CaPs

extensively (159,160). The most prevalent crystal structure of hydroxyapatite is hexagonal, with lattice parameters of $a = b = 9.432 \text{ \AA}$, $c = 6.881 \text{ \AA}$, and $\gamma = 120^\circ$. It is a member of the $P6_3/m$ space group. The structure is made up of PO_4 tetrahedral that wraps around Ca ions and occupies two different sites: one along the axis and the other in well-aligned columns (Ca^{2+}). Adjacent hydroxyl groups (OH^-) are orientated in opposite directions (161,162). The effect of sintering kinetics on the mechanical characteristics and biodegradability of hydroxyapatite was reported by Trzaskowska and coauthors. According to reports, porosity decreases while compressive strength and young's modulus prominence with the rise in sintering temperature (163).

Hydroxyapatite possesses different properties that makes it an up-and-coming approach for regeneration and biomedical applications. The physical properties of HA are greatly affected by the manner of extraction or synthesis. The Density of the hydroxyapatite found to be 3.16 g/cc with the degrading temperature above 1000°C but the melting point of hydroxyapatite reported to be 1614°C . Furthermore, the hydroxyapatite exhibits low compressive strength of $120\text{-}900 \text{ MPa}$ and Young's modulus ranging from $35\text{-}125 \text{ GPa}$ (57). Numerous methods have been employed for the synthesis of Hydroxyapatite that have been classified as dry methods, wet methods and combination methods. Hydrothermal, solvothermal, chemical precipitation and Emulsion techniques are some of the instances of the methods (164). In addition, the different fabrication methods implemented to synthesize hydroxyapatite composites that showed significant application in the field of tissue engineering and drug delivery has been tabulated in table 2.4 below. Nevertheless, different sources of the hydroxyapatite inclusive of Fishbone, Bovine bone, Oyster shells, eggshells, Mussel shells, Plant & algae and minerals have also been reported (165).

The laboratory synthesis hydroxyapatite has a poor crystallinity, large surface area and higher porosity based on the synthesis method utilized. In contrast, naturally derived HA, is typically obtained by heat treating the bones at higher temperatures usually at 800°C , leading to formation of supremely crystalline HA (166). Sintered HA extracted from bovine bone showed the similar porosity and pore structure as natural bone. The most stable form of calcium phosphate salt possesses a molar ratio of calcium to phosphorus as 1.67 and usually precipitates at a higher pH of 10. At 1360°C , the hydroxyapatite has been degraded into TTCP and alpha TCP (167). Due to its high thermal stability, the crystallinity of hydroxyapatite has been improved through various thermal processes inclusive of calcination, hot-isostatic pressing and sintering (168) and through different methods as sol-gel and ultrasonication (169). In addition, the calcium, phosphate, anionic and cationic substitutions have been made in order to improvise the physio-chemical

properties of hydroxyapatite. Moreover, the nano-hydroxyapatite is reported to be cyto-compatible on accessing MC3T3-E1 cells (170).

The hydroxyapatite in human bone is made up of extremely well-organized nanocrystals (171). Moreover, n-HA may be produced chemically from precursors or taken from biological waste or natural resources such eggshells, animal bones, microbial and plants resources (172). In order to eliminate reaction byproducts, calcination at high temperatures is typically necessary for the extraction of pure HA. HA will alter in both structure and morphology throughout the calcination process.

A further investigation revealed that when HA was calcined at a higher temperature, β -tricalcium phosphate (β -TCP) also appeared, which might be connected to the removal of hydroxyl groups (173). Studies have shown that HA would transform from nanocrystals to microcrystals under the impact of temperature when the calcination temperature is higher than 700 °C, which will impair its clinical applicability (171,174).

Table 2.4 Hydroxyapatite composites for different applications with major outcomes

Material Used	Fabrication method	Processing	Major outcomes	Application	Reference
Ti-HA	Powder Metallurgy	Sintering of a composite of Ti and bovine HA at 800°C in an argon atmosphere	Improving Biocompatible with Vero and NIH3T3 cells	Tissue engineering	(175)
nHA-PU	Foaming method	Surface modification of nano-hydroxyapatite by grafting etidronic acid	Compressive strength 22.4 MPa, Bio-compatibility	Bone tissue engineering	(176)
CNT-Fe/HA	In-situ synthesis	Fe catalyst and chemical modification by Chitosan and Folic acid	Anti-cancerous drug doxorubicin targeting	Targeted drug delivery	(177)
LDH/PCL/Gel	Electrospinning	Layered double hydroxide (LDH) prepared using co-precipitation	Biocompatible on Human neuroblastoma SH-SY5Y cells	Nerve tissue engineering	(101)
PCL/Gelatin/BC/HA	3D printing	Bacterial cellulose (BC) Glucanoacetobacter xylinus	Improved cell viability in Human osteoblast cells 1.58 ± 0.19 MPA tensile	Bone tissue engineering	(178)

			strength	
PCL/HA	Extrusion based 3D printing	Cuttlefish bones (<i>Sepia officinalis</i>), mussel shells (<i>Mytilus galloprovincialis</i>) and chicken eggshells used for extraction of Hydroxyapatite	Bioactive on Mg63 cell lines. Compressive modulus of 316 MPa obtained	(179)
PHB/HA/Alginate seeded on Mesenchymal Stem cells	3D printing	PHB has been obtained from <i>Azotobacter chroococcum</i> 7B.	Porous scaffold with pore size of 104 ± 25 μm formed and tested on Animal model Rat parietal bone showing osteogenesis	(180)
PVA/Silk Fibroin	Electrospinning	Heart patches with diameter of 228 ± 49 nm created	Biocompatible on Human cardiac fibroblast cells (HCFC)	(102)
Chitin/PLA/HA	Solvent casting	Ionic solvent 1-ethyl-3-(3-dimethylimidazolium) acetate is used	Biocompatible for Osteocyte cells, Tensile strength 20.68 MPa	(181)

2.6 Reduced graphene oxide

Carbon-based materials inclusive of graphene and its derivatives possess distinctive structure and properties, became another promising candidate in biomaterial research. A honeycomb lattice of graphene with a single carbon atom's thickness is present. It may be shaped into 0D, 1D, and 3D forms and is quite solid (182). Moreover, it has exceptional electrical qualities, highly crystalline and remarkable transparency. Though graphene exhibits a lot of good features and addition of epoxy, hydroxyl, and carboxyl groups to the basal plan of the graphite layers, graphene oxide has been generated (GO). GO is extremely hydrophilic because of these functional groups that contain polar oxygen. Because of this, GO has outstanding dispersibility in a wide range of solvents, particularly in water. Furthermore, the oxygen-containing functional groups can offer reactive sites for functionalization or chemical modification of graphene oxide, which can be utilized to generate GO-based biomaterials. While the oxygen-containing groups can help graphene overcome some of its drawbacks, they can also lead to other issues. For instance, electrically insulating GO can be produced addition of oxygen containing groups. However, GO can be chemically reduced to recover its conductivity upto an extent. Due to the fact that the reduced GO (rGO) that is obtained enhances the dispersibility in different solvents. The characteristics of the chemically reduced graphene are similar to those of pure graphene (183).

On analyzing structure of graphene and its derivatives, the presence of functional groups on its surface, that include carboxylic acid (COOH), hydroxyls (OH), and epoxides (COC), especially in graphene oxide (GO) and reduced graphene oxide (rGO), allows graphene to be paired with numerous biomolecules, which broadens the diversity of its biomedical applications (184–187). Nevertheless, the reduced graphene oxide (rGO) has poor colloidal stability and easily clumps after dispersing in water for a few hours as compared to graphene oxide (188). The colloidal stability of rGO is influenced by the proportion of C-O and C=O bonds in it. The superior hydrophilicity of GO over rGO is ascribed to the abundance of oxygen-containing functional groups in Graphene oxide (188). However, rGO with enhanced colloidal stability can be generated, contingent upon the reducing agents and consequent surface characteristics (189). Furthermore, materials generated from graphene are known to possess exceptional mechanical strength and flexibility; the effective elastic modulus of monolayer rGO, found to be 250 GPa (190) which is higher than graphene oxide which showed 207.6 GPa (191).

Lastly, because rGO is somewhat less deoxygenated, it has been demonstrated to have greater thermal stability (192).

Numerous methods have been enforced to reduce the graphene oxide. The methods that have been employed affect the certain properties of the graphene oxide. The figure 2.5 below illustrates the various methods utilized for the reduction of graphene oxide to obtain the reduced graphene oxide.

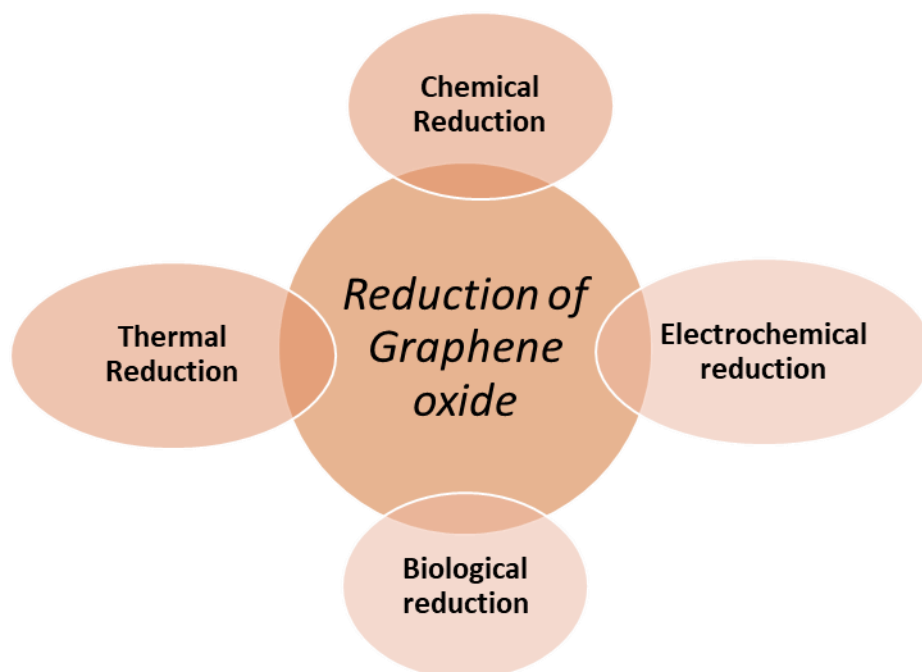


Figure 2.5: Different methods of reduction of Graphene oxide

The graphene oxide has been reduced using different methods inclusive of chemical, thermal, electrochemical and Biological. The chemical and thermal methods are the most popular method that has been extensively used for obtaining reduced graphene oxide from graphene oxide. The graphene oxide can be prepared by oxidation of graphene using Hummer's method or modified Hummer's method (193). Further, the thermal approach uses microwave assisted thermal reduction or photoreduction (194–197) whereas chemical reduction has been done using different chemicals such as hydrazine (198), Hydroiodic acid, hydroquinone, Benzoin (199–201). Electrochemical reduction is another approach of reducing the graphene oxide (202,203). The effect of reducing temperature on the conductivity, resistibility of reduced graphene oxide has been studied and

revealed that the 70°C found to be ideal temperature for obtaining better conductivity ((204). On the other hand, the impact of different chemical reductants inclusive of NaBH₄, CH₂O, NaOH, C₆H₉O₆ on the thickness of the graphene flakes in reduced graphene oxide has been investigated (205).

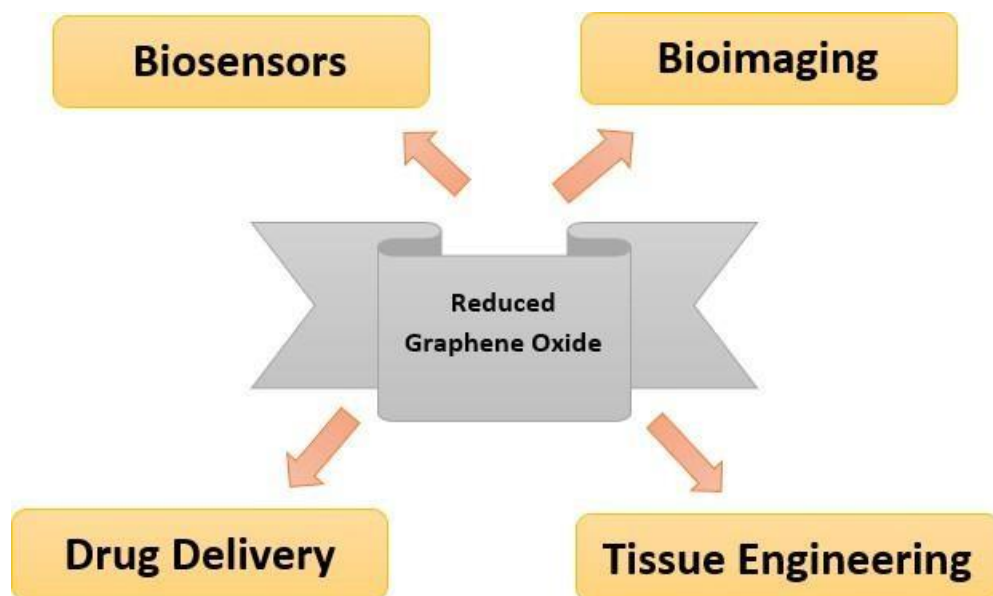


Figure 2.6: Applications of reduced graphene oxide (rGO)

The diverse applications of reduced graphene oxide have been demonstrated in the above figure 2.6. In lieu of the outstanding properties of reduced graphene oxide, the composites of reduced graphene oxide developed leapfrog opportunities in the field of tissue engineering, drug delivery, bioimaging and biosensors. The table below listed the applications of the reduced graphene oxide composite.

Table 2.5: Use of reduced graphene oxide composites for different applications

S.No.	Composite	Cells used	Application	References
1	rGO/CS	HT-29	Cancer therapy	(206)
2	rGO/HA-SP	MDCK	Bioimaging	(207)
3	Gd-rGO	H1299	Bioimaging	(208)
4	rGO-Ru-PEG	MDCK	Bioimaging	(144)
5	rGO-Polydopamine-Au	-	Biosensors for Mycobacterium Tuberculosis Detection	(209)
6	PCL/rGO	MG-63	Bone tissue engineering	(210)
7	Amine-rGO@Alg/ECM	HUVEC	Cardiac tissue engineering	(211)
8	Zn-dopamine-rGO	T-47D MCF10A	Drug delivery	(212)
9	PVA/rGO	CCD-986Sk	Skin tissue engineering	(213)
10	Gd-rGO	H1299	Drug Delivery	(208)
11	NiO/rGO	-	Biosensors	(214)

2.7 Carboxymethyl cellulose

As per the structural basis of carboxymethyl cellulose is negatively charged, water-soluble analogue of cellulose and a linear polysaccharide of anhydro-glucose. The monomers are bonded through glycosidic linkages (β -1,4-). The primary distinction between CMC and cellulose at the molecular level is limited to the presence of carboxymethyl groups (-CH₂COOH) in the CMC structure, which substitute hydrogen atoms for certain hydroxyl

groups found in the pure cellulose structure. The industrial manufacturing of the polymeric materials was initially documented in Germany during 1920s (215). Researchers are fascinated in utilising certain plant-based precursors, such as corn cobs (216), corn husk (217), corn stalks (218), pineapple peel (219), sugarcane bagasse (220), *Asparagus officinalis* stalk end (221) etc., along with some waste materials, like wastepaper to be used for the large-scale or commercial production of CMC.

Numerous industries, including biomedical, pharmaceutical, textile, construction, food, plastics, cosmetics, paper, and oil, have discovered extensive uses for CMC and CMC-based hybrid products. For example, CMC and its composites are utilised extensively in biomedical fields for a variety of purposes in tissue engineering (24), bone-tissue engineering (25,26,222), wound dressing (223–225), constructing 3D scaffolds for biocompatible implants (226) and in drug delivery (227,228).

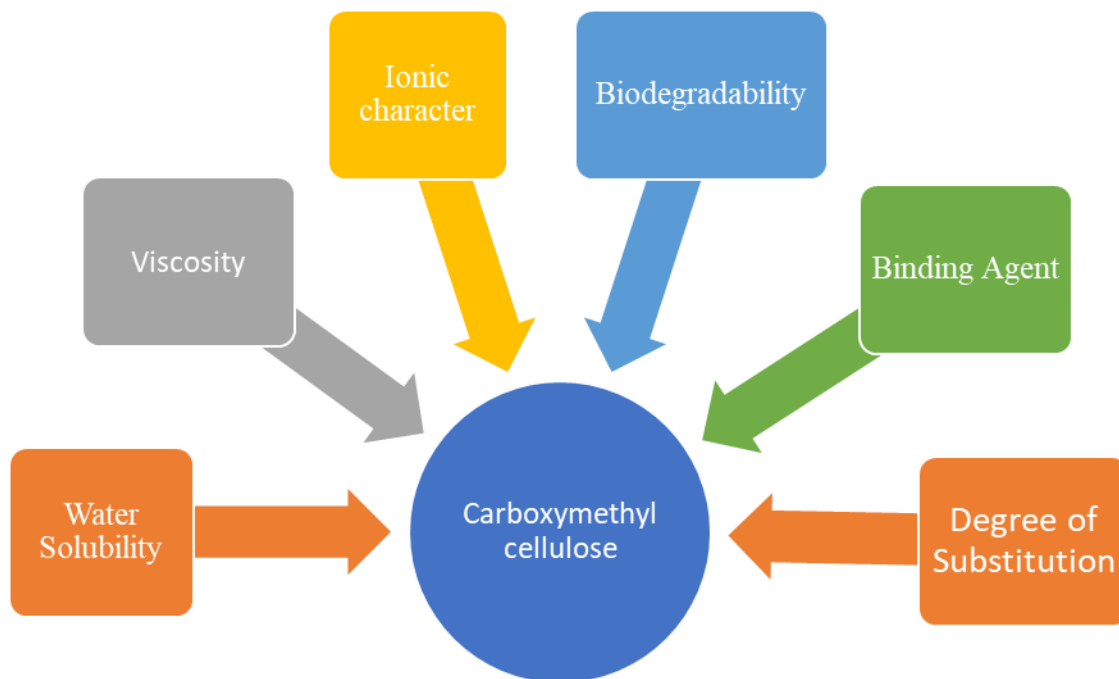


Figure 2.7: Properties of carboxymethyl cellulose

The diversified applications of the carboxymethyl cellulose depends upon the various vital properties of carboxymethyl cellulose as illustrated in the figure 2.7 above. In the process of synthesizing CMC from cellulose, the quantity of substituent groups (carboxymethyl) bonded to every anhydro glucose unit governs the quantity of DS. The solubility, emulsion property, thickening property, viscosity, stability, and salt tolerance attributes of CMC are highly dependent on the DS value (229). The DS value of CMC varies from one to another based on the cellulose source and synthesis process. According to various sources, the ideal DS values determined as 0.17 for *Musa paradisiaca* fruit, 0.28 for *Musa paradisiaca* stem (230), 0.29 for palm fiber, 0.31 for palm kernel cake (214), 0.35 for *M. sinensis* (231), 0.51 for seaweed (232).

As a result of its high hydrophilicity, CMC, a polymeric substance, generates a viscous solution in an aqueous media. Thus, in order to describe the fluid behaviors, properties (thickening, emulsifying, etc.), and property-based applications of aqueous Na-CMC (or H-CMC), the viscosity parameter is crucial. However, the synthesis conditions (concentration of NaOH, reaction temperature, and pH of solution) and source parameters (cellulose particle size, molecular weight, and DS) also affect or depend on the viscosity property of CMC derived from cellulose (221). As the high or low viscosity of the applied medium is maintained with increasing or decreasing CMC concentration, respectively. The Carboxymethyl cellulose is anionic polymer due to presence of carboxymethyl group. In textiles industries, the CMC has been extensively used as a binder because it ameliorates the bonding between the materials (233). Moreover, the mechanical properties of the composites have been enhanced with the addition of carboxymethyl cellulose (113,234,235). Nevertheless, the biodegradability of carboxymethyl cellulose has been reported which aids its applicability in tissue engineering (236,237). In order to improve the mechanical strength as well as the other biological properties of the binary blend of calcined hydroxyapatite and reduced graphene oxide, the polymer addition has been done. A number of different polymers inclusive of both natural and synthetic possess a bunch of important traits that when inculcated with other material enhances the overall properties of the composites (238). Moreover, different polymers have been added to the hydroxyapatite in order to improve its mechanical properties (239). Carboxymethyl cellulose, sometimes called cellulose gum, is an anionic substance that is made of cellulose and carboxymethyl groups. Kukrety and colleagues have provided a thorough description of the process by which carboxymethyl cellulose can be extracted from cellulase-based natural resources such as sugarcane bagasse, cotton stalks, banana stems, paper sludge, and sago waste (21). Numerous areas can benefit from the uses of carboxymethyl

cellulose owing to diverse qualities, such as biodegradability, non-toxic nature, low manufacturing costs, and abundance of resourcefulness. Recent research by Basu et al. stated the potential of CMC-based film for wound healing in both normal and diabetic animal models (33). Through solvent mixing and freeze drying, chitosan, carboxymethyl cellulose, and a zinc and iron- loaded hydroxyapatite scaffold were created and showed antimicrobial properties, decreased degradation behavior, with the ability to promote bone cell proliferation (34). Carboxymethyl cellulose has been added in various amounts to enhance the characteristics of the binary blend of hydroxyapatite and reduced graphene oxide.

2.8 NEED AND SCOPE OF RESEARCH

The valuable insights for the research gap in the synthesis of composites of hydroxyapatite has been discussed below:

- **Biomechanical properties:** Being brittle in nature, the mechanical properties of hydroxyapatite have been enhanced by incorporation of various different materials as well as by synthesizing the composites using different fabrication methods.
- **Influence of composite compositions:** The addition of appropriate fillers into the hydroxyapatite as well as the impact of varying concentration of the reinforcing materials and attaining the right composition of the composite is another aspect to look into.
- **Biodegradation:** In order to overcome the surgical issues, it is important to find an appropriate biodegradable composite of hydroxyapatite. The hydroxyapatite should be integrated with the material that mitigate the biodegradability of the composite.
- **Surface properties and biocompatibility of the composite:** The impact of fillers on the surface properties need to be explored as the surface morphology influences the cell adhesion which further impelled the biocompatibility of the composite. The composite should be biologically compatible and non-toxic in nature.

The urgency for the need of alternative treatment for tissue regeneration or repair due to several limitations associated with currently available therapies such as insufficient regeneration of tissue due to poor cell survival, immunological rejection, and severe donor site expiration leading to loss of functional tissue. Biomaterials has lately emerged as an appealing alternative strategy for the clinical treatment of injured and/or deteriorating tissue through the regenerating the function of the diseased tissue.

The key challenge is the design and production of a suitable three-dimensional (3D) artificial extracellular matrix from biocompatible and biodegradable materials with tailored properties.

Among the numerous ceramic biomaterials, hydroxyapatite has been identified as a possible contender for tissue regeneration applications. Finally, it appears that an integration of diverse polymers and carbon-based materials with other ceramic components is required to provide the appropriate composite qualities for clinical use. In this procedure, a ternary composite with desirable qualities will be developed utilizing a thermal pressing approach with hydroxyapatite, reduced graphene oxide, and Carboxymethyl cellulose polymer.

2.9 Objectives of the research

The objectives of the thesis work are:

1. Processing and Characterization of additives for biomaterial preparation
2. Study of mechanical properties of biomaterial fillers.
3. Biomaterial fabrication steps with addition of appropriate polymer to the additive and characterization
4. Biological compatibility testing parameters.

Chapter 3

MATERIALS AND METHODS

3. MATERIALS AND METHODS

The essential steps of the experimental technique for treating the components and then creating a binary composite have been outlined in this chapter. The processing of the components separately and then the blending of the same has been performed in order to develop the binary composite has been described herein. Further, the addition of polymer and heating the composites at constant pressure has been utilized to create the ternary composite, is also briefly introduced.

Finally, all pertinent characterization methods, such as biocompatibility studies, morphological analysis with FESEM analysis, mechanical property evaluation, contact angle measurement, and Physio-chemical characteristics through X-ray diffraction and Fourier transform infrared spectroscopy that has been carried out is being discussed.

High purity graphene oxide powder with bulk density $\sim 2.7 \text{ g/cm}^3$ has been purchased from Platonic Nanotech. Carboxymethyl cellulose has been purchased from Central Drug House Chemicals (CDH), Dulbecco's modified eagle's medium (DMEM) media, Fetal Bovine Serum (FBS), MTT Solution, Dimethyl Sulfoxide (DMSO) purchased from HiMedia.

3.1 Pre-Treatment of the Ceramic and Carbon-based components

The mineral type of calcium apatite that occurs naturally is called hydroxyapatite (Hap, HAp, or HA) written as $(\text{Ca}_{10}(\text{PO}_4)_6(\text{OH})_2)$. The main mineral that makes up bones and teeth is known as hydroxyapatite, and it naturally exists as calcium phosphate. Natural hydroxyapatite is biocompatible because it has a few chemical and physical characteristics that go well with bone. As a result of the hydroxyapatite's low mechanical strength, numerous attempts have been made to increase its density using a variety of techniques, including mechano-chemical cold sintering(240,241) ; spray pyrolysis (242); hydrothermal hot-pressing (243).

As compared to graphene oxide, reduced graphene oxide had superior characteristics. In comparison to graphene oxide, reduced graphene oxide (rGO) demonstrated larger surface area and higher electrical conductivity. Nevertheless, as compared to graphene oxide, the rGO demonstrated greater mechanical strength.

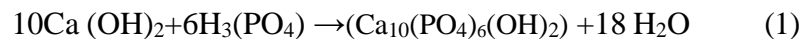
The composite's component materials underwent heat treatment to produce the proper material for binary composite due to the aforementioned characteristics. In order to improve the physicochemical characteristics, pre-treatments were applied to both graphene oxide and hydroxyapatite. FTIR and XRD are just two of the characterization methods used to look into the improvised features.

3.1.1 Synthesis of Hydroxyapatite and Calcination of prepared hydroxyapatite

Using the wet precipitation approach, HA has been successfully produced, yielding a white crystalline powder. FTIR and XRD studies have been used to characterize the precipitates that were produced. Thermal processing has been used to calcine hydroxyapatite in order to improve its density, as mentioned above. The mechanical strength of hydroxyapatite is increased through densification. In a muffle furnace, the calcination was done for two hours at 800°C. X-ray diffraction can be used to evaluate the crystallinity after calcination (168,244).

3.1.1.1 Chemical Synthesis of Hydroxyapatite (HA)

The process of creating HA entails mixing 500 mL of 10M calcium hydroxide $\text{Ca}(\text{OH})_2$ with 300 mL of 6M orthophosphoric acid (H_3PO_4) in an aqueous solution. $\text{Ca}(\text{OH})_2$ was mixed with the solution H_3PO_4 dropwise while being magnetically stirred for two hours at approximately 60°C.



The solution described above should be stirred continuously and left undisturbed overnight at the basic pH. Add 1 M of ammonium hydroxide (NH_4OH) to this mixture. Following three rounds of washing with distilled water, the solution was then left aside for four hours. Furthermore, the nanoparticles in powder form were annealed at 900°C at a rate of 10°C/min. Pure, white, and crystalline powder was the end product as shown in Figure 3.1 (245,246).

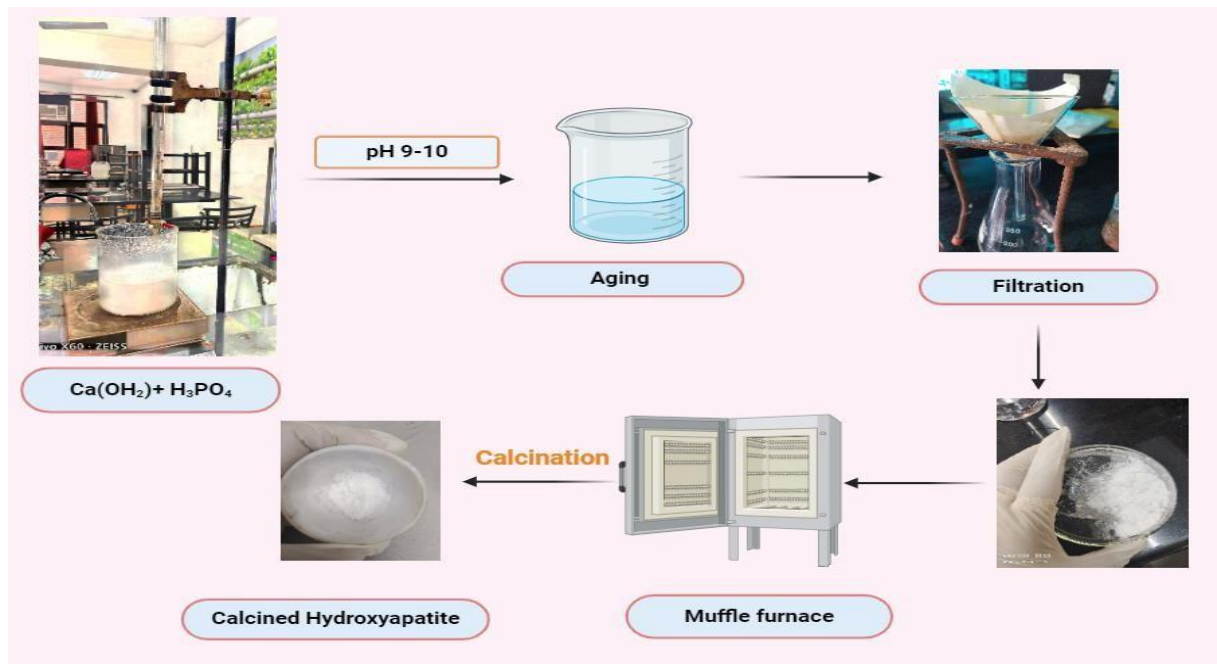


Fig 3.1 Synthesis of Hydroxyapatite through chemical precipitation method

3.1.1.2 Calcination of Hydroxyapatite

When Hydroxyapatite (HA) was calcined, its physicochemical characteristics improved. The material's crystallinity is improved by heat treatment, and when it is calcined, the crystallinity is increased but the carbonate ion and embedded pores are constrained (168,244). HA was calcined at 800°C for two hours in order to improve its physicochemical properties.

3.1.2 Reduction of Graphene oxide

The purchased graphene oxide with density 2.7g/cm^3 has been characterized through FTIR and XRD. In addition to altering its physicochemical characteristics, a reduction of Graphene Oxide (GO) enhances its mechanical behavior and dispersive power. Chemical (247), solvothermal, photocatalytic (248), thermal, and other reduction processes have all been scrutinized before generating a reduced version of Graphene Oxide (GO). It has been reported that Graphene Oxide thermally reduces in a variety of atmospheres, including nitrogen and air (249). The thermal reduction of graphene oxide has been achieved and characterized through FTIR and XRD analysis. As already stated, when compared to

graphene oxide, the reduced form of the graphene oxide exhibited greater mechanical strength. There are several ways to reduce it, but the heat treatment has been chosen as the reduction procedure. In a muffle furnace, the thermal reduction of GO was conducted for 2 hours at a temperature of 200°C, and the results were examined using FTIR and XRD analysis (249,250).

3.2 Preparation of rGO-HA composite

As shown in Table 3.1, various rGO weight concentrations (10, 20, 30, 40, and 50%) were incorporated to calcined HA. The powdered samples were contrived through the ball impact Process. Five zirconia balls with a thickness of 5 mm were used for the ball impact method, and they were vertically vibrated simultaneously mixing powder for 30 minutes. The powder was then put under a high pressure of 5 tons for 30 to 60 seconds to give it a pellet structure as shown in Figure 3.2. For further experiment, pellets with a diameter of about 15 mm and a thickness of 4 mm were used and every experiment has been performed in triplicates.

Table 3.1. Percentage of Hydroxyapatite (cHA) and reduced graphene oxide (rGO) used for different blends.

Blends	cHA (%)	rGO (%)
cHA	100	0
HrG1	90	10
HrG2	80	20
HrG3	70	30
HrG4	60	40
HrG5	50	50

Table 3.1 above described the percentage concentration of calcined hydroxyapatite that is being reinforced with reduced graphene oxide in various variants of binary blends namely HrG1 to HrG5. The concentration of calcined hydroxyapatite decreases alongside increasing the percentage contribution of reduced graphene oxide and successfully achieving the formation of binary composite.



Figure 3.2: Schematic diagram for the preparation of binary composite and ternary composites

The figure 3.2 above showed the steps for the synthesis of hydroxyapatite and reduced graphene oxide separately as well as the preparation of variants of calcined hydroxyapatite and reduced graphene oxide composites and the ternary composites after the integration of carboxymethyl cellulose (CMC). Later, the characterization of treated constituents and the composites has been accomplished.

3.3 Characterizations of materials and composites

FTIR and X-ray diffraction have been used to mark the calcined hydroxyapatite's physio-chemical properties. To ascertain the alteration that took place during the calcination process, the peaks have been assessed. FT-IR spectroscopy was carried out in the 400–4000 cm^{-1} wavelength range at room temperature. The diffraction pattern was investigated using an XRD analyzer and a Cu-K radiation source with a wavelength of 1.540\AA . The values of diffraction pattern with 2θ ranged from 0° to 80° .

Utilizing X-ray diffraction (XRD) and Fourier transform infrared (FTIR) spectroscopy, the produced samples have also been studied. Through the analysis of the scattering intensity with respect to angle 2θ , X-ray diffraction techniques were scrutinized. The diffraction pattern was investigated using an XRD analyzer and a Cu-K radiation source with a wavelength of 1.540\AA as shown in the figure 3.3 below. The values of diffraction pattern with 2θ ranged from 0° to 80° .

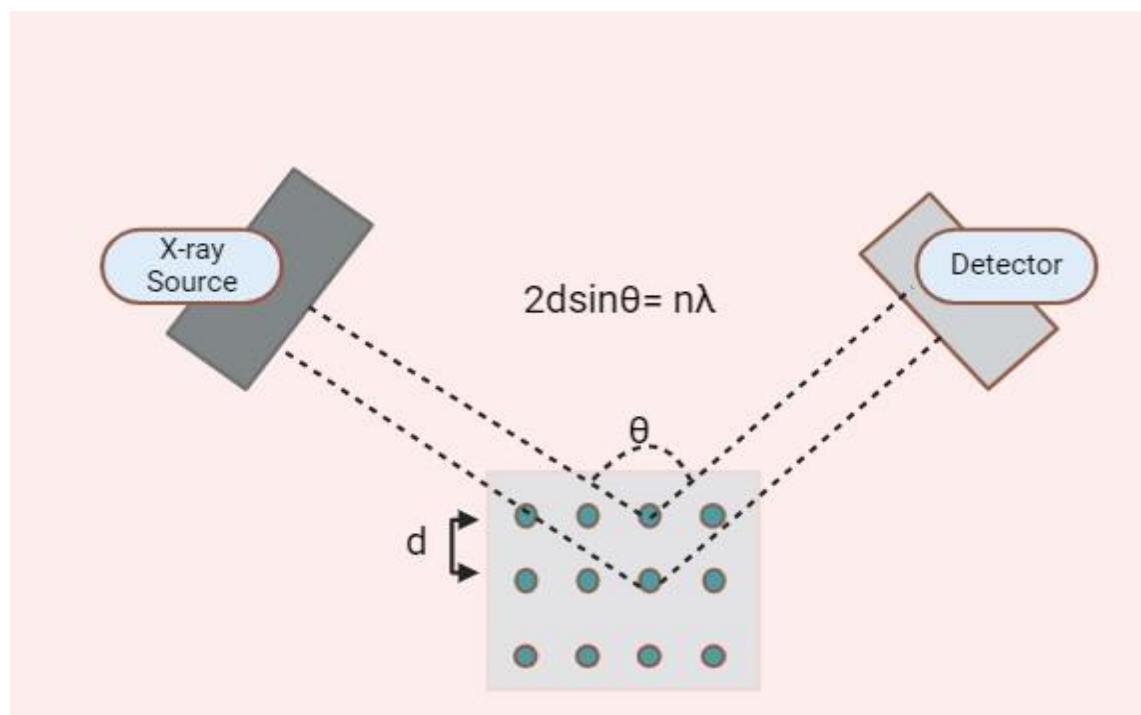


Figure 3.3 The schematic representation of X-ray Diffraction

A strong analytical method for figuring out the atomic and molecular structure of crystal is X-ray diffraction (XRD). The constructive interference of monochromatic X-rays with a crystalline

sample is the basis of X-ray scattering (XRD) concept. To ensure the detection of all crystallographic orientations, the sample has been carefully pulverized. The atoms of a crystalline material scatter X-rays when they come into contact with it. Constructive interference is the result of satisfying Bragg's Law, the fundamental principle of X-ray diffraction (XRD), which links the wavelength of X-rays to the diffraction angle and lattice spacing in the crystal (251). It occurs when the path difference between rays scattered by successive planes of atoms equals an integer multiple of the wavelength.

Additionally, the presence of various material constituents in the composite can be examined through FTIR spectroscopy by determining the bonds.

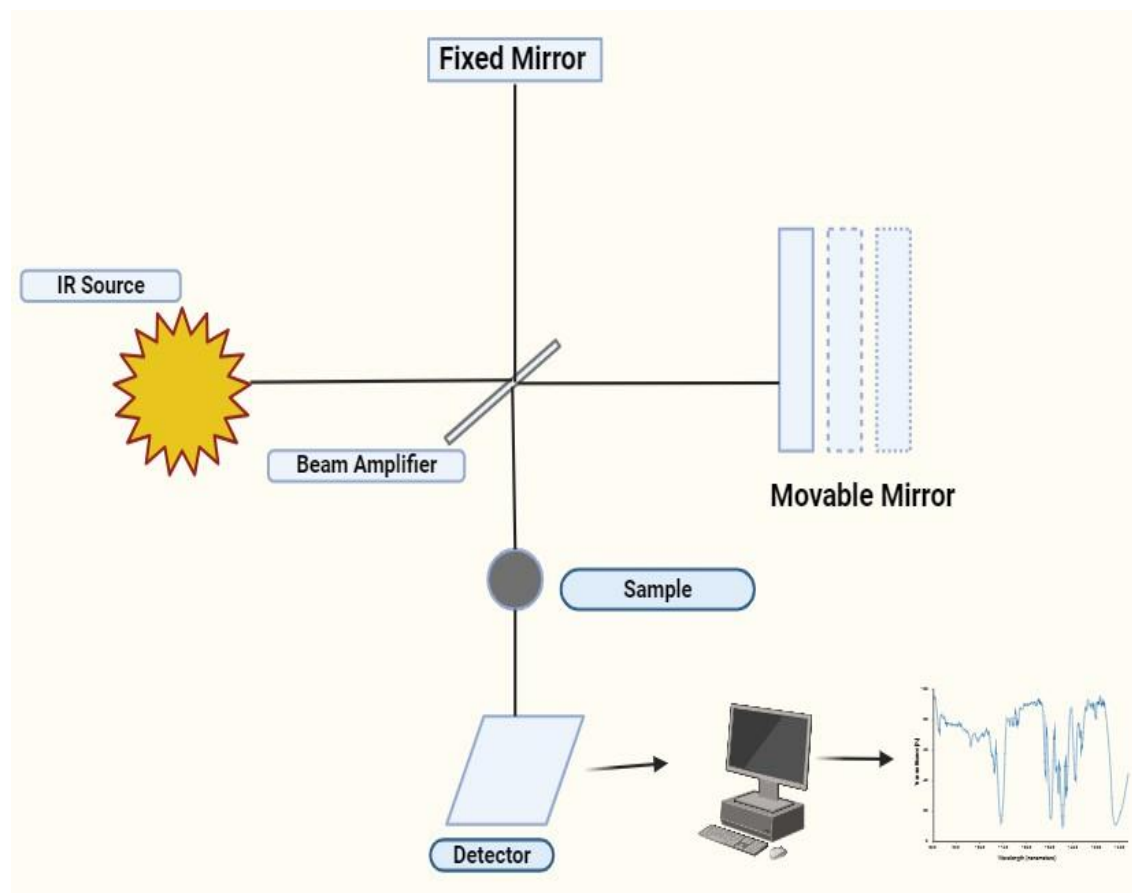


Figure 3.4 The schematic representation of FTIR spectroscopy

The infrared spectrum of absorption, emission, and photoconductivity of a solid, liquid, or gas can often be obtained using the Fourier Transform Infrared (FTIR) spectroscopy technique.

Analyzing absorption pattern of infrared light by the sample at various wavelengths yields the information for the molecular makeup and structure of the sample. The vibrational energy of the bonds that make up molecules cause them to absorb infrared light at particular frequencies. An absorption frequency is specific to each kind of bond, such as C-H, O-H, and N-H bonds (252). An interferometer produces a signal called an interferogram as shown in the figure 3.4 which is a signal that has all the information on the infrared absorption of the sample.

3.4 Thermal treatment under pressure

Ceramics materials like hydroxyapatite showed poor mechanical strength due to which various attempts have been made to enhance the mechanical behavior of the hydroxyapatite either by processing thermo-mechanically as well through addition of appropriate material. Thermal treatment is one of the inexpensive and successful approaches to obtain dense and compact material. Nevertheless, it prevents the unnecessary material loss that usually occurs while processing of the composites. Thermal treatment under pressure has been achieved by heating the material to the low temperature simultaneously pressing with the appropriate applied pressure. Various composites have been fabricated through hot pressing as ZrB_2 and SiC has been blended using ball milling and then subjected to hot pressing to obtain the final densified product (253). Khalil and co-workers also reported the hot pressing of aluminum alloys with epoxy adhesive (254). The loose powder after complete drying in hot air oven and after ball milling has been compacted into pellets which were then used to press in the hot-press machine for two different temperatures of 100°C and 150°C for three different time intervals of 5, 10 and 20 mins at constant pressure of 7.8 psi in uniaxial direction.

3.5 Preparation of ternary composite

In order to generate ternary composite addition of carboxymethyl cellulose to the optimized calcined hydroxyapatite and reduced graphene oxide has been implemented (255). The dry powder of three constituents have been blended in mortar-pestle and ball milling and then has been subjected to thermal treatment under pressure to fabricate the ceramic-based polymeric blends. The thermal treatment has been carried out at temperatures of 100°C and 150°C for holding periods of 5, 10, and 20 minutes at a constant pressure of approx. 7.8 psi. The specifics of ceramic-based polymeric blends are detailed in the Table 3.2, where B1-100 indicates the Blend-1 thermally

treated under pressure at 100°C and B1-150 indicates the Blend-1 thermally treated at 150°C, along with additional blends as well.

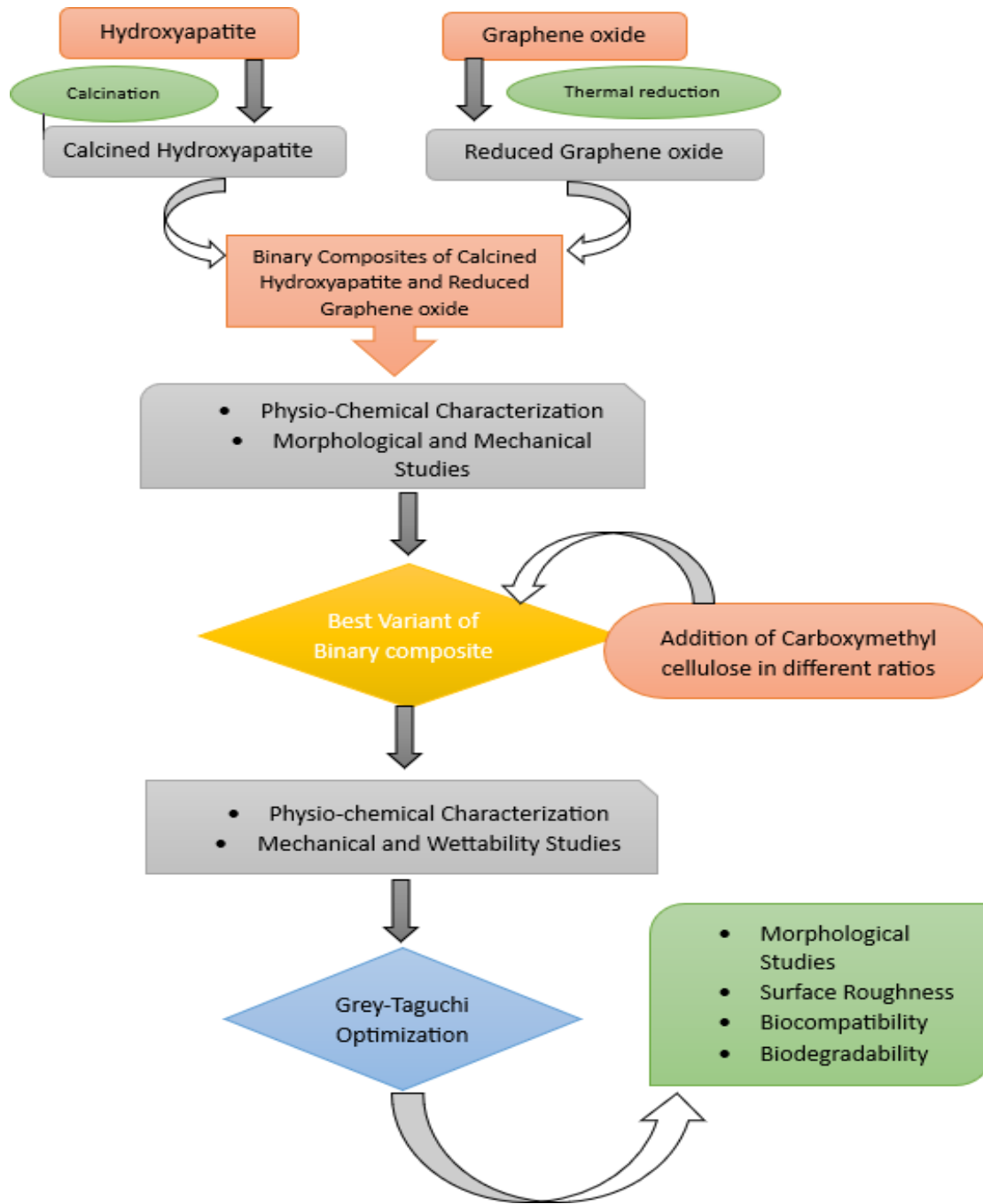


Figure 3.5: The flowchart to demonstrate the overall experimental procedure

The figure 3.5 above reveals the preparation strategy for the synthesis of ternary components. The appropriate candidate from the binary blend has been chosen and further improved with the addition of carboxymethyl cellulose polymer that has been thermally treated under pressure at

different temperatures and time periods. The Figure 3.5 demonstrates the addition of polymer as well as the overall experimental analysis.

Table 3.2: Ceramic-based blends of calcined hydroxyapatite, reduced graphene oxide and carboxymethyl cellulose Thermally treated at different temperatures and various time intervals.

Samples	Temperature (°C)	HAP (%)	rGO (%)	CMC (%)
B1-100	100	60	30	10
B1-150	150			
B2-100	100	60	20	20
B2-150	150			
B3-100	100	60	10	30
B3-150	150			

3.6 Characterization of Ternary Composites

The generated samples have also been investigated for physio-chemical analysis through X-ray diffraction, FTIR as well as for thermal analysis. Nevertheless, the variants also have been evaluated on the basis of mechanical testing. Furthermore, the cytotoxicity and the bioactivity of composites have been determined.

3.7 Physio-chemical Characterization

3.7.1 X-ray Diffraction

The individual pre-treated sample of calcined hydroxyapatite and reduced graphene oxide as well as the composites both binary and ternary were characterized by X-Ray Diffractometer. Figure 3.3 describes the fundamental principle and setup for X-ray diffraction. The X-ray Diffractometer (XRD, Bruker) with mono chromated Cu K_{α} radiation ($K_{\alpha} = 1.540 \text{ \AA}$) operated at 44 KV, 40 mA with the dwell time 1 second per step and scan rate of $2^{\circ}/\text{min}$ has been used for the phase identification of the composites. The scattering intensity has been studied with respect to the changing angle 2θ ranging from 0° to 80° (255). In order to observe the effect of calcination on hydroxyapatite the crystallinity needs to be figured out. The crystallinity of the composite has been evaluated using the equation:

$$C\% = \frac{X_c}{X_c + X_a} \times 100 \quad (2)$$

Where X_c is the area of all crystalline peaks and X_a is the area of all amorphous peaks whereas $C\%$ is the percentage crystallinity.

3.7.2 Fourier transform infrared spectroscopy (FTIR)

A FTIR spectrometer (PERKIN ELMER) interfaced with an IR microscope running in absorbance mode was used to conduct the FTIR analysis. The infrared spectrum is created when the sample interacts with IR-radiation. When subjected to IR radiation, electromagnetic (EM) radiation fluctuates in molecules with an ultimate electric dipole. These variations are the results of the sample's chemical makeup. Therefore, the spectrophotometer records the variations in EM-radiations in order to examine the chemical composition of the sample. Employing the Fourier transform, the signal is obtained. The setup has been illustrated in figure 3.4. The spectra were measured and recorded for powdered samples in the range of 500-4000 cm^{-1} . For comparison, the spectra were smoothed using a constant smooth factor (256).

3.7.3 Thermogravimetric analysis

Thermogravimetric analysis uses a piece of equipment to gauge how a sample's mass and weight change when the temperature changes. The apparatus detects numerous chemical or physical changes in a sample's mass as heat events. Desorption, absorption, sublimation, vaporization, oxidation, reduction, and decomposition are some examples of these chemical/physical changes occurring with thermal events. Using the software that comes with the instrument, the study is conducted by exposing the sample to a variety of temperatures. Excellent temperature reproducibility is provided by the equipment's broad isothermal zone. In addition to these quick furnace cooling options, it is also possible to study more samples faster by employing integrated forced air and tap water. TGA (PERKIN ELMER) was used to examine the thermal stability of composites. Each measurement used approximately 1 mg of samples, and all were heated at a rate of 10 $^{\circ}\text{C}$ per minute in flowing N_2 up to the temperature of 600 $^{\circ}\text{C}$.

3.8 Grey-Taguchi approach for optimization

The Grey-Taguchi approach is one of the best methods of optimization because it combines the Taguchi method and Grey Relational Analysis (GRA) to optimize multiple performance characteristics at once not like other methods of optimization include Response Surface Methodology (RSM), Genetic Algorithm, and Artificial Neural Networks (ANN) (153,257). To identify the ideal amounts of factors with efficient output, the Taguchi technique has been applied, systematically varying the numerous components using an orthogonal array. However, GRA normalizes the experimental data to convert various performance metrics into numbers that are similar. Determine the grey relational grade (GRG) and grey relational coefficient (GRC) as well. Selecting Grey-Taguchi optimization over alternative techniques not only minimizes the use resources and the experimentation but also optimizes several performance factors in a user-friendly manner.

To reduce the number of practical experiments, the experimental process has been optimized using grey- Taguchi approach. The L18 orthogonal array has been employed which had two columns and eighteen rows, allowing for seventeen degrees of freedom to address one parameter with three levels and another with six levels. The figure 3.6 below illustrates the process flow for the grey-Taguchi approach.

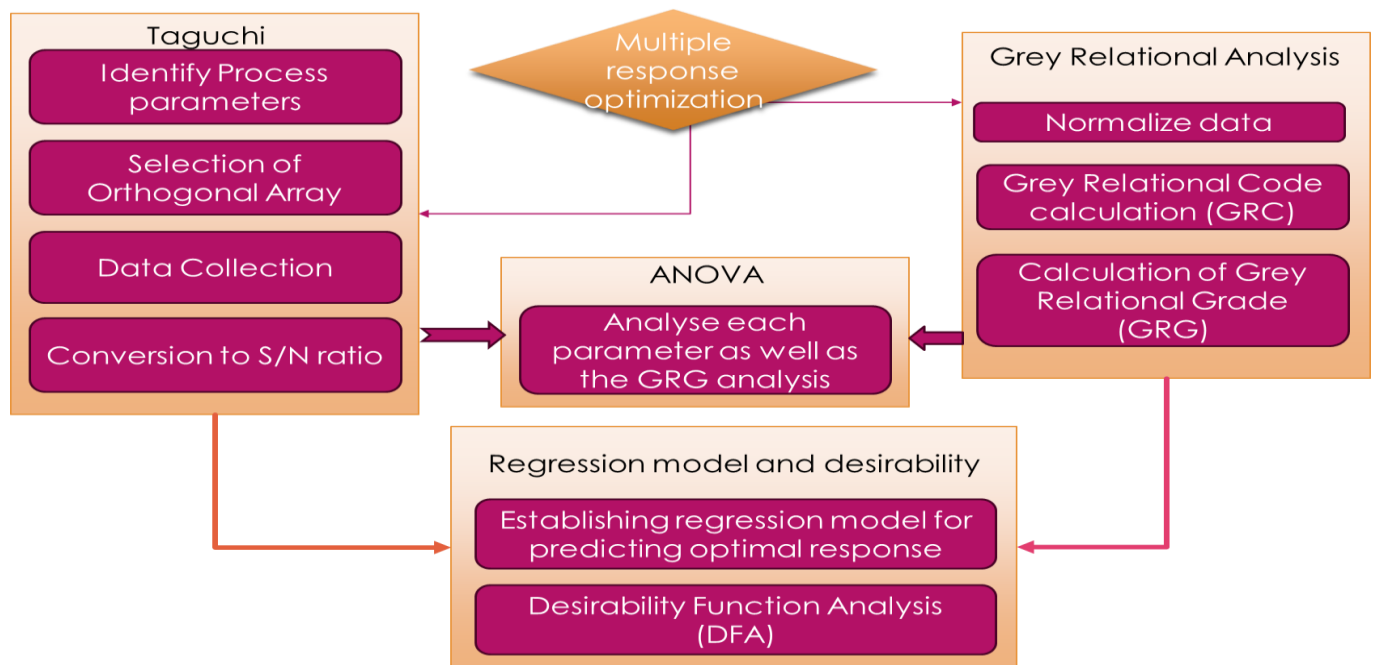


Figure 3.6 Flowchart representation of Grey-Taguchi approach for Optimization

Based on the Taguchi design of the experiment method, each parameter level is set using the L18 orthogonal array. The experimental data is then converted into a signal-to-noise ratio using the MINITAB 14 program to determine quality and evaluate a variety of factors (258,259).

3.8.1 Grey relational analysis (GRA)

The initial phase in gray relational analysis is to develop a grey grade. To generate the grey scale, the response will be set between zero and one. The grey coefficient will be calculated using the input data to show the extent to which predicted response fits the actual result. The grey relational coefficients of all the performance parameters belonging to each sample condition will then be averaged to generate the grey relational gradient. The grey relational grade is an overall assessment of all performance attributes. GRA optimization has been done in twin forms (260).

To put it another way, achieving a single grey relational grade requires optimizing a slew of difficult, complex performance parameters. The most appropriate value for the process parameter is at the top grey relational grade level. The statistical analysis of variance (ANOVA) is then used to establish the significance level of the applied process parameters. The ideal set of process parameters will be identified through ANOVA and grey grade analysis. A confirmation experiment is then carried out to confirm the optimal process parameters determined by the study. GRA is employed in the following circumstances (258).

1. GRA is utilized when there is insufficient information and to maximize many performance characteristics.
2. When calculating gray relational generation value, the larger the better or the smaller the better is used. The larger the better is used in this study because higher compressive strength is sought while a smaller is the better is required for water contact angle (WCA).

In gray relational analysis, data preprocessing is first done to standardize the raw data for analysis. The gray relational generation, also called a linear normalization of the experimental data, is carried out in the region between zero and unity (260). A study of normalized values usually identifies three kinds of performance characteristics: nominal-the-agreeable, higher- the-better, and lower-the-acceptable(259). In general, the higher the predicted value for compressive strength, the better, and the smaller the expected value for wettability of the composites. Less than a 90° water contact angle indicated hydrophilicity or wettability. Higher cell adhesion and proliferation are correlated with greater wettability (261,262). However, thermal treatment has been used to produce

harder materials with higher strength and, thus, higher compressive strength values. For the two outcomes, the normalized results can therefore be written as $x_o(k)$ ($k=1,2,\dots,8$).

$$v_i(l) = \frac{z_i(l) - \min z_i(l)}{\max y_i(l) - \min y_i(l)} \quad (2)$$

$$v_i(l) = \frac{\max z_i(l) - z_i(l)}{\max z_i(l) - \min z_i(l)} \quad (3)$$

where $i(l)$ is the experiment's k th outcome, $\max(l)$ and $\min(l)$ are the maximum and minimum values of the $i(l)$ value, respectively, and $y_i(l)$ is the normalized value of the i th experiment's k th performance characteristic. According to Deng, greater normalized results are linked to better performance, and one is the optimal normalized result (263).

The grey relational coefficient (GRC) was computed using equation 4. The grey relational coefficient shows the link between the expected and actual experimental results. It also makes it possible to compare and compute the statistical mean of the non-additive multiple experimental data.

The GRC of each reaction variable is averaged to get the Grey relational grade (GRG).

$$\gamma_i = \frac{1}{a} \sum_{i=1}^d \xi_i(k) \quad (4)$$

where a is the bulk count of the performance characteristics and γ_i is the GRG value computed for the i th experiment.

3.8.2 ANOVA analysis

An ANOVA is used to determine which combination of factors has the greatest impact on the overall quality of the experiment. To accomplish that, the commitments for every component and error were divided into squared deviations from the absolute mean of the gray relational grade, which serves as an indicator of the grade's overall inconsistency. First, using Eq. (5), was used to determine the squared deviation SST from the total grey relational grade mean m .

$$SS_T = \sum_j^{\rho} (\gamma_j - y_m)^2 \quad (5)$$

where p is the number of orthogonal array experiments and j denotes the mean of the grey relational grade (GRG) for the j th experiment.

The total squared deviation SST is composed of two parts: the total squared deviation from each factor and the total squared error SSe.

In order to analyze the influence of factor on performance characteristics, the commitment rate of every variable blend to the absolute amount of squared deviation SST must be investigated. The Fisher F test (258) can also be used to determine the component combination that has a substantial influence on performance parameters.

When the F value is quite large, a change in the variable mix usually has a considerable effect on the outcome features.

3.8.3 Desirability test

The desirability assay has been used to optimize the varied outcomes. Desirability functions are sometimes known as objective functions. Using the desirability function, all of the output responses are turned into a desirability value on a free scale. By attributing the highest composite desirability to the input parameter setting, the ideal parameters are determined. To use the DFA approach, the following steps must be followed (264).

Step 1: Calculate the desirability index for each parameter.

Step 2: Compute the composite desirability. The optimal factor configuration was determined based on the desirability of the blend.

Step 3: The Taguchi approach is used to assess the composite desirability values of each experimental run to discover the best parametric setting for the desired results.

Step 4: To establish which heat-pressing condition has the largest influence, an ANOVA is employed. To depict the influencing parameters, ANOVA used the total sum of squares approach.

Step 5: The composite desirability value is forecasted using the ideal parameter settings discovered throughout the investigation. In order to determine that the obtained parametric setting is the ideal set of input parameters, the anticipated composite desirability value of the optimal parametric setting must then be confirmed and supported.

3.9 Mechanical Behavior

The strength of calcined HA, variants of hydroxyapatite and reduced graphene oxide and ceramic-based composites has been measured using a Universal Testing Machine (UTM). Compressive moduli of the composites were determined from the slopes of compressive stress- strain curves for each version, which were examined in triplets at a rate of 5 mm per minute (265). Furthermore, Materials called bio-composites are made up of a reinforcement (natural fibers or bio-based fillers) and a matrix (often polymer-based). The kind and quality of the matrix, the chemical makeup of the reinforcement, and the interface between the two all affect the mechanical characteristics, which include compressive strength, tensile strength, Young's modulus, toughness, and hardness. The Universal Testing Machine has been used to examine the mechanical attributes. In material testing, a Universal Testing Machine (UTM) is a flexible and popular tool. It is made to carry out several mechanical testing on materials, including tensile, compressive, flexural, and shear tests. As seen in Figure, the Universal Testing Machine (UTM) consists of a load frame, load cell, grips or plates, control panel, and computing system coupled to it.

The sample specifications are mounted between the grip plates and have been developed in compliance with the American Society for Testing and Materials (ASTM D695). To carry out the experiment, the parameters such as speed, size, and the kind of test to be conducted—tension or compression—have been established. After running the test, the data obtained on the computer software in the form of the stress-strain curve has been analyzed.

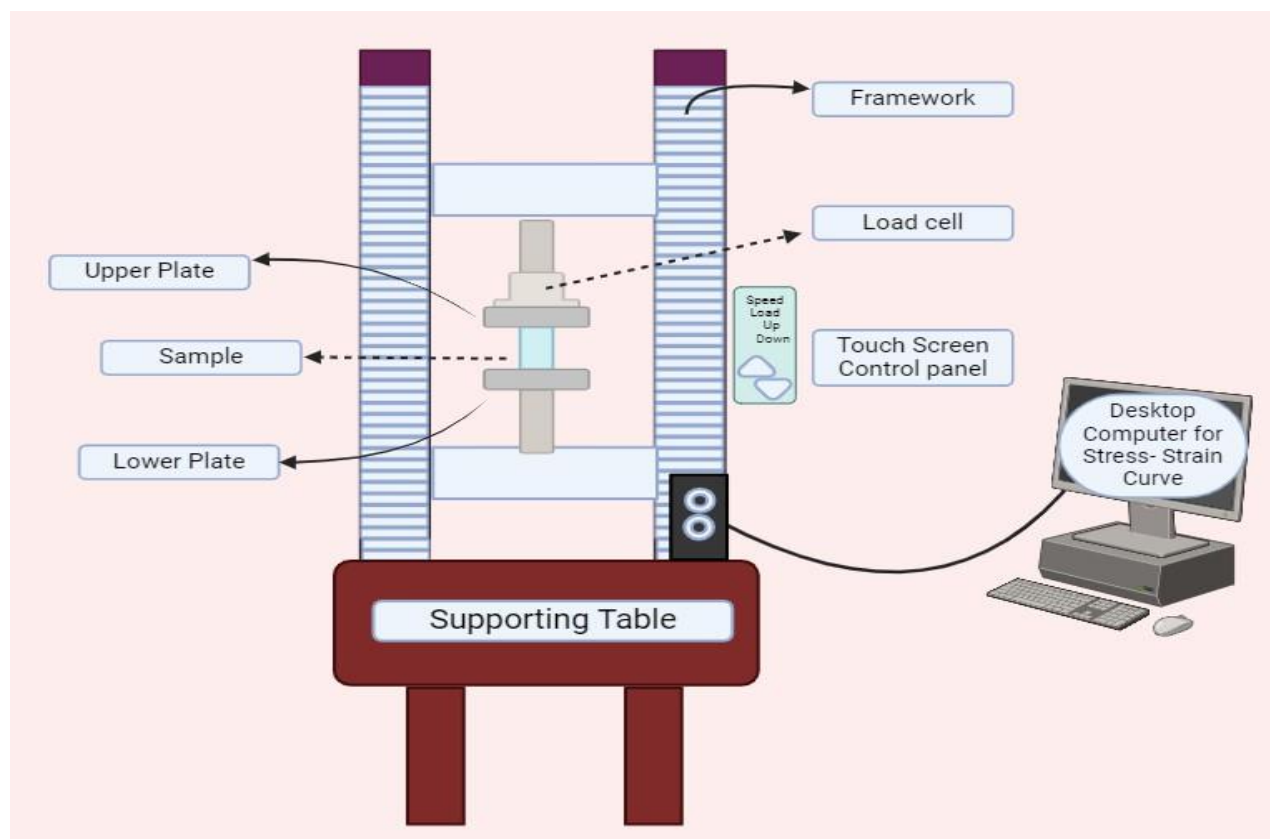


Figure 3.7 The set-up of Universal Testing Machine (UTM)

The powdered material has been shaped into circular dimensions as per the ASTM D695 (266). The final dimensions for the samples prepared found to be diameter mm and height mm. All the experiments have been performed in triplicates. The pellets were created by the KBr Press machine and had a height of 12.4 ± 0.24 mm and the diameter of approximately 5.8 ± 0.28 mm. Composites were run through the Universal Testing Machine (UTM) at a crosshead speed of 5 mm per minute to assess their mechanical characteristics. The experimental setup has been shown in the figure 3.7 above. Compressive moduli of the composites were determined from the slopes of compressive stress- strain curves for each version, which were examined in triplets at a rate of 5 mm per minute (265).

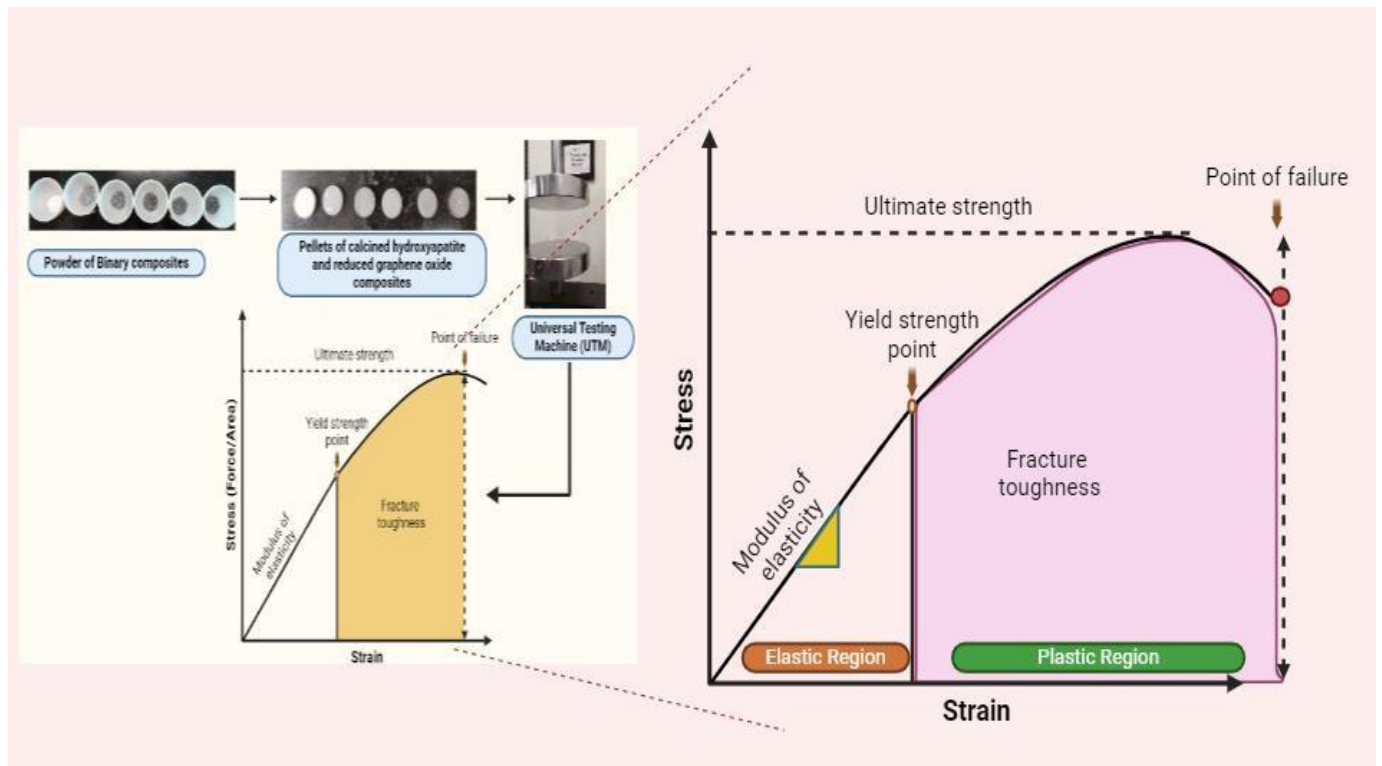


Figure 3.8 The experimental set-up for the mechanical behavior of the composites

The stress-strain plot aids to determine different mechanical characteristics of materials under compressive pressures during a compression test. An essential graph in material science and engineering that shows the link between the strain (deformation) that a material experiences and the stress that is applied to it is called a stress-strain plot. The stress-strain plot may be used to identify a number of different components as shown in the figure 3.8. Different kinds of stress-strain curves exist. The Ductile material is represented by a curve in the plot that shows a considerable plastic zone prior to deformation, whereas the Brittle material is shown by a different plot in which no plastic region appears. Furthermore, the elastic area is contributed by the initial linear segment of the curve, which bears Hooke's law and is directly proportional to strain.

$$\text{Stress } (\sigma) \propto \text{Strain } (\epsilon)$$

Young's modulus is determined by the slope of elastic region. The nonlinear section of the curve designated as the Plastic area extends beyond the Yield point. The material experiences persistent

deformation in this area. Furthermore, the Ultimate compressive strength (UCS) is the maximum stress that a material can sustain. The phrase "fracture point" or "point of fracture" refers to the location where the material breaks.

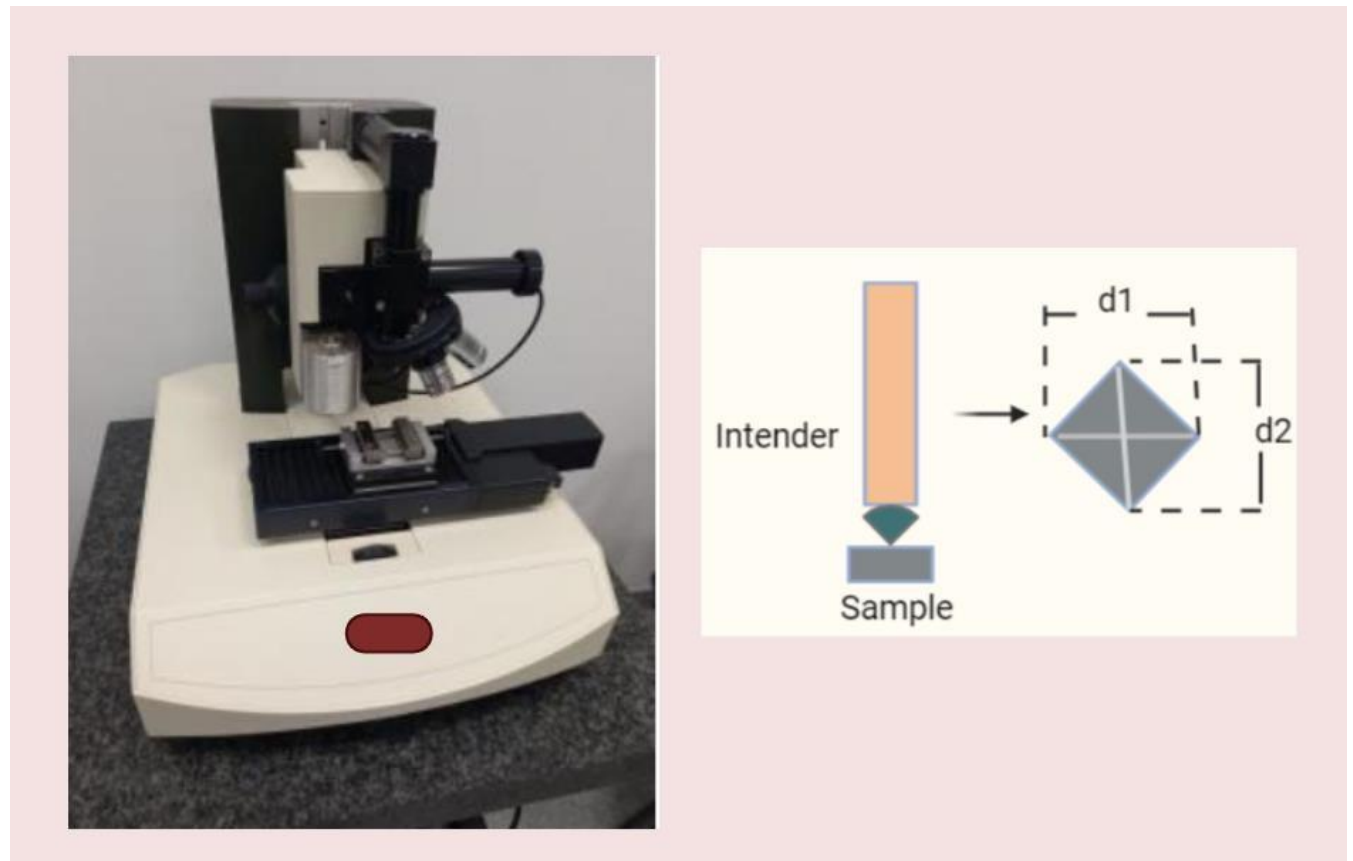


Figure 3.9 Microhardness test

One of the most important methods for assessing the hardness characteristics of bio composites at the microscopic level is microhardness testing. This test is especially crucial for materials used in biomedical applications, where surface characteristics have significant effects on longevity and performance, such in the case of dental composites, tissue scaffolds, and bone implants. The ability of a material to withstand localized plastic deformation is determined by the microhardness test. It offers information on the mechanical characteristics of the material, including its hardness, wear resistance, and capacity to tolerate mechanical stress. The following formula is used to get the Vickers hardness (HV):

$$HV = \frac{1.8544 P}{d^2}$$

Where P is the applied load in kilogram-force (Kgf) and d is the average length of the diagonals in millimeters (mm) (267).

A fully calibrated nano-indenter (TTX-NHT, CSM Instruments) was mounted to a three-sided pyramidal Berkovich diamond indenter with a nominal edge radius of 20 nm (facing 65.3 from the vertical axis) for the purpose of performing the nanoindentation measurements. A three-sided pyramidal Berkovich diamond indenter with a nominal tip radius of 20 nm was used for the nano-indentation experiments. It was connected to a nano-indenter (TTX-NHT, CSM Instruments) and operated in load control mode as shown in figure 3.9. Every test was run at ambient temperature. The conventional Oliver and Pharr approach (Beh et al., 2020).

This paper presents the correlation between the morphological characteristics and the diffuse reflectance (optical properties) of the porous hydroxyapatite/cornstarch (HAp/Cs) composites with various starch proportions (30, 40, 50, 60, 70, 80 and 90 wt%). The porous composites were measured via SEM and enhanced by image processing to find the average pore size, strut width, and average surface roughness. The average porosity of the porous composites was measured using liquid displacement method. The diffuse reflectance spectroscopy was implemented to investigate the diffuse reflectance and the corresponding optical band gap energy of the porous composites in the 500e900 nm range. A relationship between morphological characteristics and diffuse reflectance properties were established using Pearson's correlation coefficient. The findings of the study depict that a strong correlation can be noticed between optical band gap energy with porosity, pore sizes and surface roughness of the porous composites. Meanwhile, the strong correlations between the diffuse reflectance spectral gradient with surface roughness can be observed. The moderate correlations can be observed between the diffuse reflectance spectral gradient with pore sizes and strut width of the porous composites.", "container-title": "Journal of Materials Research and

Technology", "DOI": "10.1016/j.jmrt.2020.10.012", "ISSN": "22387854", "issue": "6", "journalAbbreviation": "Journal of Materials Research and Technology", "language": "en", "page": "14267-14282", "source": "DOI.org (Crossref)", "title": "Morphological and optical properties of porous

hydroxyapatite/cornstarch

(HAp/Cs)

composites", "volume": "9", "author": [{"family": "Beh", "given": "C.Y."}, {"family": "Cheng", "given": "E.M."}, {"family": "Mohd Nasir", "given": "N.F."}, {"family": "Mohd Tarmizi", "given": "Emma Ziezie"}, {"family": "Eng", "given": "S.K."}, {"family": "Abdul Majid", "given": "M.S."}, {"family": "Ridzuan", "given": "M.J.M."}, {"family": "Khor", "given": "S.F."}, {"family": "Ahmad Saad", "given": "F.S."}], "issued": {"date-parts": [{"2020", 11}]}, "schema": "https://github.com/citation-style-language/schema/raw/master/csl-citation.json"} (Beh et al., 2020) was used to examine and interpret the observed data. About 10 indentations has been made for each sample and each experiment was performed in triplicates.

3.10 Surface Roughness and Wettability of composites

The morphology of the composites has been determined through FESEM. The texture of a surface with peaks and valleys is referred to as surface roughness. As surface roughness influences the mechanical characteristics, adhesion, friction, wear, and biological interactions of the material, it is an important parameter in many domains, including materials science, engineering, and biomedical applications. Typically, measures like Ra (arithmetic average roughness), Rz (average maximum height of the profile), and Rq (root mean square roughness) are used to quantify surface roughness. Numerous methods, including as profilometry, atomic force microscopy (AFM), and field emission scanning electron microscopy (FESEM), can be used to quantify these attributes. The process flow for calculating the surface roughness parameters has been illustrated in figure 3.10 below. The FESEM image is taken and processed using appropriate software as MATLAB or ImageJ. Further the processing of the image has been done and a reconstruction of the surface topography has been done to generate a 3D analysis of the 2D image. Moreover, these images further used to plot the profile and to calculate the roughness parameters as Average roughness (Ra), Root Mean Square Roughness (Rq/RMS) and then the data has been analyzed. Average Roughness, (Ra) is the mathematical mean of the profile heights' absolute values during the testing length (L), Whereas (Rq) RMS Roughnes determines the mean square average of the heights of the profile over the testing length (L). Additionally, the Testing Length is the distance across which surface parameter values are assessed. Further, the mean line denoted as Mt is taken as the reference line and serves as the measurement point for profile deviations.

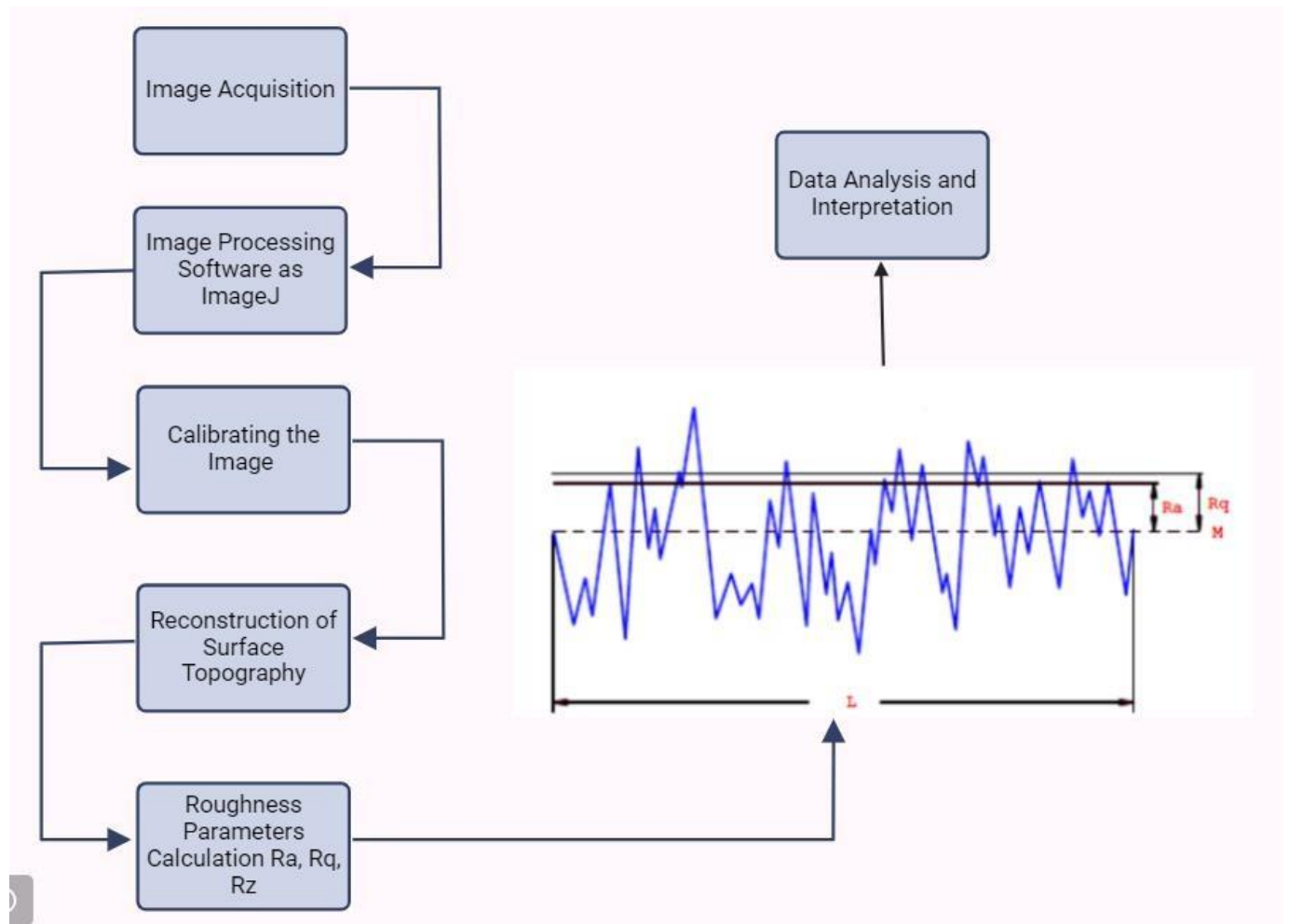


Figure 3.10 The flowchart describes calculation of Surface roughness using FESEM Images through ImageJ.

ImageJ has been used to analyze FESEM images of composites to evaluate the root means square roughness (R_q), and the average roughness means (R_a) through the Surf CharJ plugin (268). The contact angle measurement technique is used to determine the wettability of the composite surface. The wettability signifies the hydrophilicity or hydrophobicity of the several variants of composites. It is the ability of a composite to hold the liquid droplet on its surface as shown in figure 3.11 below.

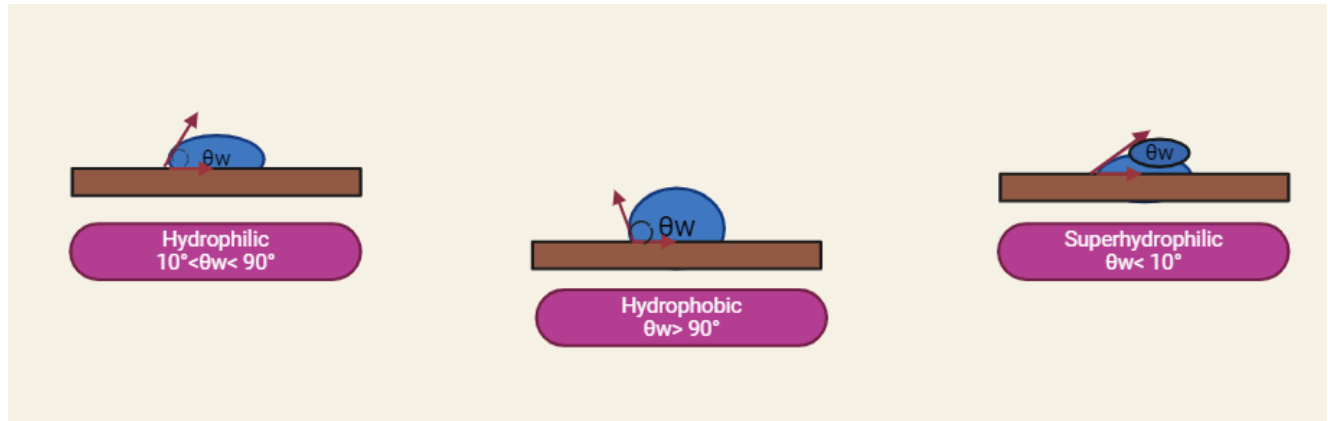


Figure 3.11 Wettability of the surface using contact angle measurement

The different variants of the composites have been shaped circular with radius of 0.66 cm and thickness of 0.5-0.6 cm approx. In this approach, a water droplet using a glass dropper pipette has been placed on the surface of the composites approximately 2 ml. The volume of the water droplet has been kept constant for all the composites that were used to determine the wettability. Using a smartphone equipped with a macro lens, the drop photographs were captured after 30 seconds, when the droplet images appeared to be the sharpest and clearest. Thereafter, utilizing ImageJ software to analyze the captured images, the contact angle of the droplet was then calculated by drop analysis plugin (269,270). For the purpose of calculating an average, five measurements of each variant of composite were made (254).

3.11 Biom mineralization in SBF Solution

The deposition of calcium and phosphorus ions in the ternary composite with significantly increased mechanical strength was further investigated. The samples spent four weeks submerged in simulated bodily fluid (SBF). In order to achieve an ions concentration similar to that of human blood plasma, the SBF solution was prepared complying with the methodology given by Kokubo et al 1990. The table 3.3 below describes the ion formulation for the SBF solution and the blood plasma (271). Each sample weighed about 5gm and it was soaked in a fixed volume 100ml of SBF solution while being kept at a temperature of about 37°C and an approximate pH of 7.4. After the immersion process, the samples were taken out of the SBF, rinsed with deionized water and dried in the ambient atmosphere. Further, the samples' microstructure was examined using a scanning electron microscope (SEM), and the levels of calcium and phosphorus ions were evaluated using an Energy dispersive spectroscopy (EDS)(102)

Table 3.3 Concentration of Ions in grams for simulated body fluid (SBF)

Ion	Concentration in grams for 1000ml of SBF solution
Na⁺	8.035
Cl⁻	40 ml
HCO₃⁻	0.355
Ca²⁺	0.292
K⁺	0.225
Mg²⁺	0.311
HPO₄	0.231
SO₄²⁻	0.072

Through soaking in SBF solution, the bioactivity of the ternary mixtures of hydroxyapatite, reduced graphene oxide, and carboxymethyl cellulose was ascertained. FESEM has been used to assess the surface of the composite for the development of a bone-like apatite layer (261). In hydroxyapatite (HA) and reduced graphene oxide (rGO) composite, matrix mineralization has previously been documented as elevated calcium deposits as early as day 14 (272). Additionally, Radha and coworkers reported on the theorized mechanism of the apatite layer in reduced graphene oxide and hydroxyapatite, exhibiting a greater Ca/P ratio as compared to pure hydroxyapatite (HA). According to Turk and colleagues' 2018 report (273), the biomineralization process improved with decreasing the amount of reduced graphene oxide.

3.12 In Vitro Biodegradation

The rate of biodegradation of the composites was assessed using an in vitro biodegradation technique. The figure 3.12 below illustrates the experimental procedure. The pellets of about 4 mm thickness and 15 mm diameter have been dipped into the 10 ml SBF solution. The ceramic-based polymeric blends possessing higher mechanical strength have been chosen and then pellets of

different variants of the composites were submerged in simulated bodily fluid (SBF) prepared following the procedure described by Kokubo and coworkers (271).



Figure 3.12 The experimental procedure for the Biodegradation assay

During 28 days of incubation, the composites were removed from the SBF, oven dried, and weighed (274). The following equation was used to calculate the percentage decrease in composite weight at a specific time:

$$\text{Weight loss \%} = \frac{W_t - W_i}{W_i}$$

where W_i is the initial weight of the composite and W_t is the weight of the composite after time t (days) in SBF solution. This experiment was enforced in triplicates.

3.13 Cell Culture and Cytotoxicity

The fibroblast cell line (NIH3T3 cell line), that had been acquired from the National Centre for Cell Science (NCCS), Pune, India, was used to test the samples for cytotoxicity. The cell line was cultured in a T25 tissue culture flask using 89% Dulbecco's modified eagle's medium (DMEM) with 10% fetal bovine serum (FBS) and 1% antibiotic-antimycotic solution 100X liquid. The cells

were incubated at 37°C and 5% CO₂. Every other day, fresh media has been introduced in order to achieve good confluency. The adherent NIH3T3 cells were separated using a Trypsin-EDTA solution (0.25%) after 80% confluency, and then centrifuged at 1500 rpm for two minutes. Additionally, the cells were resuspended in fresh culture media after the supernatant was discarded, and the cell suspension has been utilized for further experiment. The MTT test was employed to measure cytotoxicity. The powdered samples then went an hour-long UV sterilization. Following thorough ultrasonic mixing of the sterilized samples with DMEM complete growth media at two separate amounts of 25 mg/ml and 50 mg/ml for 30 minutes, sample extracts were removed after incubation at 37°C and 5% CO₂ for 24 hours. In 96 well plates with 300 µl of DMEM complete culture media, NIH3T3 cells were seeded. The medium was replaced with sample extracts (n=3) after 24 hours of incubation. The plates were incubated for 24 and 72 hours at 37°C and 5% CO₂ with two different sample extract concentrations of 25 mg/ml and 50 mg/ml. The media were removed after the previously stated time interval had passed, and the wells were then gently rinsed with sterile PBS. Then, 100µl of dimethyl sulfoxide (DMSO) was added to dissolve the purple formazan crystals formed inside cells in the 96-well plate by shaking the plate in the dark for about 20 minutes. The MTT [3-(4,5-dimethylthiazole-2-yl)-2,5-diphenyl-2H-tetrazolium bromide solution was added to each well of the plate and incubated for 4 hours. The absorbance was measured after the supernatants were taken and shaken. Using a microplate reader, at a wavelength of 570 nm the absorbance (OD values) of the obtained supernatant from each well was recorded (275). The well with only the cells and without sample has been used as the control. The cell viability (%) of the samples were calculated using the following equation:

$$\text{Cell Viability (\%)} = \frac{\text{OD of the samples}}{\text{OD of the Control}} * 100 \quad (6)$$

Additionally, the composites that had been seeded with cells were examined under a fluorescence microscope. In order to observe the cytoskeleton and nucleus of the live cells FITC and DAPI staining was employed (276,277).

3.14 Statistical Analysis

All the data described as mean± standard deviation has been evaluated through statistical analysis using GraphPad. All the variables were analyzed in triplets and the p value < 0.05 is considered as

significant. For each group of samples, statistical significance was assessed in triplicates and P values were produced by an analysis of variance (ANOVA) utilizing Tukey test for multiple comparisons. This approach is predicated on the notions of normality and homogeneity of distributional variances.

Chapter 4

RESULT AND DISCUSSION

RESULT AND DISCUSSION

In this chapter, the pre-treatment of the composites individual components is discussed along with the investigation of their mechanical strength as aforementioned following their XRD and FTIR characterization. Nevertheless, the morphology of the samples has been tested using FESEM. The premade binary composite that demonstrated the highest mechanical strength and biocompatibility later underwent an adequate polymer addition. The final composite material has been fabricated using thermal treatment under constant pressure. The Taguchi technique was used for optimization, and the best-formed composites were evaluated for their morphological, Wettability and surface roughness properties. Later, we looked into biological factors like bioactivity, biocompatibility, and biodegradation.

PART 1: Processing and characterization of additives for biomaterial preparation.

4.1 FTIR analysis

The structural study of calcined HA has been looked at employing FTIR. The various functional groups present in calcined HA are displayed in Figure 4.1. Peaks at 558.44 cm^{-1} and 1056.64 cm^{-1} show the vibrational stretching mode of the phosphate group of hydroxyapatites. The peak 1658.24 cm^{-1} is thought to have been influenced by the stretching mode of the carbonate group. The water that was absorbed also came from the top at 3437 cm^{-1} (168,278).

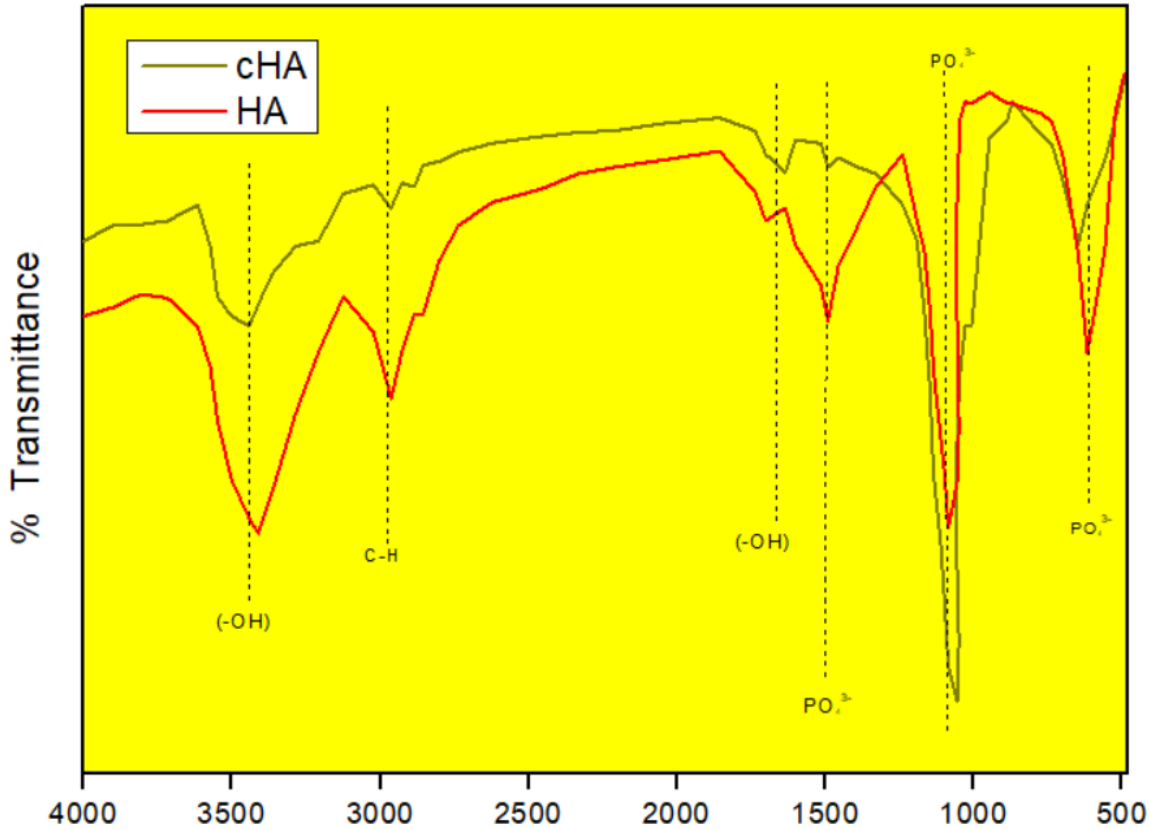


Figure 4.1. FTIR analysis of Hydroxyapatite (HA) and calcined hydroxyapatite (cHA)

4.2 XRD analysis

The Figure 4.2 contrasts the cHA along HA assessed using X-ray peaks. The crystallinity has been determined from the XRD pattern seen in Figure 4.2, which agrees with the accepted JCPDS file no. 090432 (279). According to the XRD in the figure below, the calcination procedure at 800°C enhanced the crystallinity of HA.

The formula below has been used to calculate the sample's crystallinity:

$$C\% = \frac{A_c}{A_c + A_a} \times 100 \quad (1)$$

In this formula, Aa denotes the combined area of all amorphous and crystalline peaks, Ac denotes the area of crystalline peaks, and C% is the crystallinity percentage. The crystallinity of chemically synthesized hydroxyapatite (HA) was found to be $42.49 \pm 1.2\%$ which increases on calcination to $73.09 \pm 1.5\%$ in calcined hydroxyapatite (cHA).

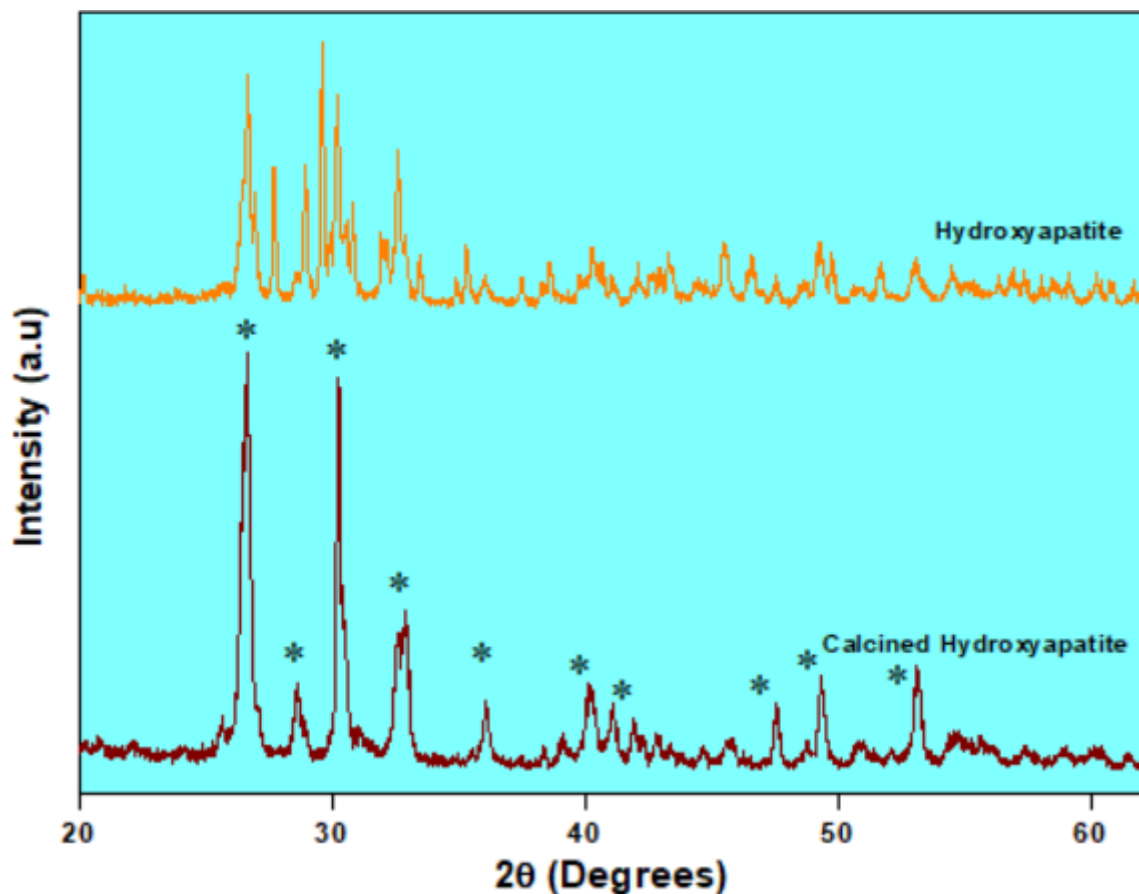


Figure 4.2. XRD Peaks of Calcined Hydroxyapatite (cHA) and synthesized Hydroxyapatite (HA).

4.3 Characterization of Graphene oxide and reduced graphene oxide

FTIR and XRD analyses were used to evaluate the thermally reduced graphene oxide. The peaks obtained from FTIR and XRD show evidence of the successful reduction of graphene oxide. FT-IR spectroscopy was performed between the wavelengths of 400 and 4000 cm^{-1} at room temperature. The diffraction pattern was analyzed using XRD equipment and a Cu-K source of radiations with a 1.540 Å wavelength. The 2θ ranged from 0° to 60° during the diffraction process.

4.3.1 FTIR analysis

The effective reduction of graphene oxide has been verified by FTIR analysis. Graphene oxide has been reduced using thermal methods. The graphene oxide and reduced graphene oxide peak patterns are depicted in the figure 4.3 below. It is possible to identify the functional groups that exist in both the GO and the rGO by FTIR analysis. When the spectra of GO and rGO were compared, it was found that the O-H bond's broad peak can be seen between 3200 and 3500 cm^{-1} . Further C-OH band at 1151 cm^{-1} , attributed to the hydroxyl groups in GO. At 1651 cm^{-1} , the stretching band for C=C, characteristic of the double bonds in the polycyclic aromatic graphene ring, is observed. Additionally, the C-O-C band, representative of epoxy groups, appears at 1078 cm^{-1} . The C=O band is shifted to a lower frequency due to interactions with the intramolecular hydrogen bond, leading to overlap with the C=C band. Thermal treatment has reduced the oxygen content, as evidenced by the lowered intensity of the oxygen-containing group in reduced graphene oxide, which includes vibrations at frequencies of 1618.94 cm^{-1} , 2344 cm^{-1} , and 1039 cm^{-1} (198,280).

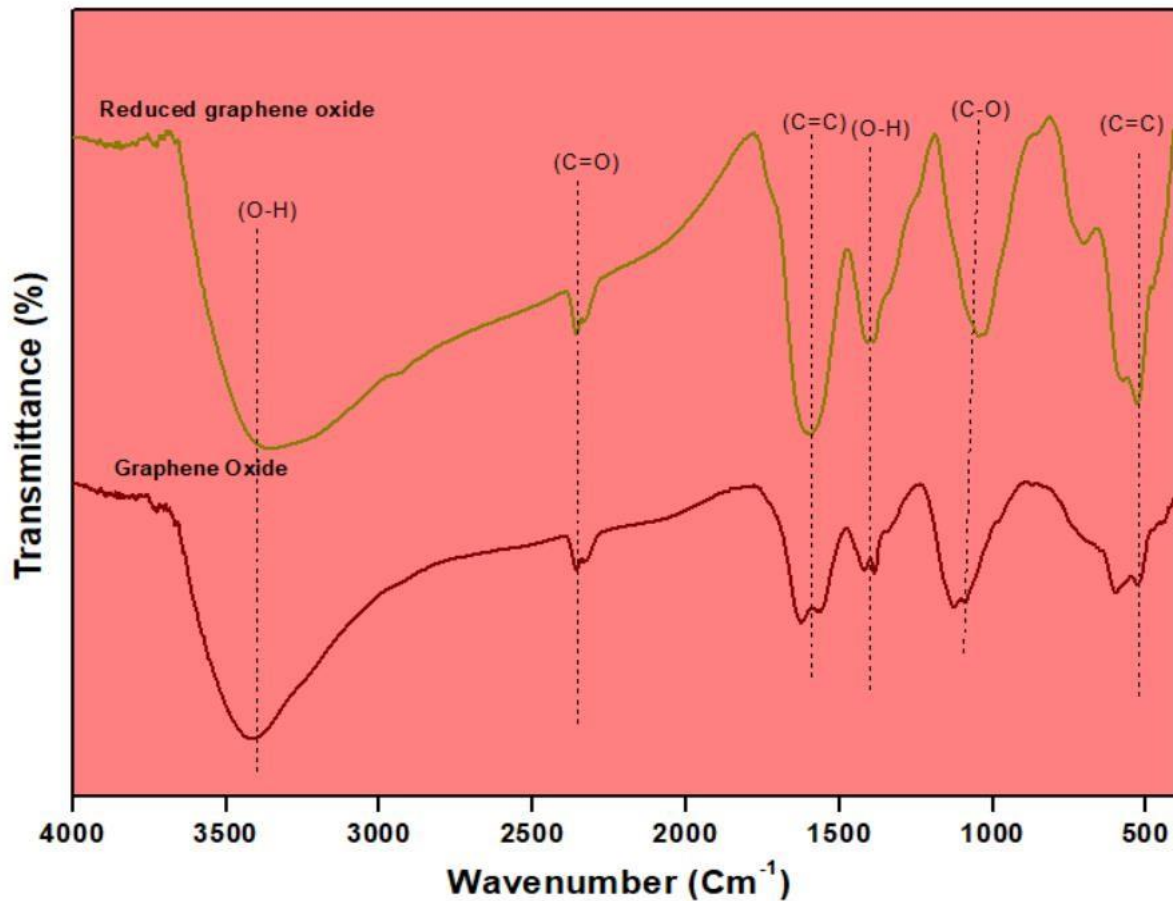


Figure 4.3: FTIR analysis of Graphene oxide (GO) and reduced graphene oxide (rGO)

4.3.2 XRD analysis

The reduction of Graphene Oxide is verified using an X-ray diffraction approach. According to the XRD pattern, the GO are polycrystalline. In contrast to rGO, which had an interlayer spacing of 0.33 nm and a sharp peak matching to (002) at 26.35° whereas XRD plot for GO revealed a sharp peak at 11.8° and the interlayer distance found to be 0.63nm. This peak is associated with (002) hkl values. The decrease in d spacing values showed the loss of oxygen- and groups containing water, and it was also in sterling accord with the findings provided by Alam and colleagues (193). As seen in Figure 4.4, the peak at 11.8° in rGO also disappears, proving that the oxygen-containing groups were successfully expunged. The peaks examined in rGO are consistent with the JCPDS file no. 75-2078 is the graphite phase of rGO.

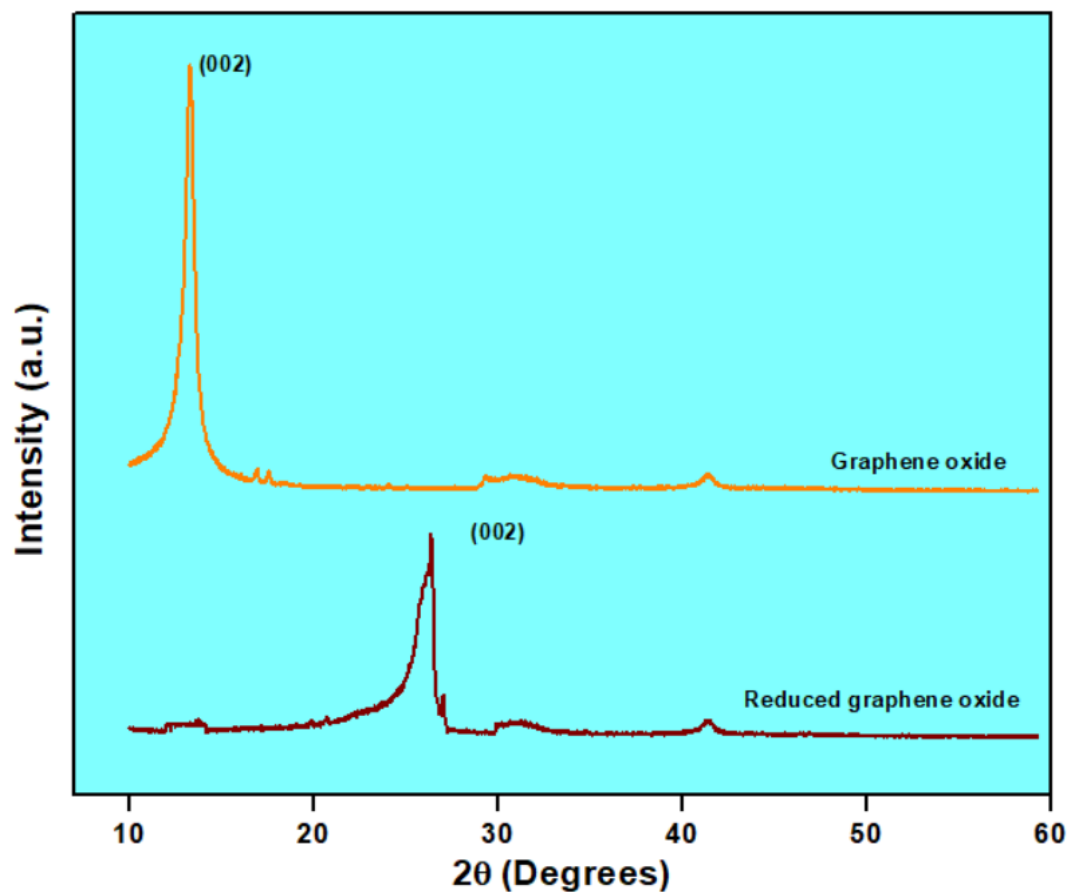


Figure 4.4. XRD peaks for Graphene oxide (GO) and Reduced Graphene Oxide(rGO)

4.4 Synthesis of binary composite of calcined hydroxyapatite and reduced graphene oxide

After undergoing pre-treatment to produce calcined hydroxyapatite and reduced graphene oxide, both materials were combined to create a binary composite. The fabrication of several reduced graphene oxide and calcined hydroxyapatite variations involved combining dry powder in a mortar and pestle and then ball milling. To create the various sorts of variations, the concentration of calcined hydroxyapatite has been steadily declining while the concentration of reduced graphene oxide has been gradually rising. The composites were finally put together and shaped as pellets with dimensions of 13 mm diameter and 3-5 mm thickness. In the calcined HA, white pellets could be seen, but as the rGO concentration was raised, the color of the pellets darkened, as seen in the Figure 4.5.



Figure 4.5: Pellets of calcined Hydroxyapatite (cHA) and Reduced graphene oxide (rGO) composites in a different ratio namely HrG1 (90 cHA: 10 rGO), HrG2 (80 cHA: 20 rGO), HrG3 (70 cHA: 30 rGO), HrG4 (60 cHA: 40 rGO) and HrG5 (50 cHA: 50 rGO)

4.4.1 Characterization of composite using FTIR

The composites of hydroxyapatite and reduced graphene oxide have been scrutinized using FTIR analysis. Almost all the peaks showed both the peaks for the hydroxyapatite and reduced graphene oxide except the peaks for absorbed water at 3437cm^{-1} which is present in Hydroxyapatite (102) and for carbonyl group at 2344cm^{-1} (281) which is present in reduced graphene oxide found to be absent due to heat treatment given to the composites which contributed to the enhanced mechanical strength as discussed in the later part. The figure 4.6 showed the FTIR analysis of the binary composites.

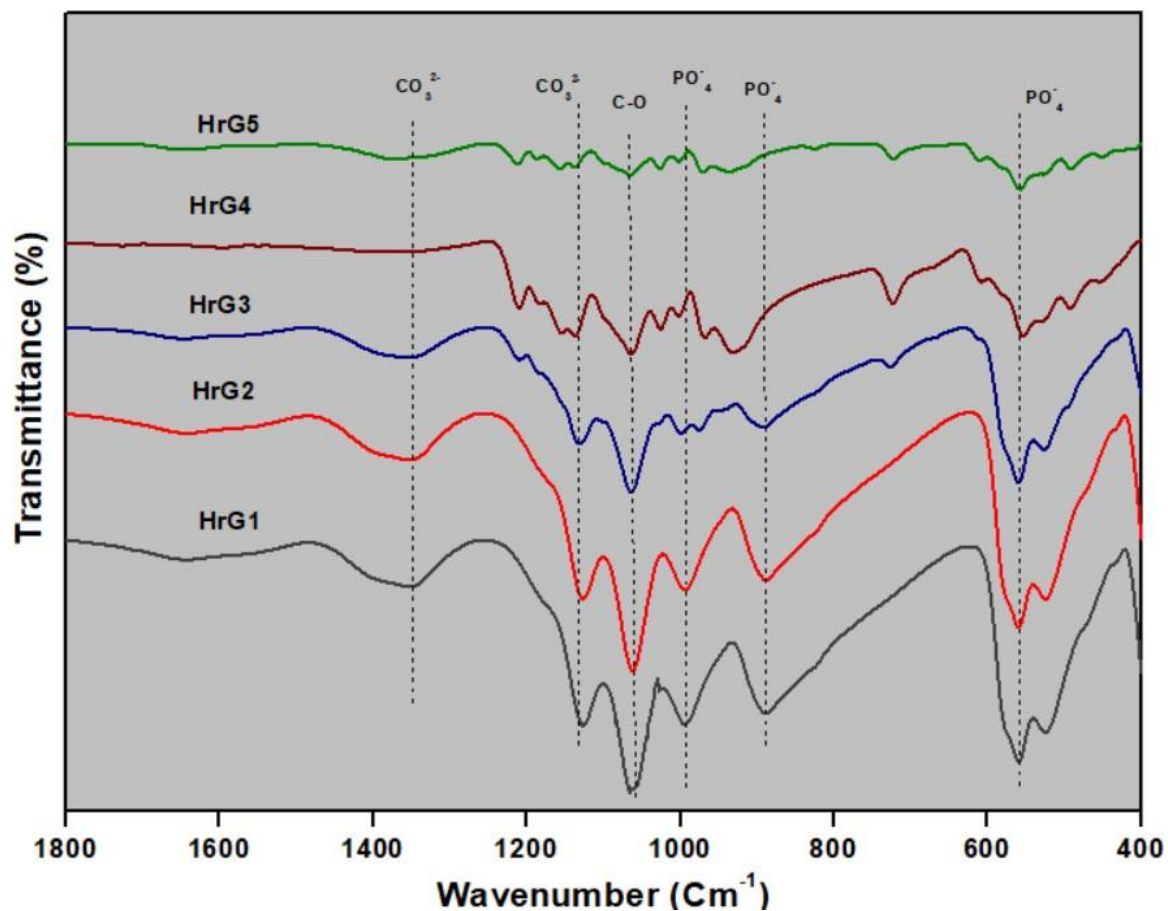


Figure 4.6. FTIR Spectra of composites of calcined hydroxyapatite(cHA) and reduced graphene oxide (rGO)

4.4.2 Characterization of composite using XRD

Figure 4.7 shows the XRD spectra for various HA and rGO variations. It is straightforward to observe convergence because of the peaks. It has been shown that HA and rGO peak in the normal

manner. Peak depth 26.5° enabled to determine the rGO peak, which also overlaps with the HA peak. The table below shows the d spacing and hkl values of the different peaks, which were calculated using Bragg's law (282).

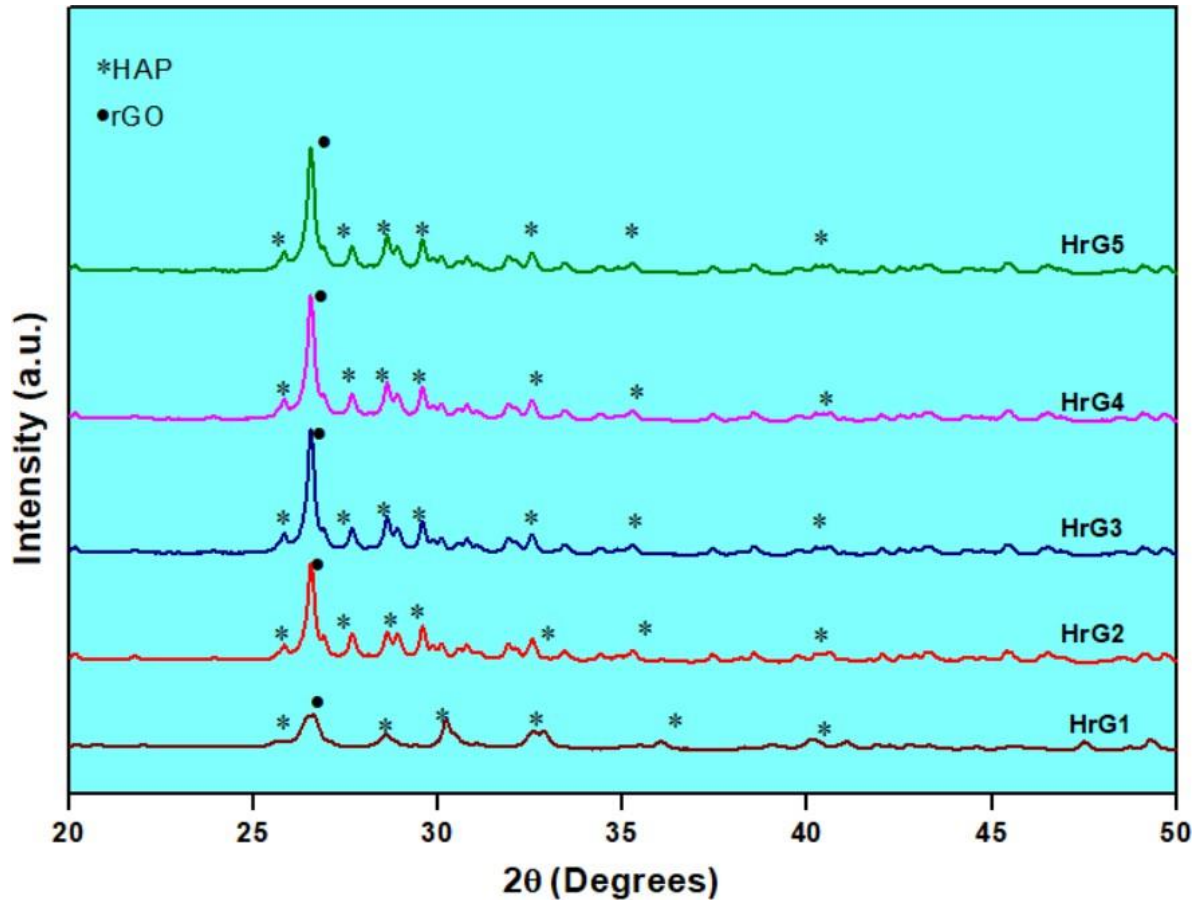


Figure 4.7. XRD analysis of blends of calcined hydroxyapatite and reduced graphene oxide.

The figure 4.7 reveals the diffraction pattern of the hydroxyapatite and reduced graphene oxide blends. The figure illustrates the successful development of the composite of HA and rGO as different versions, with peaks at angles 25.7° , 28.7° , 31.8° , and 32.8° represented as examples of the typical peaks of HA whereas the characteristic peak for rGO has been shown at angle 26.6° .

Table 4.1: Atomic spacing in blends of HA and rGO.

2 thetas	d spacing(°Å)	Hkl
25.7	0.171	(002)
31.8	0.211	(211)
32.5	0.215	(300)

4.4.3 Morphology of the binary composite

The morphology of the HA and rGO composite versions has been determined using FESEM. Figure 4.8 (a) and 4.8(b) below displays the FESEM images of the blends of Hydroxyapatite, calcined hydroxyapatite, Graphene oxide, reduced graphene oxide, variants of calcined hydroxyapatite and reduced graphene oxide designated as HrG1 to HrG4. The morphology revealed that the combination of decreased graphene oxide and calcined hydroxyapatite led to the formation of bigger crystals. Hydroxyapatite is the main component of the upper, white layer, while decreased graphene oxide is found in the lower area. The particles can be seen in morphology of calcined hydroxyapatite, whereas the variants revealed successful blending that could be observed through huge particle clumps.

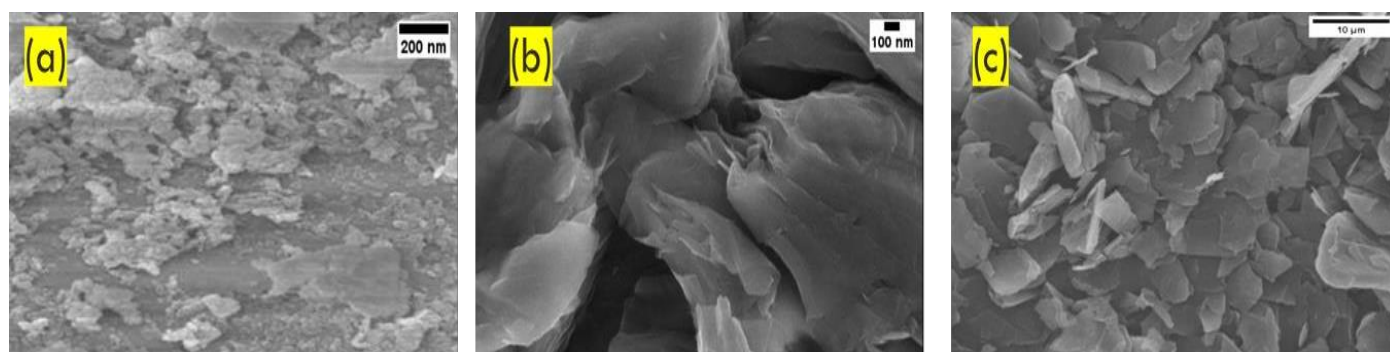


Figure 4.8(a) Morphology of the starting materials (a) Hydroxyapatite (b) Graphene oxide (c) Reduced graphene oxide

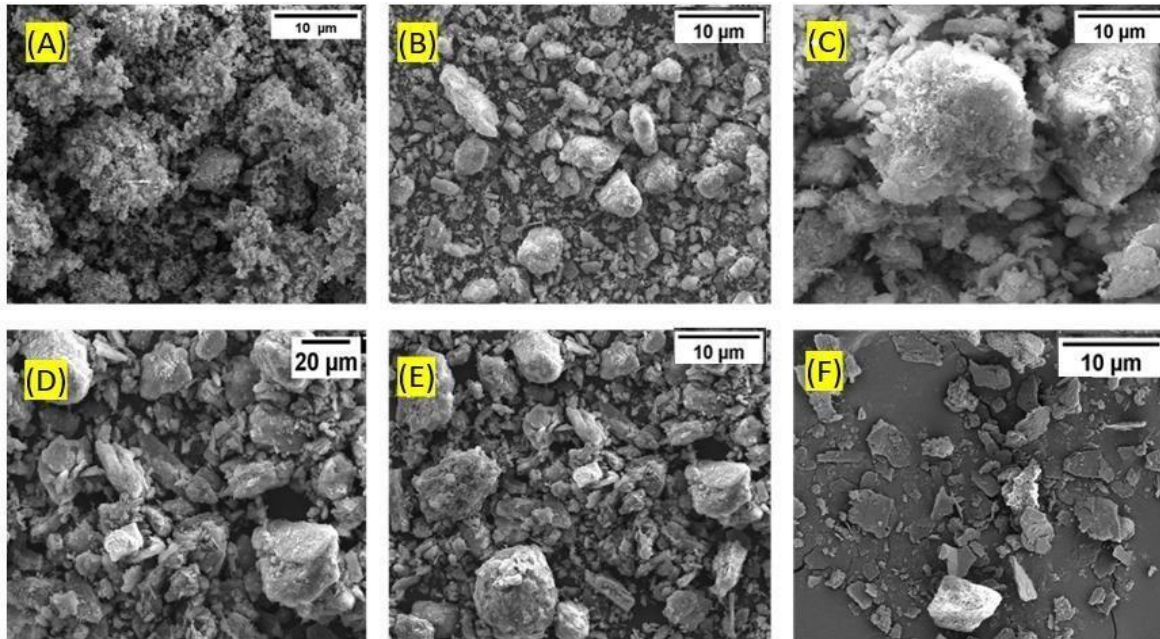


Figure 4.8 (b) Morphology of the composites of calcined hydroxyapatite and reduced graphene oxide (A) cHA, (B) HrG1(90 cHA: 10 rGO), (C) HrG2(80 cHA: 20 rGO), (D) HrG3(70 cHA: 30 rGO), (E) HrG4(60 cHA: 40 rGO), and (F) HrG5(50 cHA: 50 rGO).

Image J was used to evaluate the particle sizes of the variants. Analysis revealed that variants are microparticles, and it was shown that the particle size reduces as rGO concentration is raised. However, it was discovered that the particle sizes for HrG4 and HrG1 were roughly 12.98 μm and 17.85 μm , respectively. The particle size plot is shown in Figure 4.9.

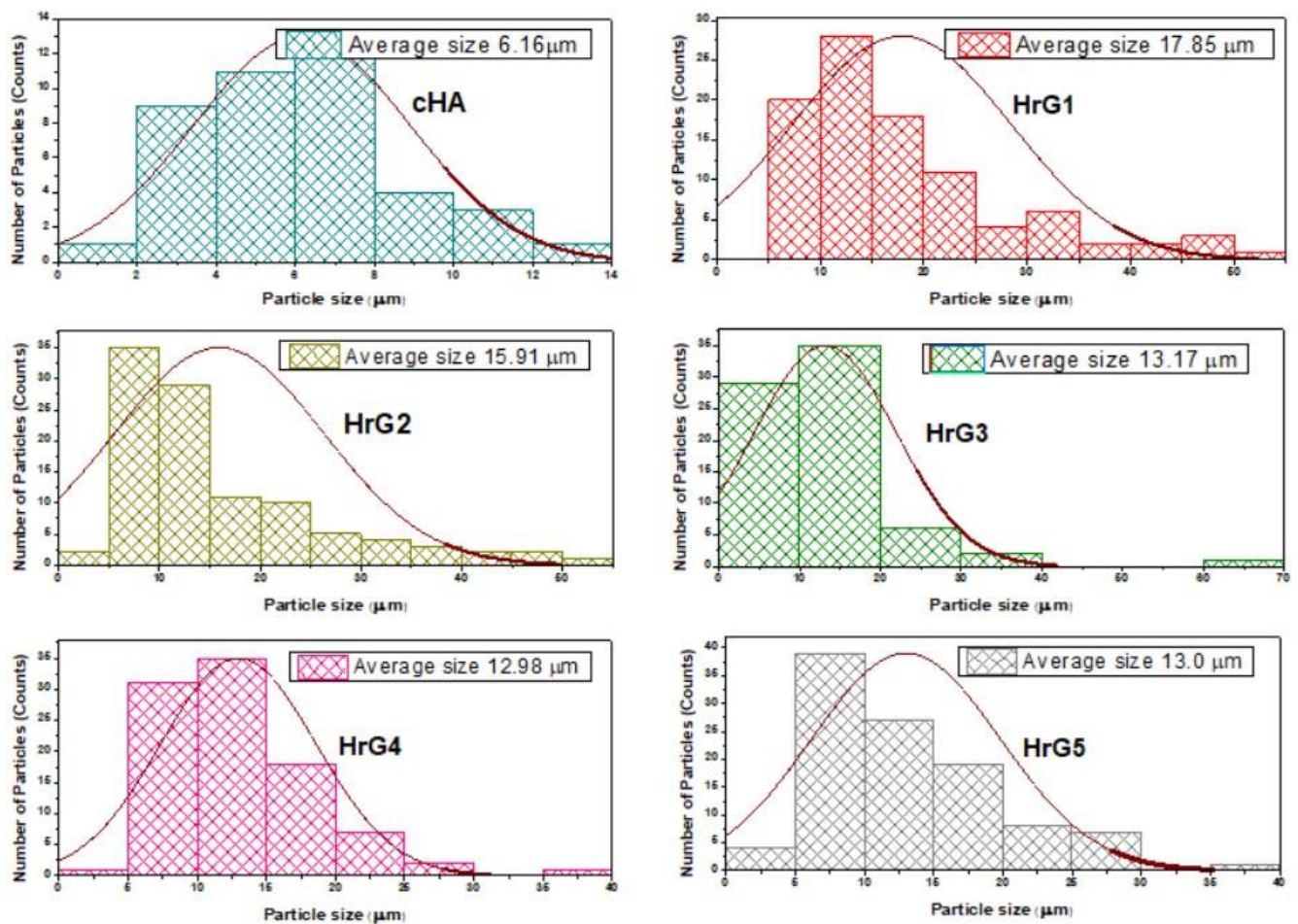
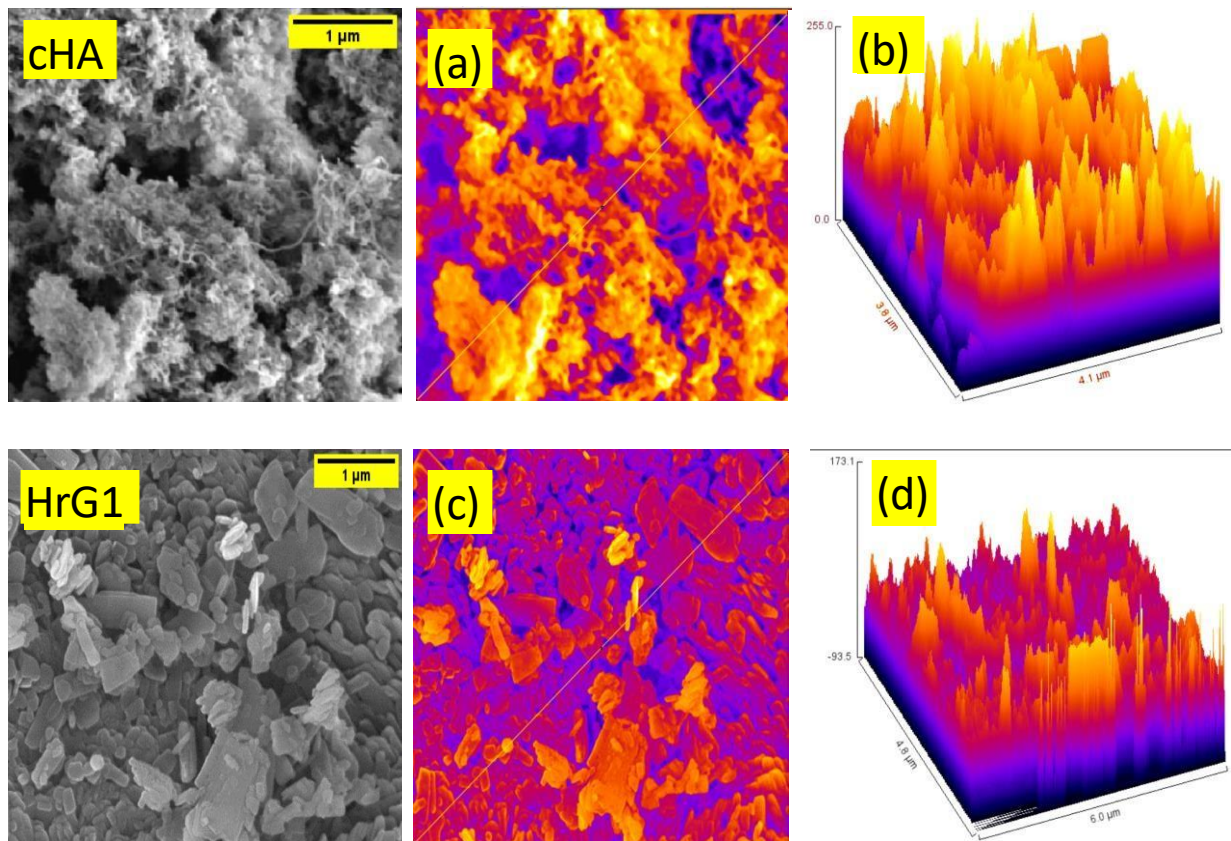


Figure 4.9. Particle size analysis of the composites of calcined hydroxyapatite and blends of calcined hydroxyapatite and reduced graphene oxide HrG1 (90 cHA: 10 rGO), HrG2(80 cHA: 20 rGO), HrG3 (70 cHA: 30 rGO), HrG4(60 cHA: 40 rGO) and HrG5(50 cHA: 50 rGO)

4.4.4 Surface roughness of the composite

Surface roughness plays a key role in regulating cell adhesion and proliferation. Surface roughness was found to enhance cellular functions. Kunzler and associates found that increasing surface roughness boosted osteoblast development. However, multiple studies showed that roughness had sped up cellular proliferation when evaluating in vitro studies (283–285). On the other hand, osteoblast MG-63 proliferation decreased as surface roughness increased (286). The surface

roughness for the HA and rGO versions is shown in the table below. By analyzing the FESEM images with image analysis tools, Ra values ranging from $38.06 \pm 0.90 \mu\text{m}$ to $28.14 \pm 0.43 \mu\text{m}$ have been found, proving that the surface roughness reduces with increasing concentrations of rGO as shown in figure 4.10. This may be due to effect of thermal treatment to the composites which make it more dense and the cracks or gaps has been filled by reduced graphene oxide arising smooth surface topography as also reported earlier (287,288).



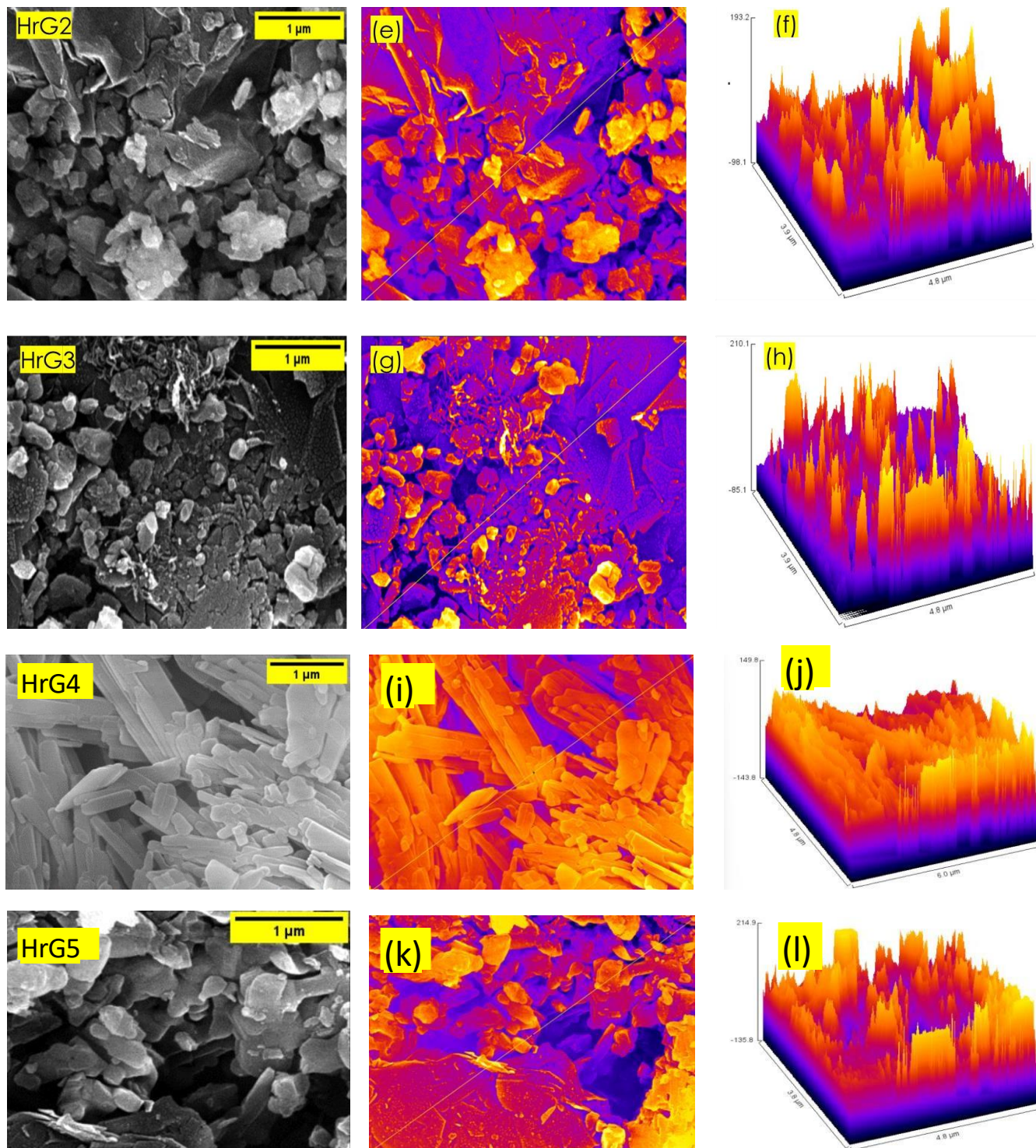


Figure 4.10. Surface Roughness (a-b)cHA, (c-d) HrG1(90 cHA: 10 rGO), (e-f) HrG2(80 cHA: 20 rGO), (g-h) HrG3(70 cHA: 30 rGO), (i-j) HrG4(60 cHA: 40 rGO) and (k-l) HrG5(50 cHA: 50 rGO)

Figure 4.10 displays both the photographs and the roughness plot. The figure reveals the surface roughness plot and the roughness parameters have been tabulated in the table 4.2 below. The relation between the surface roughness and cell adhesion can be depicted from the biocompatibility test that a decline in the surface roughness of blends increased cell adherence and proliferation.

Table 4.2. Roughness parameters of blends of calcined hydroxyapatite and reduced graphene oxide.

Blends	Arithmetic Mean Roughness (Ra) (μm)	Root Mean square (RMS) (μm)
HrG1	38.06 ± 0.90	46.46 ± 0.68
HrG2	37.73 ± 0.22	43.10 ± 0.16
HrG3	31.28 ± 0.59	36.98 ± 0.62
HrG4	28.14 ± 0.43	34.22 ± 0.93
HrG5	21.28 ± 0.98	27.92 ± 0.52

Part 2: Study of mechanical properties of biomaterial fillers.

It has already been noted that hydroxyapatite has a reduced mechanical strength. To create a mechanically robust composite, a variety of fabrication techniques and filler types have been used. Because of its superior qualities, hydroxyapatite is one of the best biomaterials for use in tissue regeneration. The hydroxyapatite in the previously published data demonstrated greater relative density and hardness after being subjected to cold isostatic pressing and sintering (289). Additionally, it has been noted that carbon fibre reinforcement of hydroxyapatite via spark plasma sintering results in increased mechanical strength (290). In a different study, PEEK was employed as a filler to enhance the hydroxyapatite's mechanical characteristics (291).

Additionally, it has been highlighted that the compressive strength was discovered to be enhanced with an increase in sintering temperature when compared to hydroxyapatite, which has a compressive strength of only 49 MPa (292). In this section, mechanical behavior has been studied after the hydroxyapatite has been reinforced with reduced graphene oxide and has undergone a heat treatment. Utilizing a universal testing machine (UTM), compressive strength and Young's

modulus were evaluated. Further the cracking behavior that determines resistance the composites has been studied.

4.5 Mechanical behavior of the composite

For various variants of calcined HA-rGO composites, the compressive strength has been determined. A significant improvement in compressive strength was noticed. HrG4 has the maximum mechanical strength, 185.16 ± 4.87 MPa. It can be summarized that by enhancing the crystallinity of HA during calcination and removing excess water from rGO during reduction, the molecules interact better, increasing the compressive strength ((293). Prior to mechanical investigation, it was found that thermally treating the pellets improved the material's strength, as illustrated in Figure 4.11. The mechanical strength of composites before and after the heat treatment was statistically analyzed, and the results show that $p < 0.0001$. The average value and standard deviation for all data were displayed.

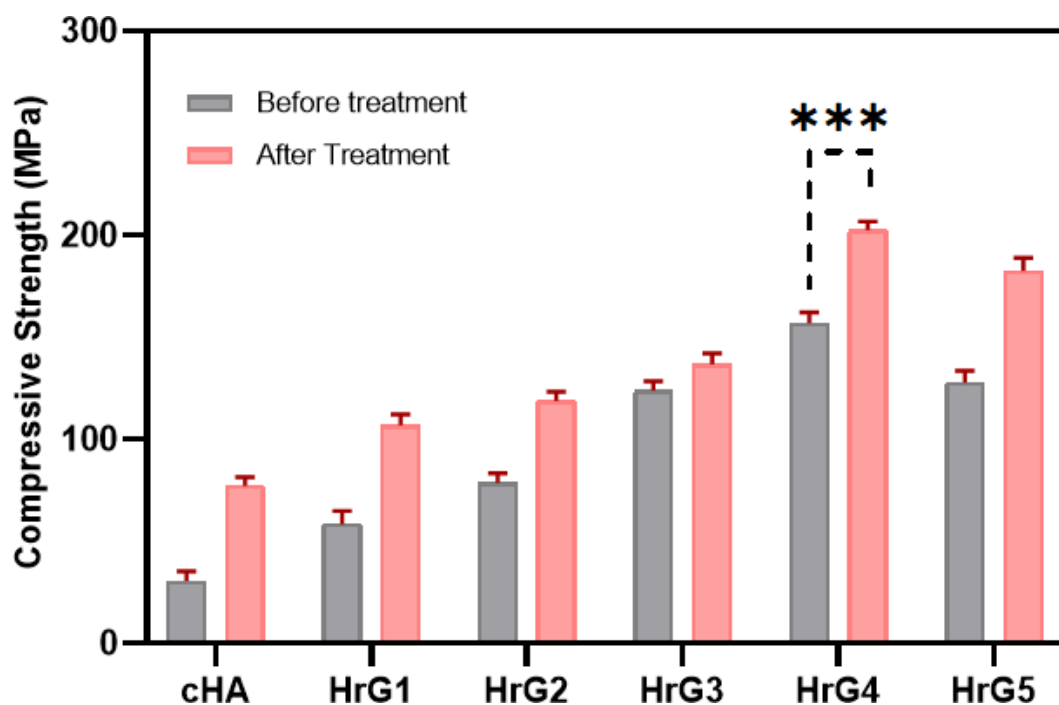


Figure 4.11 Statistical analysis of compressive strength of calcined hydroxyapatite (cHA) and binary blends of Hydroxyapatite and reduced graphene oxide namely HrG1(90 cHA: 10 rGO), HrG2(80 cHA: 20 rGO), HrG3 (70 cHA: 30 rGO), HrG4 (60 cHA: 40 rGO), HrG5(50 cHA: 50 rGO) before and after treatment *** indicates the $p < 0.0001$.

On elevating the rGO content in HA to 40% made the variations strength easier to achieve. On the other hand, as the rGO amount increased further, HrG5 showed a minor strength drop. Additionally, it was discovered that thermally treating composites boosts their strength. As the quantity of reduced graphene oxide increases, the compressive strength also increases. The maximum compressive strength found to be 185.16 ± 4.87 MPa for the blend HrG4 and on further increasing the percentage of reduced graphene oxide in HrG5, little reduction in the strength observed.

Figure 4.12 displays a stress-strain curve for each blend. A larger stress-to-strain ratio was observed in the case of HrG4, which was responsible for the highest modulus obtained. The curves showed the ductile nature of the composites.

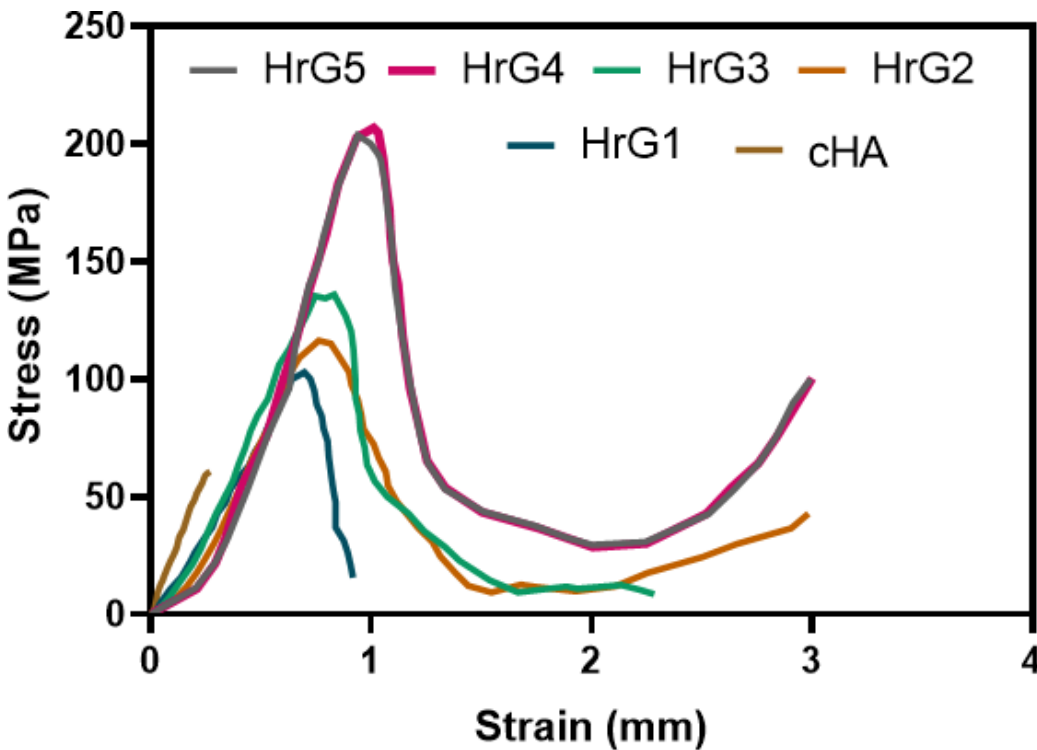


Figure 4.12: Stress-strain graph for different composite variations of binary blends of calcined Hydroxyapatite and reduced graphene oxide namely HrG1(90 cHA: 10 rGO), HrG2(80 cHA: 20 rGO), HrG3 (70 cHA: 30 rGO), HrG4 (60 cHA: 40 rGO), HrG5(50 cHA: 50 rGO)

PART 3: Biomaterial fabrication steps with addition of appropriate Polymer to the additive and characterization.

4.6 Selecting the ideal temperature for treatment

The composite of carboxymethyl cellulose, hydroxyapatite and reduced graphene oxide has been fabricated through pressing thermally in order to achieve ameliorated compressive strength. Earlier the thermal pressing was performed at 200°C and 350°C for 2 hours. The results for the same have been analyzed through FTIR demonstrated below in Figure 4.13. The FTIR results of blends showed that the peaks for hydroxyl group and for carboxyl and carbonyl group at 3500 cm⁻¹ are visible which apparently comprehend that at temperatures of 200°C and 350°C, the water molecules and oxygen containing functional groups can be seen. But the thermal degradation of Carboxymethyl cellulose reported to be started above 200°C (294).

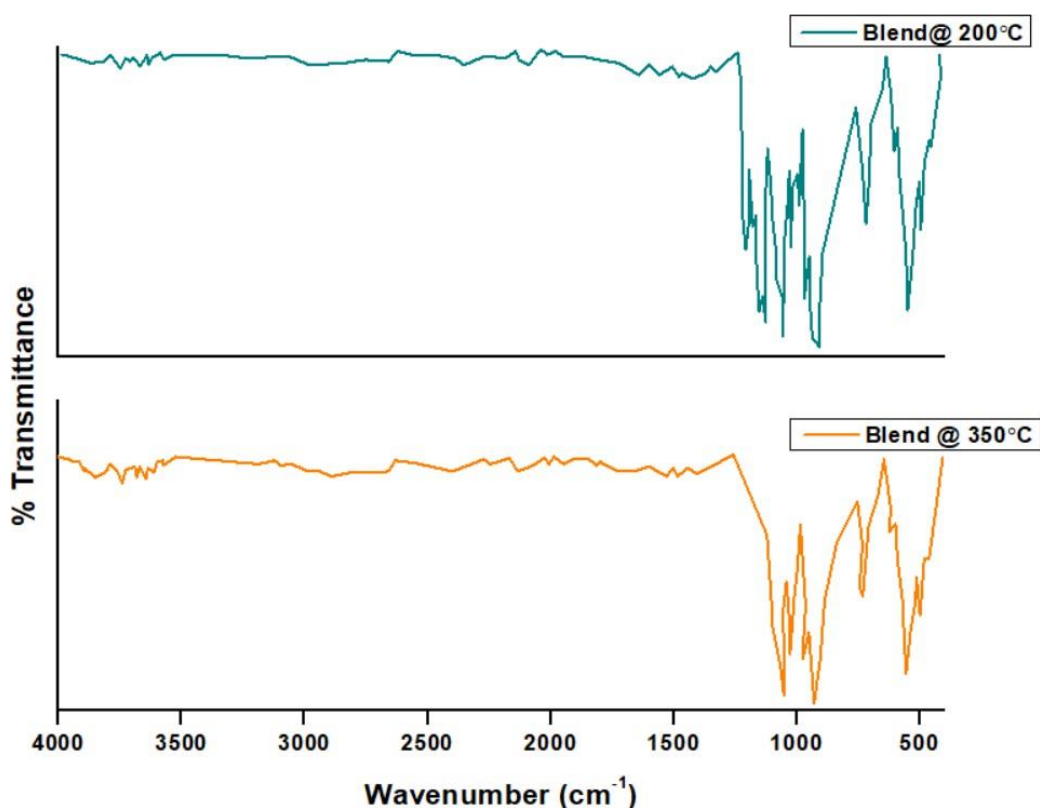


Figure 4.13: FTIR analysis of ternary blends calcined Hydroxyapatite, reduced graphene oxide and carboxymethyl cellulose thermally treated under pressure at 200°C and 350°C

On scrutinizing high temperature and risk of degradation of CMC so, to maintain the material integrity of the carboxymethyl cellulose, low temperature thermal pressing has been opted. In

addition, low temperature also maintain the structural integrity of hydroxyapatite and the bonding between the carboxymethyl cellulose and hydroxyapatite which enhances the mechanical strength of the composite.

Thereafter, thermal treatment of hydroxyapatite, reduced graphene oxide and carboxymethyl cellulose has been employed at two different temperatures of 100°C and 150°C and for three different time intervals of 5 minutes, 10 minutes and 20 minutes at constant pressure of 7.8 psi. Table represents the details for fabrication composition of carboxymethyl cellulose, reduced graphene oxide and hydroxyapatite composites whereas BX (X=1,2,3) stand for Blend of samples and 100, 150 tells the heat-treating temperature value in degree Celsius. For example, B1-100 stands for the Blend-1 thermally pressed at 100°C whereas B1-150 denotes the Blend-1 heat pressed at 150°C.

Table 4.3: Composition of Blends of hydroxyapatite, reduced graphene oxide and carboxymethyl cellulose

SAMPLES	HA:rGO:CMC (wt%)	HA(g)	rGO (g)	CMC (g)
B1-100	60:30:10	6	3	1
B1-150				
B2-100	60:20:20	6	2	2
B2-150				
B3-100	60:10:30	6	1	3
B3-150				

Furthermore, the ternary composite has also been characterized utilizing physio-chemical investigations using FTIR, XRD, and thermal studies using TGA analysis. Later, the variants of ternary composite have been evaluated for the mechanical strength and biocompatibility.

Figure 3.1 demonstrates the methods that were used to fabricate ternary blend. In the image, the composite of calcined hydroxyapatite and reduced graphene oxide (HA/rGO) was shown to have reached its maximum strength and then being mixed with carboxymethyl cellulose (CMC) in various ratios as listed in the table. These versions were shaped into pellets using Pellet making machine and were then heated for three periods of five minutes, ten minutes, and twenty minutes at temperatures of 100°C and 150°C. These blends have also been morphologically studied using

FESEM, and their physicochemical characteristics have been determined by FTIR, XRD, and other methods. Additionally, blends of Ceramic-polymeric materials were further examined for mechanical behavior and separated based on optimal strength. Thereafter, the blends were further studied for biocompatibility on murine fibroblast cells (NIH3T3) using MTT assay.

4.6.1 Physio-chemical Characterization

4.6.1.1 FTIR analysis

Figure 4.14 depicts the FTIR spectrum for the thermally pressed polymeric composites with varied concentrations of carboxymethyl cellulose and reduced graphene oxide. The phosphate group of hydroxyapatites (HA) is responsible for the bands at 1058 cm^{-1} , 549 cm^{-1} , and 924 cm^{-1} , whereas the carbonate group's ν_2 and ν_3 vibrational modes are responsible for the bands at 1190 cm^{-1} and 1417 cm^{-1} (261). The methyl group was assigned to the band at 1156 cm^{-1} . The stretching of the CH_2 group as seen in CMC is shown by the band at 1376 . According to Azzaoui and co-workers, the band seen at 1058 cm^{-1} corresponds to the CH-O-CH_2 stretching of carboxymethyl cellulose (295). According to Hidayah et al.'s research, the band at 1593 contributes to C=O stretching vibrations of carbonyl and carboxyl groups (198,280). Additionally, the effectively generated mechanically improved composite of hydroxyapatite and reduced graphene oxide displayed the characteristic peaks.

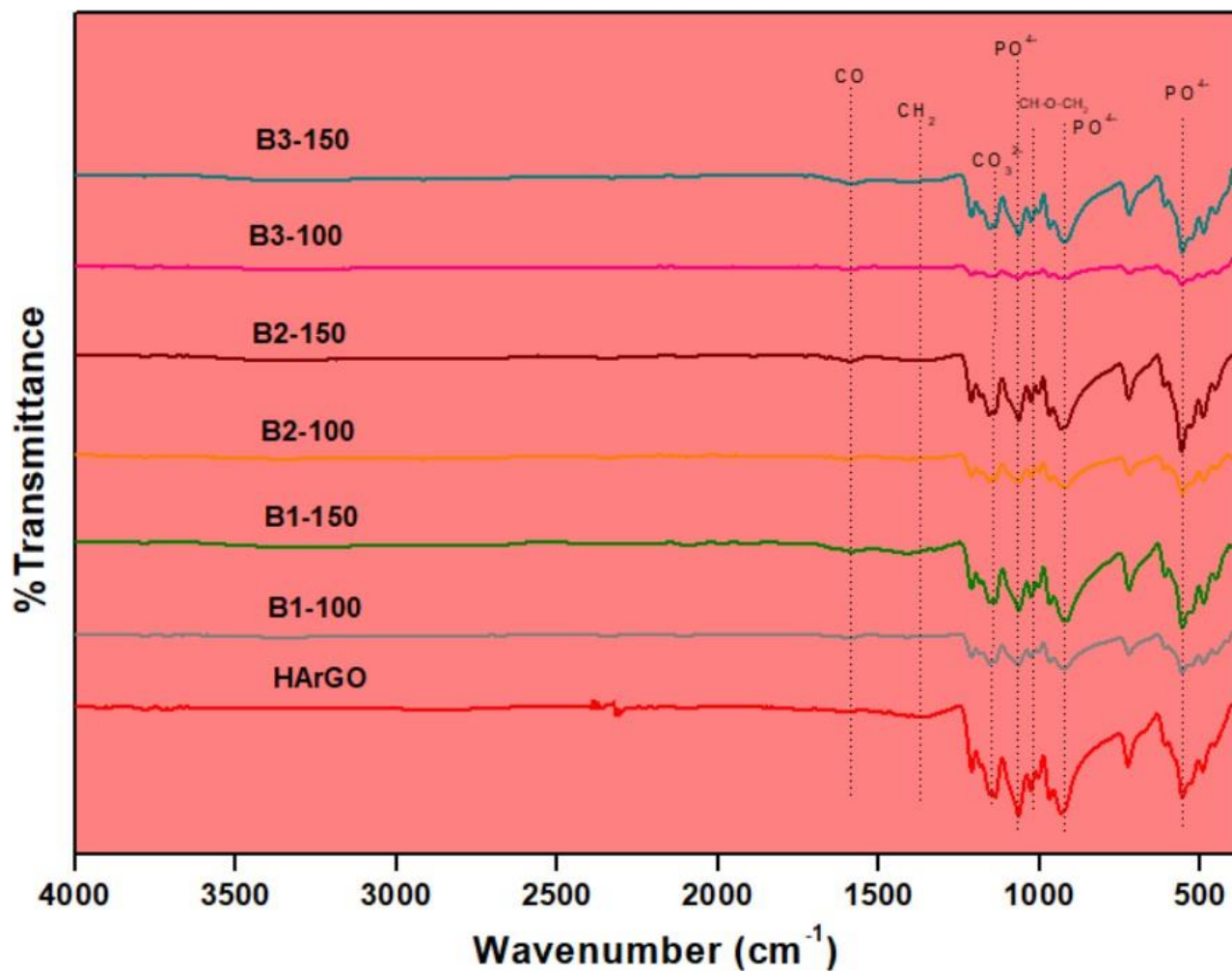


Figure 4.14: FTIR peaks for ternary Blends B1(60 cHA :30 rGO :10 CMC), B2 (60 cHA :20 rGO :20 CMC) and B3 (60 cHA :10 rGO :30 CMC) thermally treated at 100°C and 150°C and blend of calcined hydroxyapatite and reduced graphene oxide (HArGO) (60 HA:40rGO).

The peak at 2344 cm^{-1} , which corresponds to the carbonyl and carboxyl groups, has been totally wiped out in the ceramic-based polymeric blends due to thermal pressing when compared to the HArGO blend. Whereas, the bonds responsible for each of the FTIR peaks for carboxymethyl cellulose (CMC) were displayed in figure 4.15. When compared to carboxymethyl cellulose, it was discovered that heat-pressing entirely eliminated the peaks exhibiting the -OH group, which were located at 3200-3400 cm^{-1} . The thermal impact causes the loss of absorbed water from the material (198).

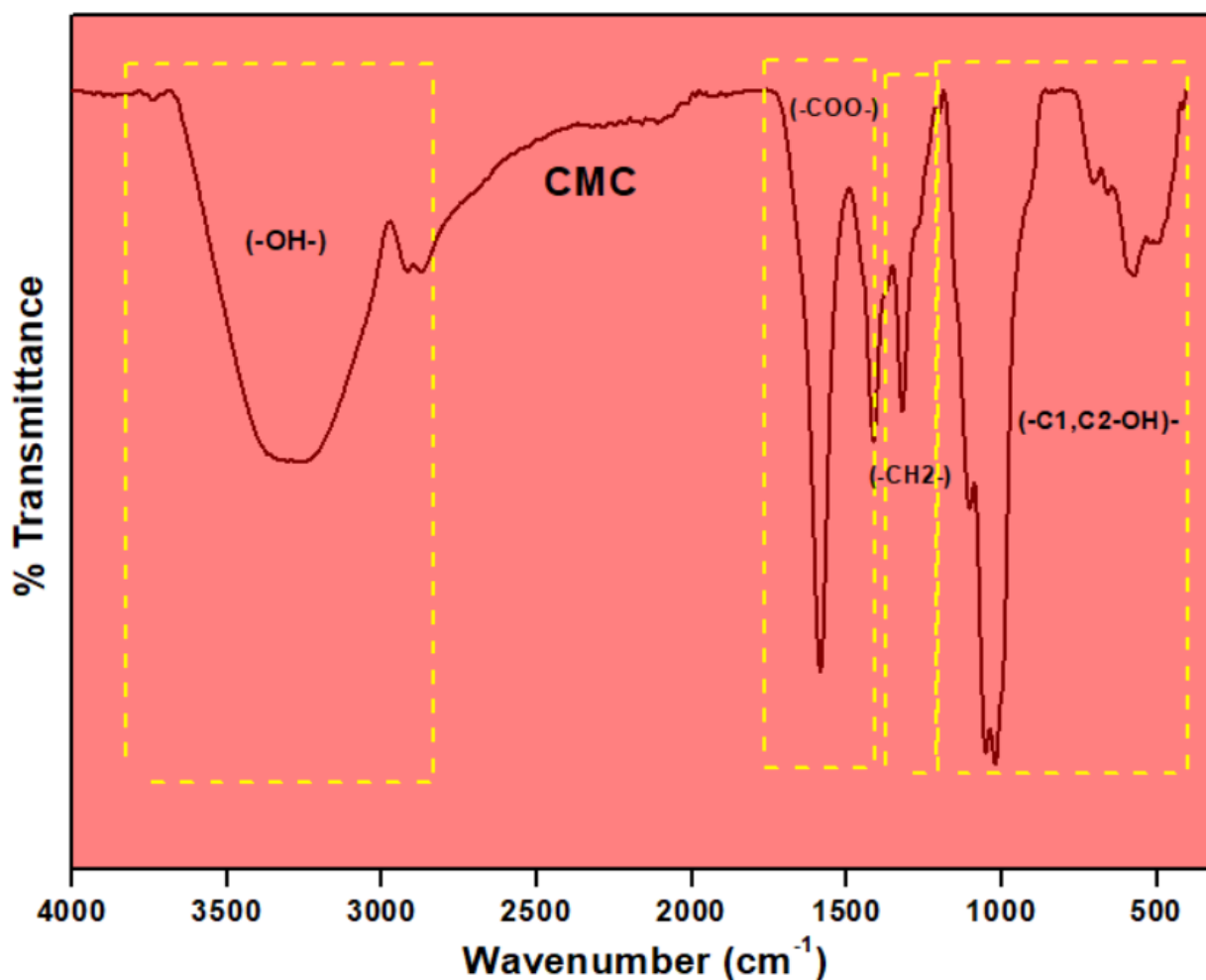


Figure 4.15: FTIR analysis of Carboxymethyl cellulose (CMC)

4.6.1.2 XRD analysis

When thermally treated at various temperatures, the XRD peaks were obtained for several Ceramic based polymeric blends. Three different materials' peaks are marked in figure 4.16(a) to ensure accurate blending of the composite. For the hydroxyapatite, the distinctive peaks were found to be at 28.8° and 31.3° , which are in good agreement with the previously published work by Manjubala and colleagues (265). The characteristic peaks for the CMC were found to be at 18.6° , 20.3° , 27.7° , 32.6° , and 45.68° . At 26.2° , the typical peak of reduced graphene oxide was visible and it overlapped the peak of hydroxyapatite. In the image below, the characteristic peak at 26.2° exhibits a diminishing strength as the content of reduced graphene oxide decreased in the blends from B1 to B3, demonstrating that the blending was done properly. The hydroxyapatite and reduced graphene oxide XRD peaks can be seen in the blend HArGO as CMC has been reinforced to the previously created Hydroxyapatite and reduced graphene oxide (HArGO) blend in the ratio of 60:40% by weight.

The degree of crystallinity for the blends was determined. As the temperature of is raised, crystallinity increases. The crystallinity's graphical representation is shown in Figure 4.16(b) below. By determining the degree of crystallinity, the impact of heat treatment under pressure on the crystallinity of the composites has been examined.

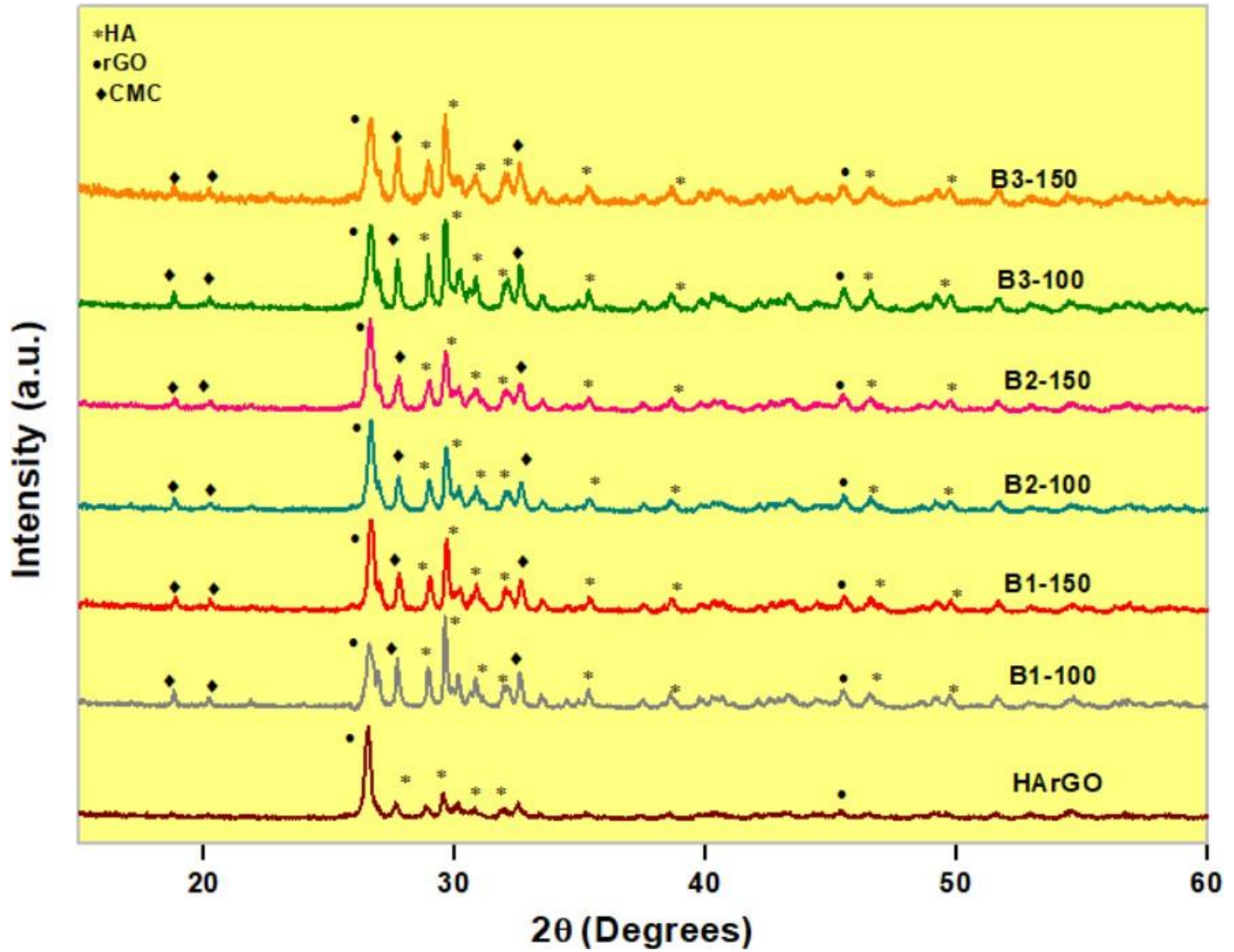


Figure 4.16(a): XRD peaks of thermally treated under pressure for ceramic based blends B1(60 cHA :30 rGO :10 CMC), B2 (60 cHA :20 rGO :20 CMC) and B3 (60 cHA :10 rGO :30 CMC) at 100°C and 150°C and binary blend of calcined hydroxyapatite and reduced graphene oxide (HArGO) (60 cHA:40rGO).

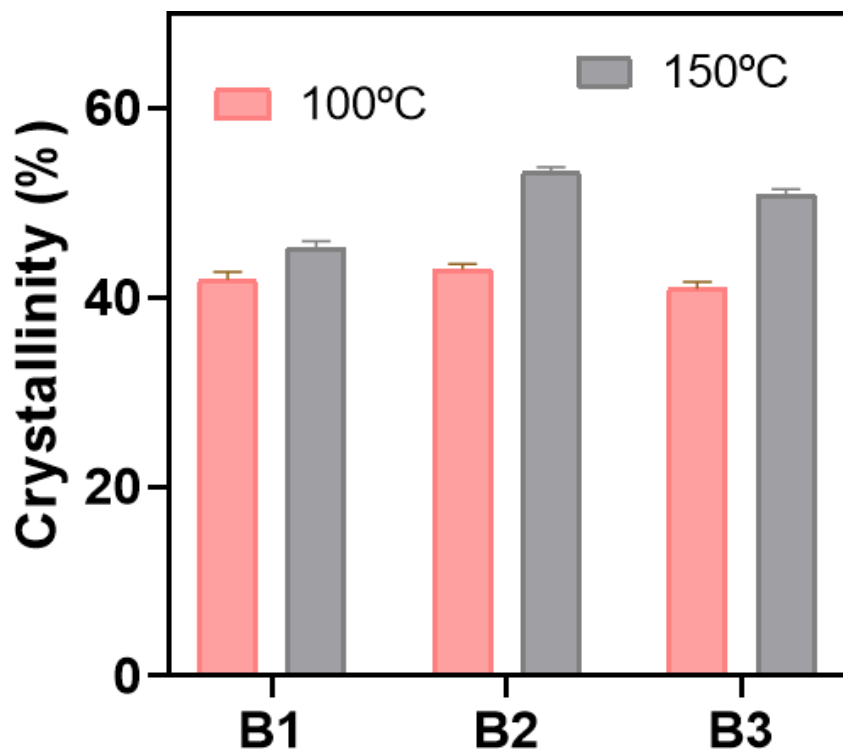


Figure 4.16(b): Crystallinity of the B1(60 cHA :30 rGO :10 CMC), B2 (60 cHA :20 rGO :20 CMC) and B3 (60 cHA :10 rGO :30 CMC) thermally-pressed at 100°C and 150°C

The crystallinity of the composites appeared to be impacted in a synergistic way by the rising temperature of thermally treated under pressure. The crystallinity unquestionably increases as the thermally treated temperature rises from 100°C to 150°C, and when the crystallinity of the polymeric blends is compared, blend B2 is proven to have the highest crystallinity. As the percentage of carboxymethyl cellulose is increased, blend B3 exhibits less crystallinity than blend B2, as seen in Figure 4.16(b). The obtained results are in good accord with the findings published by Son and coworkers, who discovered that strong hydrogen bonding and Vander Waal forces caused a composite composed of NaCMC reinforced with rGO to show increased strength at 2%. Similarly, blend B3 loses crystallinity relative to blend B2 as the amount of reduced graphene oxide is progressively reduced, as the bond between carboxymethyl cellulose and rGO weakens (296).

4.6.2. Mechanical Strength of the composites

Employing three identical copies of the composite, the compressive strength of the composites was calculated by Universal Testing Machine (UTM). Ceramic based composites made of ceramic reinforced with reduced graphene oxide and carboxymethyl cellulose that were heat treated under pressure for different intervals and at various temperatures. For temperatures between 100°C and 150°C, holding times of 5, 10, and 20 minutes have been adopted. When the thermally temperature was raised to 150°C, it was found that the mechanical strength increased, which is aligned with the previously described crystallinity data. It is clear from the data that the crystallinity of blends B1 and B2 improves with higher temperatures, but blend B3 shows a slight reduction, which also has an impact on the blend's mechanical strength when compared to blend B2 as shown in Figure 4.17.

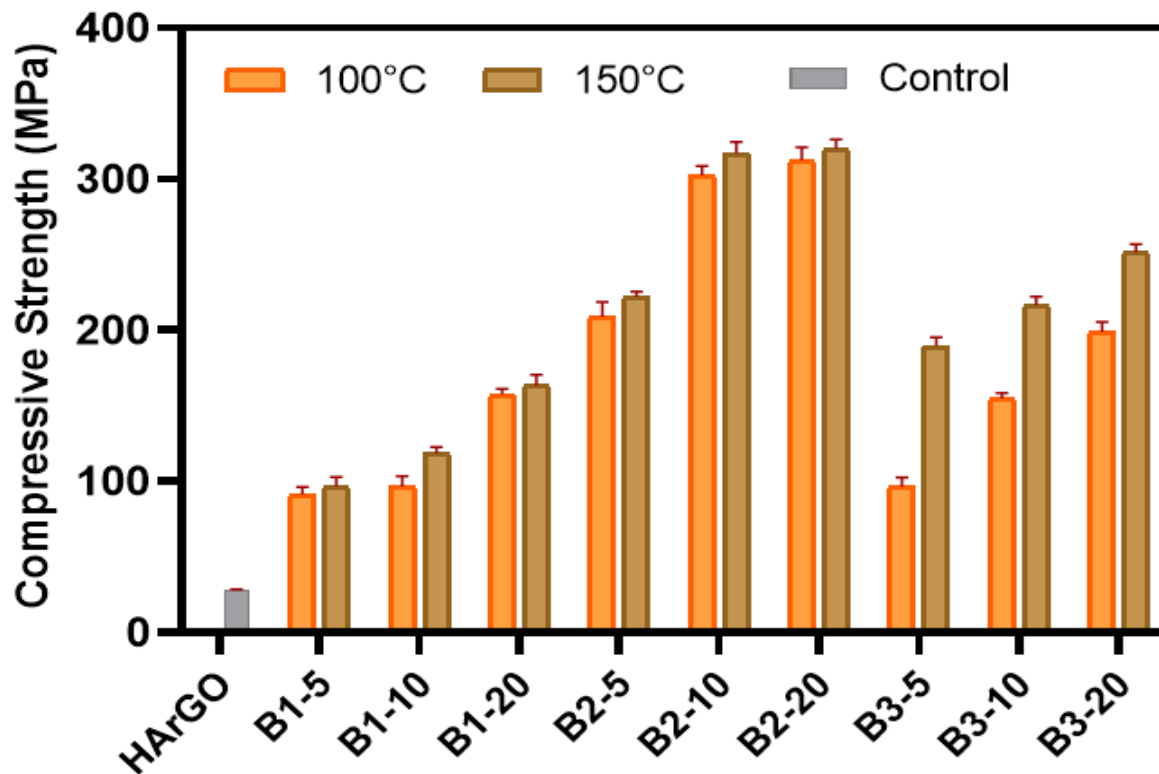


Figure 4.17: Compressive Strength of the hydroxyapatite and reduced graphene oxide blend (60cHA: 40rGO) and Ceramic based polymeric blends B1(60 cHA :30 rGO :10 CMC), B2 (60 cHA :20 rGO :20 CMC) and B3 (60 cHA :10 rGO :30 CMC) heat treated at 100°C and 150°C for the time intervals of 5min, 10min and 20min.

The maximum compressive strength was found to be 320.16 ± 6.1 MPa and a Young's modulus of 4.87 ± 5.04 GPa when the percentage concentration of both reduced graphene oxide and carboxymethyl cellulose became 20:20, i.e., in blend B2 when thermally treated at 150°C , which is in good agreement with the reported findings (17). Because of the further rise in carboxymethyl cellulose concentration to 30% while concurrently reducing the concentration of reduced graphene oxide to 10%, the strength of blend B3 is less than that of blend B2 in comparison. This is due to the fact that the bond between them becomes weaker as crystallinity decrease.

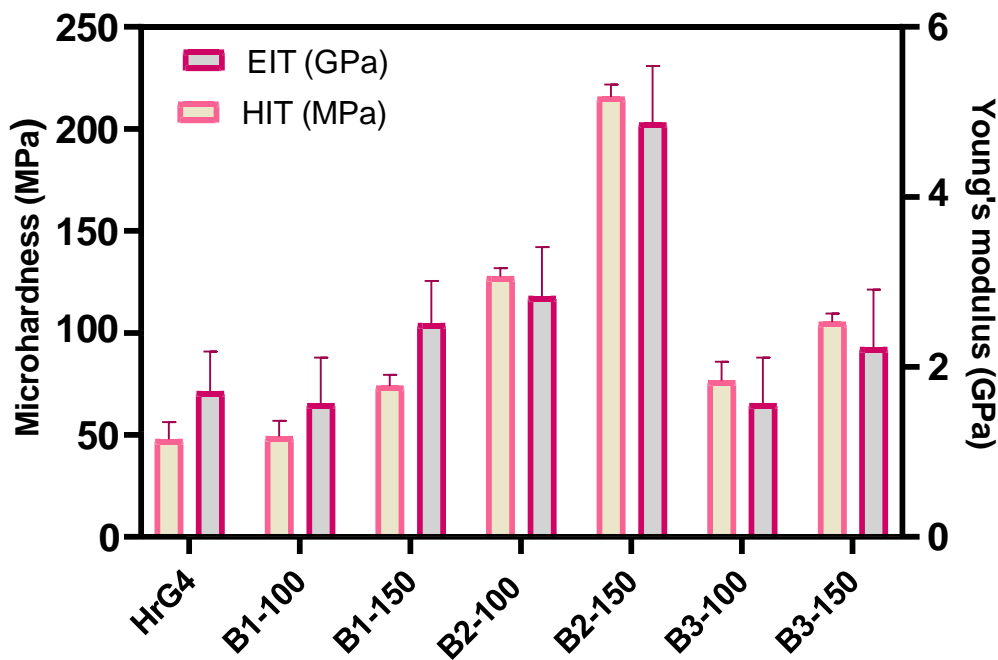


Figure 4.18: Vicker's Hardness and the modulus of the calcined Hydroxyapatite and reduced graphene oxide blend (60 cHA:40rGO) and Ceramic based polymeric blends B1(60 cHA :30 rGO :10 CMC), B2 (60 cHA :20 rGO :20 CMC) and B3 (60 cHA :10 rGO :30 CMC) thermally-pressed at 100°C and 150°C

About 10 indentations have been established on the blends with the highest compressive strength in order to analyze the hardness and modulus of the composites using the Vicker's Hardness test. Only six of the 18 blends that demonstrated their greatest compressive strength after being thermally treated under pressure for 20 minutes were used to determine hardness and young's modulus using Vicker's hardness analysis. It was discovered that as the temperature increased, so did the Young's

modulus and the Vicker hardness. The blend B2-150 had a maximum hardness of 216.22 ± 90 MPa, as illustrated in Figure 4.18. This is a novel technique, and it can be explained by the fact that blend B3 agglomeration increases while the strength drops. As previously mentioned, switching to blend B3 from blend B2 results in a decrease in crystallinity. Additionally, as the heating temperature is raised, the surface roughness reduces, which might affect the mechanical behavior of the composites composed of hydroxyapatite, reduced graphene oxide and carboxymethyl cellulose.

4.6.3 Orthogonal array experimental result

About five significant parameters, including thermally treated components and the results of the experimental data, have been chosen for optimization. The characteristics that were selected for the Taguchi optimization are the composition of carboxymethyl cellulose (%), the heating temperature (°C), and the time period (minutes). The experimental data for compressive strength (MPa) and water contact angle (°) have also been obtained using the L18 orthogonal array (24,258)

Table below highlights the experimental details and results.

Table 4.4 Experimental details for composite synthesis

Run order	Temperature (Degrees)	Composition (%)	Time (Min)	Compressive Strength (MPa)	Contact angle (°)
1	100	10	5	91.26	72.49
2	100	10	10	157.81	67.38
3	100	10	20	96.62	59.99
4	100	20	5	96.46	68.34
5	100	20	10	198.67	64.31
6	100	20	20	155.03	58.17
7	100	30	5	208.75	67.15
8	100	30	10	312.41	63.25
9	100	30	20	302.7	53.18
10	150	10	5	96.92	69.03
11	150	10	10	163.44	63.19
12	150	10	20	118.6	58.36

13	150	20	5	189.38	67.6
14	150	20	10	251.34	58.04
15	150	20	20	216.76	53.12
16	150	30	5	221.77	65.85
17	150	30	10	319.33	55.22
18	150	30	20	318.16	51.73

Table 4.5 Calculation of Grey relational grade

Run order	Normalized value of Compressive Strength	Normalized value of Wettability	Compressive Strength (MPa)	Wettability (°)	GRC Compressive Strength	GRC Wettability	GRG	Rank
ideal	1	1	0	0	1	1	1	
1	0.0000	0.0000	1.0000	1.0000	0.3333	0.3333	0.3333	18
2	0.2918	0.2461	0.7082	0.7539	0.4138	0.3988	0.4063	15
3	0.0235	0.6021	0.9765	0.3979	0.3386	0.5569	0.4478	13
4	0.0228	0.1999	0.9772	0.8001	0.3385	0.3846	0.3615	16
5	0.4710	0.3940	0.5290	0.6060	0.4859	0.4521	0.4690	10
6	0.2796	0.6898	0.7204	0.3102	0.4097	0.6171	0.5134	7
7	0.5151	0.2572	0.4849	0.7428	0.5077	0.4023	0.4550	11
8	0.9697	0.4451	0.0303	0.5549	0.9428	0.4740	0.7084	4
9	0.9271	0.9302	0.0729	0.0698	0.8727	0.8774	0.8751	2
10	0.0248	0.1667	0.9752	0.8333	0.3389	0.3750	0.3570	17
11	0.3165	0.4480	0.6835	0.5520	0.4225	0.4753	0.4489	12
12	0.1199	0.6806	0.8801	0.3194	0.3623	0.6102	0.4863	8
13	0.4302	0.2355	0.5698	0.7645	0.4674	0.3954	0.4314	14
14	0.7019	0.6961	0.2981	0.3039	0.6265	0.6219	0.6242	6
15	0.5503	0.9330	0.4497	0.0670	0.5265	0.8819	0.7042	5
16	0.5722	0.3198	0.4278	0.6802	0.5389	0.4237	0.4813	9
17	1.0000	0.8319	0.0000	0.1681	1.0000	0.7484	0.8742	3

18	0.99487	1	0.00513	0	0.989844	1	0.9949 22	1
----	---------	---	---------	---	----------	---	--------------	---

Table 4.5 describes the Taguchi data run of the experiment. Equations 2 and 3 were used to calculate the GRC once the data were normalized, and equation 4 was used to estimate the GRG. The least water contact angle (WCA) and the topmost compressive strength are the required characteristics that were determined by ranking the data following additional research. Rank one has been determined for the data run of the eighteenth array. In addition, 30% carboxymethyl cellulose (CMC) that had been thermally treated for 20 minutes at 150°C was added in the composition that produced the greatest outcomes for the processed data.

4.7 Study of Compressive strength through ANOVA analysis

ANOVA was run on the experimental data in order to analyze the impact of heating parameters on the mechanical strength, which was measured using a Universal Testing Machine (UTM) as an experimental output following the thermally treatment of the ceramic-based composites. The compressive strength (MPa) ANOVA findings are displayed in the table below. The data has first been standardized. After the compressive strength data was normalized, figure 4.19 below shows that the majority of the data points appeared to be close to the line, indicating that the data were determined to be in good agreement with the likelihood (226).

Compressive Strength

Color points by value of
Compressive Strength :
91.26  319.33

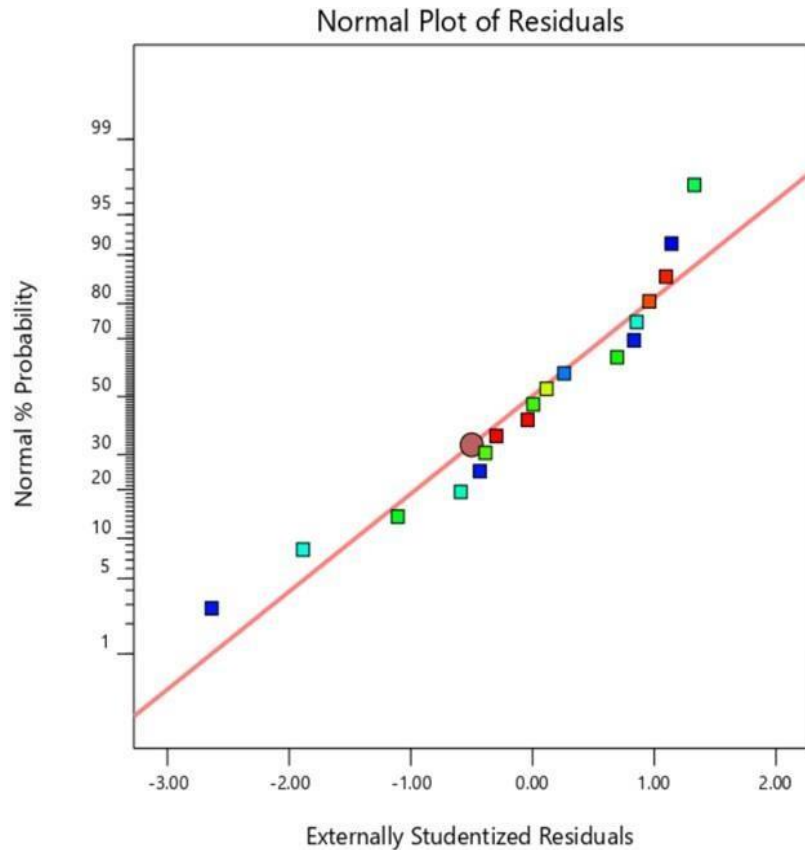


Figure 4.19: Normality plot of Compressive Strength of the composites

Second, an ANOVA analysis was conducted on the compressive strength data. Table examines the F-value, p-value, and mean square for each of the parameters, which include temperature (A), composition (B), and time (C). Furthermore, a tabulation of the combined effects of composition and time (BC) and square rooting of the time scale (C^2) has been performed.

Table 4.6: ANOVA analysis for the compressive strength

Source	Sum of Squares	dF	Mean Square	F-value	p-value	
Model	1.05E+05	5	21030.2	50.07	< 0.0001	significant
A-Temperature	4231.69	1	4231.69	10.07	0.008	
B-Composition	79465.37	1	79465.37	189.18	< 0.0001	
C-Time	7667.42	1	7667.42	18.25	0.0011	
BC	3333.5	1	3333.5	7.94	0.0155	
C²	16916.47	1	16916.47	40.27	< 0.0001	
Residual	5040.68	12	420.06			
Total	1.10E+05	17				

Additionally, the F-value of the model, 50.07 indicated was considered significant. Only 0.01% of the greater F-value may be attributed to noise.

Model terms with P-values less than 0.05 are deemed significant. In the example given, A, B, C, BC, and C² are significant model values. The model terms that are not significant are revealed by a p-value greater than 0.10. The Adjusted R² of 0.93 and the Predicted R² of 0.90 were found to differ by less than 0.2. In addition, the Adeq Precision determines the signal-to-noise ratio. The ratio ought to be more than 4. For the aforementioned experimental run, the signal strength was determined to be adequate with a ratio of 21.23 (297).

The impact of processing settings on the compressive strength of the blends can be observed in the figure below. To illustrate the influence, the figure 4.20 was divided into two sections: a surface plot and a contour plot. Figure below (a1 and a2) illustrates the relationship between concentration and heating duration and shows that the maximum compressive strength can be achieved by increasing the concentration and maintaining the time above 14 minutes.

Conversely, in figure 4.20 (b1 and b2) describes the impact of temperature and heating duration on compressive strength. The picture makes it clear that the maximum compressive strength output was found to occur at a temperature of approximately 150°C and a time interval of greater than 14 minutes.

Additionally, the relationship between composition and heating temperature has been carefully

examined, and it has been found that a greater temperature and increase in carboxymethyl cellulose concentration strengthens the composite. Figure 4.20 (c1 and c2) displays the impact of the blend's composition and the heating temperature using both a contour plot and a 3D surface plot.

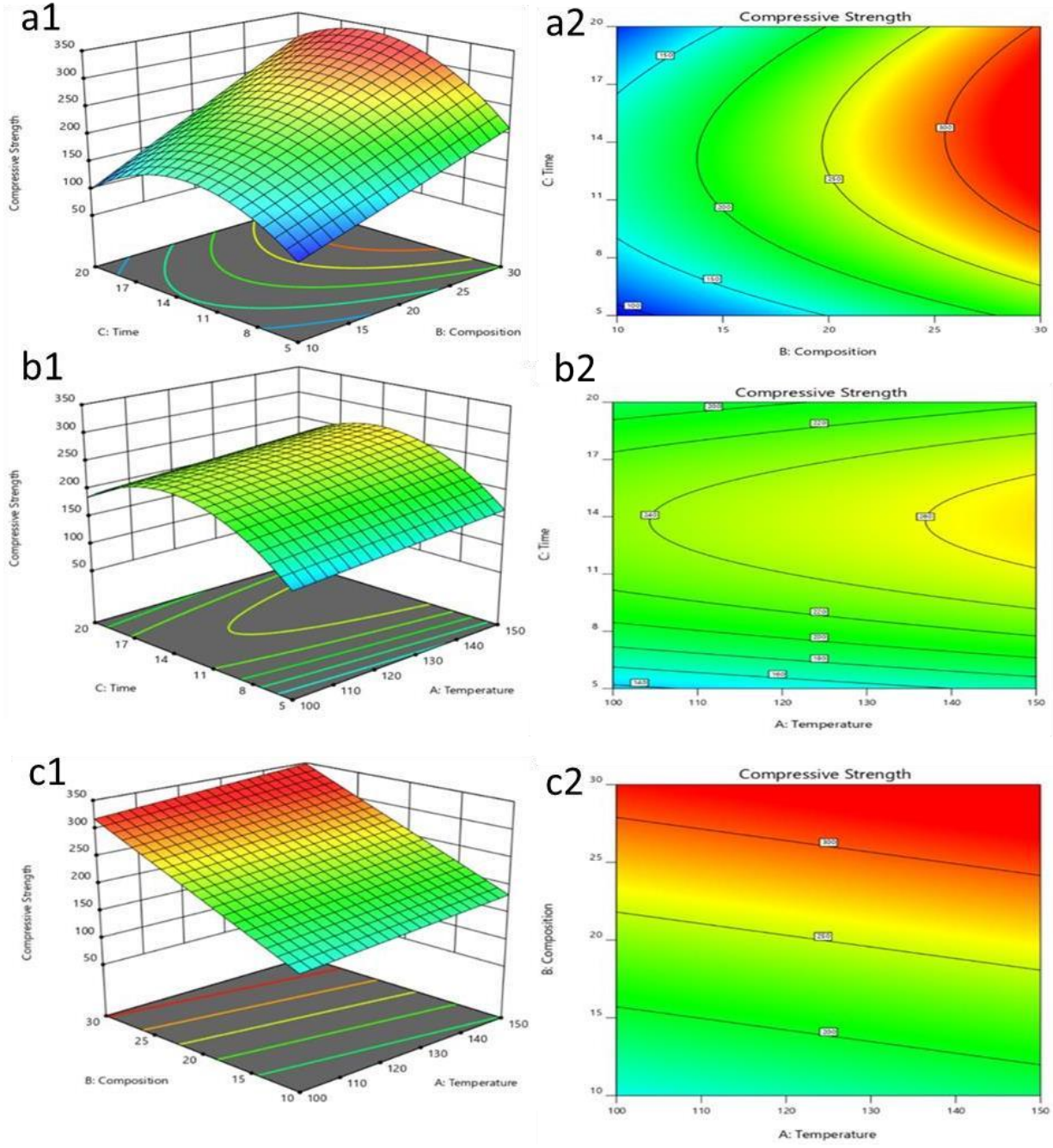


Figure 4.20: Effect of processing parameters on the compressive strength of the ceramic-based blend of calcined Hydroxyapatite, reduced graphene oxide and carboxymethyl cellulose with 3D surface (a1, b1, c1) and contour plot (a2, b2, c2)

In summary, the mechanical strength of the composites has been found to be enhanced by increasing the polymer content and thermal treatment conditions. Additionally, the factor's R^2 value was determined to be 90%, which is in good compliance with the expected value.

4.8 An examination of wettability using ANOVA

After the composites were heat-pressed, the experimental output was the static water contact angle, which was measured using ImageJ. An ANOVA was performed on the experimental data to examine the effects of the thermal treatment factors on the Wettability. The wettability ANOVA results are shown in the table below. First, the data was normalized. The bulk of the data points appeared to be closer to the line after the data were normalized for wettability, suggesting that the data were found to be in good accordance with the probability (226).

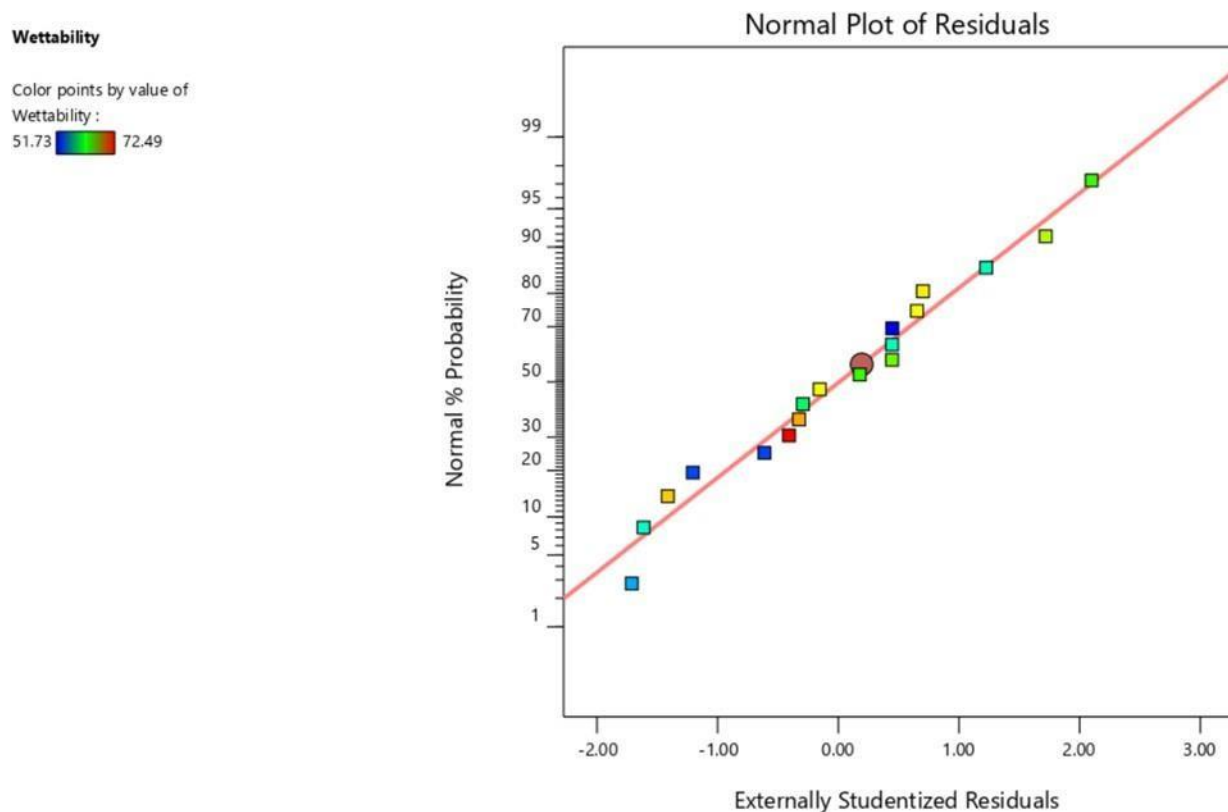


Figure 4.21: Normality Plot for wettability of ternary composite of calcined hydroxyapatite, reduced graphene oxide and carboxymethyl cellulose

Additionally, an ANOVA analysis was performed on the data related to Wettability. Temperature (A), composition (B), and time (C) are the three parameters whose F-value, p-value, and mean square are examined in Table 5. Additionally, squaring the time scale (C²) and a tabulation of the combined impacts of composition and time (BC) have been carried out.

Table 4.7: ANOVA analysis for the Wettability

Source	Sum of Squares	dF	Mean Square	F-value	p-value	
Model	634.32	4	158.58	66.46	< 0.0001	significant
A-Temperature	57.32	1	57.32	24.02	0.0003	
B-Composition	96.67	1	96.67	40.52	< 0.0001	
C-Time	480.19	1	480.19	201.25	< 0.0001	
C ²	20.31	1	20.31	8.51	0.012	
Residual	31.02	13	2.39			
Cor Total	665.34	17				

Additionally, the model was considered significant based on its F-value of 66.46. Noise can only be blamed for 0.01% of the larger F-value.

Significant model terms are those having P-values less than 0.0500. A, B, C, and C² are important model terms in the current model. A p-value more than 0.1000 reveals the model terms that are not significant. There was determined to be a less than 0.2 difference between the Expected R² of 0.9098 and the Adjusted R² of 0.9390. The signal-to-noise ratio is also determined by the Adeq Precision. More than four should be the ratio. With a ratio of 26.897, it was concluded that the signal strength for the previously described trial run was adequate.

Figure below illustrates how the wettability of the blend is affected by the processing conditions. The figure was separated into a surface plot and a contour plot to show the influence. The link between the polymer concentration and the heating temperature is

depicted in Figure 4.22 (a1 and a2), which demonstrates that raising the concentration of polymer and the heating temperature can result in good wettability.

Furthermore, Figure 4.22 (b1 and b2) depicts how temperature and processing time affect wettability. The figure illustrates that the wettability of the polymeric mix increases with increasing processing temperature and time.

However, a thorough analysis of the link between composition and heating duration revealed that a higher composition and longer processing times, as shown in Figure 4.22 (c1 and c2) utilizing both a contour plot and a 3D surface plot.

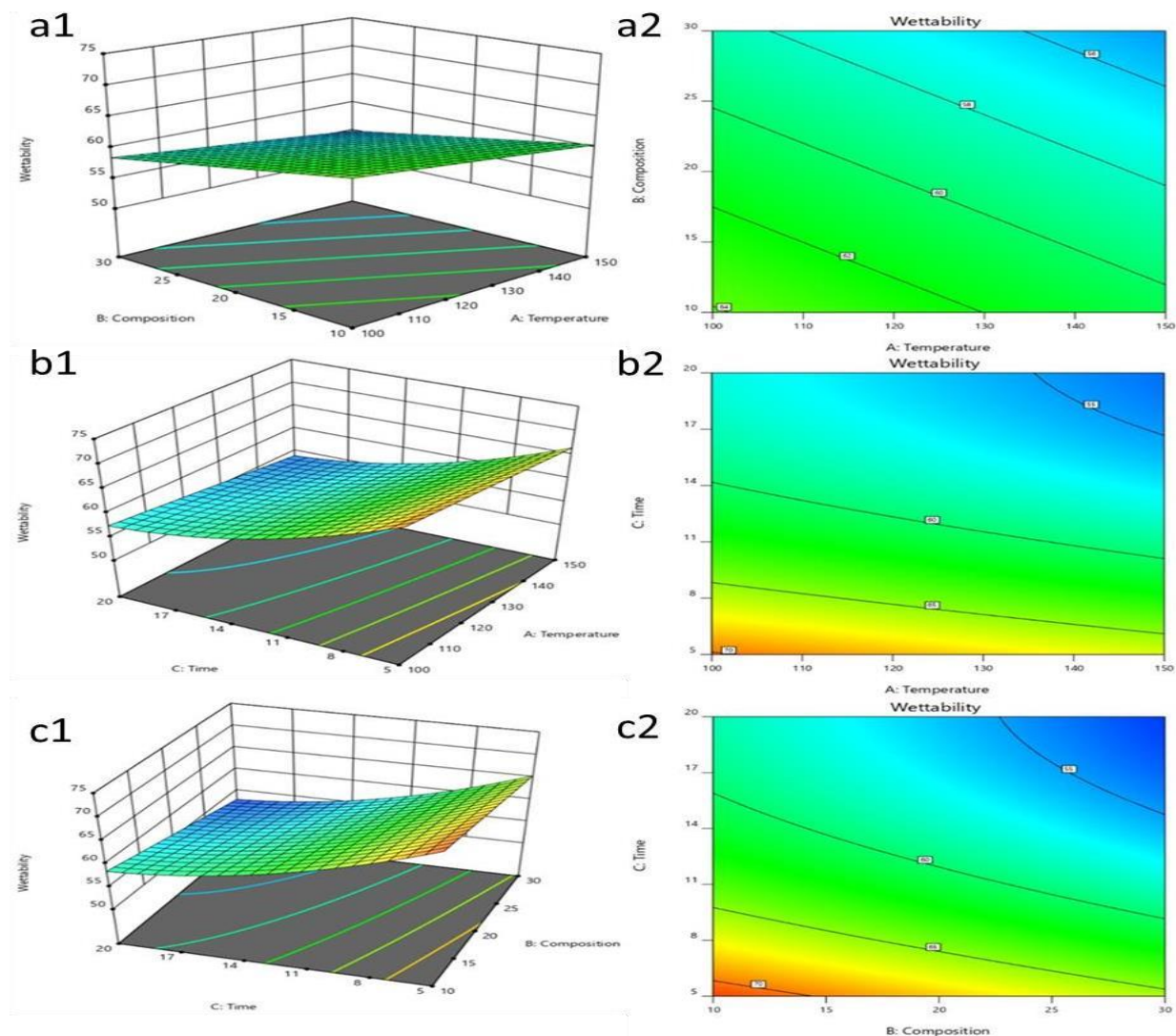


Figure 4.22: Effect of processing parameters on the wettability of the ternary blends of calcined Hydroxyapatite, Reduced graphene oxide and Carboxymethyl cellulose with 3D surface (a1, b1, c1) and contour plot (a2, b2, c2) for the composite

In the end, it has been found that the heating parameters have a positive impact on the wettability of the composite. However, the R^2 was discovered to be 0.909, indicating strong concurrence with the modified value.

4.9 GRG examination using an ANOVA

The GRG (Grey relational grade) has been calculated using the previously mentioned equation 4. The combined effect of the GRCs on wettability and compressive strength is also displayed by the GRG. A ranking based on the GRG has been carried out to identify the best composite with the optimal concentration and processing circumstances. Table 6 illustrates the GRG analysis (269) using the ANOVA.

The data was first normalized. After the data were normalized for gray relational grade, the majority of the data points seemed to be near the line, indicating that the data was deemed to be in good agreement with the statistical analysis.

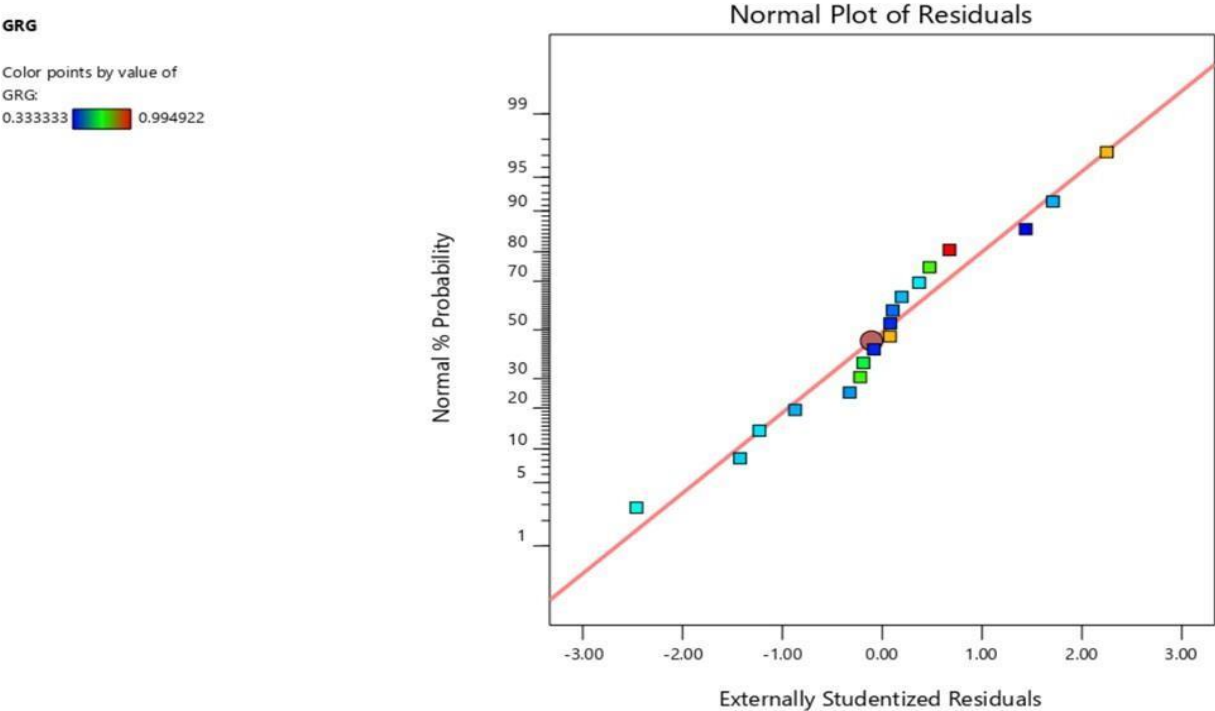


Figure 4.23: Normality plot of grey relational grade (GRG)

Table 6 showed that the model was deemed significant with an F-value of 50.07. The increased F-value has a mere 0.01% probability of being caused by noise.

Model parameters are considered significant when P-values are less than 0.0500. A (Heating temperature), B (composition of polymer), C (Processing time), BC (composition & heating time), and C² (doubling the heating time) are significant model terms in the example. A p-value greater than 0.1000 indicates the presence of irrelevant model terms.

Table 4.8: ANOVA analysis of GRG

Source	Sum of Squares	df	Mean Square	F-value	p-value	Contribution %
Model	0.6194	5	0.1239	33.57	< 0.0001	
A-Temperature	0.0385	1	0.0385	10.44	0.0072	5.722
B-Composition	0.3326	1	0.3326	90.13	< 0.0001	49.402
C-Time	0.2139	1	0.2139	57.97	< 0.0001	31.774
BC	0.0525	1	0.0525	14.22	0.0027	7.794
C²	0.0357	1	0.0357	9.68	0.009	5.305
Residual	0.0443	12	0.0037			
Cor Total	0.6636	17				

The calculated corrected R² of 0.9352 was found to be less by a margin of less than 0.2 than the estimated R² of 0.9099. Furthermore, the Adeq Precision computes the signal to noise ratio. The optimal ratio is higher than four. The aforementioned test run produced a ratio of 21.230, meaning that the signal strength was considered sufficient. Moreover, when examining the percentage contribution, composition has the biggest influence, followed by temperature and time.

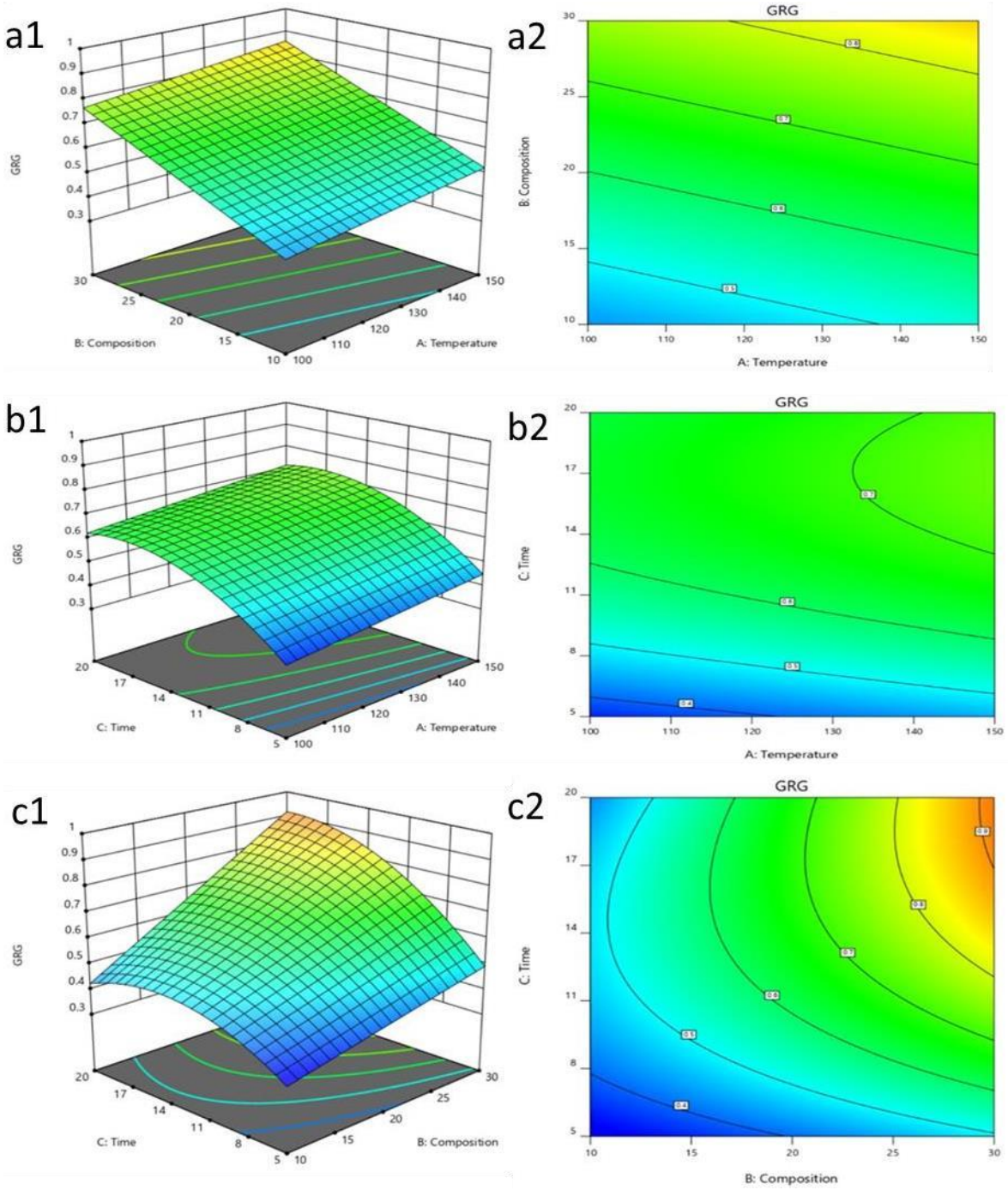


Figure 4.24: Analysis of processing conditions with the Grey relational grade (GRG) through 3D surface (a1, b1, c1) and contour plot (a2, b2, c2) for the blend of calcined Hydroxyapatite, Reduced graphene oxide and Carboxymethyl cellulose.

Figure 4.24 illustrates impact of processing conditions on GRG. The figure was separated into a surface plot and a contour plot to show the influence. A link between concentration and heating temperature is depicted in Figure 4.24 (a1 and a2), which indicates that increasing

concentration and reaching 150°C as the heating temperature will yield the maximum GRG. In a similar vein, Figure 4.24 (b1 and b2) details influence of temperature and processing time on GRG. The chart clearly shows that higher range of processing conditions were found to be optimal for GRG.

Furthermore, a thorough investigation of the relationship between blend composition and hot-pressing duration revealed that higher processing times were associated with higher concentrations of carboxymethyl cellulose, which in turn led to elevated GRG, as shown in Figure 4.24 (c1 and c2), which was visualized using both a contour plot and a 3D surface plot.

4.10 Desirability Function Analysis (DFA)-Based Optimization

Greater desirability for compressive strength and lesser desirability for Wettability have been selected in order to improve the process parameters. The desirability analysis has been analyzed using the Design-Expert program (264,297).

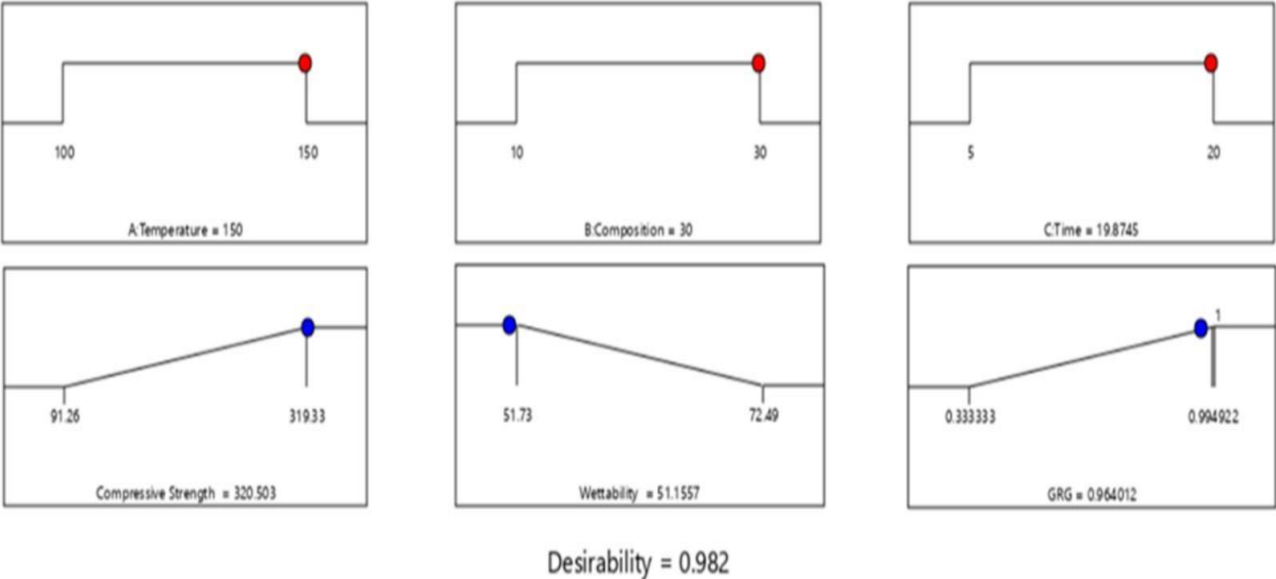


Figure 4.25: Plots for desirability for the different processing Temperature, time and composition of carboxymethyl cellulose along with the best possible output of compressive strength (MPa), Wettability (°) and Gray relational Grade (GRG) for the blend of calcined Hydroxyapatite, Reduced graphene oxide and Carboxymethyl cellulose.

Figure 4.25 provides a representation of the desirability ramp plot. Figure 4.25 shows that the ideal temperature was determined to be 150°C, with a 30% (wt.%) carboxymethyl cellulose content and a 19.87 minutes processing period. The compressive strength was determined to be 320.50 MPa at the aforementioned variables, the wettability was 51.15° and the GRG was calculated to be 0.96, which is in close proximity with the experimental findings.

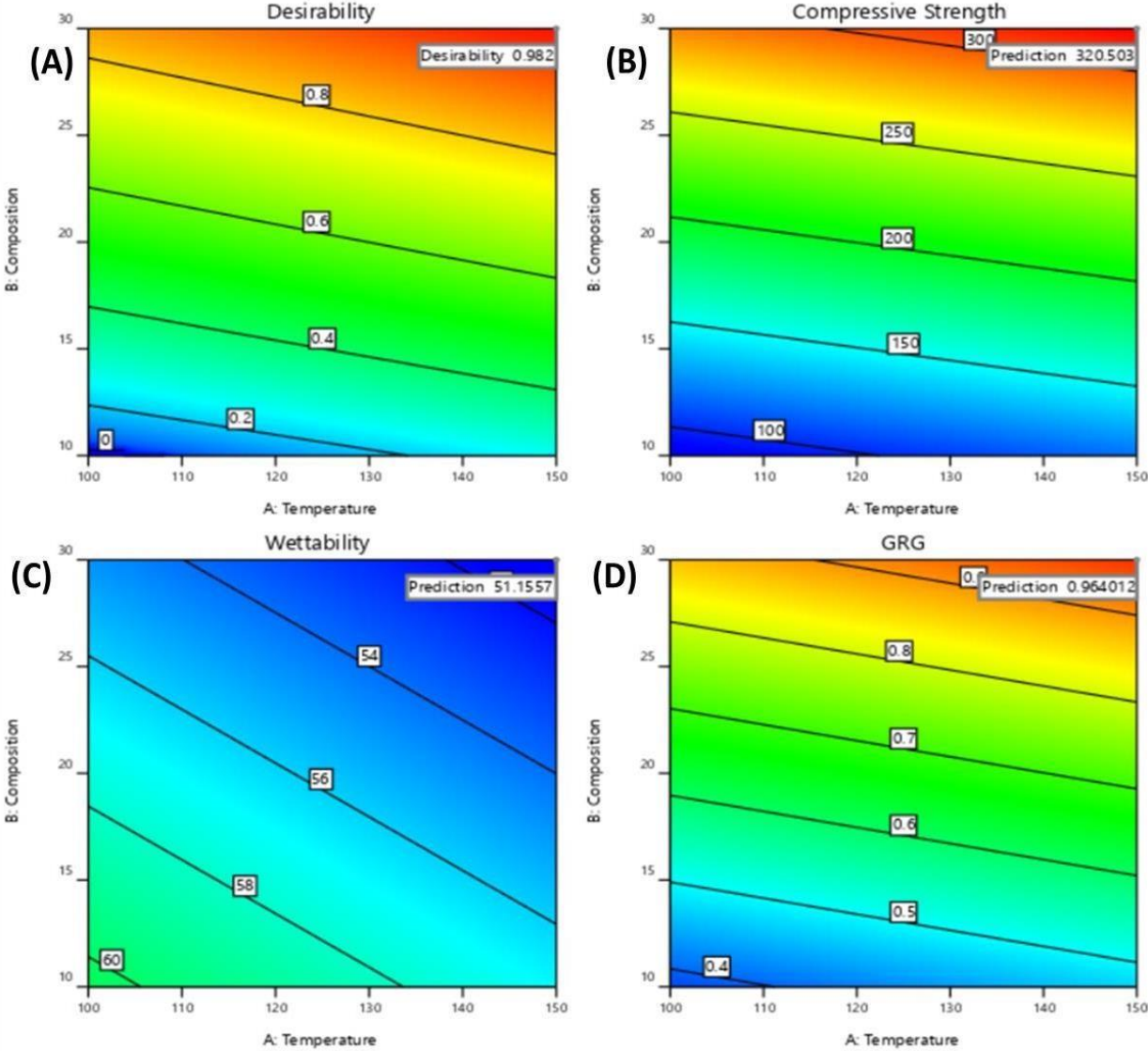


Figure 4.26: Effect of output responses with respect to composition and temperature after using desirability approach for the blend of calcined Hydroxyapatite, Reduced graphene oxide and Carboxymethyl cellulose.

Additionally, Figure 4.26 indicates that the composition and temperature of the thermal affect the following: Desirability (A), wettability (C), compressive strength (B), and Grey relational grade

(GRG) (D). The graphic clearly illustrates how compressive strength improved as carboxymethyl cellulose concentration increased and wettability angle decreased. Likewise, extreme composite circumstances were found to have a greater GRG. The expected value for GRG was determined to be 0.964 when compared to the desirability, which is in good accordance with the projected value of the desirability. Furthermore, the maximum values for Desirability, compressive strength, and GRG were seen in the red zone. But conversely. In Figure 4.26 (C), the lower the better for wettability is displayed in blue (259,264).

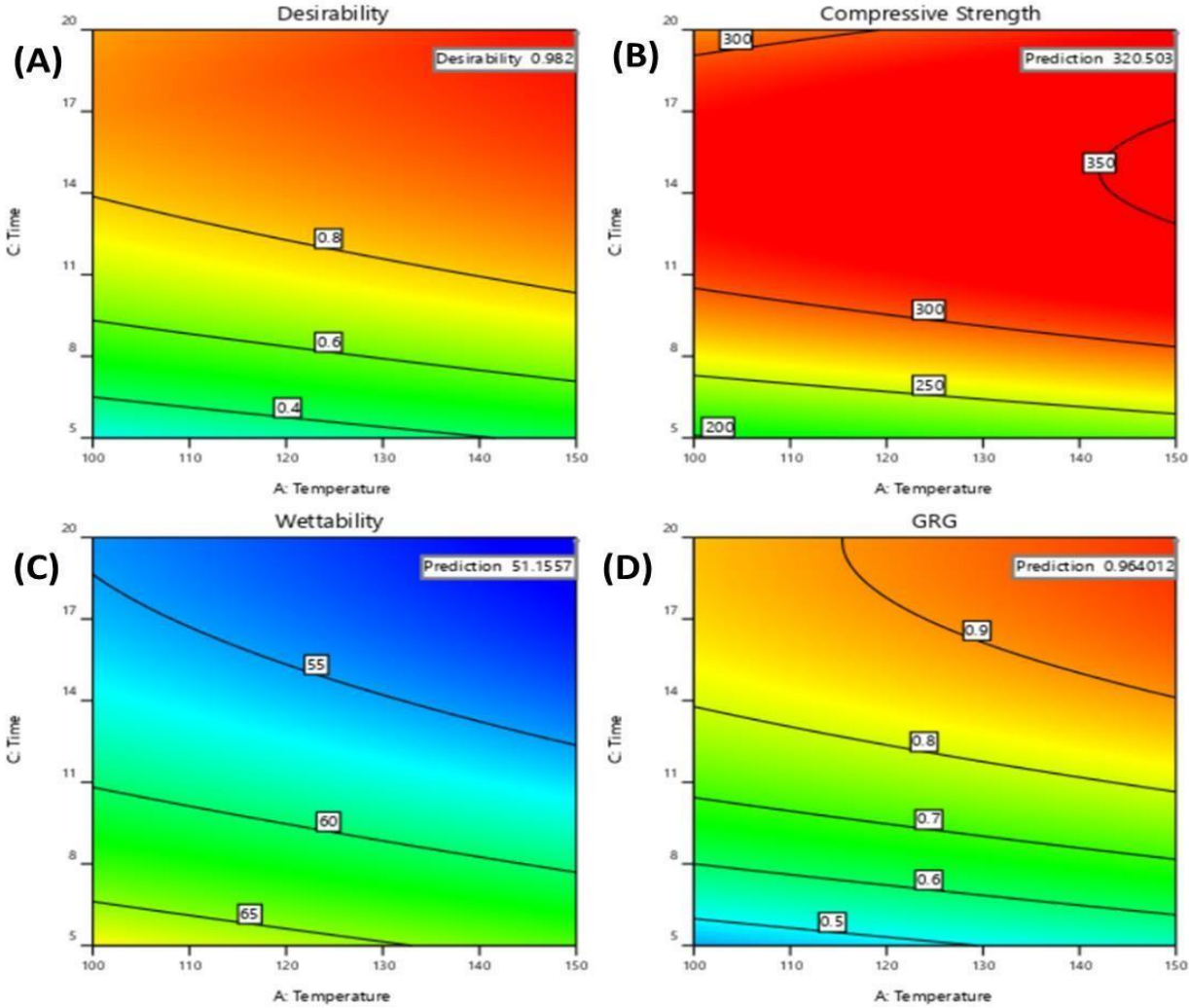


Figure 4.27: Effect of output responses with respect to time and temperature after using desirability approach

Additionally, Figure 4.27 indicates that the composition and temperature of the thermal affect the following: Desirability (A), wettability (C), compressive strength (B), and Grey relational grade (GRG) (D). The graphic clearly illustrates how compressive strength improved as carboxymethyl

cellulose concentration increased and wettability angle decreased. Likewise, extreme composite circumstances were found to have a greater GRG. The expected value for GRG was determined to be 0.964 when compared to the desirability, which is in good accordance with the projected value of the desirability. Furthermore, the maximum values for Desirability, compressive strength, and GRG were seen in the red zone. But conversely, in Figure 4.28 (C), the lower the better for wettability is displayed in blue (259).

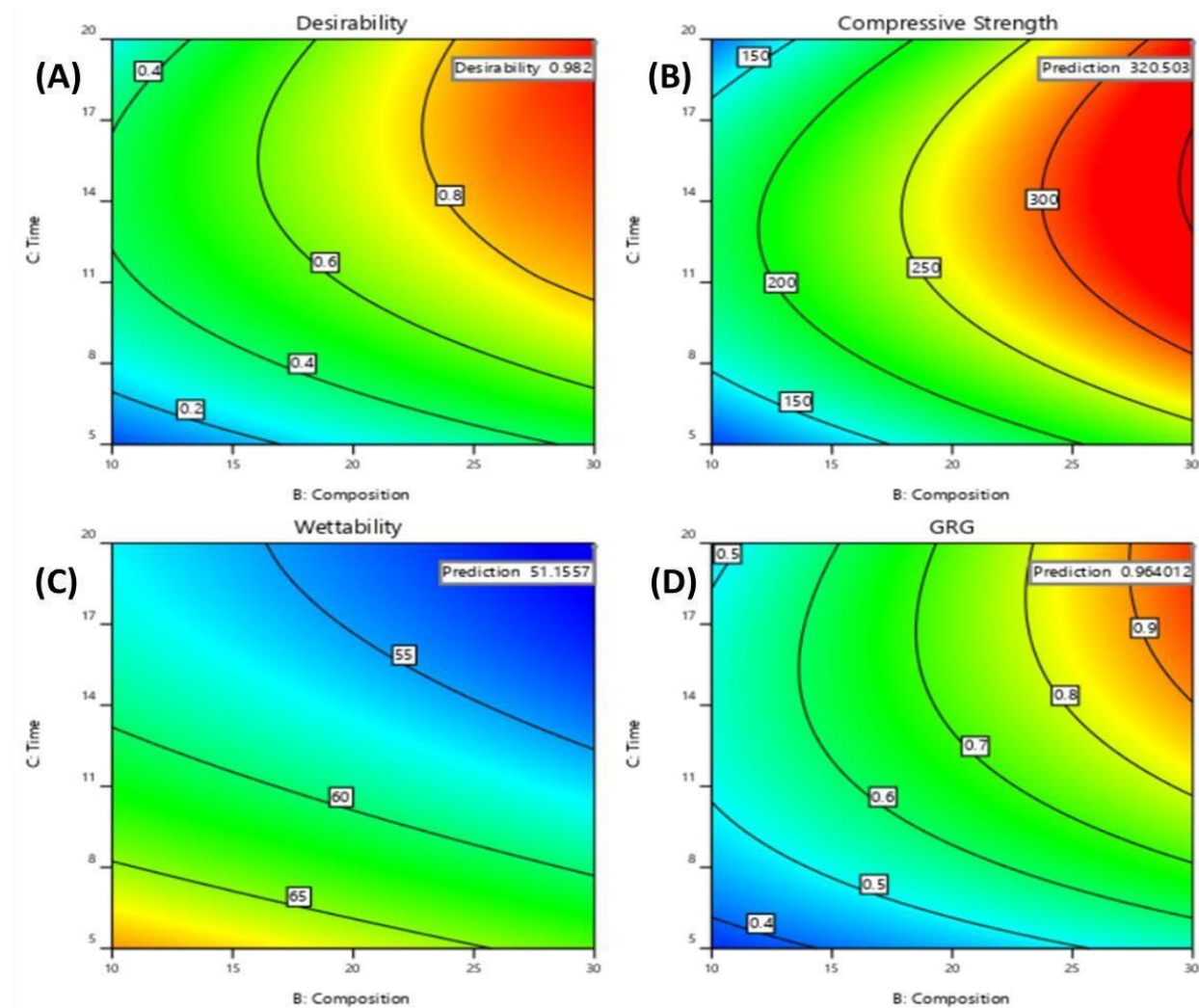


Figure 4.28: Effect of output responses with respect to time and composition after using desirability approach

Moreover, the highest carboxymethyl cellulose content and a prolonged processing duration were shown to yield the most favorable results in terms of desirability. Similar to this, a synergistic

impact was seen in the grey relationship analysis for the compressive strength and wettability in Figure 4.28 (B&C), respectively, with higher processing times and higher concentrations of the polymer.

4.11 Analysis of regression

The response prediction model for compressive strength, wettability, and GRG values was developed using regression analysis. The multiple linear regression analysis mathematical models for the compressive strength, wettability, and GRG of the composites as a function of thermal treatment parameters. The mathematical models for the results are shown in equations. The study of inorganic hydroxyapatite (HA) assembly in polymer matrix is of great interest in the bone tissue engineering field. An in-situ synthesis method is employed in this study to synthesize carboxymethyl cellulose (CMC)/HA composite scaffolds to mimic the natural bone. The formation of HA in the CMC matrix is initiated at three different temperatures (30°C, 60°C and 90°C) and the size of HA decreases with the increase of temperature. The morphology of the scaffolds as viewed by scanning electron microscope shows the formation of rough surfaces with agglomerated HA that can favor appreciable attachment of cells. The X-ray diffraction and Fourier transform infrared spectroscopy confirmed the purity of the formed HA in the polymer matrix. The mechanical properties of the scaffolds reveal that they can form suitable templates to support newly formed bone cells at the site of the defect. The cytotoxicity test of scaffolds with the fibroblast (NIH3T3) cells demonstrated that they can form a suitable template for the attachment of cells and proliferation in bone regeneration (265).

The regression equation for compressive strength was discovered to be;

Compressive Strength

$$=72.59139+0.613311\times\text{Temperature}+4.86913\times\text{Composition}+31.13748\times\text{Time}+0.267268\times\text{E3}\times\text{Time}-1.3245\times\text{Time}\times\text{Time} \quad (5)$$

On the other hand, the regression equation for wettability turned out to be;

Wettability

$$=91.815-0.071378\times\text{Temperature}-0.283833\times\text{Composition}-$$

$$1.99067 \times \text{Time} + 0.045889 \times \text{Time} \times \text{Time} \quad (6)$$

and the GRG equation has been identified to be;

GRG

=-

$$0.180308 + 0.00185 \times \text{Temperature} + 0.003543 \times \text{Composition} + 0.044711 \times \text{Time} + 0.00106 \times \text{Composition} \times \text{Time} - 0.001925 \times \text{Time} \times \text{Time} \quad (7)$$

The experimental and anticipated bar charts appeared to be comparable. In the same way, wettability and GRG. The experimental results are validated by the graph presented in Figure 4.29. The accuracy of the obtained values was confirmed by the increased linear correlation coefficient (R²).

Table 4.9: Description of Predicted and Adjusted values of the outputs

Performance Parameters	Predicted values	Adjusted values
Compressive strength	0.909	0.935
Wettability	0.909	0.939
Grey relational Grade	0.909	0.935

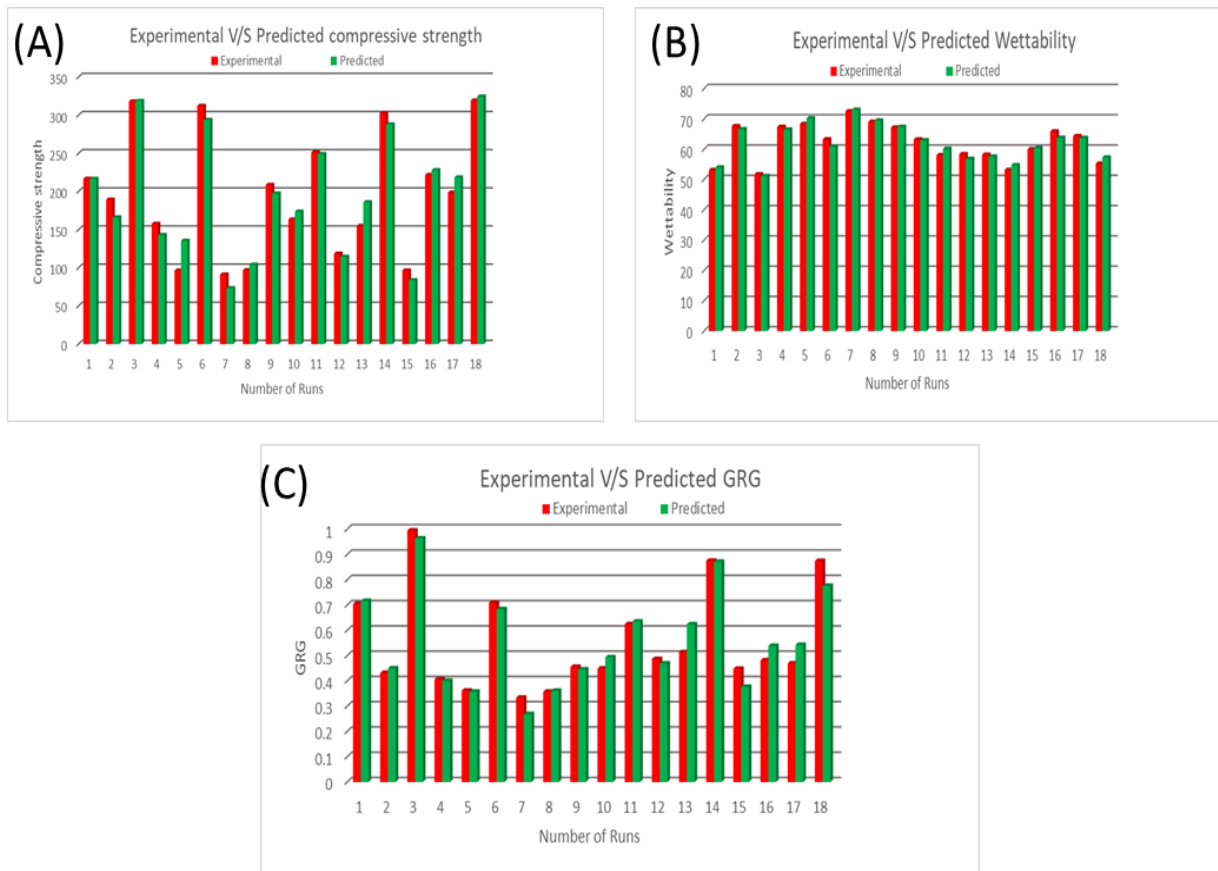


Figure 4.29: Average percentage error of (A) compressive strength (B) Wettability and (C) GRG for the blend of calcined Hydroxyapatite, Reduced graphene oxide and Carboxymethyl cellulose.

Table 4.9 and Figure 4.29 present a comparison between the predicted values obtained for the L18 optimized model and the observed data. The best fit model that can be achieved within the processing parameter range, i.e., heating temperature of 100°C-150°C and time range of 5-20 minutes, has been determined using the predicted values, which have been derived from the regression equation.

4.12 Morphological Analysis

Through the analysis of FESEM images, the morphology of various ceramic-based polymeric blends has been identified. Further in figure 4.30, the variations B1, B2, and B3 that were treated at two different temperatures are depicted in the picture below as FESEM images. The agglomeration has been seen in blends that have been heated at 100°C or 150°C under pressure, according to the FESEM images. Blends B2 and B3 showed greater agglomeration, which may have been due to inadequate mixing

of the blends. The creation of strong bonds with carboxymethyl cellulose may also be concealed by a lower concentration of reduced graphene oxide, which may potentially be a contributing factor to the agglomeration in B3. Additionally, the agglomeration has been noted in the HA/CMC composite (265) and the blending of reduced graphene oxide and carboxymethyl cellulose also exhibited agglomeration (296) due to the increased viscosity of the carboxymethyl cellulose. Additionally, the CMC has been utilized as a dispersant, but if the ratio of rGO to CMC is too low, there might not be a stable build-up and aggregates produced, which clarifies the formation of clumps in the Figure 4.30 below.

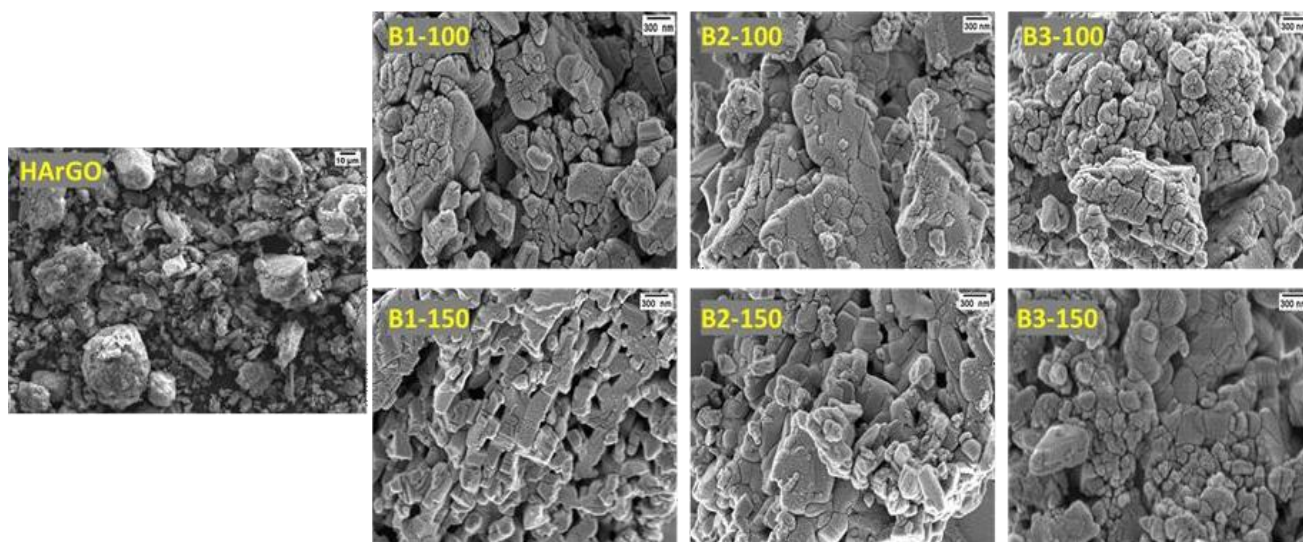


Figure 4.30: SEM micrographs of Hydroxyapatite and reduced graphene oxide (60HA:40rGO), Ceramic-based polymeric blends B1 (60 cHA :30 rGO :10 CMC), B2 (60 cHA :20 rGO :20 CMC) and B3 (60 cHA :10 rGO :30 CMC) heated under pressure at 100°C and 150°C

Particles cluster together to form bigger assemblies, or aggregates, a process known as agglomeration. This may have a substantial impact on the DLS data' overall interpretation as well as the PDI. A measure of the distribution of particle sizes in a particular sample is the polydispersity index, or PDI. The dynamic light scattering (DLS) measurements are the source of this measurement, which indicates the homogeneity of particle sizes inside a sample (298). A totally monodisperse sample (all particles have the same size) is indicated by a PDI value of 0,

which is a dimensionless number. Higher values, on the other hand, imply greater size distributions. The PDI for different composites of hydroxyapatite, reduced graphene oxide and carboxymethyl cellulose is shown in figure 4.31. The highest PDI found in B1-100 i.e. 0.693 ± 0.17 whereas the PDI lowers on increasing the processing temperature from 100°C to 150°C . Further, the B2-150 showed lower PDI of 0.499 ± 0.05 as compared to B1-150 and B3-150 which confirms the higher agglomeration in the B1-150 and B3-150 than in B2-150 hence, improving the mechanical strength. The higher concentration of reduced graphene oxide in the B1 variant can be explained by the fact that reduced graphene oxide has a tendency to agglomerate, leading to higher agglomeration and higher PDI. This is in agreement with earlier data reported by Son and peers, who found that higher concentrations of reduced graphene oxide in rGO blends with CMC resulted in higher agglomeration (296). The PDI decreases along with the reduction in decreased graphene oxide content in the B1-B3 composite.

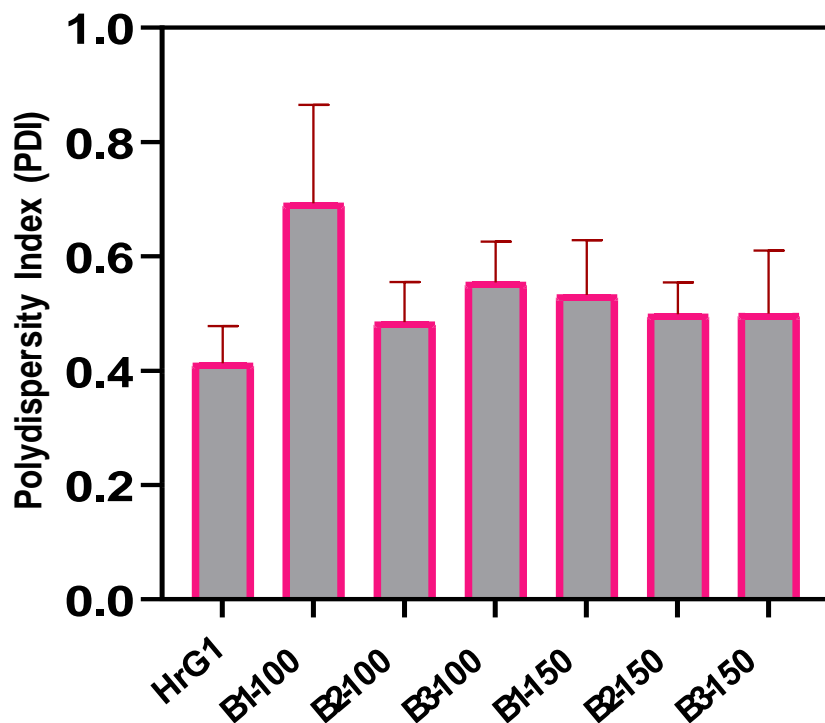


Figure 4.31 The Polydispersity Index for various blends using Dynamic Light Scattering (DLS)

4.13 Surface roughness of the composite

The most significant variable in regulating adhesion and its growth is surface roughness. Additionally, according to Kunzler and co-workers, surface roughness promotes osteoblast growth. Contrarily, numerous research demonstrated that MG-63 cell- lines showed a cutback in cellular proliferation as the roughness increased (283–285). Interestingly, the thermal treatment had an impact on the wettability and surface roughness of the ternary blends.

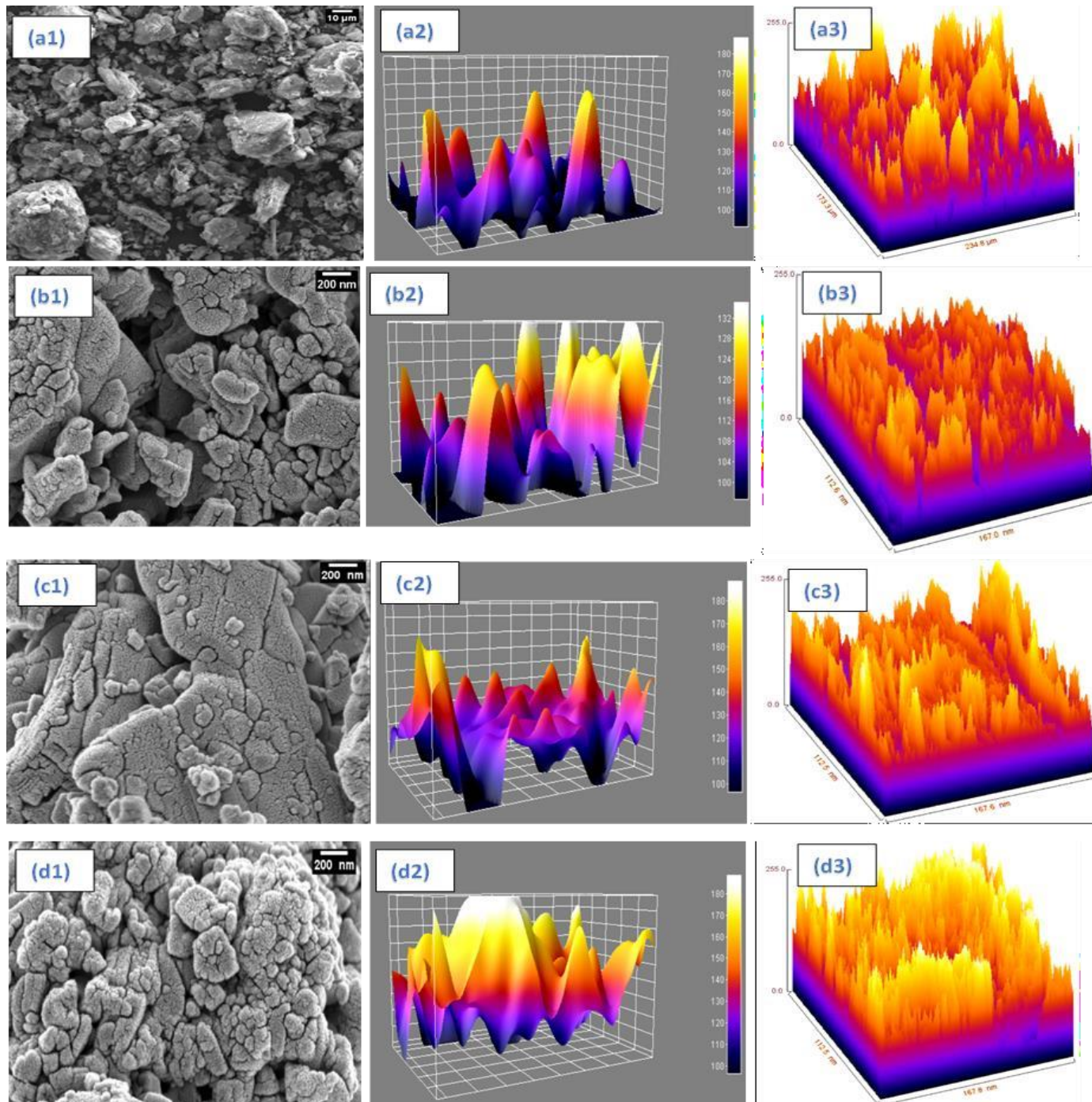


Figure 4.32(a) SEM Images, 3D plots and Surface plot for HArGO (a1-a3), B1-100 (b1-b3), B2-100 (c1-c3), B3-100 (d1-d3)

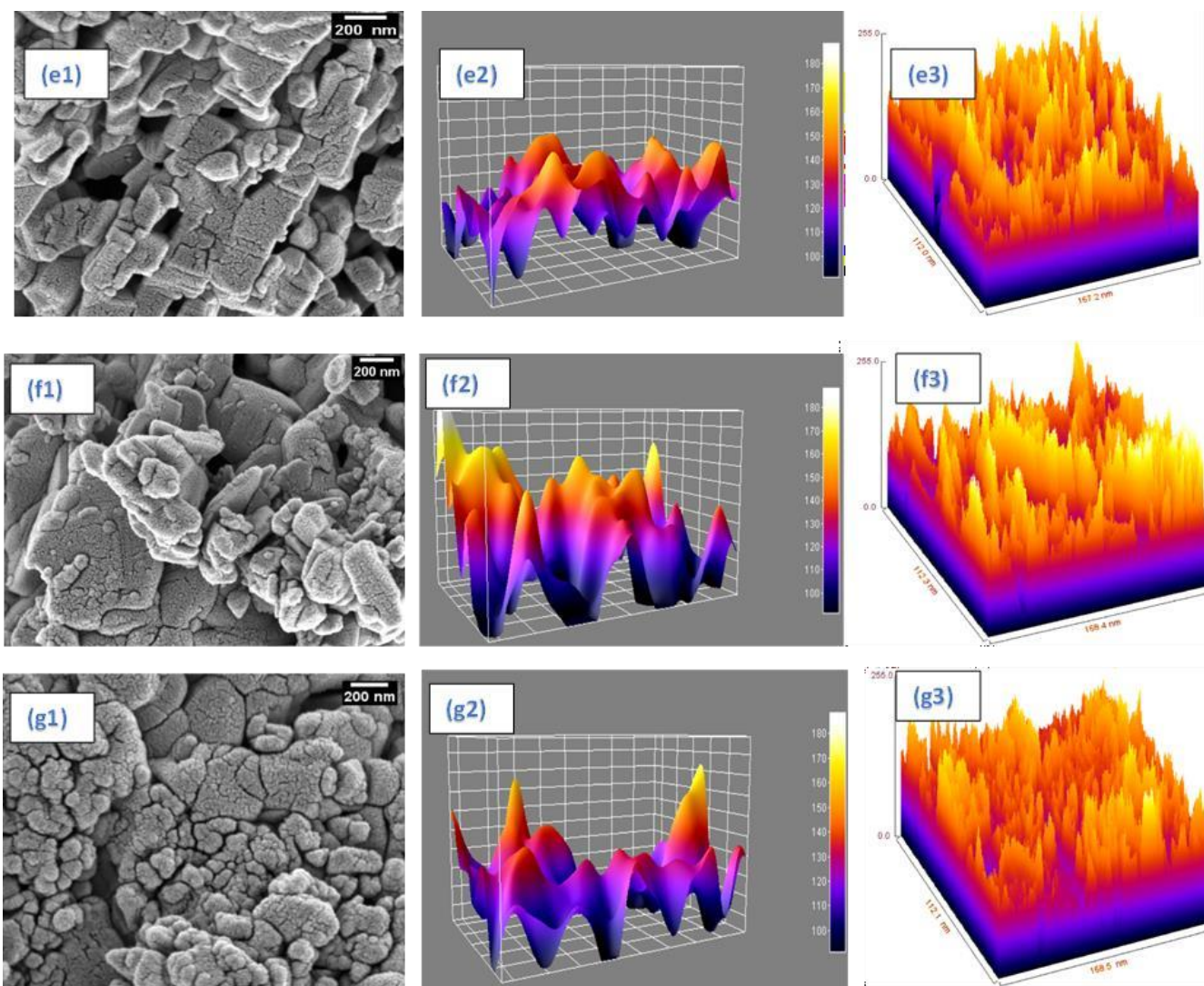


Figure 4.32(b): SEM Images, 3D plots and Surface plot for B1-150 (e1-e3), B2-150 (f1-f3), B3-150 (g1-g3)

The surface roughness of the ceramic-based carboxymethyl cellulose (CMC) blends is shown in Figures 4.32(a) and 4.32(b) in contrast to hydroxyapatite and reduced graphene oxide (HArGO). The figure up above displays SEM images alongside a 3D image of the blends and a surface plot using ImageJ after SEM image analysis. The wettability and biocompatibility of the composites are significantly influenced by the surface roughness.

Table 4.10: Roughness means and RMS of the Ceramic-based polymeric composites

BLENDS	Root mean Square (RMS) (μm)	Average Roughness (Ra) (μm)
HArGO	34.22± 0.93	28.14± 0.43
B1-100	0.46± 2.61	0.22± 0.76
B2-100	0.43± 1.62	0.22±2.11
B3-100	0.46± 2.39	0.24± 2.54
B1-150	0.44± 0.35	0.23± 0.64
B2-150	0.40± 2.36	0.20± 1.11
B3-150	0.45± 4.50	0.22±1.07

The table 4.10 above indicates that, with pressurized heating, surface roughness reduces as the temperature elevates. The fact behind may be heating tends to fill the gaps between the components of the material and smooth the surface with compaction pressure. Furthermore, compressive strength is impacted by the declining surface roughness of the material. This might be because of the improved molecular interactions that result from the smoother surface. The overall mechanical strength may have decreased as a result of the stress concentrators that the imperfections in the rough surface may have provided (299).

4.14 Wettability

Through static water contact angle (WCA) measurement using the sessile drop method, the wettability has been estimated. The pellets were covered with around 4-6 μl of water droplets, and it was found that the wettability decreased as the processing temperature raised. The DLSR macro lens was used to capture the photographs. ImageJ has been used for image acquisition and

analysis (300). The surface hydrophilicity of the ternary/ceramic-based polymeric blends has been presented in the image below.

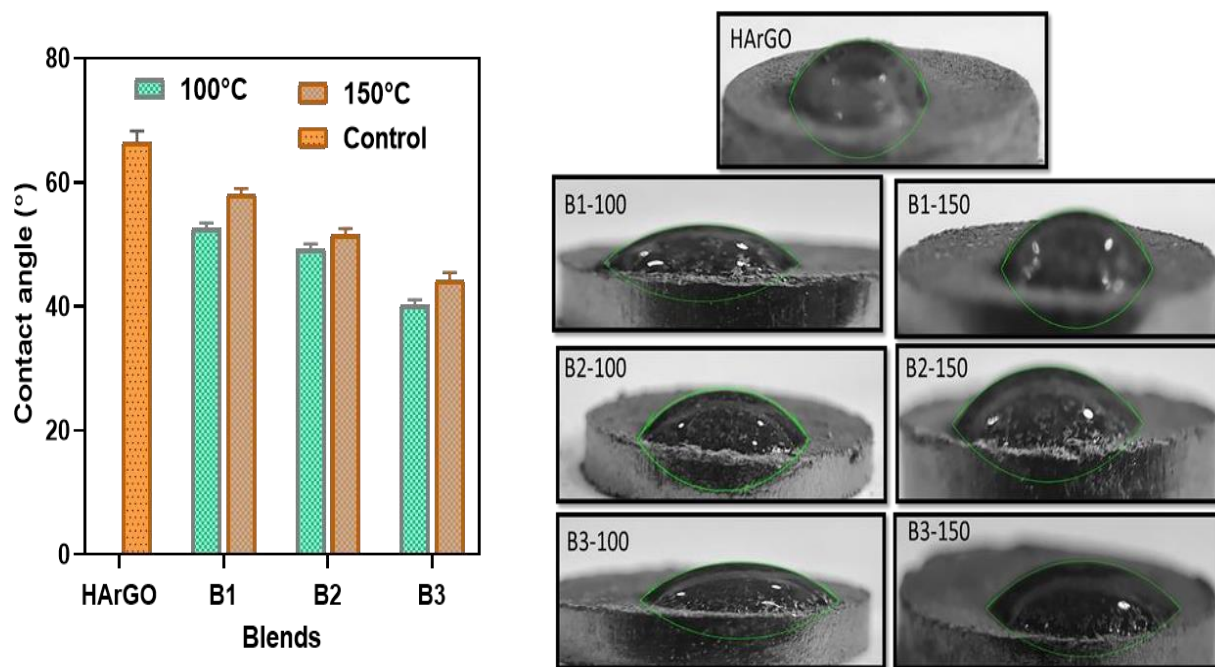


Figure 4.33: Wettability of thermally treated blend of Hydroxyapatite and reduced graphene oxide (60HA:40rGO), Polymeric blends B1 (60 cHA :30 rGO :10 CMC), B2 (60 cHA :20 rGO :20 CMC) and B3 (60 cHA :10 rGO :30 CMC) thermally-pressed at 100°C and 150°C

The increasing carboxymethyl cellulose concentrations from blends B1 to B3, ameliorated the wettability of the composites, or the hydrophobicity of the blends appears to decline as the concentration of reduced graphene oxide decreases. Furthermore, the effect of thermal treatment at constant pressure was graphically represented in Figure 4.33, which demonstrated that as thermal temperature rises, a rise in the water contact angle occurs. The rise in the water contact angle may be caused by an increase in sample density as well as porosity shrinkage, which led to a larger water drop angle. The composites still showed hydrophilicity, which provides a good foundation for cell attachment and proliferation even when the water contact angle (WCA) is rising (290).

4.15 Thermal Behavior of the composites

The thermal stability and degradation of the blends have been demonstrated by thermogravimetric analysis (TGA). Additionally, it provides quantifiable data regarding weight loss in relation to temperature. According to the TGA curve for carboxymethyl cellulose, the first weight loss started

at around 30°C and continued to approximately 220°C with a weight loss of about 17.9%, while the second weight loss started at approximately 320°C and ended with complete degradation at approximately 700°C (294,301).

However, the TGA of reduced graphene oxide demonstrates the considerable weight loss at or above 600°C, demonstrating that the phase remained unchanged until 150°C. The TGA for the blend is presented in Figure 4.34 below for viewing the impact of heating under pressure at various time intervals. As the evaporation of absorbed water is responsible for the weight loss up to 200°C. Quantifying the weight loss for the composites after being heat-pressed for 5 minutes, 10 minutes, and 20 minutes revealed losses of 12.75%, 12.25%, and 21.09%, respectively which is found to be significantly less than the weight loss for CMC, which was discovered to be 63.48% hence, improve the thermal stability of the composites.

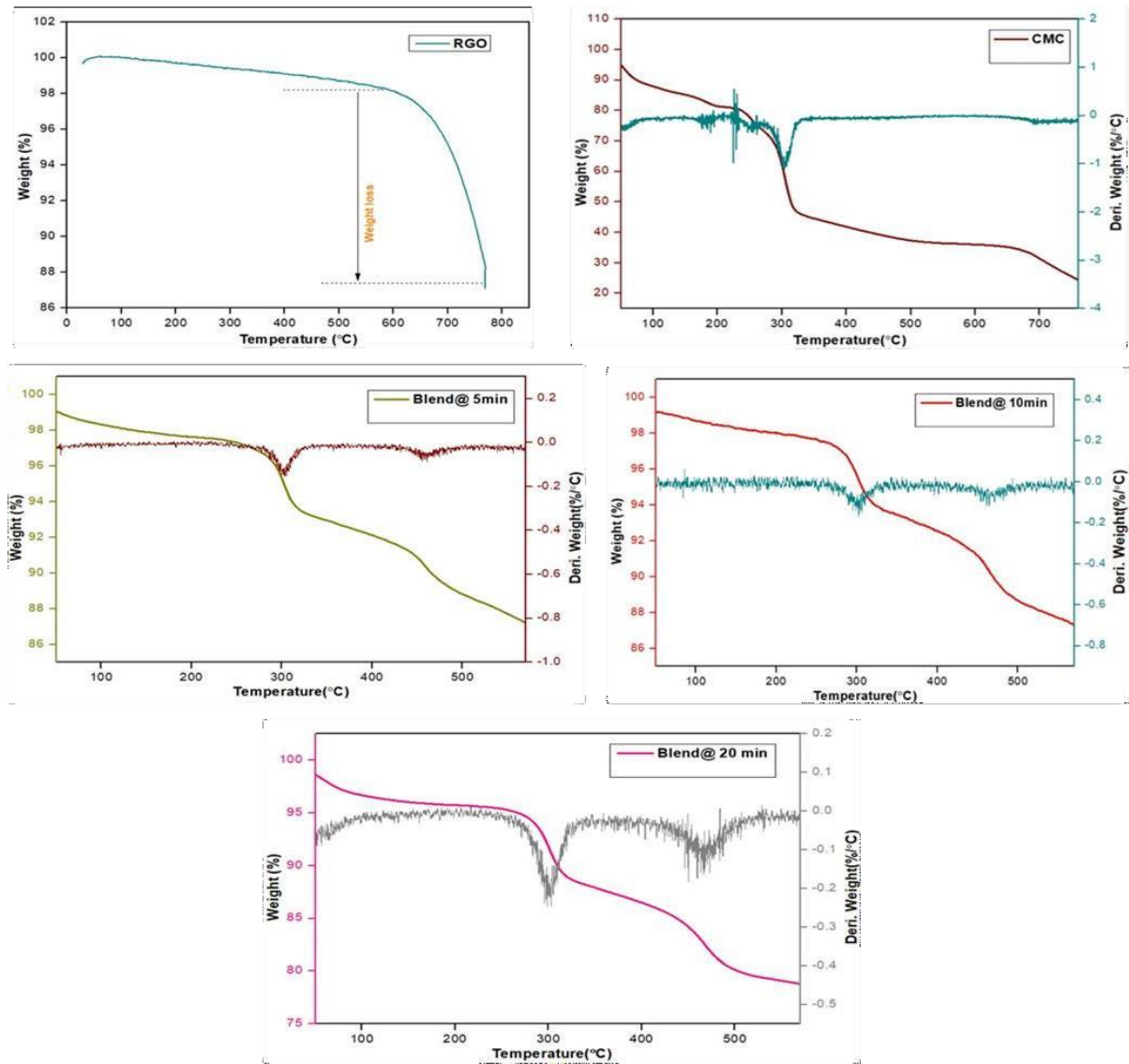


Figure 4.34: TGA analysis of Carboxymethyl Cellulose (CMC), Reduced Graphene oxide (rGO) and heat-pressed blend of Calcined Hydroxyapatite, Reduced Graphene oxide and Carboxymethyl Cellulose for 5min, 10min and 20min.

Specifically, it has been determined that the composites' thermal stability increases with the increase in time period. The figure displayed both the derivative weight and the percentage change in weight as a function of temperature. When compared to the blend pressurized heating at various times, CMC demonstrated more weight loss. When comparing the blends, the largest weight loss was discovered to occur after 20 minutes.

PART 4: Biological compatibility testing parameters.

The biological compatibility of the aforementioned hydroxyapatite-based polymeric blend has been examined in this chapter. The biomineralization and cytocompatibility using MTT assay have been accessed. In addition to being a polymeric blend, biodegradability has also been examined.

4.16 In vitro Biomineralization of composites

The Figure above showed the SEM images of B2 in which apatite layer is formed for the 1st (a), 3rd as (b) and 4th week as (c) in the figure 4.35 inclusive of the EDX spectra that shows the Ca^{2+} and PO_4 ions present in each week. After allowing the composites soak in the SBF solution for around 28 days, the Ca/P ratio in the first week of soaking was higher in blend B2, which had a ratio of 1.49 due to calcium deficient region, which increases in the 4th week as shown in Figure 4.33. The drop in the Ca/P ratio in the 3rd week has also been linked to the presence of an existing calcium phosphate layer. A layer of calcium and phosphate has already formed, which is supposed to be stabilized by the bonding between HA, rGO, and CMC, which is in good tuning with an explanation of the outcomes for the previously reported composite of hydroxyapatite and reduced graphene oxide (274). This causes a sharp decrease in the concentration of Ca^{2+} and PO_4^{4-} ions.

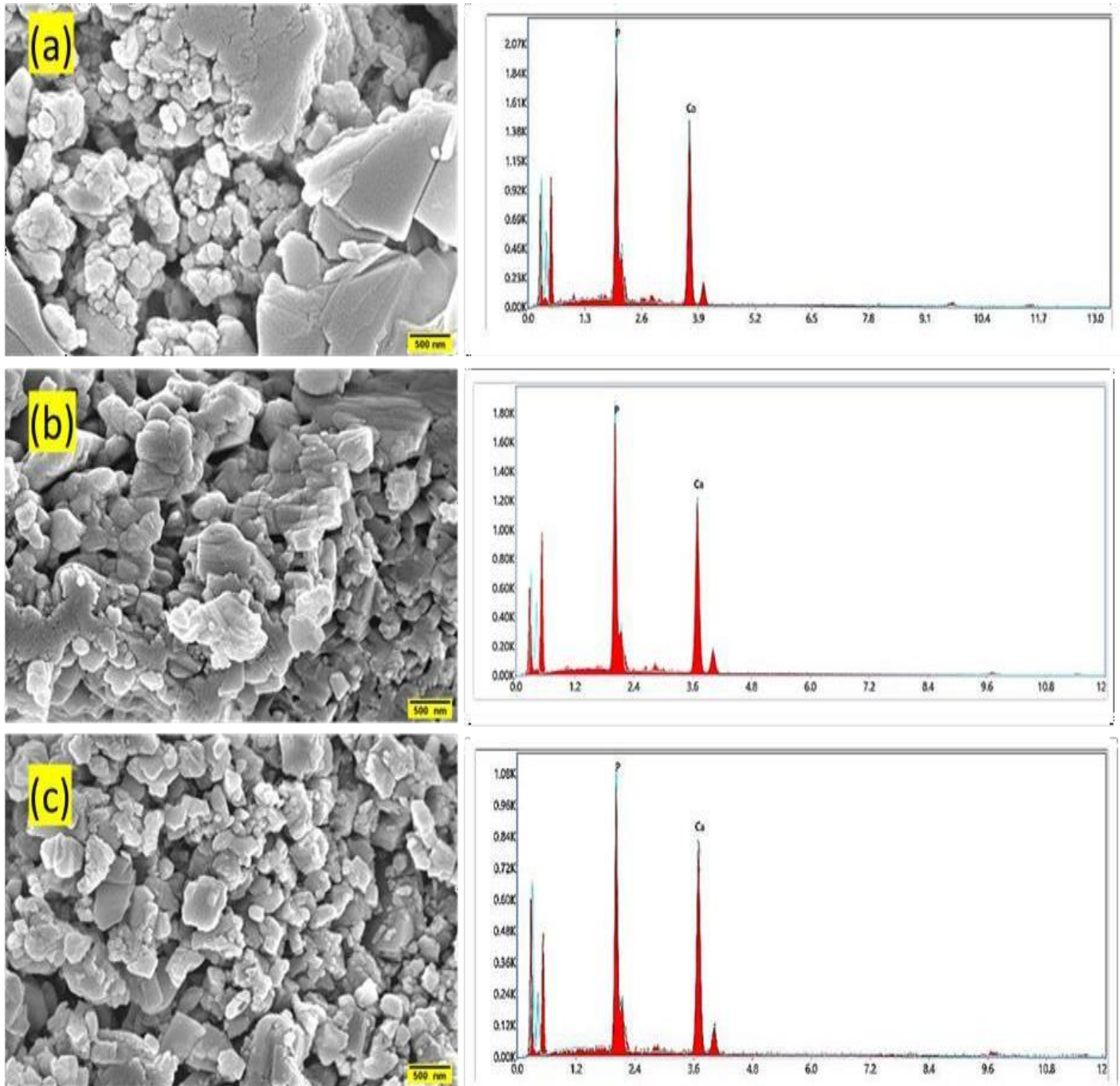


Figure 4.35: Apatite layer formed on 1st week, 3rd week and 4th week for blend B2 (60 cHA :20 rGO :20 CMC) (a-c) respectively.

4.17 Cytotoxicity Assay

NIH3T3 fibroblast cells were used to analyze the composites over the course of three days. The MTT test was used to determine the cell viability of the blends B1, B2, and B3

heated to 150°C. Murine fibroblast cells were grown in DMEM medium, and sample extracts were added to 96-well plates. The cells were then incubated for 24 and 72 hours. The experiment has also been run with samples at two different concentrations, 50 mg/ml and 25 mg/ml. It has been found that the relative cell viability of the composites increased when the period of incubation increased.

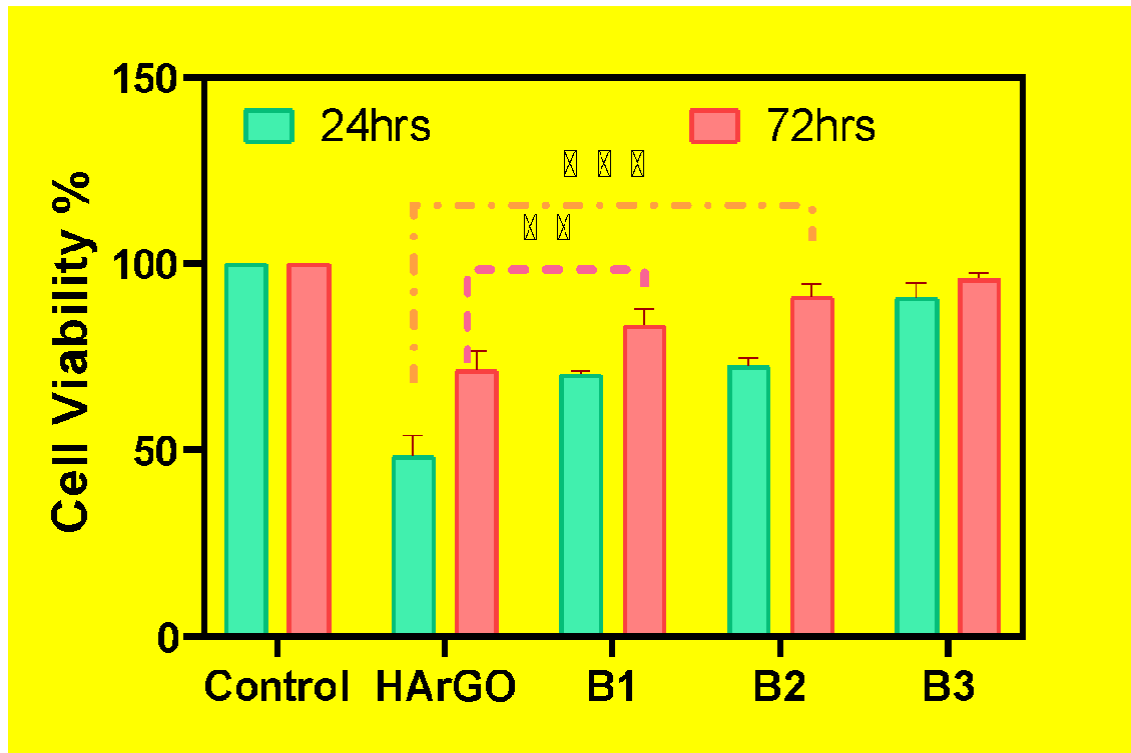


Figure 4.36: Cell Viability study using MTT assay of blends calcined Hydroxyapatite and reduced graphene oxide (60cHA:40rGO), Ceramic-based polymeric blends B1 (60 cHA :30 rGO :10 CMC), B2 (60 cHA :20 rGO :20 CMC) and B3 (60 cHA :10 rGO :30 CMC) cultured for 24hrs and 72hrs (n=4, **p<0.001)

In addition to this, when compared to a blend of hydroxyapatite and reduced graphene oxide (HArGO), the blends exhibit increased cell viability as the concentration of carboxymethyl cellulose is elevated. The biocompatibility of hydroxyapatite and carboxymethyl cellulose composite has been reported to enhance with higher carboxymethyl cellulose concentrations (274). Furthermore, figure 4.36 shows the significant difference between the ternary composites and the control was seen after analysis using the two-way ANOVA and the Tukey test. The decreasing concentration of reduced graphene oxide together with the duration of incubation

have both been found to have a substantial impact. The cell survival of various Hydroxyapatite-based polymeric blends at various concentrations for 72 hours is also shown in Figure 4.37.

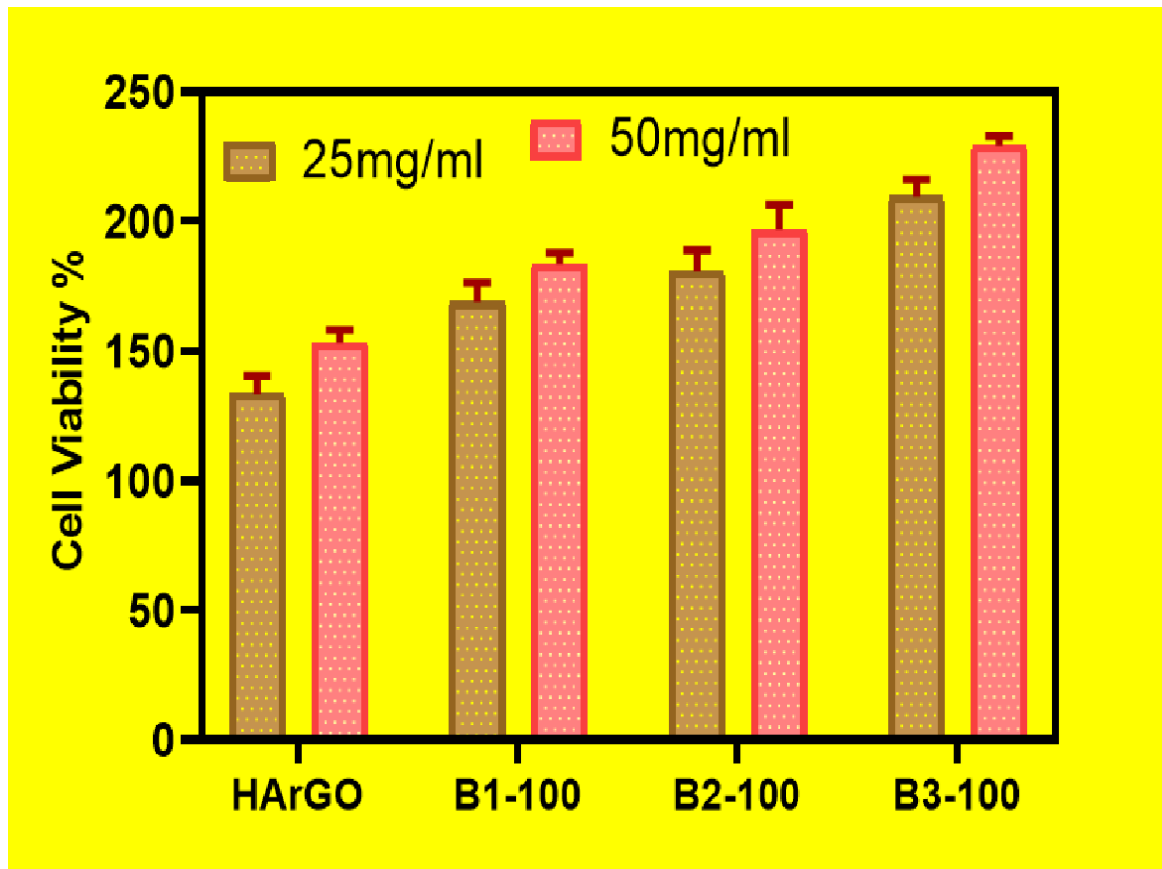


Figure 4.37: Cell viability of calcined Hydroxyapatite and reduced graphene oxide blend HArGO (60cHA:40rGO), ceramic-based polymeric blends B1 (60 cHA :30 rGO :10 CMC), B2 (60 cHA :20 rGO :20 CMC) and B3 (60 cHA :10 rGO :30 CMC) thermally-pressed at 100°C different concentrations of 25mg/ml and 50mg/ml

By doubling the concentration of the sample extracts, it can be seen from the data in Figure 4.37 that the ability of the cells to proliferate was improved. Similarly, an increase in cell survival has been noted when carboxymethyl cellulose (CMC) increased as reported earlier by Chakraborty and co-workers (256).

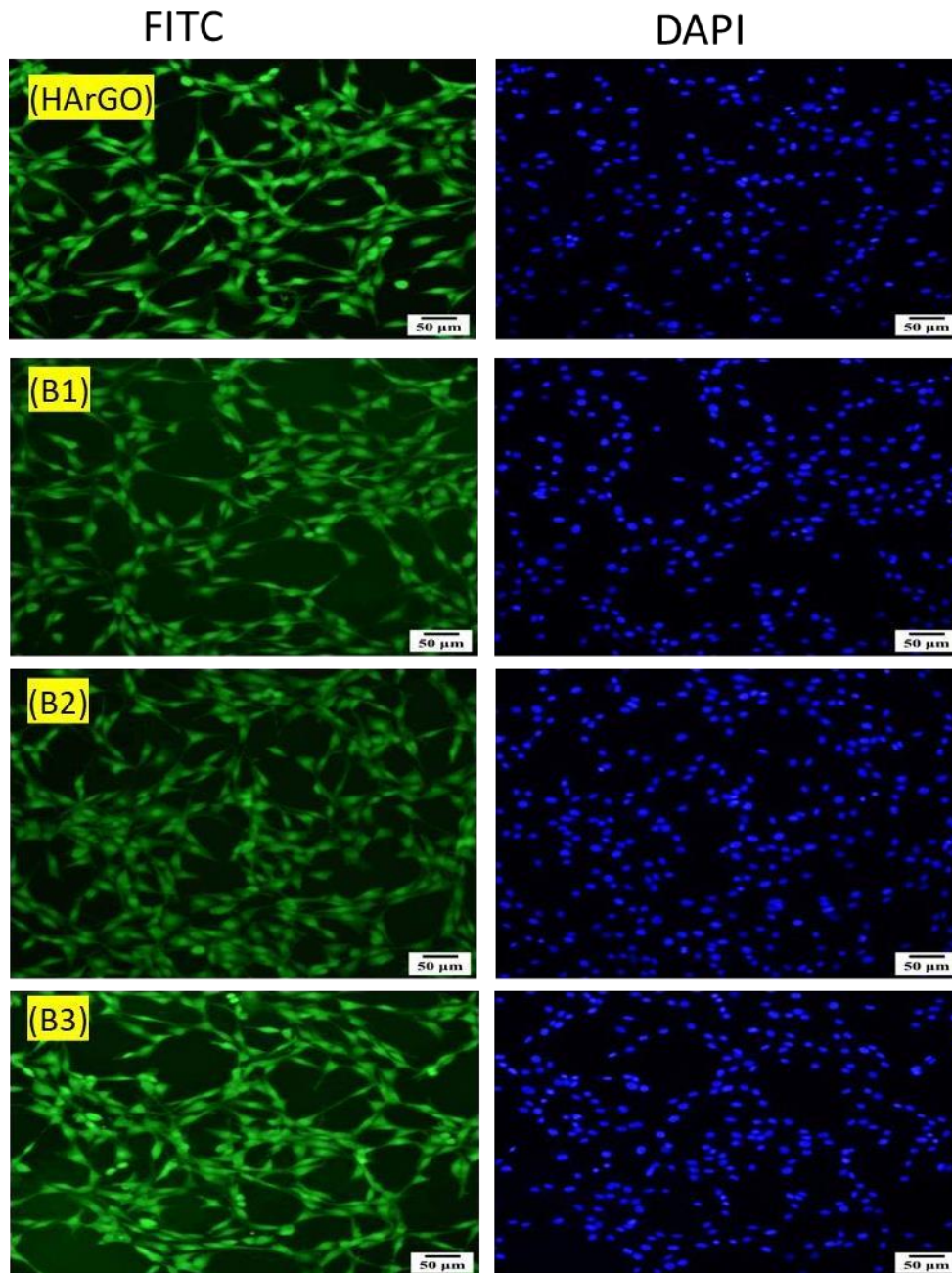


Figure 4.38: FITC and DAPI stained blends calcined Hydroxyapatite and reduced graphene oxide cHArGO (60cHA:40rGO), ternary blends B1 (60 cHA :30 rGO :10 CMC), B2 (60 cHA :20 rGO :20 CMC) and B3 (60 cHA :10 rGO :30 CMC).

Through staining, figure 4.38 illustrates the manner in which cell attachment occurs in the cytoskeleton and nucleus. Fluorescein isothiocyanate (FITC) and 4,6-diamidino-2-phenylindole (DAPI) staining have been used to visualize the cytoskeleton and nucleus of the murine fibroblast

cells (NIH3T3) that adhere and multiply to the various blends in the 96-well plate. The figure above displayed stained images of the cell proliferation using the MTT assay blends. Figure shows that cell adhesion and proliferation improved as carboxymethyl cellulose concentration was raised which is in good tuning with the reported data (225,302).

4.18 In vitro Biodegradation

The biodegradation of blends has been analyzed through soaking in SBF maintained at pH 7 and at 37°C. It has been observed that due to presence of reduced graphene oxide which is not biodegradable, the blend of hydroxyapatite and reduced graphene oxide show low biodegradability (256). On further analyzing the biodegradability of the ceramic-based polymer composites both dried initial and final weight has been determined. The biodegradability of the composites found to be one of the vital necessities for the appropriate biomaterial that can be used as promising candidate for therapeutic use (303).

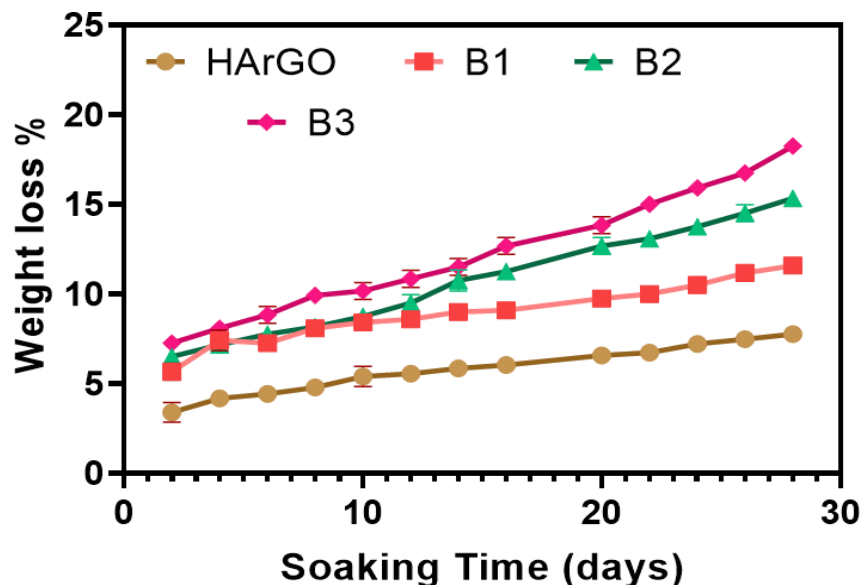


Figure 4.39 Biodegradation % weight loss with respect to time for the blends of calcined Hydroxyapatite and reduced graphene oxide (60cHA:40rGO), ternary blends B1 (60 cHA :30 rGO :10 CMC), B2 (60 cHA :20 rGO :20 CMC) and B3 (60 cHA :10 rGO :30 CMC)

The figure 4.39 showed the weight loss % of the ceramic-polymer composites with respect to the number of days for which the composites have been soaked in the SBF solution. On comparison among the ceramic based polymeric variants, it has been observed that the weight loss ameliorated with increasing the concentration of CMC from composites B1 to B3 which is in good compliance with the reported data of hydroxyapatite, Chitosan and CMC showing degradability due to biodegradable polymer (304). The weight loss % for B1 found to be increased from 5.33% to 11.8 % on 28th day. Similarly for others, the weight loss% found to be 6.66 % to 15.16% and 7.5% to 18.5 % for Composite B2 and B3 respectively.

Chapter 5

SUMMARY AND CONCLUSION

SUMMARY

In recent years, tissue engineering has been looked upon as a possible alternative to traditional therapeutic methods for treating patients with tissue-related disorders. The key feature of this novel technology is the production of tissue engineered composites from blending of biomaterials with a set of desirable qualities that can imitate the extracellular matrix. Hydroxyapatite has been recognized as a promising biomaterial for usage as a matrix material in this context. Keeping this in mind, the current study aims to create hydroxyapatite-based composite with improved mechanical, and biological properties by blending it with another polymer. The results of this research project are summarized below.

Part 1

Initially, the hydroxyapatite was prepared using the chemical precipitation technique. It was then effectively calcined at 800°C, increasing its crystallinity to 73.09±1.5%. In addition, thermal reduction of the graphene oxide was performed for two hours at 200°C to obtain the reduced graphene oxide. The final products obtained following the aforementioned procedures have been validated using FTIR and XRD analysis. Additionally, a binary composite comprising reduced graphene oxide and calcined hydroxyapatite in the following ratios: HrG1 (90:10), HrG2 (80:20), HrG3 (70:30), HrG4 (60:40), and HrG5 (50:50) has been created and morphologically examined. Additionally, ImageJ was used to examine the particle size research, and it showed that when the concentration of reduced graphene oxide increased, the particle size appeared to be decreasing. On the other hand, the SEM visuals also demonstrated a decrease in mean roughness with increasing reduced graphene oxide concentration i.e. from HrG1 to HrG5, which could potentially improve the cell adhesion. In short in this part, the Blend HrG4, or as 60cHA: 40rGO, exhibited the highest degree of crystallinity with the particle size of 12.98 μm.

Part 2:

This section of the study has looked at the mechanical properties of the composite made of calcined hydroxyapatite and reduced graphene oxide. A comparison study has been carried out comparing hydroxyapatite and its composites reinforced by reduced graphene oxide. After a 2-hour heat treatment at 200°C, the composites with different ratios of calcined hydroxyapatite and reduced

graphene oxide (HrG1 to HrG5) were evaluated for mechanical strength using a universal testing machine (UTM). A mechanical strength enhancement was seen when the heat-treated composites (HrG1 to HrG5) were compared to those that were not heat-treated. The maximum compressive strength of the blend HrG4 is around 185.16 ± 4.87 MPa. Strength rises in direct proportion to the measured crystallinity levels. Moreover, the heat treatment fortifies the connections among the constituents, leading to a notable rise in the mechanical strength of the binary composite in contrast to their untreated counterparts.

Part 3:

In this part, polymer addition has been carried out to enhance the properties of the binary composite of calcined hydroxyapatite and reduced graphene oxide. The binary composite showing maximum compressive strength has been further reinforced with carboxymethyl cellulose in different ratios as B1 (60cHA:30rGo:10CMC), B2 (60cHA:20rGo:20CMC), B3(60 cHA :10rGo:30CMC) yielding ternary composite and has been fabricated using heat treatment under pressure for 5 10, and 20 minutes at 100°C and 150°C . It has been observed that polymers excel the biocompatibility when examined through MTT assay. In addition, XRD and FTIR analysis of the ternary blend has been performed to validate the successful production of a ceramic based ternary composite. Additionally, the compressive strength of the ternary composite has been assessed utilizing the Universal Testing Machine (UTM) and microhardness and young's modulus through Vicker's hardness analysis.

In addition, the ternary composites were optimized with the orthogonal L18 model by applying the Grey Taguchi method. It has been established through statistical analysis utilizing ANOVA and grade analysis using Grey relational grade. However, regression analysis and desirability have also been accomplished, and optimum regression equations have been obtained. Both the polymer concentration and the processing parameters has been taken as the input parameters for optimization. The ideal parameters for thermal-pressing at 30% polymer concentration was determined to be 150°C for 20 minutes. In addition, using a FESEM, the morphology of the ternary composite has been studied. Also, the surface roughness was determined after the FESEM pictures were analysed using Image J. Furthermore, while determining the water contact angle, the wettability of the composites appears to be improving. The ternary composite B2 was found to possess the maximum compressive strength, measuring 320.16 ± 6.1 MPa, after being thermally-pressed for 20 minutes at

150°C. Based on Vicker's microhardness analysis, Blend B2 i.e. (60cHA: 20rGO: 20CMC) has an outstanding Young's modulus of 4.87 ± 5.04 GPa and a microhardness of 216.221 ± 90 MPa.

Part 4:

This section of the research has examined biological studies concerning biomineralization, biodegradability, and biocompatibility. FESEM study demonstrated the occurrence of biomineralization. The EDX spectra have confirmed the presence of an apatite layer resembling bone in the FESEM visuals. The composite variations were submerged in Simulated Body Fluid (SBF) for around 28 days in order to investigate biomineralization. Successful apatite layer deposition is indicated by the Ca/P ratio increasing in the second week and decreasing in the fourth week. Using the MTT assay, the cytocompatibility of the NIH3T3 cell lines has also been evaluated. During three days, two different composite concentrations of MTT were used in the experiment. Analysis showed that the cytocompatibility increased in proportion to the rise in carboxymethyl cellulose concentration from blend B1 to blend B3 in ternary composite.

CONCLUSION

In this thesis overall research suggests a potential Hydroxyapatite-based composite (HA-rGO/CMC). The composite is made of hydroxyapatite that has been reinforced with reduced graphene oxide and subsequently with carboxymethyl cellulose that has fabricated using thermal pressing. The composite (HA-rGO/CMC) with exceptional surface properties (hydrophilicity), biological properties (cell adhesion and proliferation), and extraordinary compressive strength required for tissue engineering. As a result, it comes to light that the novel ternary HA-rGO/CMC composite has the potential biomaterial to be employed for tissue engineering applications. The study focused on enhancing the properties of hydroxyapatite by incorporating reduced graphene oxide and carboxymethyl cellulose. Calcination of hydroxyapatite at 800°C and thermal reduction of graphene oxide were performed, followed by blending and morphological characterization. The composite containing 40% reduced graphene oxide (HrG4) showed the highest crystallinity and improved surface roughness and particle size. Mechanical strength tests revealed that heat-treated samples demonstrated significant improvements, with HrG4 showing the maximum compressive strength of 185.16 MPa. The inclusion of carboxymethyl cellulose further enhanced mechanical, thermal, and biological properties, with Blend B2 showing the highest strength and hardness. The

optimized processing conditions were identified through the Grey-Taguchi method. Biomineralization, cytocompatibility, and biodegradability were successfully demonstrated, indicating that the HA-rGO/CMC composite is a potential candidate for tissue engineering applications.

5.1 Future Perspective

Looking ahead in this tech-driven world, advancements in fabrication techniques within biomaterials offer immense potential for the development of superior composites. As society faces evolving challenges, biomaterials have grown into a distinct field, particularly during the era of rapid globalization. The following points outline key areas for future exploration:

1. Implementing advanced manufacturing processes for the cost-efficient synthesis of composites.
2. Using animal models like rats and rabbits for further in vivo testing.
3. Utilizing advanced fabrication techniques and alternative sintering mechanisms to enhance the mechanical and physicochemical properties of composites, expanding their applications in bone regeneration and other biomedical fields.

BIBLIOGRAPHY

1. Xue N, Ding X, Huang R, Jiang R, Huang H, Pan X, et al. Bone Tissue Engineering in the Treatment of Bone Defects. *Pharmaceuticals*. 2022 Jul 17;15(7):879.
2. Chandramohan. PROGRESS OF BIOMATERIALS IN THE FIELD OF ORTHOPAEDICS. *American Journal of Applied Sciences*. 2014 Apr 1;11(4):623–30.
3. Reith G, Schmitz-Greven V, Hensel KO, Schneider MM, Tinschmann T, Bouillon B, et al. Metal implant removal: benefits and drawbacks – a patient survey. *BMC Surg*. 2015 Dec;15(1):96.
4. Elbadawi M, Meredith J, Hopkins L, Reaney I. Progress in Bioactive Metal and, Ceramic Implants for Load- Bearing Application. In: Zorzi AR, De Miranda JB, editors. *Advanced Techniques in Bone Regeneration* [Internet]. InTech; 2016 [cited 2023 Dec 23]. Available from: <http://www.intechopen.com/books/advanced-techniques-in-bone-regeneration/progress-in-bioactive-metal-and-ceramic-implants-for-load-bearing-application>
5. Davis R, Singh A, Jackson MJ, Coelho RT, Prakash D, Charalambous CP, et al. A comprehensive review on metallic implant biomaterials and their subtractive manufacturing. *Int J Adv Manuf Technol*. 2022 May;120(3–4):1473–530.
6. Kaygili O, Keser S, Ates T, Tatar C, Yakuphanoglu F. Controlling of dielectric parameters of insulating hydroxyapatite by simulated body fluid. *Materials Science and Engineering: C*. 2015 Jan;46:118–24.
7. Kaygili O, Keser S, Kom M, Bulut N, Dorozhkin SV. The effect of simulating body fluid on the structural properties of hydroxyapatite synthesized in the presence of citric acid. *Prog Biomater*. 2016 Dec;5(3–4):173–82.
8. Kebiroglu MH, Orek C, Bulut N, Kaygili O, Keser S, Ates T. Temperature dependent structural and vibrational properties of hydroxyapatite: A theoretical and experimental study. *Ceramics International*. 2017 Dec;43(17):15899–904.
9. Kaygili O, Tatar C. The investigation of some physical properties and microstructure of Zn-doped hydroxyapatite bioceramics prepared by sol–gel method. *J Sol-Gel Sci Technol*. 2012 Feb;61(2):296–309.
10. Ma G. Three common preparation methods of hydroxyapatite. *IOP Conf Ser: Mater Sci Eng*. 2019 Nov 1;688(3):033057.
11. Hama C, Umeda T, Musha Y, Koda S, Itatani K. Preparation of novel hemostatic material containing spherical porous hydroxyapatite/alginate granules. *J Ceram Soc Japan*. 2010;118(1378):446–50.
12. Song L, Sun L, Jiang N, Gan Z. Structural control and hemostatic properties of porous microspheres fabricated by hydroxyapatite- graft -poly(D,L-lactide) nanocomposites. *Composites Science and Technology*. 2016 Oct;134:234–41.

13. Yang Y, Zhou H, Ni X, Yang M, Hou S, Bi Y, et al. Hydroxyapatite: a promising hemostatic component in orthopaedic applications. *Biol Eng Med* [Internet]. 2017 [cited 2023 Dec 19];2(1). Available from: <http://oatext.com/Hydroxyapatite-a-promising-hemostatic-component-in-orthopaedic-applications.php>
14. Afshar A, Ghorbani M, Ehsani N, Saeri MR, Sorrell CC. Some important factors in the wet precipitation process of hydroxyapatite. *Materials & Design*. 2003 May;24(3):197–202.
15. Gerhardt LC, Boccaccini AR. Bioactive Glass and Glass-Ceramic Scaffolds for Bone Tissue Engineering. *Materials*. 2010 Jul 6;3(7):3867–910.
16. Feng P, Wei P, Shuai C, Peng S. Characterization of Mechanical and Biological Properties of 3-D Scaffolds Reinforced with Zinc Oxide for Bone Tissue Engineering. Soncini M, editor. *PLoS ONE*. 2014 Jan 31;9(1):e87755.
17. Ampaiwong J, Rattanawaleedirojn P, Saengkiattiyut K, Rodthongkum N, Potiyaraj P, Soatthiyanon N. Reduced Graphene Oxide/Carboxymethyl Cellulose Nanocomposites: Novel Conductive Films. *J nanosci nanotechnol*. 2019 Jun 1;19(6):3544–50.
18. Jabbari F, Hesarakı S, Houshmand B. The physical, mechanical, and biological properties of silk fibroin/chitosan/reduced graphene oxide composite membranes for guided bone regeneration. *Journal of Biomaterials Science, Polymer Edition*. 2019 Dec 12;30(18):1779–802.
19. Bahrami S, Baheiraei N, Shahrezaee M. Biomimetic reduced graphene oxide coated collagen scaffold for in situ bone regeneration. *Sci Rep*. 2021 Dec;11(1):16783.
20. Tavares KM, Campos AD, Luchesi BR, Resende AA, Oliveira JED, Marconcini JM. Effect of carboxymethyl cellulose concentration on mechanical and water vapor barrier properties of corn starch films. *Carbohydrate Polymers*. 2020 Oct;246:116521.
21. Kukrety A, Singh RK, Singh P, Ray SS. Comprehension on the Synthesis of Carboxymethylcellulose (CMC) Utilizing Various Cellulose Rich Waste Biomass Resources. *Waste Biomass Valor*. 2018 Sep;9(9):1587–95.
22. Jiao Z, Zhang B, Li C, Kuang W, Zhang J, Xiong Y, et al. Carboxymethyl cellulose-grafted graphene oxide for efficient antitumor drug delivery. *Nanotechnology Reviews*. 2018 Aug 28;7(4):291–301.
23. Karzar Jeddi M, Mahkam M. Magnetic nano carboxymethyl cellulose-alginate/chitosan hydrogel beads as biodegradable devices for controlled drug delivery. *International Journal of Biological Macromolecules*. 2019 Aug;135:829–38.
24. Verma N, Pramanik K, Singh AK, Biswas A. Design of magnesium oxide nanoparticle incorporated carboxy methyl cellulose/poly vinyl alcohol composite film with novel composition for skin tissue engineering. *Materials Technology*. 2022 Jul 3;37(8):706–16.
25. Matinfar M, Mesgar AS, Mohammadi Z. Evaluation of physicochemical, mechanical and biological properties of chitosan/carboxymethyl cellulose reinforced with multiphasic calcium phosphate whisker-like fibers for bone tissue engineering. *Materials Science and Engineering: C*.

2019 Jul;100:341–53.

26. Sharmila G, Muthukumaran C, Kirthika S, Keerthana S, Kumar NM, Jeyanthi J. Fabrication and characterization of *Spinacia oleracea* extract incorporated alginate/carboxymethyl cellulose microporous scaffold for bone tissue engineering. *International Journal of Biological Macromolecules*. 2020 Aug;156:430–7.

27. Ali NH, Amin MCIM, Ng SF. Sodium carboxymethyl cellulose hydrogels containing reduced graphene oxide (rGO) as a functional antibiofilm wound dressing. *Journal of Biomaterials Science, Polymer Edition*. 2019 May 24;30(8):629–45.

28. Capanema NSV, Mansur AAP, de Jesus AC, Carvalho SM, de Oliveira LC, Mansur HS. Superabsorbent crosslinked carboxymethyl cellulose-PEG hydrogels for potential wound dressing applications. *International Journal of Biological Macromolecules*. 2018 Jan;106:1218–34.

29. Saber-Samandari S, Saber-Samandari S, Heydaripour S, Abdouss M. Novel carboxymethyl cellulose based nanocomposite membrane: Synthesis, characterization and application in water treatment. *Journal of Environmental Management*. 2016 Jan;166:457–65.

30. An J, Chua CK, Mironov V. Application of Machine Learning in 3D Bioprinting: Focus on Development of Big Data and Digital Twin. *Int J Bioprint*. 2021 Jan 29;7(1):342.

31. Obele CM, Ibenta ME, Chukwunke JL, Nwanonyi SC. Carboxymethyl cellulose and cellulose nanocrystals from cassava stem as thickeners in reactive printing of cotton. *Cellulose*. 2021 Mar;28(4):2615–33.

32. Riaz A, Lagnika C, Luo H, Nie M, Dai Z, Liu C, et al. Effect of Chinese chives (*Allium tuberosum*) addition to carboxymethyl cellulose based food packaging films. *Carbohydrate Polymers*. 2020 May;235:115944.

33. Basu P, Narendrakumar U, Arunachalam R, Devi S, Manjubala I. Characterization and Evaluation of Carboxymethyl Cellulose-Based Films for Healing of Full-Thickness Wounds in Normal and Diabetic Rats. *ACS Omega*. 2018 Oct 31;3(10):12622–32.

34. Saxena V, Hasan A, Pandey LM. Antibacterial nano-biocomposite scaffolds of Chitosan, Carboxymethyl Cellulose and Zn & Fe integrated Hydroxyapatite (Chitosan-CMC-FZO@HAp) for bone tissue engineering. *Cellulose*. 2021 Sep;28(14):9207–26.

35. Hasirci V, Hasirci N. *Fundamentals of Biomaterials* [Internet]. New York, NY: Springer New York; 2018 [cited 2023 Dec 20]. Available from: <http://link.springer.com/10.1007/978-1-4939-8856-3>

36. Rathore A, Cleary M, Naito Y, Rocco K, Breuer C. Development of tissue engineered vascular grafts and application of nanomedicine. *WIREs Nanomed Nanobiotechnol*. 2012 May;4(3):257–72.

37. Pramanik S, Agarwal AK, Rai KN. *Chronology of Total Hip Joint Replacement and Materials Development*.

38. Sudhakar KV, Wang J. Fatigue Behavior of Vitallium-2000 Plus Alloy for Orthopedic Applications. *J of Materi Eng and Perform*. 2011 Aug;20(6):1023–7.
39. Todros S, Todesco M, Bagno A. Biomaterials and Their Biomedical Applications: From Replacement to Regeneration. *Processes*. 2021 Oct 29;9(11):1949.
40. Basara G, Saeidi-Javash M, Ren X, Bahcecioglu G, Wyatt BC, Anasori B, et al. Electrically conductive 3D printed Ti3C2T MXene-PEG composite constructs for cardiac tissue engineering. *Acta Biomaterialia*. 2020 Dec;S1742706120307479.
41. Lodhi MJK, Deen KM, Greenlee-Wacker MC, Haider W. Additively manufactured 316L stainless steel with improved corrosion resistance and biological response for biomedical applications. *Additive Manufacturing*. 2019 May;27:8–19.
42. Bai, Gong, Chen, Sun, Zhang, Cai, et al. Additive Manufacturing of Customized Metallic Orthopedic Implants: Materials, Structures, and Surface Modifications. *Metals*. 2019 Sep 12;9(9):1004.
43. Spezi E, Palleri F, Angelini AL, Ferri A, Baruffaldi F. Characterization of materials for prosthetic implants using the BEAMnrc Monte Carlo code. *J Phys: Conf Ser*. 2007 Jun 1;74:021016.
44. Chen Q, Thouas GA. Metallic implant biomaterials. *Materials Science and Engineering: R: Reports*. 2015 Jan;87:1–57.
45. Findik F. Recent developments of metallic implants for biomedical applications. 2020;8(1).
46. Toghyani S, Khodaei M, Razavi M. Magnesium scaffolds with two novel biomimetic designs and MgF2 coating for bone tissue engineering. *Surface and Coatings Technology*. 2020 Aug;395:125929.
47. Cockerill I, Su Y, Sinha S, Qin YX, Zheng Y, Young ML, et al. Porous zinc scaffolds for bone tissue engineering applications: A novel additive manufacturing and casting approach. *Materials Science and Engineering: C*. 2020 May;110:110738.
48. Bhaskar A, Assadi M, Nikpey Somehsaraei H. Decarbonization of the Iron and Steel Industry with Direct Reduction of Iron Ore with Green Hydrogen. *Energies*. 2020 Feb 9;13(3):758.
49. Kern F, Bernstein A, Killinger A. Design of ceramic materials for orthopedic devices. In: *Advances in Ceramic Biomaterials* [Internet]. Elsevier; 2017 [cited 2023 Dec 23]. p. 331–53. Available from: <https://linkinghub.elsevier.com/retrieve/pii/B9780081008812000117>
50. Heimann RB. Structure, properties, and biomedical performance of osteoconductive bioceramic coatings. *Surface and Coatings Technology*. 2013 Oct;233:27–38.
51. Ibrahim MZ, Sarhan AAD, Yusuf F, Hamdi M. Biomedical materials and techniques to improve the tribological, mechanical and biomedical properties of orthopedic implants – A review article. *Journal of Alloys and Compounds*. 2017 Aug;714:636–67.
52. Hernigou P, Roubineau F, Bouthors C, Flouzat-Lachaniette CH. What every surgeon should know about Ceramic-on-Ceramic bearings in young patients. *EFORT Open Reviews*. 2016

Apr;1(4):107–11.

53. Goswami C, Bhat IK, Patnaik A, Singh T, Fekete G. Fabrication of Ceramic Hip Implant Composites: Influence of Silicon Nitride on Physical, Mechanical and Wear Properties. *Silicon*. 2020 May;12(5):1237–45.

54. Rahmati B, Sarhan AhmedAD, Zalnezhad E, Kamiab Z, Dabbagh A, Choudhury D, et al. Development of tantalum oxide (Ta-O) thin film coating on biomedical Ti-6Al-4V alloy to enhance mechanical properties and biocompatibility. *Ceramics International*. 2016 Jan;42(1):466–80.

55. Zhou H, Lee J. Nanoscale hydroxyapatite particles for bone tissue engineering. *Acta Biomaterialia*. 2011 Jul;7(7):2769–81.

56. Rahaman MN, Day DE, Sonny Bal B, Fu Q, Jung SB, Bonewald LF, et al. Bioactive glass in tissue engineering. *Acta Biomaterialia*. 2011 Jun;7(6):2355–73.

57. Eliaz N, Metoki N. Calcium Phosphate Bioceramics: A Review of Their History, Structure, Properties, Coating Technologies and Biomedical Applications. *Materials*. 2017 Mar 24;10(4):334.

58. Gul H, Zahid S, Zahid S, Kaleem M, Khan AS, Shah AT. Sol-gel derived fluoride-doped bioactive glass powders: Structural and long-term fluoride release/pH analysis. *Journal of Non-Crystalline Solids*. 2018 Oct;498:216–22.

59. Shekhawat D, Singh A, Banerjee MK, Singh T, Patnaik A. Bioceramic composites for orthopaedic applications: A comprehensive review of mechanical, biological, and microstructural properties. *Ceramics International*. 2021 Feb;47(3):3013–30.

60. Jurak M, Wiącek AE, Ładniak A, Przykaza K, Szafran K. What affects the biocompatibility of polymers? *Advances in Colloid and Interface Science*. 2021 Aug;294:102451.

61. Bharadwaz A, Jayasuriya AC. Recent trends in the application of widely used natural and synthetic polymer nanocomposites in bone tissue regeneration. *Materials Science and Engineering: C*. 2020 May;110:110698.

62. Ryan EJ, Ryan AJ, González-Vázquez A, Philippart A, Ciraldo FE, Hobbs C, et al. Collagen scaffolds functionalised with copper-eluting bioactive glass reduce infection and enhance osteogenesis and angiogenesis both in vitro and in vivo. *Biomaterials*. 2019 Mar;197:405–16.

63. Wang X, Molino BZ, Pitkänen S, Ojansivu M, Xu C, Hannula M, et al. 3D Scaffolds of Polycaprolactone/Copper-Doped Bioactive Glass: Architecture Engineering with Additive Manufacturing and Cellular Assessments in a Coculture of Bone Marrow Stem Cells and Endothelial Cells. *ACS Biomater Sci Eng*. 2019 Sep 9;5(9):4496–510.

64. Dou DD, Zhou G, Liu HW, Zhang J, Liu ML, Xiao XF, et al. Sequential releasing of VEGF and BMP-2 in hydroxyapatite collagen scaffolds for bone tissue engineering: Design and characterization. *International Journal of Biological Macromolecules*. 2019 Feb;123:622–8.

65. Hasanzadeh E, Ebrahimi-Barough S, Mirzaei E, Azami M, Tavangar SM, Mahmoodi N, et al. Preparation of fibrin gel scaffolds containing MWCNT/PU nanofibers for neural tissue

engineering. *J Biomedical Materials Res.* 2019 Apr;107(4):802–14.

66. Pezzoli D, Di Paolo J, Kumra H, Fois G, Candiani G, Reinhardt DP, et al. Fibronectin promotes elastin deposition, elasticity and mechanical strength in cellularised collagen-based scaffolds. *Biomaterials.* 2018 Oct;180:130–42.

67. Giannelli M, Barbalinardo M, Riminucci A, Belvedere K, Boccalon E, Sotgiu G, et al. Magnetic keratin/hydroxylapatite sponges as potential scaffolds for tissue regeneration. *Applied Clay Science.* 2021 Jun;207:106090.

68. Kolathupalayam Shanmugam B, Rangaraj S, Subramani K, Srinivasan S, Aicher WK, Venkatachalam R. Biomimetic TiO₂-chitosan/sodium alginate blended nanocomposite scaffolds for tissue engineering applications. *Materials Science and Engineering: C.* 2020 May;110:110710.

69. Narayanan KB, Zo SM, Han SS. Novel biomimetic chitin-glucan polysaccharide nano/microfibrous fungal-scaffolds for tissue engineering applications. *International Journal of Biological Macromolecules.* 2020 Apr;149:724–31.

70. Russo L, Cipolla L. Glycomics: New Challenges and Opportunities in Regenerative Medicine. *Chemistry A European J.* 2016 Sep 12;22(38):13380–8.

71. Mi HY, Jing X, Turng LS. Fabrication of porous synthetic polymer scaffolds for tissue engineering. *Journal of Cellular Plastics.* 2015 Mar;51(2):165–96.

72. Maitz MF. Applications of synthetic polymers in clinical medicine. *Biosurface and Biotribology.* 2015 Sep;1(3):161–76.

73. Mironov AV, Grigoryev AM, Krotova LI, Skaletsky NN, Popov VK, Sevastianov VI. 3D printing of PLGA scaffolds for tissue engineering. *J Biomedical Materials Res.* 2017 Jan;105(1):104–9.

74. Khosravi A, Ghasemi-Mobarakeh L, Mollahosseini H, Ajallouei F, Masoudi Rad M, Norouzi M, et al. Immobilization of silk fibroin on the surface of PCL nanofibrous scaffolds for tissue engineering applications. *J of Applied Polymer Sci.* 2018 Oct 5;135(37):46684.

75. Grémare A, Guduric V, Bareille R, Heroguez V, Latour S, L'heureux N, et al. Characterization of printed PLA scaffolds for bone tissue engineering. *J Biomedical Materials Res.* 2018 Apr;106(4):887–94.

76. Chen P, Xie F, Tang F, McNally T. Structure and properties of thermomechanically processed chitosan/carboxymethyl cellulose/graphene oxide polyelectrolyte complexed bionanocomposites. *International Journal of Biological Macromolecules.* 2020 Sep;158:420–9.

77. Gao G, Kim BS, Jang J, Cho DW. Recent Strategies in Extrusion-Based Three-Dimensional Cell Printing toward Organ Biofabrication. *ACS Biomater Sci Eng.* 2019 Mar 11;5(3):1150–69.

78. Yan R, Chen Y, Gu Y, Tang C, Huang J, Hu Y, et al. A collagen-coated sponge silk scaffold for functional meniscus regeneration. *J Tissue Eng Regen Med.* 2019 Feb;13(2):156–73.

79. Wu L, Shrestha P, Iapichino M, Cai Y, Kim B, Stoeber B. Characterization method for

calculating diffusion coefficient of drug from polylactic acid (PLA) microneedles into the skin. *Journal of Drug Delivery Science and Technology*. 2021 Feb;61:102192.

80. Wang Y, Lei M, Wei Q, Wang Y, Zhang J, Guo Y, et al. 3D printing biocompatible l-Arg/GNPs/PLA nanocomposites with enhanced mechanical property and thermal stability. *J Mater Sci*. 2020 Apr;55(12):5064–78.
81. Bailly N, Thomas M, Klumperman B. Poly(*N*-vinylpyrrolidone)- *block* -poly(vinyl acetate) as a Drug Delivery Vehicle for Hydrophobic Drugs. *Biomacromolecules*. 2012 Dec 10;13(12):4109–17.
82. Ghafari R, Jonoobi M, Amirabad LM, Oksman K, Taheri AR. Fabrication and characterization of novel bilayer scaffold from nanocellulose based aerogel for skin tissue engineering applications. *International Journal of Biological Macromolecules*. 2019 Sep;136:796–803.
83. Pollot BE, Rathbone CR, Wenke JC, Guda T. Natural polymeric hydrogel evaluation for skeletal muscle tissue engineering. *J Biomed Mater Res*. 2018 Feb;106(2):672–9.
84. Yoshimoto I, Sasaki JI, Tsuboi R, Yamaguchi S, Kitagawa H, Imazato S. Development of layered PLGA membranes for periodontal tissue regeneration. *Dental Materials*. 2018 Mar;34(3):538–50.
85. Ekanem EE, Nabavi SA, Vladislavljević GT, Gu S. Structured Biodegradable Polymeric Microparticles for Drug Delivery Produced Using Flow Focusing Glass Microfluidic Devices. *ACS Appl Mater Interfaces*. 2015 Oct 21;7(41):23132–43.
86. Colobatiu L, Gavan A, Potarniche AV, Rus V, Diaconeasa Z, Mocan A, et al. Evaluation of bioactive compounds-loaded chitosan films as a novel and potential diabetic wound dressing material. *Reactive and Functional Polymers*. 2019 Dec;145:104369.
87. Sukul M, Sahariah P, Lauzon HL, Borges J, Måsson M, Mano JF, et al. In vitro biological response of human osteoblasts in 3D chitosan sponges with controlled degree of deacetylation and molecular weight. *Carbohydrate Polymers*. 2021 Feb;254:117434.
88. Levato R, Webb WR, Otto IA, Mensinga A, Zhang Y, Van Rijen M, et al. The bio in the ink: cartilage regeneration with bioprintable hydrogels and articular cartilage-derived progenitor cells. *Acta Biomaterialia*. 2017 Oct;61:41–53.
89. Mondal S, Nguyen TP, Pham VH, Hoang G, Manivasagan P, Kim MH, et al. Hydroxyapatite nano bioceramics optimized 3D printed poly lactic acid scaffold for bone tissue engineering application. *Ceramics International*. 2020 Feb;46(3):3443–55.
90. Semyari H, Salehi M, Taleghani F, Ehterami A, Bastami F, Jalayer T, et al. Fabrication and characterization of collagen–hydroxyapatite-based composite scaffolds containing doxycycline via freeze-casting method for bone tissue engineering. *J Biomater Appl*. 2018 Oct;33(4):501–13.
91. Koç Demir A, Elçin AE, Elçin YM. Strontium-modified chitosan/montmorillonite composites as bone tissue engineering scaffold. *Materials Science and Engineering: C*. 2018

Aug;89:8–14.

92. Lian H, Zhang L, Meng Z. Biomimetic hydroxyapatite/gelatin composites for bone tissue regeneration: Fabrication, characterization, and osteogenic differentiation in vitro. *Materials & Design*. 2018 Oct;156:381–8.
93. Kim W, Kim G. Collagen/bioceramic-based composite bioink to fabricate a porous 3D hASCs-laden structure for bone tissue regeneration. *Biofabrication*. 2019 Nov 6;12(1):015007.
94. Aghajanian AH, Bigham A, Khodaei M, Hossein Kelishadi S. Porous titanium scaffold coated using forsterite/poly-3-hydroxybutyrate composite for bone tissue engineering. *Surface and Coatings Technology*. 2019 Nov;378:124942.
95. Dziadek M, Kudlackova R, Zima A, Slosarczyk A, Ziabka M, Jelen P, et al. Novel multicomponent organic–inorganic WPI/gelatin/CaP hydrogel composites for bone tissue engineering. *J Biomedical Materials Res*. 2019 Nov;107(11):2479–91.
96. Du X, Wei D, Huang L, Zhu M, Zhang Y, Zhu Y. 3D printing of mesoporous bioactive glass/silk fibroin composite scaffolds for bone tissue engineering. *Materials Science and Engineering: C*. 2019 Oct;103:109731.
97. Kilic Bektas C, Kimiz I, Sendemir A, Hasirci V, Hasirci N. A bilayer scaffold prepared from collagen and carboxymethyl cellulose for skin tissue engineering applications. *Journal of Biomaterials Science, Polymer Edition*. 2018 Sep 22;29(14):1764–84.
98. Jiménez Vázquez J, San Martín Martínez E. Collagen and elastin scaffold by electrospinning for skin tissue engineering applications. *J Mater Res*. 2019 Aug 28;34(16):2819–27.
99. Zarei M, Samimi A, Khorram M, Abdi MM, Golestaneh SI. Fabrication and characterization of conductive polypyrrole/chitosan/collagen electrospun nanofiber scaffold for tissue engineering application. *International Journal of Biological Macromolecules*. 2021 Jan;168:175–86.
100. Zhang X, Jia C, Qiao X, Liu T, Sun K. Silk fibroin microfibers and chitosan modified poly (glycerol sebacate) composite scaffolds for skin tissue engineering. *Polymer Testing*. 2017 Sep;62:88–95.
101. Ahmadi S, Shafiei SS, Sabouni F. Electrospun Nanofibrous Scaffolds of Polycaprolactone/Gelatin Reinforced with Layered Double Hydroxide Nanoclay for Nerve Tissue Engineering Applications. *ACS Omega*. 2022 Aug 16;7(32):28351–60.
102. Sayed MM, Mousa HM, El-Aassar MR, El-Deeb NM, Ghazaly NM, Dewidar MM, et al. Enhancing mechanical and biodegradation properties of polyvinyl alcohol/silk fibroin nanofibers composite patches for Cardiac Tissue Engineering. *Materials Letters*. 2019 Nov;255:126510.
103. Liu Y, Wang S, Zhang R. Composite poly(lactic acid)/chitosan nanofibrous scaffolds for cardiac tissue engineering. *International Journal of Biological Macromolecules*. 2017 Oct;103:1130–7.
104. Ho CMB, Mishra A, Lin PTP, Ng SH, Yeong WY, Kim Y, et al. 3D Printed

Polycaprolactone Carbon Nanotube Composite Scaffolds for Cardiac Tissue Engineering. *Macromolecular Bioscience*. 2017 Apr;17(4):1600250.

105. Guo Y, Ghobeira R, Aliakbarshirazi S, Morent R, De Geyter N. Polylactic Acid/Polyaniline Nanofibers Subjected to Pre- and Post-Electrospinning Plasma Treatments for Refined Scaffold-Based Nerve Tissue Engineering Applications. *Polymers*. 2022 Dec 24;15(1):72.

106. Zhao Y, Liang Y, Ding S, Zhang K, Mao H quan, Yang Y. Application of conductive PPy/SF composite scaffold and electrical stimulation for neural tissue engineering. *Biomaterials*. 2020 Oct;255:120164.

107. Afolalu SA, Soetan SB, Ongbali SO, Abioye AA, Oni AS. Morphological characterization and physio-chemical properties of nanoparticle - review. *IOP Conf Ser: Mater Sci Eng*. 2019 Nov 1;640(1):012065.

108. Bayda S, Adeel M, Tuccinardi T, Cordani M, Rizzolio F. The History of Nanoscience and Nanotechnology: From Chemical–Physical Applications to Nanomedicine. *Molecules*. 2019 Dec 27;25(1):112.

109. Bayford R, Rademacher T, Roitt I, Wang SX. Emerging applications of nanotechnology for diagnosis and therapy of disease: a review. *Physiol Meas*. 2017 Jul 24;38(8):R183–203.

110. Lim S, Park J, Shim MK, Um W, Yoon HY, Ryu JH, et al. Recent advances and challenges of repurposing nanoparticle-based drug delivery systems to enhance cancer immunotherapy. *Theranostics*. 2019;9(25):7906–23.

111. Cardoso VF, Francesko A, Ribeiro C, Bañobre-López M, Martins P, Lanceros-Mendez S. Advances in Magnetic Nanoparticles for Biomedical Applications. *Adv Healthcare Materials*. 2018 Mar;7(5):1700845.

112. Wallyn, Anton, Vandamme. Synthesis, Principles, and Properties of Magnetite Nanoparticles for In Vivo Imaging Applications—A Review. *Pharmaceutics*. 2019 Nov 12;11(11):601.

113. Hasan A, Waibhaw G, Saxena V, Pandey LM. Nano-biocomposite scaffolds of chitosan, carboxymethyl cellulose and silver nanoparticle modified cellulose nanowhiskers for bone tissue engineering applications. *International Journal of Biological Macromolecules*. 2018 May;111:923–34.

114. Fathi-Achachelouei M, Knopf-Marques H, Ribeiro Da Silva CE, Barthès J, Bat E, Tezcaner A, et al. Use of Nanoparticles in Tissue Engineering and Regenerative Medicine. *Front Bioeng Biotechnol*. 2019 May 24;7:113.

115. Wong CY, Al-Salami H, Dass CR. Potential of insulin nanoparticle formulations for oral delivery and diabetes treatment. *Journal of Controlled Release*. 2017 Oct;264:247–75.

116. Yuan S, Zheng Y, Chua CK, Yan Q, Zhou K. Electrical and thermal conductivities of MWCNT/polymer composites fabricated by selective laser sintering. *Composites Part A: Applied Science and Manufacturing*. 2018 Feb;105:203–13.

117. Jin K, Luo Z, Zhang B, Pang Z. Biomimetic nanoparticles for inflammation targeting. *Acta Pharmaceutica Sinica B*. 2018 Jan;8(1):23–33.
118. Pardi N, Hogan MJ, Porter FW, Weissman D. mRNA vaccines — a new era in vaccinology. *Nat Rev Drug Discov*. 2018 Apr;17(4):261–79.
119. Maryam Faiyaz. Nanomaterials in Alzheimer’s disease treatment: a comprehensive review. *Front Biosci (Landmark Ed)*. 2021;26(10):851.
120. Singh V, Yadav P, Mishra V. Recent Advances on Classification, Properties, Synthesis, and Characterization of Nanomaterials. In: Srivastava N, Srivastava M, Mishra PK, Gupta VK, editors. *Green Synthesis of Nanomaterials for Bioenergy Applications [Internet]*. 1st ed. Wiley; 2020 [cited 2023 Dec 19]. p. 83–97. Available from: <https://onlinelibrary.wiley.com/doi/10.1002/9781119576785.ch3>
121. Wang Z, Hu T, Liang R, Wei M. Application of Zero-Dimensional Nanomaterials in Biosensing. *Front Chem*. 2020 Apr 17;8:320.
122. Jeevanandam J, Sundaramurthy A, Sharma V, Murugan C, Pal K, Abdel Kodous MH, et al. Sustainability of One-Dimensional Nanostructures. In: *Sustainable Nanoscale Engineering [Internet]*. Elsevier; 2020 [cited 2023 Dec 21]. p. 83–113. Available from: <https://linkinghub.elsevier.com/retrieve/pii/B9780128146811000047>
123. Chen Y, Fan Z, Zhang Z, Niu W, Li C, Yang N, et al. Two-Dimensional Metal Nanomaterials: Synthesis, Properties, and Applications. *Chem Rev*. 2018 Jul 11;118(13):6409–55.
124. Ho DT, Ho VH, Babar V, Kim SY, Schwingenschlögl U. Complex three-dimensional graphene structures driven by surface functionalization. *Nanoscale*. 2020;12(18):10172–9.
125. Freudenberg U, Liang Y, Kiick KL, Werner C. Glycosaminoglycan-Based Biohybrid Hydrogels: A Sweet and Smart Choice for Multifunctional Biomaterials. *Advanced Materials*. 2016 Oct;28(40):8861–91.
126. Shodeinde AB, Murphy AC, Oldenkamp HF, Potdar AS, Ludolph CM, Peppas NA. Recent Advances in Smart Biomaterials for the Detection and Treatment of Autoimmune Diseases. *Adv Funct Materials*. 2020 Sep;30(37):1909556.
127. Kowalski PS, Bhattacharya C, Afewerki S, Langer R. Smart Biomaterials: Recent Advances and Future Directions. *ACS Biomater Sci Eng*. 2018 Nov 12;4(11):3809–17.
128. Amukarimi S, Ramakrishna S, Mozafari M. Smart biomaterials—A proposed definition and overview of the field. *Current Opinion in Biomedical Engineering*. 2021 Sep;19:100311.
129. Whitaker R, Hernaez-Estrada B, Hernandez RM, Santos-Vizcaino E, Spiller KL. Immunomodulatory Biomaterials for Tissue Repair. *Chem Rev*. 2021 Sep 22;121(18):11305–35.
130. Guerrieri AN, Montesi M, Sprio S, Laranga R, Mercatali L, Tampieri A, et al. Innovative Options for Bone Metastasis Treatment: An Extensive Analysis on Biomaterials-Based Strategies for Orthopedic Surgeons. *Front Bioeng Biotechnol*. 2020 Oct 6;8:589964.

131. Yu X, Tang X, Gohil SV, Laurencin CT. Biomaterials for Bone Regenerative Engineering. *Adv Healthcare Materials*. 2015 Jun;4(9):1268–85.
132. Allo BA, Costa DO, Dixon SJ, Mequanint K, Rizkalla AS. Bioactive and Biodegradable Nanocomposites and Hybrid Biomaterials for Bone Regeneration. *JFB*. 2012 Jun 20;3(2):432–63.
133. Dos Santos GG, Malherbi MS, De Souza NS, César GB, Tominaga TT, Miyahara RY, et al. 4th Generation Biomaterials Based on PVDF-Hydroxyapatite Composites Produced by Electrospinning: Processing and Characterization. *Polymers*. 2022 Oct 6;14(19):4190.
134. Ning C, Zhou L, Tan G. Fourth-generation biomedical materials. *Materials Today*. 2016 Jan;19(1):2–3.
135. Zhang Q, Zhou Z, Peng C, Huang T, Liu W, Liu Q, et al. Preparation and Properties of Novel Maleated Poly (D, L-lactide-co-glycolide) Porous Scaffolds for Tissue Engineering. *Journal of Macromolecular Science, Part B*. 2017 Jul 3;56(7):505–15.
136. Li ZH, Wang L, Dai HL, Wang XY, Li JS, Zhao Z. Fabrication, characterization, and in vitro evaluation of biomimetic silk fibroin porous scaffolds via supercritical CO₂ technology. *The Journal of Supercritical Fluids*. 2019 Aug;150:86–93.
137. Mansour FR, Waheed S, Paull B, Maya F. Porogens and porogen selection in the preparation of porous polymer monoliths. *J of Separation Science*. 2020 Jan;43(1):56–69.
138. Mouriño V, Boccaccini AR. Bone tissue engineering therapeutics: controlled drug delivery in three-dimensional scaffolds. *J R Soc Interface*. 2010 Feb 6;7(43):209–27.
139. Haider A, Haider S, Rao Kummara M, Kamal T, Alghyamah AAA, Jan Iftikhar F, et al. Advances in the scaffolds fabrication techniques using biocompatible polymers and their biomedical application: A technical and statistical review. *Journal of Saudi Chemical Society*. 2020 Feb;24(2):186–215.
140. Wubneh A, Tsekoura EK, Ayranci C, Uludağ H. Current state of fabrication technologies and materials for bone tissue engineering. *Acta Biomaterialia*. 2018 Oct;80:1–30.
141. Kishan AP, Robbins AB, Mohiuddin SF, Jiang M, Moreno MR, Cosgriff-Hernandez EM. Fabrication of macromolecular gradients in aligned fiber scaffolds using a combination of in-line blending and air-gap electrospinning. *Acta Biomaterialia*. 2017 Jul;56:118–28.
142. Seidi A, Sampathkumar K, Srivastava A, Ramakrishna S, Ramalingam M. Gradient Nanofiber Scaffolds for Tissue Engineering. *j nanosci nanotech*. 2013 Jul 1;13(7):4647–55.
143. Eltom A, Zhong G, Muhammad A. Scaffold Techniques and Designs in Tissue Engineering Functions and Purposes: A Review. *Advances in Materials Science and Engineering*. 2019 Mar 7;2019:1–13.
144. Zhang XY, Fang G, Zhou J. Additively Manufactured Scaffolds for Bone Tissue Engineering and the Prediction of their Mechanical Behavior: A Review. *Materials*. 2017 Jan 10;10(1):50.

145. Mirzaali MJ, Moosabeiki V, Rajaai SM, Zhou J, Zadpoor AA. Additive Manufacturing of Biomaterials—Design Principles and Their Implementation. *Materials*. 2022 Aug 8;15(15):5457.
146. Gu Z, Fu J, Lin H, He Y. Development of 3D bioprinting: From printing methods to biomedical applications. *Asian Journal of Pharmaceutical Sciences*. 2020 Sep;15(5):529–57.
147. Papaioannou TG, Manolesou D, Dimakakos E, Tsoucalas G, Vavuranakis M, Tousoulis D. 3D Bioprinting Methods and Techniques: Applications on Artificial Blood Vessel Fabrication. *Acta Cardiol Sin*. :6.
148. Parak A, Pradeep P, du Toit LC, Kumar P, Choonara YE, Pillay V. Functionalizing bioinks for 3D bioprinting applications. *Drug Discovery Today*. 2019 Jan;24(1):198–205.
149. Moroni L, Burdick JA, Highley C, Lee SJ, Morimoto Y, Takeuchi S, et al. Biofabrication strategies for 3D in vitro models and regenerative medicine. *Nat Rev Mater*. 2018 May;3(5):21–37.
150. Flora B, Kumar R, Mahdiah R, Zarei K, Chehrazi S, Kaur SD, et al. Recent Updates on Metal-Polymer Nanocomposites in 3D Bioprinting for Tissue Engineering Applications. *Nanofab [Internet]*. 2023 Jan 19 [cited 2023 Dec 19];8. Available from: <https://eaapublishing.org/journals/index.php/nanofab/article/view/291>
151. Li J, Chen M, Fan X, Zhou H. Recent advances in bioprinting techniques: approaches, applications and future prospects. *J Transl Med*. 2016 Dec;14(1):271.
152. Roseti L, Parisi V, Petretta M, Cavallo C, Desando G, Bartolotti I, et al. Scaffolds for Bone Tissue Engineering: State of the art and new perspectives. *Materials Science and Engineering: C*. 2017 Sep;78:1246–62.
153. Kumar A, Jacob A. Techniques in scaffold fabrication process for tissue engineering applications: A review. *j app biol biotech*. 2022 Apr 10;163–76.
154. Bajaj P, Schweller RM, Khademhosseini A, West JL, Bashir R. 3D Biofabrication Strategies for Tissue Engineering and Regenerative Medicine. *Annu Rev Biomed Eng*. 2014 Jul 11;16(1):247–76.
155. Du X, Fu S, Zhu Y. 3D printing of ceramic-based scaffolds for bone tissue engineering: an overview. *J Mater Chem B*. 2018;6(27):4397–412.
156. Martelli N, Serrano C, Van Den Brink H, Pineau J, Prognon P, Borget I, et al. Advantages and disadvantages of 3-dimensional printing in surgery: A systematic review. *Surgery*. 2016 Jun;159(6):1485–500.
157. Akbarzadeh R, Yousefi A. Effects of processing parameters in thermally induced phase separation technique on porous architecture of scaffolds for bone tissue engineering. *J Biomed Mater Res*. 2014 Aug;102(6):1304–15.
158. Ashammakhi N, Ahadian S, Zengjie F, Suthiwanich K, Lorestani F, Orive G, et al. Advances and Future Perspectives in 4D Bioprinting. *Biotechnol J*. 2018 Dec;13(12):1800148.
159. Jazayeri HE, Rodriguez-Romero M, Razavi M, Tahriri M, Ganjawalla K,

- Rasoulianboroujeni M, et al. The cross-disciplinary emergence of 3D printed bioceramic scaffolds in orthopedic bioengineering. *Ceramics International*. 2018 Jan;44(1):1–9.
160. Jeong J, Kim JH, Shim JH, Hwang NS, Heo CY. Bioactive calcium phosphate materials and applications in bone regeneration. *Biomater Res*. 2019 Dec;23(1):4.
161. Indrani DJ, Soegijono B, Adi WA, Trout N. PHASE COMPOSITION AND CRYSTALLINITY OF HYDROXYAPATITE WITH VARIOUS HEAT TREATMENT TEMPERATURES. *Int J App Pharm*. 2018 Jan 1;9:87.
162. Roopalakshmi S, Ravishankar R, Belaldavar Shrisha, Prasad RGSV, Phani AR. Investigation of Structural and Morphological Characteristic of Hydroxyapatite Synthesized by Sol-Gel Process. *Materials Today: Proceedings*. 2017;4(11):12026–31.
163. Trzaskowska M, Vivcharenko V, Przekora A. The Impact of Hydroxyapatite Sintering Temperature on Its Microstructural, Mechanical, and Biological Properties. *IJMS*. 2023 Mar 7;24(6):5083.
164. Khalid H, Chaudhry AA. Basics of hydroxyapatite—structure, synthesis, properties, and clinical applications. In: *Handbook of Ionic Substituted Hydroxyapatites* [Internet]. Elsevier; 2020 [cited 2023 Dec 22]. p. 85–115. Available from: <https://linkinghub.elsevier.com/retrieve/pii/B9780081028346000045>
165. Mohd Pu'ad NAS, Koshy P, Abdullah HZ, Idris MI, Lee TC. Syntheses of hydroxyapatite from natural sources. *Heliyon*. 2019 May;5(5):e01588.
166. Sobczak-Kupiec A, Malina D, Wzorek Z. COMPARATIVE STUDY OF HYDROXYAPATITE PREPARED BY THE AUTHORS WITH SELECTED COMMERCIALY AVAILABLE CERAMICS.
167. Bulina NV, Makarova SV, Baev SG, Matvienko AA, Gerasimov KB, Logutenko OA, et al. A Study of Thermal Stability of Hydroxyapatite. *Minerals*. 2021 Nov 24;11(12):1310.
168. Ahmed YMZ, El-Sheikh SM, Zaki ZI. Changes in hydroxyapatite powder properties via heat treatment. *Bull Mater Sci*. 2015 Dec;38(7):1807–19.
169. Waheed S, Sultan M, Jamil T, Hussain T. Comparative Analysis of Hydroxyapatite Synthesized by Sol-gel, Ultrasonication and Microwave Assisted Technique. *Materials Today: Proceedings*. 2015;2(10):5477–84.
170. Kavasi RM, Coelho CC, Platania V, Quadros PA, Chatzinikolaidou M. In Vitro Biocompatibility Assessment of Nano-Hydroxyapatite. *Nanomaterials*. 2021 Apr 28;11(5):1152.
171. Londoño-Restrepo SM, Millán-Malo BM, Del Real-López A, Rodríguez-García ME. In situ study of hydroxyapatite from cattle during a controlled calcination process using HT-XRD. *Materials Science and Engineering: C*. 2019 Dec;105:110020.
172. Balu SK, Andra S, Jeevanandam J, S MV, V S. Emerging marine derived nanohydroxyapatite and their composites for implant and biomedical applications. *Journal of the*

Mechanical Behavior of Biomedical Materials. 2021 Jul;119:104523.

173. Swain S, Bhaskar R, Gupta MK, Sharma S, Dasgupta S, Kumar A, et al. Mechanical, Electrical, and Biological Properties of Mechanochemically Processed Hydroxyapatite Ceramics. *Nanomaterials*. 2021 Aug 28;11(9):2216.

174. Castillo-Paz AM, Londoño-Restrepo SM, Tirado-Mejía L, Mondragón MA, Rodríguez-García ME. Nano to micro size transition of hydroxyapatite in porcine bone during heat treatment with low heating rates. *Progress in Natural Science: Materials International*. 2020 Aug;30(4):494–501.

175. Comín R, Cid MP, Grinschpun L, Oldani C, Salvatierra NA. Titanium-Hydroxyapatite Composites Sintered at Low Temperature for Tissue Engineering: In vitro Cell Support and Biocompatibility. *Journal of Applied Biomaterials & Functional Materials*. 2017 Apr;15(2):176–83.

176. Kumar L, Ahuja D. Preparation and characterization of aliphatic polyurethane and modified hydroxyapatite composites for bone tissue engineering. *Polym Bull*. 2020 Nov;77(11):6049–62.

177. Li H, Sun X, Li Y, Li B, Liang C, Wang H. Preparation and properties of carbon nanotube (Fe)/hydroxyapatite composite as magnetic targeted drug delivery carrier. *Materials Science and Engineering: C*. 2019 Apr;97:222–9.

178. Cakmak AM, Unal S, Sahin A, Oktar FN, Sengor M, Ekren N, et al. 3D Printed Polycaprolactone/Gelatin/Bacterial Cellulose/Hydroxyapatite Composite Scaffold for Bone Tissue Engineering. *Polymers*. 2020 Aug 29;12(9):1962.

179. Cestari F, Petretta M, Yang Y, Motta A, Grigolo B, Sglavo VM. 3D printing of PCL/nano-hydroxyapatite scaffolds derived from biogenic sources for bone tissue engineering. *Sustainable Materials and Technologies*. 2021 Sep;29:e00318.

180. Volkov AV, Muraev AA, Zharkova II, Voinova VV, Akoulina EA, Zhuikov VA, et al. Poly(3-hydroxybutyrate)/hydroxyapatite/alginate scaffolds seeded with mesenchymal stem cells enhance the regeneration of critical-sized bone defect. *Materials Science and Engineering: C*. 2020 Sep;114:110991.

181. Chakravarty J, Rabbi MF, Chalivendra V, Ferreira T, Brigham CJ. Mechanical and biological properties of chitin/poly(lactide) (PLA)/hydroxyapatite (HAP) composites cast using ionic liquid solutions. *International Journal of Biological Macromolecules*. 2020 May;151:1213–23.

182. Dideikin AT, Vul' AY. Graphene Oxide and Derivatives: The Place in Graphene Family. *Front Phys*. 2019 Jan 28;6:149.

183. Hwang TY, Choi Y, Song Y, Eom NSA, Kim S, Cho HB, et al. A noble gas sensor platform: linear dense assemblies of single-walled carbon nanotubes (LACNTs) in a multi-layered ceramic/metal electrode system (MLES). *J Mater Chem C*. 2018;6(5):972–9.

184. Aliyev E, Filiz V, Khan MM, Lee YJ, Abetz C, Abetz V. Structural Characterization of Graphene Oxide: Surface Functional Groups and Fractionated Oxidative Debris. *Nanomaterials*. 2019 Aug 18;9(8):1180.

185. Eckhart KE, Holt BD, Laurencin MG, Sydlík SA. Covalent conjugation of bioactive peptides to graphene oxide for biomedical applications. *Biomater Sci.* 2019;7(9):3876–85.
186. Tabish T, Pranjol M, Horsell D, Rahat A, Whatmore J, Winyard P, et al. Graphene Oxide-Based Targeting of Extracellular Cathepsin D and Cathepsin L As A Novel Anti-Metastatic Enzyme Cancer Therapy. *Cancers.* 2019 Mar 6;11(3):319.
187. Veclani D, Tolazzi M, Melchior A. Molecular Interpretation of Pharmaceuticals' Adsorption on Carbon Nanomaterials: Theory Meets Experiments. *Processes.* 2020 May 27;8(6):642.
188. Azizighannad S, Mitra S. Stepwise Reduction of Graphene Oxide (GO) and Its Effects on Chemical and Colloidal Properties. *Sci Rep.* 2018 Jul 4;8(1):10083.
189. Qi Y, Xia T, Li Y, Duan L, Chen W. Colloidal stability of reduced graphene oxide materials prepared using different reducing agents. *Environ Sci: Nano.* 2016;3(5):1062–71.
190. Gómez-Navarro C, Burghard M, Kern K. Elastic Properties of Chemically Derived Single Graphene Sheets. *Nano Lett.* 2008 Jul 1;8(7):2045–9.
191. Suk JW, Piner RD, An J, Ruoff RS. Mechanical Properties of Monolayer Graphene Oxide. *ACS Nano.* 2010 Nov 23;4(11):6557–64.
192. Konios D, Stylianakis MM, Stratakis E, Kymakis E. Dispersion behaviour of graphene oxide and reduced graphene oxide. *Journal of Colloid and Interface Science.* 2014 Sep;430:108–12.
193. Alam SN, Sharma N, Kumar L. Synthesis of Graphene Oxide (GO) by Modified Hummers Method and Its Thermal Reduction to Obtain Reduced Graphene Oxide (rGO)*. *Graphene.* 2017;06(01):1–18.
194. Mangadlao JD, Cao P, Choi D, Advincula RC. Photoreduction of Graphene Oxide and Photochemical Synthesis of Graphene–Metal Nanoparticle Hybrids by Ketyl Radicals. *ACS Appl Mater Interfaces.* 2017 Jul 26;9(29):24887–98.
195. Tai XH, Chook SW, Lai CW, Lee KM, Yang TCK, Chong S, et al. Effective photoreduction of graphene oxide for photodegradation of volatile organic compounds. *RSC Adv.* 2019;9(31):18076–86.
196. Tamang S, Rai S, Mondal MK, Bhattacharyya NK, Swain BP, Biswas J. Microwave-assisted reduction of graphene oxide using *Artemisia vulgaris* extract for supercapacitor application. *J Mater Sci: Mater Electron.* 2023 Mar;34(7):575.
197. Xiang X, Zhu Y, Yin M, Xia S, Guo C. Study of microwave reduction of graphene oxide suspension: structure and functional groups. *J Mater Sci.* 2022 Feb;57(5):3280–94.
198. Hidayah NMS, Liu WW, Lai CW, Noriman NZ, Khe CS, Hashim U, et al. Comparison on graphite, graphene oxide and reduced graphene oxide: Synthesis and characterization. In Penang, Malaysia; 2017 [cited 2022 Jun 14]. p. 150002. Available from: <http://aip.scitation.org/doi/abs/10.1063/1.5005764>
199. Dutta S, Sarkar S, Ray C, Pal T. Benzoin derived reduced graphene oxide (rGO) and its

- nanocomposite: application in dye removal and peroxidase-like activity. *RSC Adv.* 2013;3(44):21475.
200. Liu W, Speranza G. Chemical Reduction of GO: Comparing Hydroiodic Acid and Sodium Borohydride Chemical Approaches by X-ray Photoelectron Spectroscopy. *C.* 2022 Mar 22;8(2):20.
201. Wang BY, Hsu S, Chou CM, Wu TI, Hsiao VKS. Improved Mechanical Properties of Ultra-High Shear Force Mixed Reduced Graphene Oxide/Hydroxyapatite Nanocomposite Produced Using Spark Plasma Sintering. *Nanomaterials.* 2021 Apr 12;11(4):986.
202. Edward II, Abdul Manaf N, Tahir Abdul Muthalib SA, Musram Rakunman MR, Tan LS, Tsuji T. Synthesis of graphene oxide via electrochemical process: A short review towards flexible synthesis method. *IOP Conf Ser: Mater Sci Eng.* 2021 Apr 1;1142(1):012019.
203. Hung YF, Cheng C, Huang CK, Yang CR, Tseng SF. Investigation of electrochemical reduction effects on graphene oxide powders for high-performance supercapacitors. *Int J Adv Manuf Technol.* 2021 Mar;113(3–4):1203–13.
204. Jaafar E, Kashif M, Sahari SK, Ngaini Z. Effects of reduction temperatures on morphological, optical, and electrical properties of reduced graphene oxide (rGO) thin films. *Materials Today: Proceedings.* 2019;16:1702–7.
205. Lesiak B, Trykowski G, Tóth J, Biniak S, Kövér L, Rangam N, et al. Chemical and structural properties of reduced graphene oxide—dependence on the reducing agent. *J Mater Sci.* 2021 Feb;56(5):3738–54.
206. Dhanavel S, Revathy TA, Sivaranjani T, Sivakumar K, Palani P, Narayanan V, et al. 5-Fluorouracil and curcumin co-encapsulated chitosan/reduced graphene oxide nanocomposites against human colon cancer cell lines. *Polym Bull.* 2020 Jan;77(1):213–33.
207. Nahain AA, Lee JE, Jeong JH, Park SY. Photoresponsive Fluorescent Reduced Graphene Oxide by Spiropyran Conjugated Hyaluronic Acid for in Vivo Imaging and Target Delivery. *Biomacromolecules.* 2013 Nov 11;14(11):4082–90.
208. Chawda N, Basu M, Majumdar D, Poddar R, Mahapatra SK, Banerjee I. Engineering of Gadolinium-Decorated Graphene Oxide Nanosheets for Multimodal Bioimaging and Drug Delivery. *ACS Omega.* 2019 Jul 31;4(7):12470–9.
209. Chaturvedi M, Patel M, Bisht N, Shruti, Das Mukherjee M, Tiwari A, et al. Reduced Graphene Oxide-Polydopamine-Gold Nanoparticles: A Ternary Nanocomposite-Based Electrochemical Genosensor for Rapid and Early Mycobacterium tuberculosis Detection. *Biosensors.* 2023 Mar 4;13(3):342.
210. Haji Mohammadi Gohari P, Haghbin Nazarpak M, Solati-Hashjin M. The effect of adding reduced graphene oxide to electrospun polycaprolactone scaffolds on MG-63 cells activity. *Materials Today Communications.* 2021 Jun;27:102287.
211. Mousavi A, Mashayekhan S, Baheiraei N, Pourjavadi A. Biohybrid oxidized alginate/myocardial extracellular matrix injectable hydrogels with improved electromechanical

properties for cardiac tissue engineering. *International Journal of Biological Macromolecules*. 2021 Jun;180:692–708.

212. Alipour N, Namazi H. Chelating ZnO-dopamine on the surface of graphene oxide and its application as pH-responsive and antibacterial nanohybrid delivery agent for doxorubicin. *Materials Science and Engineering: C*. 2020 Mar;108:110459.

213. Narayanam PK, Soni P, Botcha VD, Singh G, Major SS. Transparent and Hydrophobic “Reduced Graphene Oxide–Titanium Dioxide” Nanocomposites for Nonwetting Device Applications. *ACS Appl Nano Mater*. 2018 Oct 26;1(10):5691–701.

214. Huang W, Ding S, Chen Y, Hao W, Lai X, Peng J, et al. 3D NiO hollow sphere/reduced graphene oxide composite for high-performance glucose biosensor. *Sci Rep*. 2017 Jul 12;7(1):5220.

215. Heinze T, Liebert T, Klüfers P. Carboxymethylation of cellulose in unconventional media.

216. Singh R, Singh J, Sonika, Singh H. Green synthesis of carboxymethyl cellulose from agricultural waste its characterization. *J Phys: Conf Ser*. 2022 May 1;2267(1):012144.

217. Mondal MdIH, Yeasmin MstS, Rahman MdS. Preparation of food grade carboxymethyl cellulose from corn husk agrowaste. *International Journal of Biological Macromolecules*. 2015 Aug;79:144–50.

218. Shui T, Feng S, Chen G, Li A, Yuan Z, Shui H, et al. Synthesis of sodium carboxymethyl cellulose using bleached crude cellulose fractionated from cornstalk. *Biomass and Bioenergy*. 2017 Oct;105:51–8.

219. Dai H, Zhang Y, Ma L, Zhang H, Huang H. Synthesis and response of pineapple peel carboxymethyl cellulose-g-poly (acrylic acid-co-acrylamide)/graphene oxide hydrogels. *Carbohydrate Polymers*. 2019 Jul;215:366–76.

220. Golbaghi L, Khamforoush M, Hatami T. Carboxymethyl cellulose production from sugarcane bagasse with steam explosion pulping: Experimental, modeling, and optimization. *Carbohydrate Polymers*. 2017 Oct;174:780–8.

221. Rachtanapun P, Jantrawut P, Klunklin W, Jantanasakulwong K, Phimolsiripol Y, Leksawasdi N, et al. Carboxymethyl Bacterial Cellulose from Nata de Coco: Effects of NaOH. *Polymers*. 2021 Jan 22;13(3):348.

222. Sarkar C, Anuvrat K, Garai S, Sahu SK, Chakraborty J. One pot method to synthesize three-dimensional porous hydroxyapatite nanocomposite for bone tissue engineering. *J Porous Mater*. 2020 Feb;27(1):225–35.

223. Koneru A, Dharmalingam K, Anandalakshmi R. Cellulose based nanocomposite hydrogel films consisting of sodium carboxymethylcellulose–grapefruit seed extract nanoparticles for potential wound healing applications. *International Journal of Biological Macromolecules*. 2020 Apr;148:833–42.

224. Sadeghi S, Nourmohammadi J, Ghaee A, Soleimani N. Carboxymethyl cellulose-human

- hair keratin hydrogel with controlled clindamycin release as antibacterial wound dressing. *International Journal of Biological Macromolecules*. 2020 Mar;147:1239–47.
225. Saladino ML, Markowska M, Carmone C, Cancemi P, Alduina R, Presentato A, et al. Graphene Oxide Carboxymethylcellulose Nanocomposite for Dressing Materials. *Materials*. 2020 Apr 23;13(8):1980.
226. Singh BN, Panda NN, Mund R, Pramanik K. Carboxymethyl cellulose enables silk fibroin nanofibrous scaffold with enhanced biomimetic potential for bone tissue engineering application. *Carbohydrate Polymers*. 2016 Oct;151:335–47.
227. Javanbakht S, Pooresmaeil M, Namazi H. Green one-pot synthesis of carboxymethylcellulose/Zn-based metal-organic framework/graphene oxide bio-nanocomposite as a nanocarrier for drug delivery system. *Carbohydrate Polymers*. 2019 Mar;208:294–301.
228. Maver U, Khanari K, Žižek M, Gradišnik L, Repnik K, Potočnik U, et al. Carboxymethyl cellulose/diclofenac bioactive coatings on AISI 316LVM for controlled drug delivery, and improved osteogenic potential. *Carbohydrate Polymers*. 2020 Feb;230:115612.
229. Casaburi A, Montoya Rojo Ú, Cerrutti P, Vázquez A, Foresti ML. Carboxymethyl cellulose with tailored degree of substitution obtained from bacterial cellulose. *Food Hydrocolloids*. 2018 Feb;75:147–56.
230. Alabi FM, Lajide L, Ajayi OO, Adebayo AO, Emmanuel S, Fadeyi AE. Synthesis and characterization of carboxymethyl cellulose from *Musa paradisiaca* and *Tithonia diversifolia*. *Afr J Pure Appl Chem*. 2020 Mar 31;14(1):9–23.
231. Kimani P, Kareru P, Madivoli S, Kairigo P, Maina E, Rechab O. Comparative Study of Carboxymethyl Cellulose Synthesis from Selected Kenyan Biomass. *CSIJ*. 2016 Jan 10;17(4):1–8.
232. Lakshmi DS, Trivedi N, Reddy CRK. Synthesis and characterization of seaweed cellulose derived carboxymethyl cellulose. *Carbohydrate Polymers*. 2017 Feb;157:1604–10.
233. An F, Fang K, Liu X, Li C, Liang Y, Liu H. Rheological properties of carboxymethyl hydroxypropyl cellulose and its application in high quality reactive dye inkjet printing on wool fabrics. *International Journal of Biological Macromolecules*. 2020 Dec;164:4173–82.
234. Dobaj Štiglic A, Kargl R, Beaumont M, Strauss C, Makuc D, Egger D, et al. Influence of Charge and Heat on the Mechanical Properties of Scaffolds from Ionic Complexation of Chitosan and Carboxymethyl Cellulose. *ACS Biomater Sci Eng*. 2021 Aug 9;7(8):3618–32.
235. Tabari M. Investigation of Carboxymethyl Cellulose (CMC) on Mechanical Properties of Cold Water Fish Gelatin Biodegradable Edible Films. *Foods*. 2017 May 27;6(6):41.
236. Karimi M, Naimi-Jamal MR. Carboxymethyl cellulose as a green and biodegradable catalyst for the solvent-free synthesis of benzimidazoloquinazolinone derivatives. *Journal of Saudi Chemical Society*. 2019 Feb;23(2):182–7.
237. Yaradoddi JS, Banapurmath NR, Ganachari SV, Soudagar MEM, Mubarak NM, Hallad S,

- et al. Biodegradable carboxymethyl cellulose based material for sustainable packaging application. *Sci Rep*. 2020 Dec 15;10(1):21960.
238. Donnalaja F, Jacchetti E, Soncini M, Raimondi MT. Natural and Synthetic Polymers for Bone Scaffolds Optimization. *Polymers*. 2020 Apr 14;12(4):905.
239. Annael Orozco-Díaz C, Moorehead R, Reilly GC, Gilchrist F, Miller C. Characterization of a composite polylactic acid-hydroxyapatite 3D-printing filament for bone-regeneration. *Biomed Phys Eng Express*. 2020 Mar 1;6(2):025007.
240. Obada DO, Dauda ET, Abifarin JK, Dodoo-Arhin D, Bansod ND. Mechanical properties of natural hydroxyapatite using low cold compaction pressure: Effect of sintering temperature. *Materials Chemistry and Physics*. 2020 Jan;239:122099.
241. Shen H, Larsen MB, Roessler AG, Zimmerman PM, Boydston AJ. Mechanochemical Release of *N*-Heterocyclic Carbenes from Flex-Activated Mechanophores. *Angew Chem Int Ed*. 2021 Jun 7;60(24):13559–63.
242. Cho JS, Rhee S. The densification mechanism of hydroxyapatite particles during spray pyrolysis with variable carrier gas rates of flow. *J Biomed Mater Res*. 2012 Feb;100B(2):493–500.
243. Kim JH, Yanagisawa K, Onda A, Sasabe E, Yamamoto T. Densification behavior of hydroxyapatite green pellets prepared by different methods. *J Ceram Soc Japan*. 2015;123(1444):1097–101.
244. Figueiredo M, Fernando A, Martins G, Freitas J, Judas F, Figueiredo H. Effect of the calcination temperature on the composition and microstructure of hydroxyapatite derived from human and animal bone. *Ceramics International*. 2010 Dec;36(8):2383–93.
245. Yelten A, Yilmaz S. Various Parameters Affecting the Synthesis of the Hydroxyapatite Powders by the Wet Chemical Precipitation Technique. *Materials Today: Proceedings*. 2016;3(9):2869–76.
246. Yelten-Yilmaz A, Yilmaz S. Wet chemical precipitation synthesis of hydroxyapatite (HA) powders. *Ceramics International*. 2018 Jun;44(8):9703–10.
247. Mehrali M, Moghaddam E, Shirazi SFS, Baradaran S, Mehrali M, Latibari ST, et al. Synthesis, Mechanical Properties, and in Vitro Biocompatibility with Osteoblasts of Calcium Silicate–Reduced Graphene Oxide Composites. *ACS Appl Mater Interfaces*. 2014 Mar 26;6(6):3947–62.
248. Pei S, Cheng HM. The reduction of graphene oxide. *Carbon*. 2012 Aug;50(9):3210–28.
249. Le GTT, Manyam J, Opaprakasit P, Chanlek N, Grisdanurak N, Sreearunothai P. Divergent mechanisms for thermal reduction of graphene oxide and their highly different ion affinities. *Diamond and Related Materials*. 2018 Oct;89:246–56.
250. Sengupta I, Chakraborty S, Talukdar M, Pal SK, Chakraborty S. Thermal reduction of graphene oxide: How temperature influences purity. *J Mater Res*. 2018 Dec 14;33(23):4113–22.

251. Ali A, Chiang YW, Santos RM. X-ray Diffraction Techniques for Mineral Characterization: A Review for Engineers of the Fundamentals, Applications, and Research Directions. *Minerals*. 2022 Feb 6;12(2):205.
252. Patrizi B, Siciliani De Cumis M, Viciani S, D'Amato F. Dioxin and Related Compound Detection: Perspectives for Optical Monitoring. *IJMS*. 2019 May 30;20(11):2671.
253. Nguyen PH, Derreumaux P. Structures of the intrinsically disordered A β , tau and α -synuclein proteins in aqueous solution from computer simulations. *Biophysical Chemistry* [Internet]. 2020 Sep [cited 2021 Aug 17];264. Available from: <https://linkinghub.elsevier.com/retrieve/pii/S0301462220301290>
254. Khalil NZ, Johanne MF, Ishak M. Influence of Al₂O₃ nanoreinforcement on the adhesion and thermomechanical properties for epoxy adhesive. *Composites Part B: Engineering*. 2019 Sep;172:9–15.
255. Gupta B, Agarwal R, Sarwar Alam M. Preparation and characterization of polyvinyl alcohol-polyethylene oxide-carboxymethyl cellulose blend membranes. *J Appl Polym Sci*. 2013 Jan 15;127(2):1301–8.
256. Chakraborty S, Ponrasu T, Chandel S, Dixit M, Muthuvijayan V. for enhancing angiogenesis in tissue engineering applications. :14.
257. Pandey V, Haider T, Jain P, Gupta PN, Soni V. Silk as a leading-edge biological macromolecule for improved drug delivery. *Journal of Drug Delivery Science and Technology*. 2020 Feb;55:101294.
258. Abifarin JK. Taguchi grey relational analysis on the mechanical properties of natural hydroxyapatite: effect of sintering parameters. *Int J Adv Manuf Technol*. 2021 Nov;117(1–2):49–57.
259. Kumar PN, Rajadurai A, Muthuramalingam T. Multi-Response Optimization on Mechanical Properties of Silica Fly Ash Filled Polyester Composites Using Taguchi-Grey Relational Analysis. *Silicon*. 2018 Jul;10(4):1723–9.
260. Pandya VJ, Rathod PP. Optimization of mechanical properties of green composites by gray relational analysis. *Materials Today: Proceedings*. 2020;27:19–22.
261. Sridevi S, Sutha S, Kavitha L, Gopi D. Physicochemical and biological behaviour of biogenic derived hydroxyapatite and carboxymethyl cellulose/sodium alginate biocomposite coating on Ti6Al4V alloy for biomedical applications. *Materials Chemistry and Physics*. 2020 Nov;254:123455.
262. Verma AS, Cheema MS, Kant S, Suri NM. Statistical analysis and optimization of process parameters in development of metal matrix composite using industrial waste. *Sādhanā*. 2020 Dec;45(1):200.
263. Topuz M, Dikici B, Gavgali M. Titanium-based composite scaffolds reinforced with hydroxyapatite-zirconia: Production, mechanical and in-vitro characterization. *Journal of the Mechanical Behavior of Biomedical Materials*. 2021 Jun;118:104480.

264. Pradhan S, Maity K. Optimization of Machining Parameter Characteristics during Turning of Ti-6Al-4V using Desirability Function Analysis. *Materials Today: Proceedings*. 2018;5(11):25740–9.
265. Manjubala I, Basu P, Narendrakumar U. In situ synthesis of hydroxyapatite/carboxymethyl cellulose composites for bone regeneration applications. *Colloid Polym Sci*. 2018 Oct;296(10):1729–37.
266. Raj SS, Michailovich KA, Subramanian K, Sathiamoorthy S, Kandasamy KT. Philosophy of Selecting ASTM Standards for Mechanical Characterization of Polymers and Polymer Composites. *Mater Plast*. 2021 Oct 5;58(3):247–56.
267. Darmawan AS, Siswanto WA, Febrianto BW, Sujitno T. THE INFLUENCES OF ION IMPLANTATION DOSES TO COMMERCIALY PURE TITANIUM SURFACE HARDNESS. 2012;
268. Beh CY, Cheng EM, Mohd Nasir NF, Mohd Tarmizi EZ, Eng SK, Abdul Majid MS, et al. Morphological and optical properties of porous hydroxyapatite/cornstarch (HAp/Cs) composites. *Journal of Materials Research and Technology*. 2020 Nov;9(6):14267–82.
269. Akbari R, Antonini C. Contact angle measurements: From existing methods to an open-source tool. *Advances in Colloid and Interface Science*. 2021 Aug;294:102470.
270. Reid JA, Callanan A. Influence of aorta extracellular matrix in electrospun polycaprolactone scaffolds. *J of Applied Polymer Sci*. 2019 Nov 20;136(44):48181.
271. Kokubo T, Takadama H. How useful is SBF in predicting in vivo bone bioactivity? *Biomaterials*. 2006 May;27(15):2907–15.
272. Lee JH, Shin YC, Lee SM, Jin OS, Kang SH, Hong SW, et al. Enhanced Osteogenesis by Reduced Graphene Oxide/Hydroxyapatite Nanocomposites. *Sci Rep*. 2015 Dec;5(1):18833.
273. Türk S, Altınsoy I, Efe GÇ, Ipek M, Özacar M, Bindal C. The effect of reduction of graphene oxide on the formation of hydroxyapatite and tricalcium phosphate. *Vacuum*. 2018 Feb;148:1–10.
274. Sayed . M. 3D Carboxymethyl Cellulose/Hydroxyapatite (CMC/HA) Scaffold Composites Based on Recycled Eggshell. *J App Pharm Sci [Internet]*. 2018 [cited 2023 Jul 22]; Available from: http://www.japsonline.com/abstract.php?article_id=2572
275. He X, Tang K, Li X, Wang F, Liu J, Zou F, et al. A porous collagen-carboxymethyl cellulose/hydroxyapatite composite for bone tissue engineering by bi-molecular template method. *International Journal of Biological Macromolecules*. 2019 Sep;137:45–53.
276. Shishatskaya E, Nemtsev I, Lukyanenko A, Vasiliev A, Kiselev E, Sukovatyi A, et al. Polymer Films of Poly-3-hydroxybutyrate Synthesized by *Cupriavidus necator* from Different Carbon Sources. *J Polym Environ*. 2021 Mar;29(3):837–50.
277. Venkataprasanna KS, Prakash J, Anusuya T, Devanand Venkatasubbu G. Size dependent

- mechanistic activity of titanium dioxide nanoparticles for enhanced fibroblast cell proliferation and anti-bacterial activity. *J Sol-Gel Sci Technol*. 2021 Sep;99(3):565–75.
278. Alshemary AZ, Akram M, Taha A, Tezcaner A, Evis Z, Hussain R. Physico-chemical and biological properties of hydroxyapatite extracted from chicken beaks. *Materials Letters*. 2018 Mar;215:169–72.
279. Ramesh S, Natasha AN, Tan CY, Bang LT, Ramesh S, Ching CY, et al. Direct conversion of eggshell to hydroxyapatite ceramic by a sintering method. *Ceramics International*. 2016 May;42(6):7824–9.
280. Muniyalakshmi M, Sethuraman K, Silambarasan D. Synthesis and characterization of graphene oxide nanosheets. *Materials Today: Proceedings*. 2020;21:408–10.
281. Xiang C, Wang C, Guo R, Lan J, Lin S, Jiang S, et al. Synthesis of carboxymethyl cellulose-reduced graphene oxide aerogel for efficient removal of organic liquids and dyes. *J Mater Sci*. 2019 Jan;54(2):1872–83.
282. Nosrati H, Sarraf-Mamoory R, Zolfaghari Emameh R, Aidun A, Canillas Perez M. Enhancing mechanical properties of hydroxyapatite-reduced graphene oxide nanocomposites by increasing the spark plasma sintering temperature. *Inorganic and Nano-Metal Chemistry*. 2020 Nov 30;1–11.
283. Faia-Torres AB, Guimond-Lischer S, Rottmar M, Charnley M, Goren T, Maniura-Weber K, et al. Differential regulation of osteogenic differentiation of stem cells on surface roughness gradients. *Biomaterials*. 2014 Nov;35(33):9023–32.
284. Kunzler TP, Drobek T, Schuler M, Spencer ND. Systematic study of osteoblast and fibroblast response to roughness by means of surface-morphology gradients. *Biomaterials*. 2007 May;28(13):2175–82.
285. Rausch-fan X, Qu Z, Wieland M, Matejka M, Schedle A. Differentiation and cytokine synthesis of human alveolar osteoblasts compared to osteoblast-like cells (MG63) in response to titanium surfaces. *Dental Materials*. 2008 Jan;24(1):102–10.
286. Andrukhov O, Huber R, Shi B, Berner S, Rausch-Fan X, Moritz A, et al. Proliferation, behavior, and differentiation of osteoblasts on surfaces of different microroughness. *Dental Materials*. 2016 Nov;32(11):1374–84.
287. Zeng Y, Pei X, Yang S, Qin H, Cai H, Hu S, et al. Graphene oxide/hydroxyapatite composite coatings fabricated by electrochemical deposition. *Surface and Coatings Technology*. 2016 Jan;286:72–9.
288. Kang MS. Reduced graphene oxide coating enhances osteogenic differentiation of human mesenchymal stem cells on Ti surfaces. 2021;9.
289. Heidari F, Razavi M, Ghaedi M, Forooghi M, Tahriri M, Tayebi L. Investigation of mechanical properties of natural hydroxyapatite samples prepared by cold isostatic pressing method. *Journal of Alloys and Compounds*. 2017 Feb;693:1150–6.

290. Zhao X, Chen X, Gui Z, Zheng J, Yang P, Liu A, et al. Carbon fiber reinforced hydroxyapatite composites with excellent mechanical properties and biological activities prepared by spark plasma sintering. *Ceramics International*. 2020 Dec;46(17):27446–56.
291. Liu X, Ouyang L, Chen L, Qiao Y, Ma X, Xu G, et al. Hydroxyapatite composited PEEK with 3D porous surface enhances osteoblast differentiation through mediating NO by macrophage. *Regenerative Biomaterials*. 2022 Apr 8;9:rbab076.
292. Ramli MI, Sulong AB, Muhamad N, Muchtar A, Arifin A, Mohd Foudzi F, et al. Effect of sintering parameters on physical and mechanical properties of powder injection moulded stainless steel-hydroxyapatite composite. Riveiro Rodríguez A, editor. *PLoS ONE*. 2018 Oct 25;13(10):e0206247.
293. Elif Ö, Belma Ö, İlkay Ş. Production of biologically safe and mechanically improved reduced graphene oxide/hydroxyapatite composites. *Mater Res Express*. 2017 Jan 16;4(1):015601.
294. El-Sakhawy M, Tohamy HAS, Cellulose and Paper Department, National Research Centre, 33, El Bohouth Str., P.O. 12622, Dokki Giza, Egypt, Salama A, Cellulose and Paper Department, National Research Centre, 33, El Bohouth Str., P.O. 12622, Dokki Giza, Egypt, Kamel S, et al. THERMAL PROPERTIES OF CARBOXYMETHYL CELLULOSE ACETATE BUTYRATE. *Cellulose Chem Technol*. 2019 Aug 28;53(7–8):667–75.
295. Azzaoui K, Mejdoubi E, Lamhamdi A, Jodeh S, Hamed O, Berrabah M, et al. Preparation and characterization of biodegradable nanocomposites derived from carboxymethyl cellulose and hydroxyapatite. *Carbohydrate Polymers*. 2017 Jul;167:59–69.
296. Son YR, Rhee KY, Park SJ. Influence of reduced graphene oxide on mechanical behaviors of sodium carboxymethyl cellulose. *Composites Part B: Engineering*. 2015 Dec;83:36–42.
297. Adalarasan R, Santhanakumar M, Rajmohan M. Application of Grey Taguchi-based response surface methodology (GT-RSM) for optimizing the plasma arc cutting parameters of 304L stainless steel. *Int J Adv Manuf Technol*. 2015;
298. Harun NA, Benning MJ, Horrocks BR, Fulton DA. Gold nanoparticle-enhanced luminescence of silicon quantum dots co-encapsulated in polymer nanoparticles. *Nanoscale*. 2013;5(9):3817.
299. Petrakova NV, Lysenkov AS, Ashmarin AA, Egorov AA, Fedotov AY, Shvorneva LI, et al. Effect of hot pressing temperature on the microstructure and strength of hydroxyapatite ceramic. *Inorg Mater Appl Res*. 2013 Jul;4(4):362–7.
300. Han W, Shin J, Ho Shin J. Low-cost, open-source contact angle analyzer using a mobile phone, commercial tripods and 3D printed parts. *HardwareX*. 2022 Oct;12:e00327.
301. de Britto D, Assis OBG. Thermal degradation of carboxymethylcellulose in different salty forms. *Thermochimica Acta*. 2009 Oct;494(1–2):115–22.
302. Hasan A, Morshed M, Memic A, Hassan S, Webster T, Marei H. Nanoparticles in tissue engineering: applications, challenges and prospects. *IJN*. 2018 Sep;Volume 13:5637–55.

303. Shi H, Zhou Z, Li W, Fan Y, Li Z, Wei J. Hydroxyapatite Based Materials for Bone Tissue Engineering: A Brief and Comprehensive Introduction. *Crystals*. 2021 Feb 1;11(2):149.

304. Liuyun J, Yubao L, Chengdong X. Preparation and biological properties of a novel composite scaffold of nano-hydroxyapatite/chitosan/carboxymethyl cellulose for bone tissue engineering. *J Biomed Sci*. 2009;16(1):65.

LIST OF PUBLICATIONS

Communicated:

1. The research paper on “Development of Hydroxyapatite/Reduced Graphene Oxide/Carboxymethyl Cellulose-based Nanocomposite with Ameliorated Mechanical Properties for Possible Bone Regeneration” has been communicated in **Macromol** published by mdpi, under Manuscript ID: macromol-3162747

PUBLISHED

1. Development of chemically synthesized hydroxyapatite composite with reduced graphene oxide for enhanced mechanical properties **B Flora**, R Kumar, P Tiwari, A Kumar, J Ruokolainen... - journal of the mechanical behavior of biomedical materials, 2023
2. Recent Updates on Metal-Polymer Nanocomposites in 3D Bioprinting for Tissue Engineering Applications **B Flora**, R Kumar, R Mahdieh, K Zarei, S Chehrazi... - Nanofabrication, 2023

CONFERENCES AND WORKSHOP

1. Attended the Gian course on “Hepatic and Bone Tissue Development for Drug Metabolism and Tissue Engineering” held at IIT Kanpur, 2019.
2. Successfully attended one week FDP/STC on “Recent Advancement in Biomaterials and Nanotechnology for Biomedical Applications” held at Dr. B.R Ambedkar National Institute of Technology, Jalandhar, 2019.
3. Successfully completed the Nptel course on “ Biomaterials by Mukesh Doble “ and got .
4. Participated in the DBT sponsored Webinar on” Neural Circuits in Health and Disease” through Google Meet, 2020.

5. Participated in SPARC-INDO_US Immunology Workshop organized by IIT Ropar and The George Washington University, USA, 2020.
6. Participated in International Webinar on “Green Synthesized Bionanomaterials towards Cancer Therapy “, by Dr SNS Rajalakshmi College of Arts and Science, Tamilnadu, 2020.
7. Successfully delivered Oral presentation on “Chemical synthesis of hydroxyapatite and reduced graphene oxide composite with improved mechanical properties” in International Conference on Biomacromolecules and Cellular Interface (ICBCI-2021) held at Dr B.R.Ambedkar National Institute of Technology, Jalandhar.
8. Participated in International Webinar on “Advanced Transparent Ceramic Materials for Defence Applications organized by Centre for Research and Development in Education and Social Integration (CRESIHRD),2022.
9. Successfully attended one week FDP/STC on “Recent Advancement in Biomaterials and Nanotechnology for Biomedical Applications” held at Dr. B.R Ambedkar National Institute of Technology, Jalandhar, 2019.

10. Successfully delivered Poster presentation on “Improved mechanical properties of Hot-pressed ternary blend of hydroxyapatite, reduced graphene oxide and carboxymethyl cellulose” in the International Conference on Fundamental and Industrial Research (iConFIRM2023) at IIT Ropar.